CARBONATITE METASOMATISM IN THE MANTLE: SOURCES AND ROLES OF CARBONATE IN METASOMATIC ENRICHMENT PROCESSES IN THE LITHOSPHERE

by

Gregory M. Yaxley BSc. (Hons). Dip. Ed.

Submitted in fulfilment of the requirements
for the degree of
Doctor of Philosophy (Geology)
University of Tasmania

June, 1993.

STATEMENT

This thesis contains the results of research done in the Geology Department, University of Tasmania between 1989 and 1993. Part of the material presented in Chapters 2 and 3 comprise the following published article;

YAXLEY GM, CRAWFORD AJ and GREEN DH, (1991): Evidence for carbonatite metasomatism in spinel peridotite xenoliths from western Victoria, Australia: Earth Planet. Sci. Lett. 107, 305-317.

The co-authors for this paper were supervisors for the author's PhD research.

This thesis contains no material which has been accepted or submitted for the award of any other higher degree or graduate diploma in any tertiary institution and to the best of the author's knowledge and belief, the thesis contains no material previously published or written by another person, except where due reference is made in the text of the thesis.

Gregory M. Yaxley
University of Tasmania
June, 1993.

CONTENTS

LIST OF TABLES

LIST OF FIGURES

ACKNOWLEDGMENTS

A large number of people have contributed significantly in many different ways to the completion of this project. The author wishes therefore to acknowledge (in no particular order) the following;

• Professor David Green, for suggesting the research topic, and for patient and enthusiastic supervision, support and leadership throughout.

• Dr Tony Crawford, for good-humoured encouragement, enthusiasm and thoughtful supervision.

• Mr Keith Harris, for initiating me into the often bizarre rituals and practises of high pressure experimental petrology, for his rather anhydrous humour, and for his wry acceptance of the inevitable fact that not everyone is as good at welding capsules shut as he is.

• Mr Wis Jablonski, for his expertise, instruction and assistance with scanning electron microscopy, electron probe microanalysis and related problematica.

• Dr Rick Varne for a number of valuable discussions, for arranging some financial support in the final stages of the project, and for signing countless bits of paper.

• Mr Phil Robinson and Nilar Zhaw for instruction and assistance with sample preparation for, and running of the XRF machine. Massimo Gasparon is also thanked for assistance with compilation of a table of XRF operating conditions.

• Many and assorted post-doctoral and visiting fellows who have worked in this department at various times over the last few years, but in particular Drs Russell Sweeney, Chris Ballhaus, Wayne Taylor, Trevor Falloon, Steve Eggins, Leonid Danyushevsky, Dima Kamenetsky, John Sinton and many others.

• Many and even more assorted postgraduate students, including Ingvar (The Viking) Sigurdsson, Massimo (The Italian) Gasparon, Fernando (The Argentinian) Della Pasqua, Ruth (just call me Ruth) Lanyon, Andrew (Bear) McNeill, Marcel (The Dutchman) Kampermann, Geoff (OHA) Nichols, Paul (Paul) Kitto, Mike Seitz, Ai Yang, Udi Hartono, Rob Lewis, and many others.

• Jeanette Hankin and Julie Beattie for secretarial assistance, and June Pongratz for ironing out the odd software problem, and for providing the coffee.

• Simon Stevens, for some startlingly skilful lapidary work, particularly with many fragile experimental runs full of all sorts of mechanically weak and soluble carbonates.

• Drs Roberta Rudnick, and Bill McDonough of RSES, and Prof. Trevor Green of Macquarie University for their interest and assistance with the carbonatite metasomatism story.

• Finally, I wish to make special mention of my gratitude to Jennie, Kerrie and Keaghan for their continuing patience and support throughout the last few years.

ABSTRACT

Recent high pressure experimental work in the Hawaiian pyrolite+H_2O+CO_2 system (Wallace and Green, 1988; Falloon and Green, 1990) has revealed the presence of a stability field for high Mg/(Mg+ΣFe), sodic dolomitic carbonatite melt in equilibrium with pargasitic lherzolite at pressures greater than the decarbonation reaction opx + dol = ol + cpx + CO_2. Carbonatite melts could therefore be formed as low degree primary melts of carbonated peridotite at depths greater than ≈60km, or by crystallization and reaction of amphibole+clinopyroxene from carbonated, undersaturated silicate melts within the upper mantle at depths of 60-90 km. Such carbonatite melts could segregate and ascend from their source regions at very low melt fractions (<0.02%; Hunter and MacKenzie, 1988). Analogy with natural eruptive carbonatites suggests that primary carbonatites would possess extreme LILE enrichment, and may therefore have an important role in metasomatism of the lithosphere at pressures of 15-20 kbars (Green and Wallace, 1988).

A suite of mantle xenoliths (apatite+amphibole bearing magnesian wehrlites, lherzolites and harzburgites) from western Victoria, Australia, display the predicted (Green and Wallace, 1988) petrographic and geochemical signatures of carbonatite metasomatism, namely, an unusual assemblage of magnesian olivine and diopsidic clinopyroxene in the absence of orthopyroxene (wehrlites), textural evidence of replacement of primary orthopyroxene by jadeitic clinopyroxene and forsteritic olivine (lherzolites and harzburgites), the almost ubiquitous presence of significant accessory apatite, unusually high whole-rock CaO/Al_2O_3 and Na_2O/Al_2O_3 values, and extreme LILE enrichment without concomitant TiO_2 enrichment.

Comparison of the trace element and isotopic characteristics of this carbonatite metasomatised suite of apatite+amphibole-bearing magnesian spinel wehrlites with other, previously reported (O'Reilly and Griffin, 1988; Stolz and Davies, 1988), southeastern Australian spinel peridotite xenoliths, suggests that those containing apatite+low-Ti pargasite have also been metasomatised by ephemeral, dolomitic carbonatite melts. Low Ti/Eu, high Zr/Hf, and restricted bulk earth-like Sr-Nd isotopic characteristics are characteristic of this metasomatic style within the southeastern Australian lithosphere. This contrasts with metasomatism related to hydration or basaltic intrusion of the lithosphere, in which Ti/Eu and Zr/Hf remain unfractionated at primitive mantle values of around 7740 and 36 respectively.

A model for carbonatite metasomatism is proposed in which undersaturated mafic silicate melts, derived from asthenospheric upwelling or diapirism, crystallize clinopyroxene + amphibole ± phlogopite as they ascend into the stability field of hydrous garnet peridotite+carbonatite melt at P≤30 kbars. The residual liquid evolves to sodic dolomitic carbonatite with low Ti/Eu, high Zr/Hf, and extreme enrichment in Sr and REE. This carbonatite melt segregates at low melt fractions and ascends rapidly, finally being absorbed by the lithosphere as it intersects a series of end-member decarbonation reactions at around 15-20 kbars. The nett effect of these is to react the enstatite and Mg-Tschermak's components of primary orthopyroxene, and $MgAl_2O_4$ component in spinel, with sodium carbonate and dolomitic components of the carbonatite, producing jadeite-ureiite solid solution in clinopyroxene, forsteritic olivine and CO_2-rich fluid. Evolution of the reacting carbonatite leads to deposition of pargasitic amphibole and apatite. In some cases, replacement of primary orthopyroxene by sodic Cr-diopsidic clinopyroxene and forsteritic olivine was complete. Subsequent annealing produced the texturally equilibrated wehrlites. Interruption of the metasomatic process by entrainment in the host magma produced apatite+amphibole-bearing spinel lherzolites and harzburgites which retain direct textural evidence of the decarbonation reactions, namely rims and veins of olivine+clinopyroxene on primary orthopyroxene grains. The extreme LILE enrichment of the carbonatite, and the ephemeral style of metasomatism resulted in imposition of its distinctive trace element and isotopic signature onto refractory spinel peridotite at this level.

This model was tested experimentally by reversing the decarbonation reactions. Synthetic amphibole±apatite bearing wehrlite compositions with 1, 5 or 7 wt% CO_2 were run at PT conditions within the carbonatite melt stability field of Wallace and Green (1988). This produced lherzolite or harzburgite residue in equilibrium with sodic dolomitic melt. The model implies the release of large CO_2 fluxes of the order of several wt% in the lithosphere in regions of carbonatite metasomatism (<15-20 kbars). This may provide a mechanism for incorporating a carbonatite component into some intra-plate volcanic products as has recently been proposed by Nelson et al. (1988) and Dupuy et al. (1992).

A second major theme of this study relates to the fate of subducted carbonate. Many DSDP reports allude to the presence of calcitic carbonate in veins and vugs in ocean-floor basalts, related to low temperature alteration processes. A series of high pressure experiments was conducted at 15<P<35 kbars, in which a composition representative of altered ocean-floor basalt (synthesized with excess H_2O at 20 kbars and 700°C, producing a quartz-bearing garnet amphibolite assemblage) was run with 0, 3 or 10

wt% calcite. These experiments revealed that carbonate is stable as a residual phase to temperatures of at least 1000°C at 20-35 kbars. At these conditions, a hydrous silicate melt coexists with a carbonate+rutile eclogite assemblage. An end-member exchange reaction between garnet and carbonate (calcite + pyrope = grossular + dolomite) resulted in an increased grossular component in garnet, and increasing MgO content in carbonate, with increasing pressure at near-solidus temperatures. Dolomite was found to be the stable carbonate phase at P>25 kbar and T≤750°C.

Reconnaissance experiments using magnesite instead of calcite revealed the presence of a bulk compositional control on the equilibrium carbonate composition. A shift to more magnesian bulk compositions resulted in stabilization of Ca-bearing magnesite, whereas runs conducted at identical PT conditions using calcite contained Mg-bearing calcite as the equilibrium carbonate composition.

The results of the hydrous basalt+carbonate experiments are supported by a study of a suite of natural carbonate-bearing eclogites from the Krusné hory Mountains in the Bohemian part of the Czechoslovakian segment of the Saxothuringicum (Klapova, 1990). The suite contains textural and mineralogical evidence of the above garnet+carbonate reactions in both the prograde and retrograde senses. For example, some samples show patches of calcite, surrounded by magnesite, surrounded in turn by thin rims of dolomite, in contact with garnet. The garnet is often markedly pyrope-rich on the rim, compared with the core. Textures and compositions imply prograde conversion of primary calcite to magnesite, with retrograde conversion to dolomite. Analysis of garnet and carbonate compositions and textures in these samples, and comparison with the basalt+carbonate experimental data suggest that the rocks achieved peak metamorphic conditions of 25 kbar and 650-700°C, followed by a near-isobaric heating event, and subsequent uplift and retrogression.

The study suggests that at least some carbon involved in the Earth's carbon budget can be recycled through subduction related processes. The ultimate fate of subducted carbon may depend on oxygen fugacity conditions in the deeper mantle. Recycled carbonate may result in diamond formation at low fO_2 conditions, in particular those diamonds included in eclogitic xenoliths hosted by kimberlites, or containing garnet±omphacite inclusions. Alternatively, if fO_2 is sufficiently high, carbon could be fixed in the mantle as dolomite or magnesite, and may be involved in carbonatite or fluid metasomatism, or in petrogenesis of undersaturated silicate melts (melilitites, nephelinites) or carbonatites (Brey and Green, 1976).

CHAPTER 1

MANTLE METASOMATISM - EXPERIMENTAL CONSTRAINTS ON THE PETROGENESIS, AND METASOMATIC ROLE OF PRIMARY CARBONATITE MELTS IN THE MANTLE

1.1 Aims and approach of this study

The purpose of this study is to use petrographic, mineralogical, geochemical and experimental evidence from a suite of petrographically-selected spinel peridotite xenoliths from southeastern Australia (SEA), to demonstrate that a process of metasomatism by ephemeral, dolomitic carbonatite melts has occurred. In addition, a model for carbonatite metasomatism in the SEA lithosphere is presented, in which a mechanism for the petrogenesis of the carbonatite is proposed, its trace element and isotopic characteristics are estimated, and the mineralogical and geochemical effects which the metasomatic process has on the lithosphere are described in detail. The relationship of this metasomatic style to other samples represented in the SEA xenolith suite is also established. These aspects comprise chapters 2-4.

Chapters 5 and 6 present a second aspect of the study which explores how carbonate may be recycled into the upper mantle through subduction of altered oceanic crust. A combined experimental and natural rock investigation is aimed at constraining the behaviour of calcitic carbonate in a hydrous basaltic system under high pressures and temperatures. The results of this study have implications for recycling of oxidized carbon back into the mantle via subduction in which carbonate minerals act as relatively refractory phases. Redox reactions between subducted crust and lithosphere or asthenopshere may have implications for the formation of some eclogitic diamonds. The experimental study is used to constrain the pressure-temperature history of carbonated eclogites in which corona textures on carbonate are well developed.

The purpose of the first chapter is to review evidence that metasomatic enrichment processes have exercised significant control on the trace element abundances in many mantle-derived peridotite xenoliths, and to briefly describe some models which have been proposed for mantle metasomatism. In addition, experimental studies of the

melting behaviour and phase relations in the peridotite-CO_2-H_2O system are reviewed, as a background for describing the predicted metasomatic effects of ephemeral carbonatite melts (Green and Wallace, 1988).

1.2 Evidence for the existence of metasomatic enrichment processes in the lithosphere.

The major element geochemistry of spinel peridotite xenoliths which are usually hosted by intra-plate alkali basalts, displays coherent trends which are generally interpreted to result from partial melting events (Frey and Green, 1974; O'Hara et al. 1975; Frey and Prinz, 1978; BVSP, 1981; Nickel and Green, 1984; Palme and Nickel, 1985; Frey et al. 1985; Galer and O'Nions, 1989; Fan and Hooper, 1990). For example, on plots of Al_2O_3, CaO, TiO_2 and several other oxides against MgO, world-wide spinel peridotites exhibit strong negative correlations (figure 1.2.1a-c). These elements have been demonstrated experimentally (eg; Jacques and Green, 1980) to strongly favour the mafic melt phase produced during partial melting of a peridotite source, resulting in their relative depletion in the residual peridotite. MgO, on the other hand, is strongly compatible, and is dominantly retained by peridotite, resulting in relative enrichment in MgO in the residue. Ni is another example of a compatible element, which is strongly retained by olivine during partial melting of peridotite, resulting in systematically increasing Ni with MgO contents (figure 1.2.1d).

Thus, spinel peridotites xenoliths from around the world are interpreted as residues from partial melting of a more primitive peridotitic source, with complete or incomplete segregation of mafic silicate melts, resulting in a spectrum of residual compositions from the fertile (low MgO, rich in Ca, Al, Ti, Na etc) to the refractory (high MgO, poor in Ca, Al, Ti, Na etc)

However, in recent years ample evidence has been presented suggesting that the trace element characteristics of peridotite xenoliths cannot simply reflect a single stage melting event in the same manner as the major element compositions. Many trace elements in these rocks are highly incompatible. For example, Rb, Sr, LREE, Th, K, Nb, Hf and a host of other elements partition very strongly into the melt phase during a partial melting event. Therefore, if the interpretation of peridotites as residues on the basis of their major element geochemistry is correct, these trace elements should be very strongly depleted. However, in many samples, trace element abundances are decoupled from major element chemistry, and incompatible trace elements are often

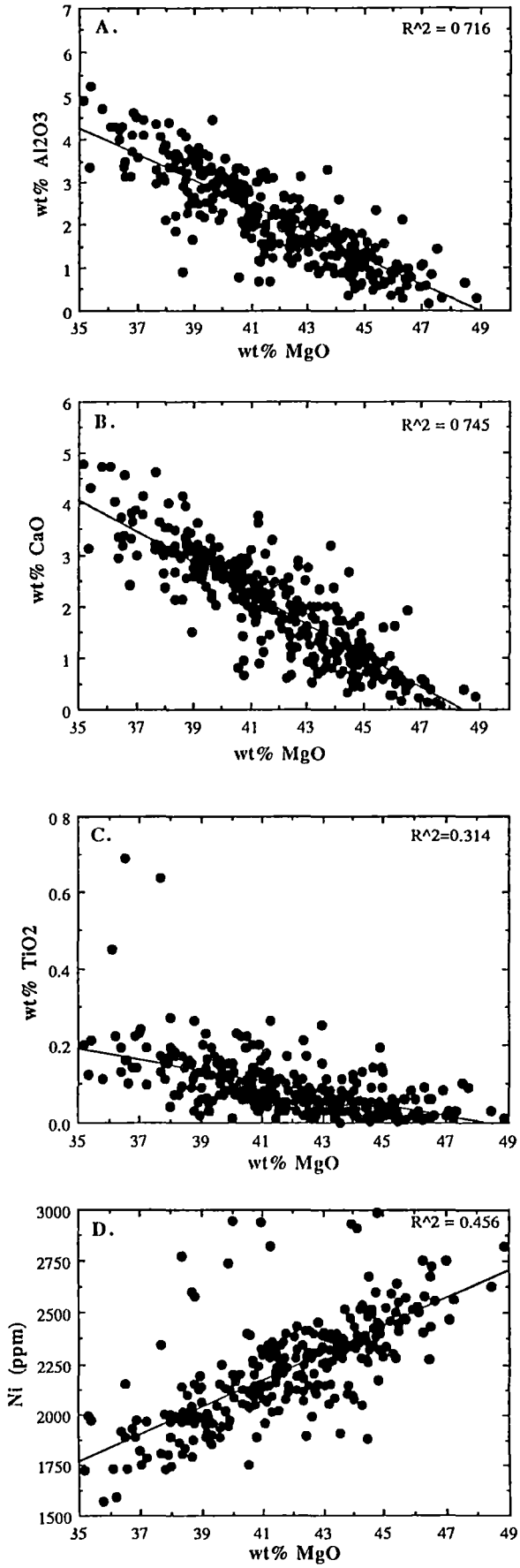

Figure 1.2.1: Plots against wt% MgO of (A) Al_2O_3, (B) CaO, (C) TiO_2 and (D) Ni for >300 spinel peridotite xenoliths from various localities around the world. A-C demonstrate the incompatible nature of Al, Ca and Ti during partial melting of peridotite, resulting in their gradual depletion in the residue with increasing melt extraction. Ni on the other hand, is compatible, being concentrated in the residue with increasing degrees of partial melting.

strongly enriched, and/or show relative enrichments of more incompatible elements above moderately incompatible, or compatible elements (eg; LREE-enriched signatures). These features are present although the major element chemistry suggests a residual character for the peridotite. Figure 1.2.2 illustrates that the most refractory (lowest Al_2O_3) xenoliths are often the most LREE-enriched. As a result, two stage models have been invoked to explain the geochemistry of peridotite xenoliths (Varne and Graham, 1971; Frey and Green, 1974). Stage 1 is a partial melting and melt segregation event, and dominantly controls the major element geochemistry of the residue (termed component A, by Frey and Green, 1974) in the manner described above. Stage 2 is a superimposed incompatible trace element enrichment event (or events), more commonly known as a metasomatic event. This is usually postulated to involve introduction of a small fraction of highly large ion lithophile element (LILE) enriched melt or fluid (component B) to component A, resulting in the decoupling of major and trace element abundances.

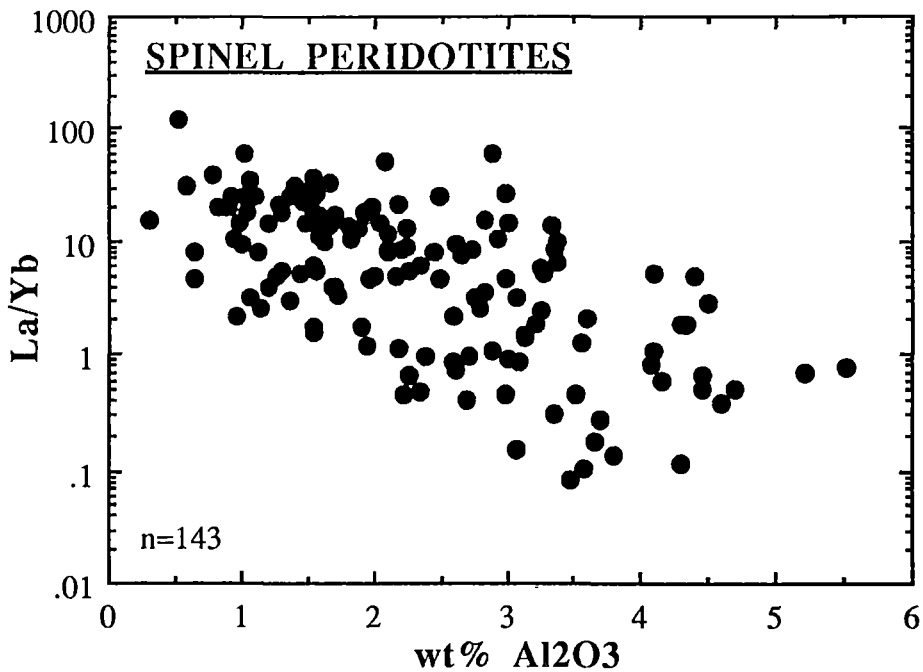

Figure 1.2.2; Plot of wt% Al_2O_3 vs. La/Yb (normalized to primitive mantle of Sun and McDonough, 1989) for 143 spinel peridotites from localities around the world, illustrating that the most refractory, in terms of major element chemistry (lowest Al_2O_3) are the most LREE enriched. See also, figure 3.5.8.

Two broad categories of metasomatism have been recognised (Bailey, 1982; Dawson, 1984). Peridotite which has undergone cryptic metasomatism contains no additional metasomatic phases, but remains an ol>opx>cpx>sp assemblage, with LILE

enrichment controlled by melt-fluid/cpx partitioning relationships (O'Reilly et al. 1991), or possibly by the presence of a LILE-enriched grain boundary phase (Zindler and Jagoutz, 1988). On the other hand, modal or patent metasomatism results in addition of one or more of a range of (usually hydrous) metasomatic phases, such as pargasitic or kaersutitic amphibole, phlogopite, apatite, or rare carbonate. These phases host the LILE-enrichment.

1.3 Models for mantle metasomatism

Much debate has centred on the nature and origin of the metasomatic agent(s). Various fugitive or metasomatic phases have been proposed, including H_2O or CO_2-rich supercritical fluids (eg; Kurat et al. 1980; Wass and Rogers, 1980; Menzies and Wass 1983; Stosch and Lugmair, 1986; O'Reilly and Griffin, 1988; Griffin et al. 1988; O'Reilly et al. 1991), hydrous silicate melts and the fluid differentiates thereof (eg; Wilshire et al. 1980; Roden et al. 1984; Kempton et al. 1984; Menzies et al. 1987), carbonated hyperalkaline melts (Meen, 1987; Meen et al. 1989; Thibault and Edgar, 1990), kimberlitic melts (Wass, 1981; Menzies and Wass, 1983) and dolomitic carbonatites (Green and Wallace, 1988; Yaxley et al. 1991; Dautria et al. 1992; Rudnick et al. 1992; Rudnick et al. 1993). Metasomatic fluids may derive from crystallizing mafic magmas intruding as dykes and veins within the mantle. These mafic lithologies are recognised as type II or Al-augite-bearing pyroxenite or amphibolite xenoliths (Frey and Prinz, 1978) found in many xenolith provinces from around the world (eg; Frey and Prinz, 1978; Griffin et al. 1984; Griffin et al. 1988). Evidence of their intrusive relationships with peridotitic lithosphere occurs in composite xenoliths, in which sharp contacts between type I and type II lithologies are observed (Wilshire and Pike, 1975; Nicolas and Jackson, 1982; Neilson and Noller, 1987). A number of workers have therefore attributed much metasomatic activity to interaction through fluids expelled from mafic bodies crystallizing within the lithosphere. Penetration of these fluids into the wall-rock can result in cryptic metasomatism, and/or deposition of hydrous phases such as amphibole, mica, or apatite. This can result in a range of geochemical effects, including Fe-Ti, and LILE enrichment in the wall-rock (Wilshire and Shervais, 1975; Irving, 1980; Kempton et al. 1984; Bodinier et al. 1987; Navon and Stolper, 1987; O'Reilly and Griffin, 1988; Griffin et al. 1988; Stolz and Davies, 1988; O'Reilly et al. 1991).

Bodinier et al. (1990) made a detailed study of a section of harzburgite from the Lherz orogenic peridotite, from the contact of an amphibolite vein with peridotite, a distance of 65 cm into the peridotite wall-rock. This study revealed strong mineralogical and chemical zonation. Close to the vein wall (<20 cm), modal metasomatism, involving amphibole+mica addition was observed. Elements such as Fe, Ti, Al, Ca, Na and REE increased in abundance towards the vein margin. Beyond 20 cm, the harzburgite was cryptically metasomatised with LREE enrichment in the absence of observable hydrous phases. This zonation was explained in terms of infiltration of alkali basalt from the vein into the surrounding wall-rock. At <15-20 cm from the vein wall, the melt was poorly evolved, due to continual and substantial chemical exchange with the vein conduit, resulting in strong modal metasomatism and chemical gradients for some elements. At greater distances, however, the melt composition is buffered by amphibole-peridotite, rather than by chemical exchange with the conduit. Chromatographic fractionation during long range porous flow percolation resulted in cryptic LREE enrichment.

O'Reilly and Griffin (1988) and O'Reilly et al. (1991) attributed metasomatism of the SEA lithosphere to fluids released by crystallizing silicate melts (Anderson et al. 1984; O'Reilly and Griffin 1988). The composition of these fluids changed as different metasomatic minerals formed successively during fluid infiltration of wallrock, resulting in a series of metasomatic zones with differing modal mineralogies. In the wallrock adjacent to the crystallizing basalt magma, olivine, orthopyroxene, clinopyroxene and spinel would reflect, or approach equilibration with the magma, and hydrous, trace element-bearing phases such as amphibole ± mica ± apatite would form. Further from the contact would be a zone of amphibole formation and LREE-enrichment of clinopyroxene, followed by a zone of apatite formation. Beyond this would be a further zone, which would retain an anhydrous mineralogy, with only cryptic LREE enrichment of clinopyroxene occurring. Outside this zone is unmetasomatised lherzolite.

However, evidence as to the extent to which H_2O+CO_2-fluids can transport minor and trace elements is currently ambivalent. Experimental studies by Schneider and Eggler (1986) have shown that the solutes in such fluids in equilibrium with harzburgitic assemblages will be dominantly normative quartz and feldspar. The solubility of more mafic components and Ti is small. Meen et al. (1989), and Schneider and Eggler (1986) have shown that the addition of small amounts of CO_2 to a hydrous,

supercritical fluid markedly reduces the solubility of major and trace elements. On the other hand, experimental studies of Wendlandt and Harrison (1979) and Mysen (1983) have suggested that REE will partition strongly into the fluid phase during silicate/CO_2-rich fluid equilibrium, possibly due to REE-carbonate complexing. Mysen (1983) found that partition coefficients for Ce, Sm and Tm between CO_2-rich fluid and diopside increased with increasing pressure, with decreasing temperature and with increasing mole fraction of H_2O in the fluid phase. The partition coefficients ranges from 4.3 to 200 over a temperature range of 900-1100°C, a pressure range of 20-30 kbar, and a range of fluid compositions from pure CO_2 to pure H_2O. Such a fluid could then cryptically metasomatise parts of the lithosphere. Wendlandt and Harrison (1979) found that minimum REE partition coefficients for vapour/carbonate melt and vapour/silicate melt favour strong enrichment in the vapour of all REE, particularly LREE.

However, a more recent, careful experimental study (Meen et al. 1989) has indicated that REE solubility in CO_2-rich fluids may be much lower than previously believed. A value for the CO_2-fluid/diopside partition coefficient for Nd of less than 0.05 was obtained. Furthermore, recent surface-energy studies (Brennan and Watson, 1988; Watson and Brennan, 1987) have suggested that CO_2-rich fluids cannot infiltrate peridotite assemblages without the presence of applied external forces. Therefore, the importance of CO_2-rich fluids in transport of LILE in the lithosphere is by no means unequivocal. On the other hand, CO_2-rich fluid inclusions appear to be abundant in many metasomatised mantle xenoliths (Anderson et al. 1984), strongly suggesting the presence of a CO_2-rich fluid at lithospheric depths.

Thus, although evidence of the type presented by O'Reilly and Griffin (1988) and related papers, and Bodinier et al. (1990), strongly support involvement of crystallizing mafic melts in the lithospheric mantle for Fe-Ti enrichment, there are clearly problems in the concept of CO_2-rich fluid involvement. Carbonatite metasomatism as proposed by Green and Wallace (1988) constitutes an alternative metasomatic style, which has the potential to resolve some of these problems. In sections 1.4 and 1.5, the experimental basis behind genesis of dolomitic carbonatites as primary melts of carbonated peridotite is briefly reviewed. Section 1.6 outlines the metasomatic effect of primary carbonatites in the lithosphere, as predicted by Green and Wallace (1988).

1.4 Phase relations in the system peridotite-CO_2-H_2O; Genesis of primary carbonatites

CO_2 and H_2O are major components of gases associated with mantle-derived melts. In addition, many mantle derived peridotite xenoliths contain accessory hydrous phases (amphibole, phlogopite, apatite) and/or carbon-bearing phases (apatite, carbonate) (eg; Frey and Green, 1974; Wilshire et al. 1980; Nickel and Green, 1984; Stolz and Davies, 1988; O'Reilly and Griffin, 1988; Witt and Seck, 1989). This suggests that experimental studies of the phase relations and partial melting products of the peridotite-CO_2-H_2O system have the potential to constrain petrogenetic models for volcanic products ranging from tholeiites, through undersaturated mafic silicate melts (eg; nephelinites, melilitites) to kimberlites and carbonatites. Reviews of such studies is outside the scope of this study, but have been presented by Eggler (1987), Wyllie (1987) and Green (1990). Below, recent experimental studies in pyrolite+H_2O and pyrolite+H_2O+CO_2 performed by Green (1973), Wallace and Green (1988), Wallace (1989) and Falloon and Green (1989 and 1990) are briefly reviewed. Phase relations as determined by Falloon and Green (1990) are summarized in figure 1.4.1.

Addition of carbon to the oxidised (fO_2≈FMQ) pyrolite-H_2O system considerably complicates melting behaviour and phase relations, because of the divariant decarbonation reaction dolomite + opx = olivine + diopside + CO_2. This reaction has a positive dP/dT, and intersects the solidus at approximately 22 kbar and 1000°C. It divides the subsolidus PT field into a low T, high P regime in which solid dolomitic or magnesitic carbonate ± hydrous fluid are stable, in equilibrium with pargasite-bearing garnet or spinel lherzolite, and a low P high T field in which CO_2+H_2O fluids are in equilibrium with spinel lherzolite, and pargasite stability is dependent on bulk H_2O/CO_2 values.

The solidus of the low T, high P field occurs at 925°C over the pressure interval 21-31 kbar (Wallace and Green 1988; Falloon and Green 1990). Low degree melts on the solidus at P≥21 kbar are sodic, dolomitic carbonatites. These may be in equilibrium with a H_2O-rich fluid of fixed composition (ie; independent of bulk CO_2/H_2O value; ZIVC of Eggler, 1978) under fluid saturated conditions (H_2O>0.4% as CO_2 apporaches zero; Falloon and Green, 1990). In fluid undersaturated conditions, this part of the solidus will be fluid absent, all H_2O being retained in pargasite and the melt phase, and CO_2 in either the carbonate, or the carbonatite melt (Wallace and Green, 1988). The amphibole breakdown curve occurs at 1000°C over the pressure interval 21

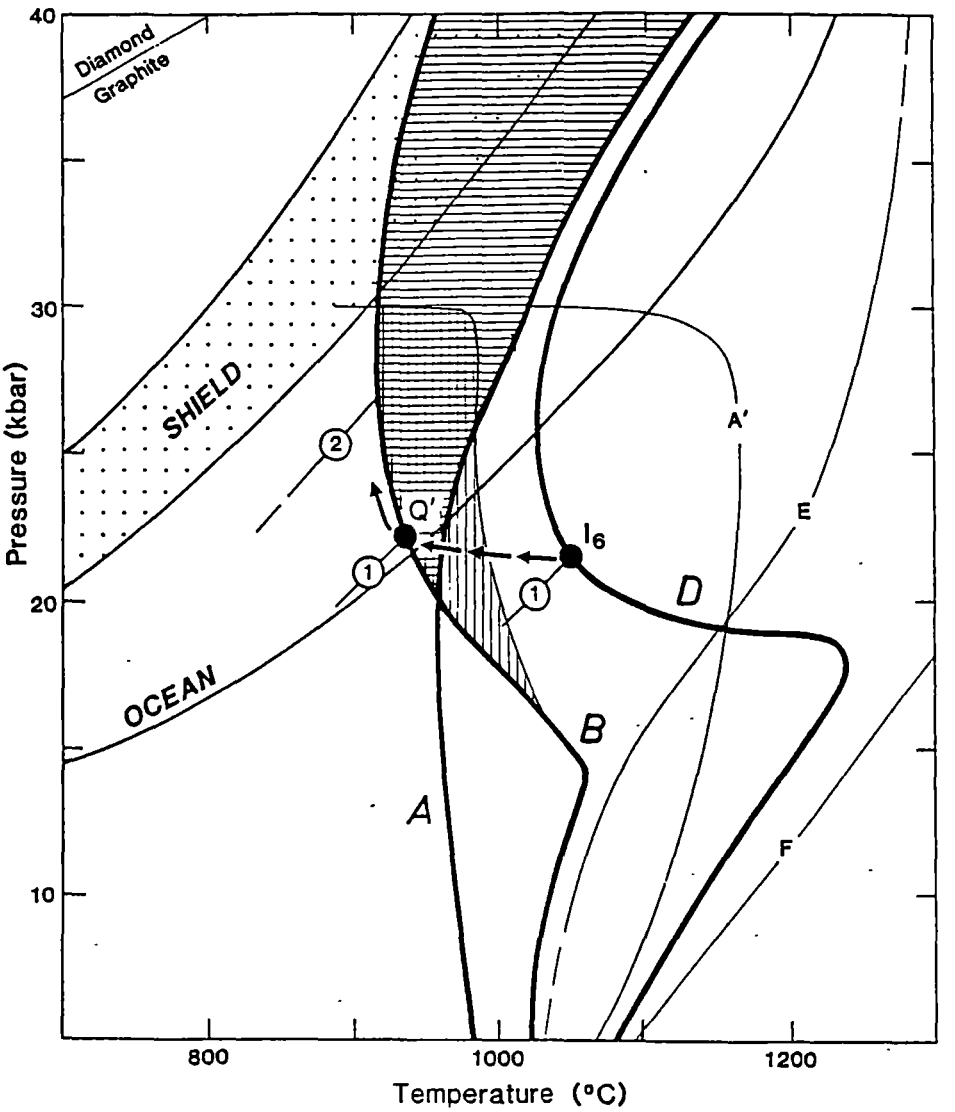

Figure 1.4.1: Phase relations for pyrolite-CHO, showing transgression of carbonatite melt fields by shield and oceanic geotherms. Curve A is H_2O-saturated solidus, A' is vapour undersaturated solidus for pyrolite+CO_2+H_2O, B is solidus for pyrolite+CO_2+H_2O (vapour excess), D is solidus for pyrolite-CO_2, E is solidus for pyrolite-CH_4, and F is anhydrous pyrolite solidus. Reaction 1 is opx + dol = ol + cpx =CO_2, and reaction 2 is the vapour absent reaction mag + di = fo + dol. Horizontal striped region is field of carbonatite melt in equilibrium with phlogopite, vertical stripes are carbonatite melt field in equilibrium with amphibole (delineated on the high temperature side by amphibole-out curve). After Falloon and Green (1990).

to 28 kbar in the fluid saturated system (Falloon and Green, 1990). In the fluid undersaturated system, pargasitic amphibole persists to 1080°C. At temperatures above the amphibole-out curves, pargasite breaks down and undersaturated silicate melts (nephelinites) occur, in which CO_3^{2-} and OH^- dissolve.

Pargasite is also unstable at P>30 kbar, being replaced by phlogopite. A field of carbonatite melt in equilibrium with phlogopite garnet lherzolite exists from ≈30 to 40 kbar at temperatures below that of the water-saturated silicate solidus. Because magnesite is the stable subsolidus carbonate at these high pressures, the carbonatitic melts may be more magnesitic than their low pressure equivalents. At temperatures above the H_2O-rich fluid saturated silicate solidus, the carbonatite melt is replaced by highly undersaturated silicate melts, such as olivine melilitites, in which CO_3^{2-} is very soluble (Brey and Green, 1975; 1976).

Genesis of primary carbonatite melt from carbonated hydrous peridotite assemblages can be understood in terms of a eutectic between subsolidus carbonate (dolomite at low pressures, magnesite at high pressures) and silicate phases, particularly involving jadeite and diopside components in clinopyroxene, and forsterite in olivine, according to the following reactions (Wallace and Green, 1988; Wallace, 1989)

1.1 $10MgCO_3 + 2NaAlSi_2O_6 + 4CaMgSi_2O_6 + 3Mg_2SiO_4 =$
magnesite jadeite diopside forsterite
$2Mg_{2.5}Ca_2Na(CO_3)_5 + 12MgSiO_3 + MgAl_2Si_3O_{12}$
carbonatite enstatite garnet

1.2 $5CaMg(CO_3)_2 + 2NaAlSi_2O_6 + 3Mg_2SiO_4 =$
dolomite jadeite forsterite
$2Mg_{2.5}Ca_2Na(CO_3)_5 + 2MgSiO_3 + CaMgSi_2O_6 + Mg_3Al_2Si_3O_{12}$
carbonatite enstatite diopside garnet

It is important to note that these melting reactions increase the enstatite/olivine and garnet/clinopyroxene values of residual peridotites.

Falloon and Green (1990), and Green (1990) demonstrated that both the estimated continental shield, and oceanic geotherms transect carbonatite melt fields (figure 1.4.1). Therefore, beneath shield regions, at depths of ≥100 km, carbonatite melt

could coexist with phlogopite-bearing garnet lherzolite. This melt may be more magnesitic in composition than the Wallace and Green (1988) carbonatite. On the other hand, the oceanic geotherm passes through a melt field in which primary, sodic, dolomitic carbonatite melts can exist in equilibrium with pargasitic garnet lherzolite residue.

1.5 Composition of primary carbonatite

Wallace and Green (1988) determined the composition of their primary carbonatite by conducting a series of five iterative "sandwich" experiments in which a layer containing the estimated melt composition was equilibrated with amphibole-bearing pyrolite + 5% dolomite. A melt was generated in which the silicate mineral compositions matched those in the forward experiment at identical PT conditions (22 kbar, 1000°C). The composition of this melt (CM1) was taken to be that of the primary carbonatite, and was determined by microprobe analysis of quench aggregates using a defocussed beam to minimize volatilization of the sample. It was found to have a sodic dolomitic composition, with $100*Mg/(Mg+\sum Fe)$ of 84.5, and significant amounts of K_2O and P_2O_5. The melt quenched to dolomite and a (Na,Mg)-carbonate phase.

This composition agrees well with one recently determined by Thibault et al. (1992) for carbonated phlogopite-bearing lherzolite at 30 kbar and 1100°C. Significantly, this composition had a similarly high $100*Mg/(Mg+\sum Fe)$ of 86, but was higher in K (due to partial breakdown of phlogopite) than that of Wallace and Green (1988).

Sweeney et al. (1992) determined the liquidus phase relations of CM1+2wt% and 4wt% H_2O at pressures from 5 to 30 kbar. Phase relations were broadly similar in both systems. In the 2% H_2O system, dolomite was found to be the major near-liquidus phase, with olivine saturation occurring at $P<18$ kbar, and amphibole stable on the liquidus between 18 and 27 kbar. At $P>27$ kbar, amphibole was replaced by garnet. Garnet saturation was delayed to $P>27$ kbar in the 4% H_2O system.

Multiple saturation of CM1+H_2O in lherzolite phases (olivine + orthopyroxene + clinopyroxene + garnet + pargasite) was not observed by Sweeney et al. (1992) under any PT conditions, although it should be noted that liquid and silicate phases were in reaction relationship (reactions 1.1 and 1.2). The authors considered that further

investigation by varying the CO_2 and H_2O, and small variations in oxide components of CM1 may result in appropriate changes to the liquidus silicate mineralogy.

1.6 Metasomatic role of dolomitic carbonatites

Dolomitic carbonatite melts may form as low degree primary melts of previously carbonated peridotite, as described above. Alternatively, carbonated undersaturated silicate melts (eg; olivine melilitites) may ascend from asthenospheric source regions. Ascent may occur by porous flow, ie; along geothermal gradients, or trapped within upwelling mantle diapirs. Depending on the nature of the geotherm (eg; oceanic or elevated geotherms) or PT path of an upwelling diapir, the melt+lherzolite could enter a stability field of carbonatite melt + amphibole. This would result in crystallization of amphibole and additions to the lherzolite mineralogy, and thus to evolution of the silicate melt to carbonatite (figure 1.6.1).

There is experimental evidence that the carbonatite melts can form an interconnected grain boundary network at very low melt fractions of <<1% (Hunter and MacKenzie, 1989). This, coupled with their low density and viscosity, may ensure rapid and pervasive ascent from their source regions (Hunter and MacKenzie, 1989; Watson et. al. 1990). This behaviour, together with their LILE-enriched nature, renders carbonatite melts as potentially effective metasomatic agents in the lithosphere (Green and Wallace, 1988). Such melts, on ascending from their source regions through cooler, overlying lithosphere, could eventually cross the carbonate solidus. This may occur at pressures greater than the decarbonation reaction orthopyroxene + dolomite = olivine + clinopyroxene + CO_2, resulting in "thermal death" of the carbonatite, and the production of enriched dolomite-bearing peridotite.

Alternatively, the carbonatite melt could cross the solidus at pressures less than the decarbonation reaction, resulting in conversion of refractory spinel lherzolite or harzburgite to magnesian wehrlite mineralogy, with or without low-Ti pargasite, accompanied by release of a CO_2-rich fluid (Green and Wallace, 1988). Evolution of the reacting carbonatite may result in increasing P_2O_5+halogen and H_2O contents, possibly forming a late-stage fugitive saline melt or "brine" from which accessory apatite is deposited. The carbonatite is "ephemeral" in the sense that it is absorbed by the lithosphere, with release of ≈50 wt% of CO_2>>H_2O fluid. The result of these mineralogical changes would be to drive wholerock geochemistry of the affected

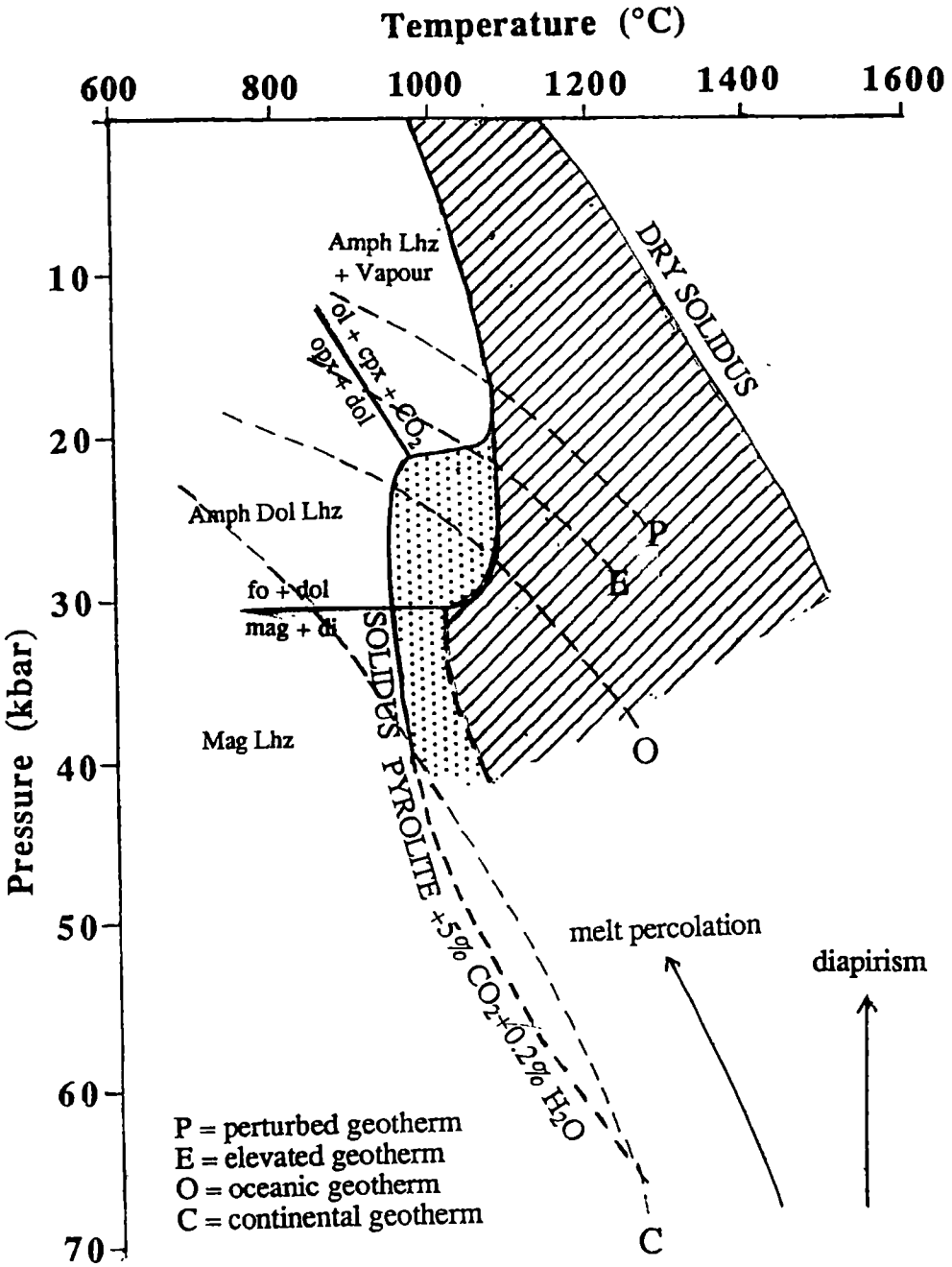

Figure 1.6.1: Intersection of various geotherms with enriched or 'Hawaiian' pyrolite+CO_2+H_2O solidus and carbonate melt field. Stippled area is region of carbonatite melt stability, and striped area is field of incipient silicate melting. This figure outlines various scenarios affecting ascending carbonatite melts. For example, in continental lithosphere, partial melting of carbonated hydrous pyrolite at ≈65 kbar could produce magnesitic carbonatite, which would ascend along geotherm C (Finnerty and Boyd, 1987), and freeze at ≈40 kbar, producing magnesite-bearing lherzolite. On the other hand, silicate melts ascending along geotherm O (Nixon and Boyd, 1979) from the asthenosphere under oceanic regions could enter the carbonate melt + amphibole field, fractionate hydrous silicate phases and evolve to dolomitic carbonatite. This could ascend, cross the solidus and form enriched dolomite-bearing amphibole lherzolite. Hotter, elevated geotherms (E) could result in decarbonation of the carbonatite, and metasomatism as described in Chapters 2 and 3. Silicate melt ascending along geotherm P (O'Reilly and Griffin, 1985), would cross the solidus at pressures less than the decarbonation reaction opx + dol = fo + cpx + CO_2, and freeze, exsolving CO_2>H_2O fluid.

regions of the lithosphere towards high Ca/Al and Na/Al values, to higher P_2O_5 abundances, and to moderate to extreme LILE enrichment decoupled from Ti abundances (Green and Wallace, 1988; see also figures 3.3.1 and 3.3.2).

In chapters 2-4, petrographic, mineralogical, geochemical and experimental evidence is used to establish that this style of metasomatism is a viable process in the lithosphere. In addition, it is demonstrated that the mineralogical and geochemical characteristics of many, previously described, metasomatised peridotite xenoliths, the enrichment of which has previously been attributed to basaltic, or CO_2-rich fluid metasomatism, can be adequately explained by carbonatite metasomatism.

CHAPTER 2

PETROGRAPHIC AND MINERALOGICAL EVIDENCE FOR CARBONATITE METASOMATISM OF THE SOUTHEASTERN AUSTRALIAN LITHOSPHERE IN NATURAL SPINEL PERIDOTITE XENOLITHS

2.1 Introduction

This chapter describes the petrography and mineralogy of a suite of unusual, mantle-derived spinel peridotite xenoliths from western Victoria, Australia, and demonstrates that they display the characteristics predicted by Green and Wallace (1988) and reviewed in Chapter 1, of lithospheric material which has suffered metasomatism by ephemeral carbonatite melts.

Spinel peridotite nodules, collected from Mt Leura, Mt Shadwell, Lake Bullenmerri, The Anakies and Mt Noorat (see figure 2.1.1 and table 2.1 for localities), are hosted by Recent olivine basanites of the Newer Volcanics, which are widespread in western and central Victoria, Australia. Examination of hand specimens and thin sections was used as a basis for selection of members of the suite. Selection was deliberately biased towards apatite+amphibole+glass-bearing spinel peridotites, and particularly towards the wehrlites, which display abundant, apple-green Cr-diopside in hand specimen. The wehrlites have not been previously reported, suggesting that they are relatively uncommon, particularly in comparison with apatite-bearing lherzolites and harzburgites reported in earlier studies (Griffin et al. 1984; O'Reilly and Griffin, 1988; Stolz and Davies, 1988; O'Reilly et al. 1991). However, once familiarity with the rock-type was achieved, it was not difficult to collect samples - an impression of 1-5% of samples 'opened' is noted.

Electron probe microanalysis (EPMA) was performed on constituent mineral and glass phases in the nodules, using a Cameca SX50 electron microprobe at the Central Science Laboratory, University of Tasmania. The electron beam diameter used was routinely 1μm, except for analyses of volatile-rich phases (eg; carbonates, silicate glasses, apatites etc), where a defocussed, or rastered beam of varying cross-sectional area was used. The accelerating voltage was 15kV, and beam current 20nA for

Table 2.1: List of samples localities and lithologies. Abbreviations: Ap=apatite; Gl=glass derived from decompression fusion of pre-existing hydrous phases; Am=relict amphibole; Ph=relict phlogopite; Cb=calcitic carbonate; Sp=spinel; Weh=wehrlite; Lhz=lherzolite; Hz=harzburgite. Catalogue numbers refer to University of Tasmania, Geology Department collection. Numbers 2631 and 2638 refer to Research School of Earth Sciences (ANU) collection.

Field No.	Catalogue No.	Locality	Lithology
AN8	76987	The Anakies	ApGlWeh
	70965	Mt Shadwell	GlSpWeh
	70969	Mt Shadwell	ApGlSpWeh
	70972	Mt Shadwell	ApGlSpWeh
	71000	Mt Leura	ApAmGlSpWeh
	71001	Mt Leura	ApGlSpWeh
	71007	Mt Leura	ApAmPhGlSpWeh
	2631	Mt Leura	ApGlSpWeh
	2638	Mt Leura	ApGlSpWeh
SH19	76988	Mt Shadwell	ApGlSpWeh
	73797	Bullenmerri	ApGlSpWeh
SH1	76989	Mt Shadwell	ApGlSpWeh
SH52	76990	Mt Shadwell	ApGlSpWeh
LE17	76991	Mt Leura	ApGlSpWeh
NO11	76992	Mt Noorat	GlSpWeh
	70987	Mt Leura	ApGlSpLhz
	70997	Mt Leura	ApGlSpLhz
	71004	Mt Leura	ApAmPhGlSpLhz
	71008	Mt Leura	ApGlSpLhz
	70961	Mt Shadwell	ApGlSpLhz
SH34	76993	Mt Shadwell	CbApGlSpLhz
LE10	76994	Mt Leura	ApGlSpLhz
	71003	Mt Leura	ApGlSpHz
	71006	Mt Leura	ApAmGlSpHz
	70982	Mt Leura	ApSpHz
SH20	76995	Mt Shadwell	CbApGlSpHz
SH8	76998	Mt Shadwell	ApGlSpHz
	71023	Mt Leura	ApGlSpHz
SH40	76997	Mt Shadwell	ApGlSpHz
SH31	76998	Mt Shadwell	ApGlSpHz
SH11	76999	Mt Shadwell	ApGlSpHz
NO7	77000	Mt Noorat	ApGlSpHz

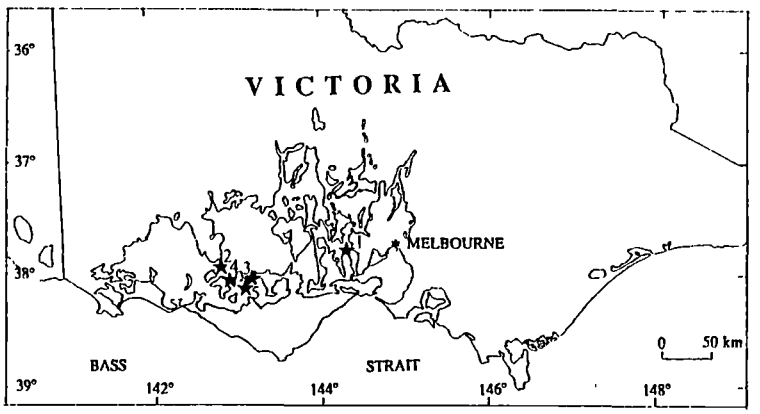

Figure 2.1.1: Map of Victoria, Australia, showing localities from which samples listed in table 2.1 were collected. Outlined area shows distribution of Newer Volcanics after Johnson (1989). 1=The Anakies; 2=Mt Shadwell; 3=Mt Leura; 4= Mt Noorat and 5=Lake Bullenmerri.

olivine, clinopyroxene, amphibole, orthopyroxene, spinel and apatite analyses. Carbonate and silicate glass analyses were performed with a beam current of 10nA at 15 kV to minimize sample volatilization. Count times varied from 10-40 seconds on peaks and 5-20 seconds on backgrounds, depending on the elemental abundance. Instrument calibration was performed using a variety of natural mineral primary standards, and was routinely checked at the beginning of, and during each EPMA session, on appropriate secondary standards (Delegate clinopyroxene for most silicate analyses, Durango apatite for apatites, and a natural chromite for spinels). Details of standards and EPMA calibration have been included in Appendix A.

2.2 Petrography

Petrographically, the 32 samples comprising this suite are apatite-bearing wehrlites (15), lherzolites (7) or harzburgites (10). Most samples display unfoliated, porphyroclastic textures in which large primary olivine (ol), clinopyroxene (cpx) and/or orthopyroxene (opx) porhyroclasts are separated by moderately- to well-annealed neoblastic regions (figure 2.2.1). The porphyroclasts commonly contain evidence of strain, such as undulose extinction, or kink-banding. In the lherzolites and harzburgites, neoblastic orthopyroxene is rare. Clinopyroxene is found in both textural settings, but more commonly as neoblasts. The neoblastic regions are well-annealed and display little or no evidence for strain. They usually exhibit an equigranular texture which contains abundant 120° triple grain boundary junctions. Exsolution lamellae of clinopyroxene occur in orthopyroxene in a few of the samples. Individual lamellae are invariably smaller than the resolution of the microprobe beam, and could not be directly analysed. However, a defocussed, broad electron beam was used in analysing orthopyroxene grains bearing lamellae in order to establish "bulk" orthopyroxene compositions.

All but one (71007) of the wehrlites are completely free of primary orthopyroxene, and contain abundant, distinctive, apple-green Cr-diopside. In these samples, olivine and clinopyroxene are well crystallized and appear texturally equilibrated. However, the lherzolites and harzburgites appear to record interruption of an aggressive alteration event in which the coarse primary orthopyroxene is being replaced penetratively by fine-grained olivine + clinopyroxene with growth of patchily distributed anhedral apatite on grain boundaries (figure 2.2.2).

Figure 2.2.1: Photomicrograph of sample 70969, taken in plane polarized light at 25x magnification, showing moderately well-annealed, clinopyroxene rich, neoblastic region on right, and olivine-rich porphroclastic region on the left.

Figure 2.2.2: Photomicrographs of sample 71008, at 50x magnification. (A) is in plane polarized light, and (B) is view of same area with crossed nicols. The large central grey grain in (B) is primary orthopyroxene (OPX), and is clearly being replaced by a thin rim of more birefringent, fine-grained olivine and clinopyroxene (unlabelled). Above the OPX grain is a patch of vesicular amphibole-derived glass, filled with euhedral secondary microphenocrysts of olivine, clinopyroxene and spinel (labelled "Glass"). A turbid apatite (AP) grain is visible immediately below the orthopyroxene grain. Textures similar to this are ubiquitous in the lherzolites and harzburgites of this suite, and are interpreted as preserved evidence of the reaction opx + dolomite = olivine + cpx + CO_2. See text for further explanation.

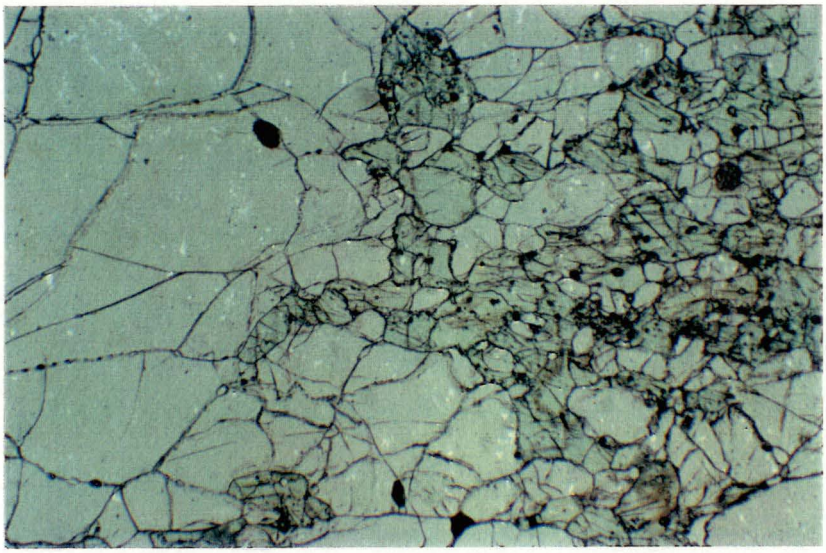

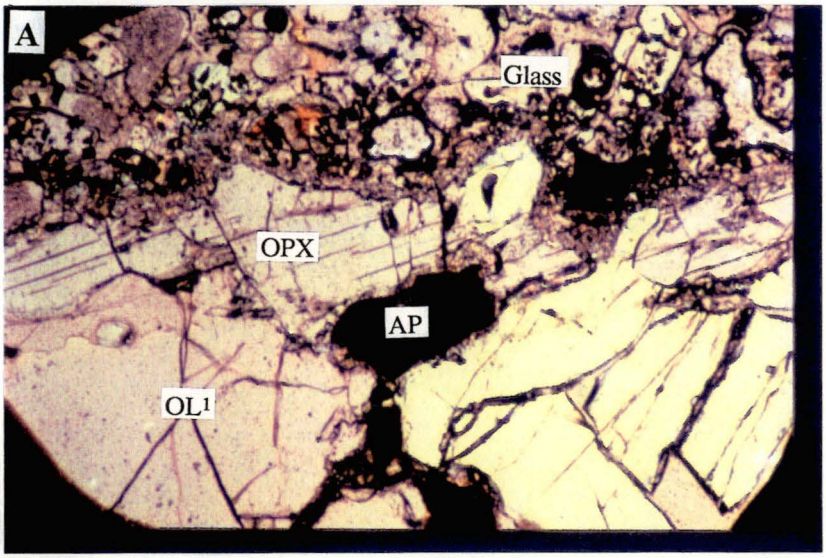
A
Glass
OPX
AP
OL1

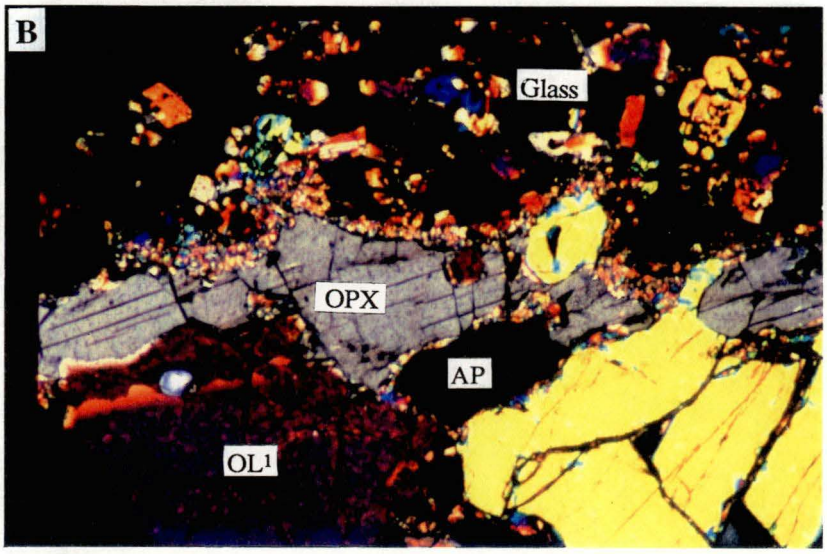
B
Glass
OPX
AP
OL1

All samples contain patches of light brown to colourless, crystal-rich glass, which are typically irregular in shape, often vesicular, and range in size up to several millimetres across (figure 2.2.3). The glass from these patches usually extends into very thin veinlets along grain boundaries, coating other phases with a thin, intergranular glass film. Occasional pooling of this glass at grain boundary junctions results in formation of small, sometimes aphyric, triangular pools of glass. Near the margins of some samples, petrographic evidence suggests limited mixing of internal glass with deep brown glass derived from the host basanite. This is, however, confined to a maximum of a few millimeters from the nodule margin.

The larger, irregular shaped glass patches usually contain clusters of large, reddish brown, embayed, relict Cr-spinel grains (figure 2.2.3). Low-Ti pargasitic amphibole is found in samples 71006, 71007 and 71000 (figure 2.2.4). Samples 71004 and 70987 contain high-Ti pargasitic amphibole. Samples 71004 and 71007 contained minor phlogopite. In each case, the amphibole grains are included within glass patches described earlier, and have embayed, curved grain boundaries, consistent with partial melting (figure 2.2.4). They are often closely associated with the primary Cr-spinels described earlier. The surrounding glass in turn contains abundant euhedral microphenocrysts of secondary brown spinel, clinopyroxene and olivine, and frequent microlites of acicular, quenched plagioclase and apatite. Frequent inclusion of euhedral secondary spinel octahedra in secondary olivine and/or clinopyroxene suggests that spinel was an early crystallizing phase (figure 2.2.5). In many cases, intergranular glass veins contain acicular quenched apatite needles. Where these glass films are in contact with metasomatically introduced apatite, a rim of clear, recrystallized apatite is often present (figure 2.2.6). This apatite is petrographically and chemically distinct from the core apatite, being clear and free of fluid inclusions. Green et al. (1965), and Frey and Green (1974) made a similar observation on their sample 2700, as did Kleeman et al. (1969) on sample 2638.

The glassy pools in the wehrlites and lherzolites usually appear to be reacting with and partially replacing large, adjacent clinopyroxene grains (figure 2.2.3), although no compositional zoning of clinopyroxene adjacent to glass contact was observed within analytical uncertainty. This evident replacement of primary phases adjacent to primary spinel by hydrous phases such as pargasitic amphibole (or glass+secondary phases after amphibole) and/or phlogopite has been well documented in studies of mantle xenoliths which have undergone metasomatism by influxing basic hydrous silicate

Figure 2.2.3: Photomicrograph of sample 70969, taken in plane polarized light at 50x magnification. It shows irregularly-shaped patches of brown glass (GL), associated with primary, reddish Cr-rich spinel (SP^1) (large, irregular shapes), and clearly reacting with green clinopyroxene grain (CPX^1). The glass contains secondary microphenocrysts of spinel (tiny euhedral opaque grains) and olivine (ol^2).

Figure 2.2.4: Photomicrograph of sample 71000, taken in plane light at 50x magnification. This shows relict embayed amphibole grains (AM) sitting in a glassy patch (GL) which also contains secondary microphenocrysts of clinopyroxene and spinel. A cluster of primary spinel (SP^1), and a couple of relict primary clinopyroxene grains (CPX^1) are also preserved within the glass patch.

Figure 2.2.5: Photomicrograph of sample 76993, taken in plane light at 100x magnification, showing close view of a patch of amphibole-derived glass, with abundant included euhedral microphenocrysts of secondary olivine and spinel. Many secondary spinels are included in secondary olivines, indicating that spinel was an early phase to crystallize. Acicular crystals forming radiating clumps are plagioclase. Two large circular vesicles are also plainly visible, indicating the presence of a fluid phase.

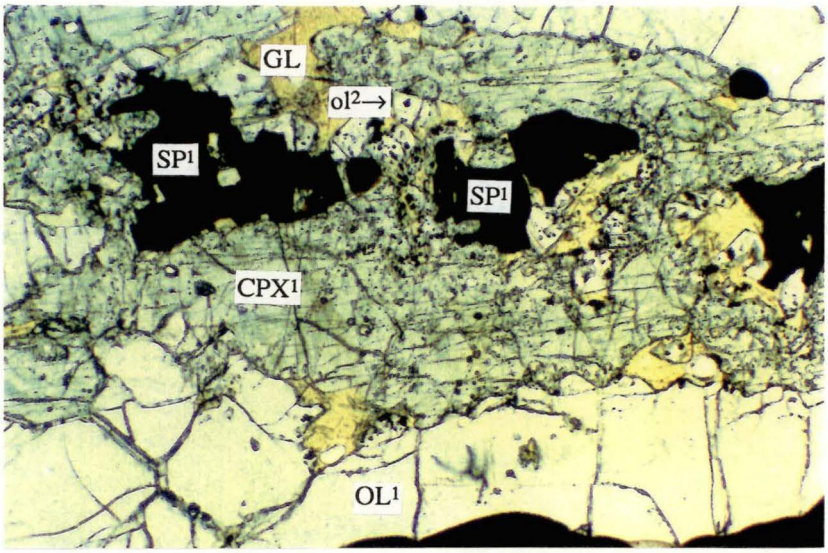
GL
ol2→
SP1
SP1
CPX1
OL1

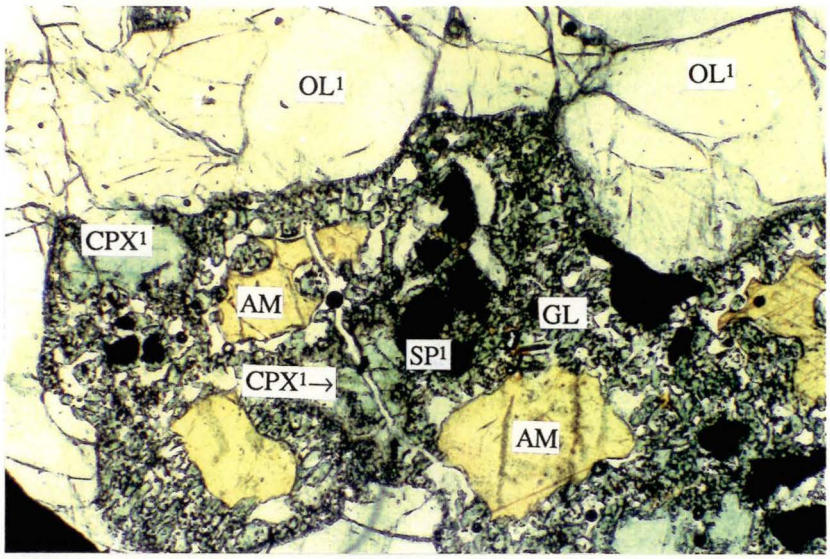
OL1
OL1
CPX1
AM
GL
SP1
CPX1→
AM

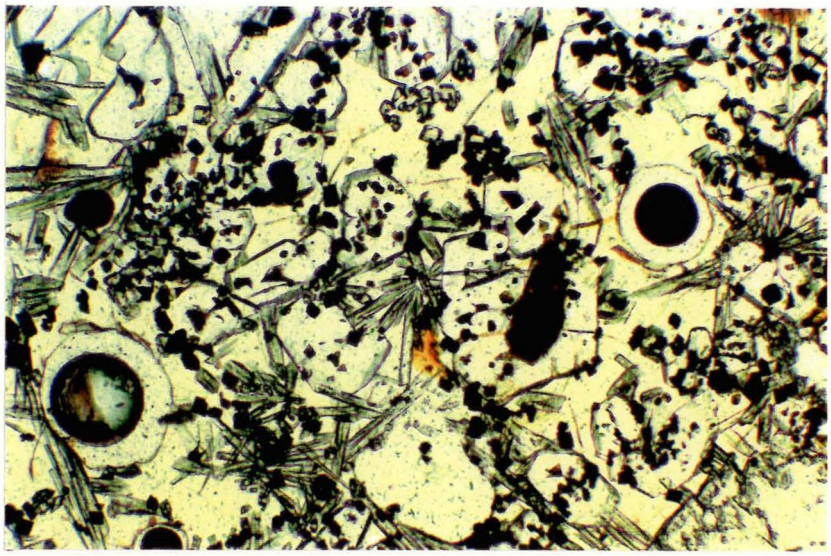

melts (eg; Nickel and Green, 1984; O'Reilly and Griffin, 1988), or H_2O-rich fluids derived from them. It has been attributed to reaction between primary spinel and clinopyroxene, in the presence of a water-rich phase, producing amphibole (eg. Nickel and Green, 1984).

In addition, in the lherzolite xenoliths, which contain primary orthopyroxene, relict orthopyroxene cores are usually present within or adjacent to these glass pools (figure 2.2.2). These cores are surrounded by rims of very fine-grained olivine + clinopyroxene (average grain-size around 5μm), which appear to be replacing the orthopyroxene. These replacement rims are commonly in contact with amphibole-derived glass, and are often spatially associated with apatite of metasomatic origin. However, they have also been observed along primary olivine/orthopyroxene grain boundary contacts in the absence of glass (eg; sample 70961), and filling glass-free fractures in primary orthopyroxene grains. Frey and Green (1974) also reported similar rims on orthopyroxene grains in sample 2700. In many lherzolite samples (eg; 71008, 71004, LE10), orthopyroxene grains are present as small, relict cores, and the olivine+clinopyroxene rims may be quite thick, indicating substantial replacement has occurred. In the harzburgites, large porphyroclastic orthopyroxene grains are undergoing extensive replacement by olivine+clinopyroxene around grain boundaries, on the outer rims of vesicular glass pools often completely enclosed within the pyroxene grain (figure 2.2.7), or along the margins of veins cutting through the porphyroclasts.

Fe- and Mg-bearing calcitic carbonate was found in samples SH34 (lherzolite), SH20 (harzburgite) and 73797 (wehrlite). In SH34 and SH20, it occurs as inclusions within amphibole-derived glass pools enclosed within porphyroclastic orthopyroxene grains (figure 2.2.7). These pools are commonly lined with a spinel-free rim of very fine-grained forsteritic olivine and clinopyroxene, which appears to be replacing the surrounding orthopyroxene grain. The cores of the pools contain euhedral spinel, olivine and clinopyroxene microphenocrysts, with minor interstitial glass, and large, irregularly-shaped patches of carbonate. These glassy patches also frequently contain a single large vesicle, which may occupy up to 50% of the volume of the patch. In addition, adjacent orthopyroxene bears an abundance of CO_2-bearing fluid inclusions in the vicinity of the glassy patch. These observations indicate the presence of an abundant fluid phase during the formation of these patches.

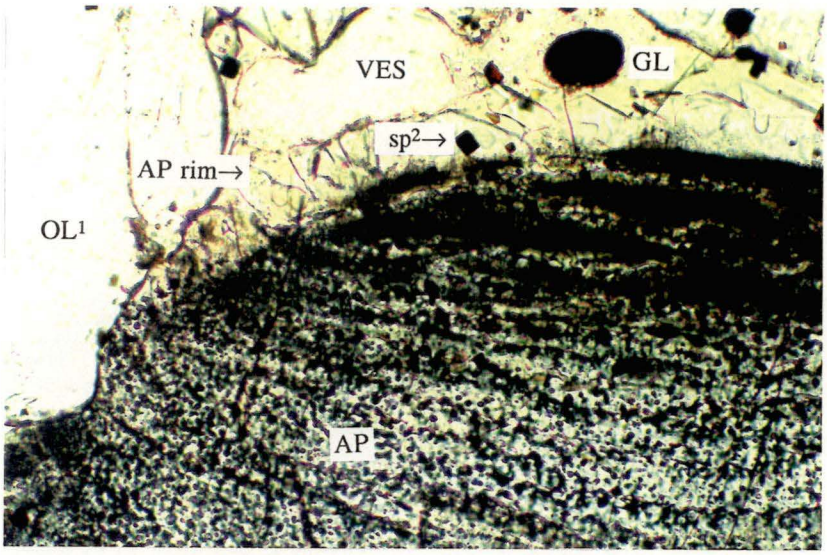

Figure 2.2.6: Photomicrograph of edge of apatite (AP) grain from sample 76987 (100x magnification), with overgrowth of a rim of clear recrystallized apatite, in contact with vesicular (VES) glass (GL). The secondary spinel grain (sp^2) included in the rim indicates that the rim crystallized from the glass.

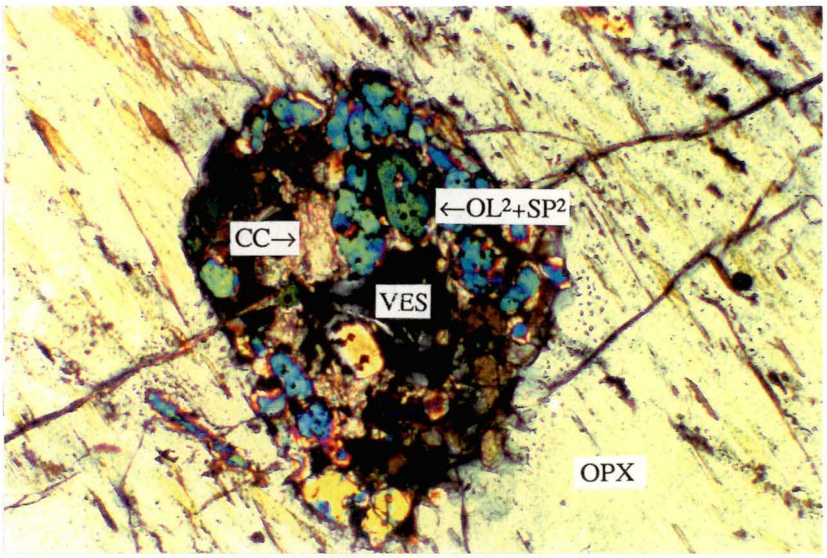

Figure 2.2.7: Glassy patch hosted by a large orthopyroxene (OPX) porphyroclast from sample 76995 (100x magnification). The patch contains minor glass, abundant secondary olivine and spinel microphenocrysts (OL^2+SP^2), a large vesicle (VES) and an irregularly shaped patch of calcitic carbonate (CC). Note abundance of fluid inclusions in OPX grain around glass patch.

In sample 73797, carbonate occurs rarely as discrete inclusions in primary olivine grains, or abundantly in veins between, and cutting across primary phases (figure 2.2.8). In the former setting, the primary olivine immediately surrounding the calcitic inclusion contains an extreme abundance of necked-down fluid inclusions which line annealed fractures in the host olivine.

The presence of up to 2 modal % apatite is almost ubiquitous in these nodules (only samples 70965 and 76992 are free of apatite). It displays an interstitial, anhedral habit, and is invariably turbid in appearance, due to an extreme abundance of tiny fluid inclusions (figure 2.2.9). Fluid inclusion stage studies show that many of these are CO_2-rich, and contain a vapour bubble surrounded by a thin rim of CO_2-rich liquid, associated with a smaller amount of aqueous fluid. Apatite distribution is generally patchy, often being associated with the glassy pools described above.

2.3 Mineral Chemistry

2.3.1 Introduction

In this section, the mineral chemistry of the constituent phases in the xenoliths is documented and compared with that exhibited by a variety of other type I (Frey and Prinz, 1978) spinel peridotite xenoliths from continental alkali-basalt provinces from around the world. These include modally metasomatised samples which contain various different hydrous, metasomatic phases. Based on their reported mineralogy, the spinel peridotite xenoliths of the dataset used for comparisons with the suite described herein, have been divided into the following groups, (1) anhydrous, (2) amphibole-bearing (or glass after amphibole), (3) mica-bearing, and (4) apatite±amphibole-bearing xenoliths. Data sources are listed in the caption for figure 2.3.1.

2.3.2 Primary olivine

Representative primary olivine compositions from this suite are presented in table B1 (Appendix B). They are typical of those from other mantle-derived peridotite nodules (eg; Frey and Green, 1974; Nickel and Green, 1984; Frey et al. 1985), with forsterite (Fo) contents ranging from Fo_{86} (sample 70987) up to $Fo_{91.5}$ (sample 76995). Primary olivines from the harzburgites are (in nearly all cases) more Fo-rich (mean 90.4) than in the wehrlites or lherzolites (mean 89.4). NiO contents vary from 0.27 to 0.43 wt%, averaging 0.36 wt%. No compositional distinction was observed between

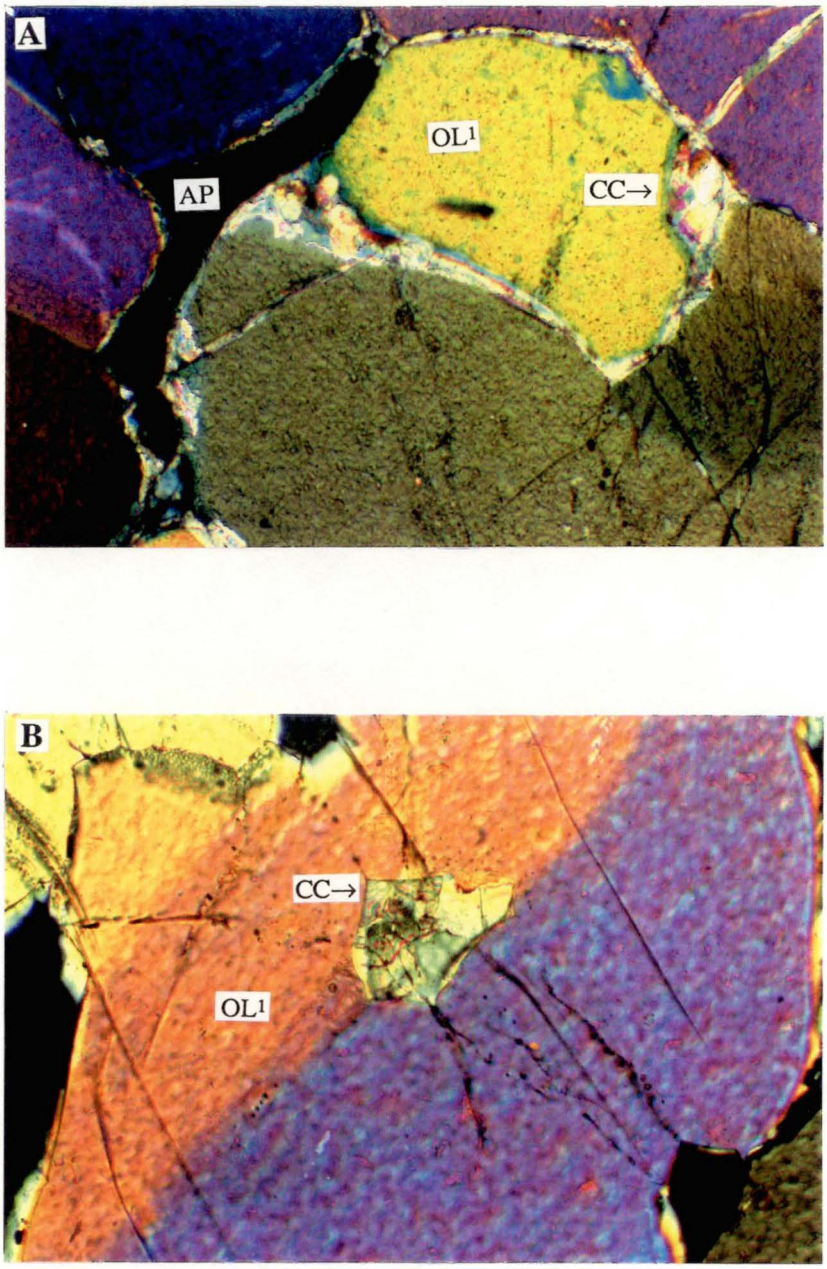

Figure 2.2.8: (A) Secondary calcite veins (CC) in sample 73797, near an apatite grain (AP) (100x magnfication), and (B) calcite inclusion (CC) hosted by primary olivine from same sample (200x magnification).

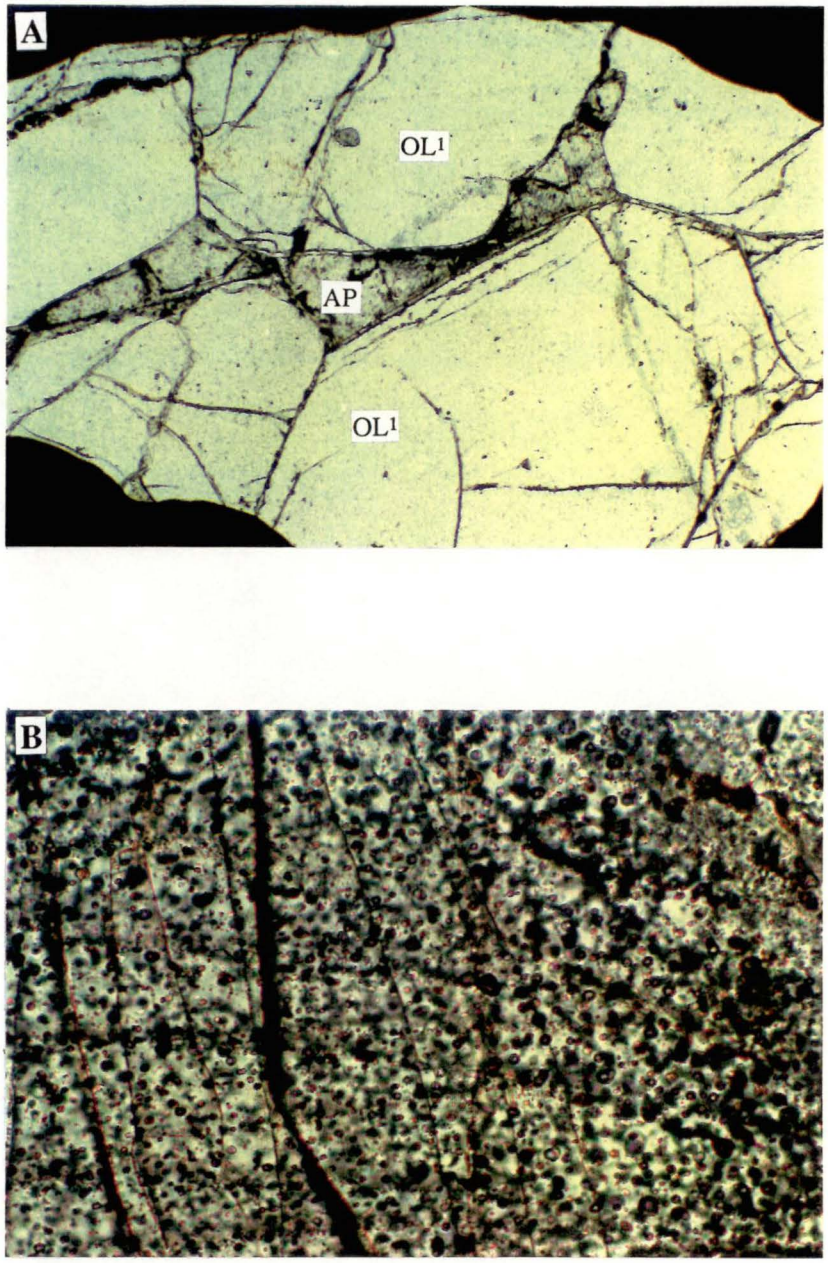

Figure 2.2.9: (A) Apatite (AP) from sample 70969, showing its typical anhedral, intergranular habit. The thin clear rim visible on some parts of the apatite grain is intergranular glass derived from an adjacent patch of amphibole-decompression glass (magnification 50x). (B) Fluid inclusions in apatite from sample 76987 (Magnification 400x).

the porphyroclastic or neoblastic textural varieties. Chemical zoning across individual grains is restricted to minor increases in Fo-content very close to some grain boundaries, probably related to low pressure melting and Fe-Mg exchange between the intergranular glass film and adjacent primary olivine grains. Table B1 (Appendix B) contains representative primary olivine analyses.

Figure 2.3.1 compares the forsterite contents (in mol%) of primary olivine from this suite with those of olivines from peridotites hosted in continental alkali basalts from a number of locations around the world, and displaying a variety of metasomatic mineralogies. The average value for the suite described herein is 89.7 mol%. This compares very favourably with the anhydrous group (average 90.2 mol%) and the amphibole-bearing group (average 90.3 mol%). The fact that the olivine compositions from this suite, and more particularly from the wehrlites, are typical of those in many other mantle-derived spinel peridotites, coupled with the abundance of Cr-diopsidic clinopyroxene and absence of orthopyroxene is consistent with the wehrlites being the result of interaction of lherzolitic or harzburgitic lithosphere with dolomitic carbonatite, as predicted by Green and Wallace (1988).

2.3.3 Primary orthopyroxene

Orthopyroxenes from a large number of anhydrous nodules from various world-wide localities define scattered trends of decreasing Al_2O_3 and CaO with increasing MgO (eg; Nickel and Green, 1984; Galer and O'Nions, 1989; Frey and Prinz, 1978; Fan and Hooper, 1989). These trends have been interpreted as the result of partial melting of peridotite (see figures 2.3.2a and b). Orthopyroxenes in the lherzolites and harzburgites in this suite (table B2) have slightly higher SiO_2 (56.20-59.04 wt%) than many of the other xenoliths. They tend to be lower in Al_2O_3 (0.21-2.54 wt%) and higher in MgO (32.90-34.92 wt%) than orthopyroxene from the majority of other reported anhydrous xenoliths (figure 2.3.2). CaO (0.34-0.86 wt%) and ΣFeO (5.52-7.40 wt%) contents are fairly typical. Wo-En-Fs end-members range from 0.63-1.63, 87.58-91.25 and 8.09-11.09 respectively. 100*Mg/(Mg+ΣFe) varies from 88.79 to 91.83. Core to rim compositional variation within individual orthopyroxene porphyroclasts was not resolvable within microprobe analytical uncertainty. However, minor intergrain variation, particularly in Al_2O_3 content, was observed in some samples.

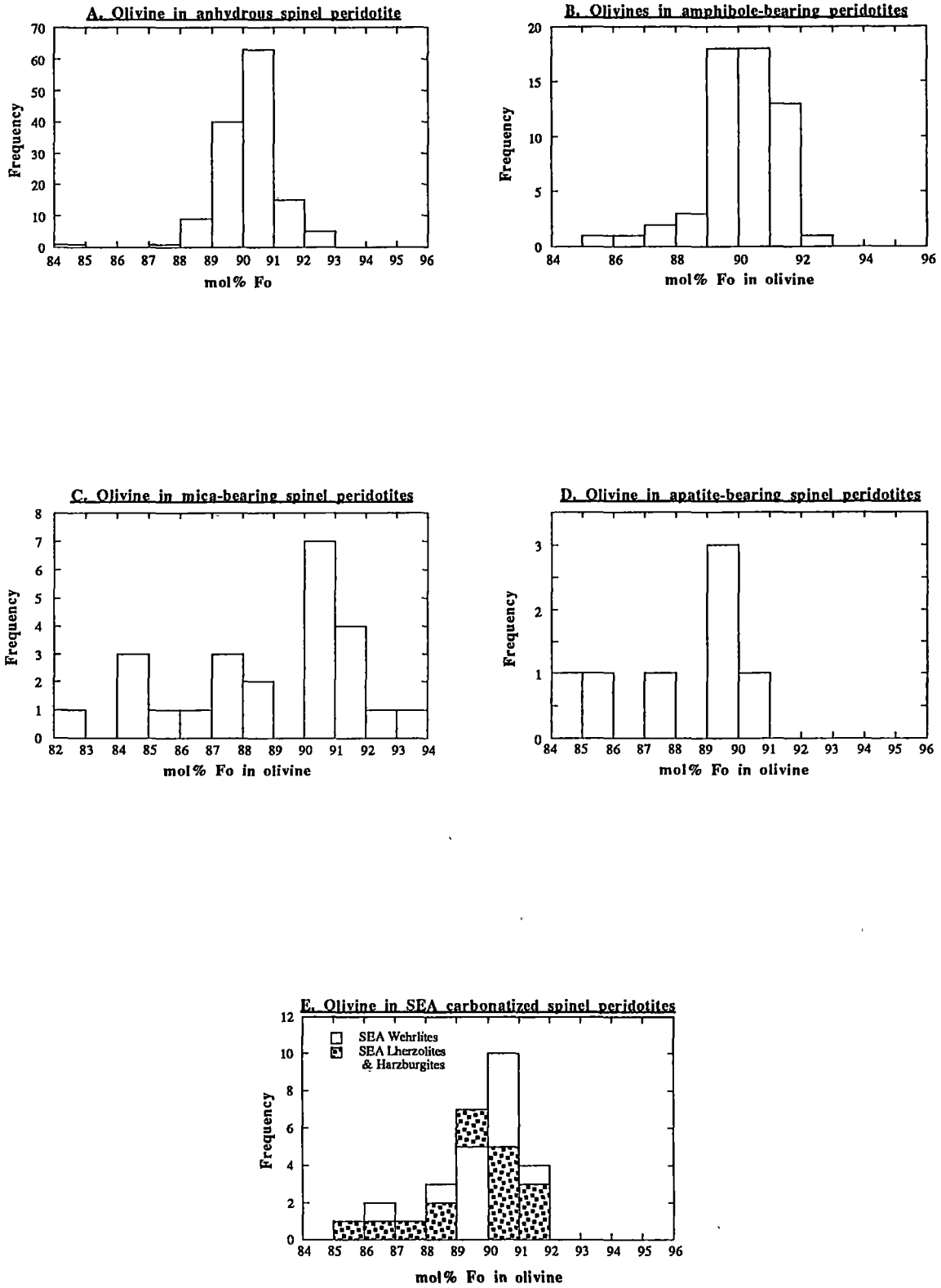

Figure 2.3.1: Histograms of olivine forsterite content in (A) anhydrous, (B) amphibole-bearing, (C) mica-bearing, (D) apatite+amphibole-bearing, and (E) carbonatized spinel peridotites, illustrating that carbonatite metasomatised samples exhibit typical "mantle" Fo values in their olivine, a characteristic shared by amphibole-bearing, and many of the apatite-bearing nodules. This contrasts with the metasomatic style associated with mica addition, in which significant Fe-enrichment is clearly evident in many of the xenoliths. Data sources are Brown et al. (1980), Canil and Scarfe (1989), Chen et al. (1989), Conticello and Peccerillo (1990), Dostal and Capredi (1976), Fan and Hooper (1989), Frey and Green (1974), Frey and Prinz (1978), Galer and O'Nions (1989), Kurat et al. (1991), Liang and Elthon (1989), Nickel and Green (1984), Preß et al. (1986), Rudnick et al. (1992), Song and Frey (1989), Stolz and Davies (1988), Stosch and Seck (1980) and Varne (1977).

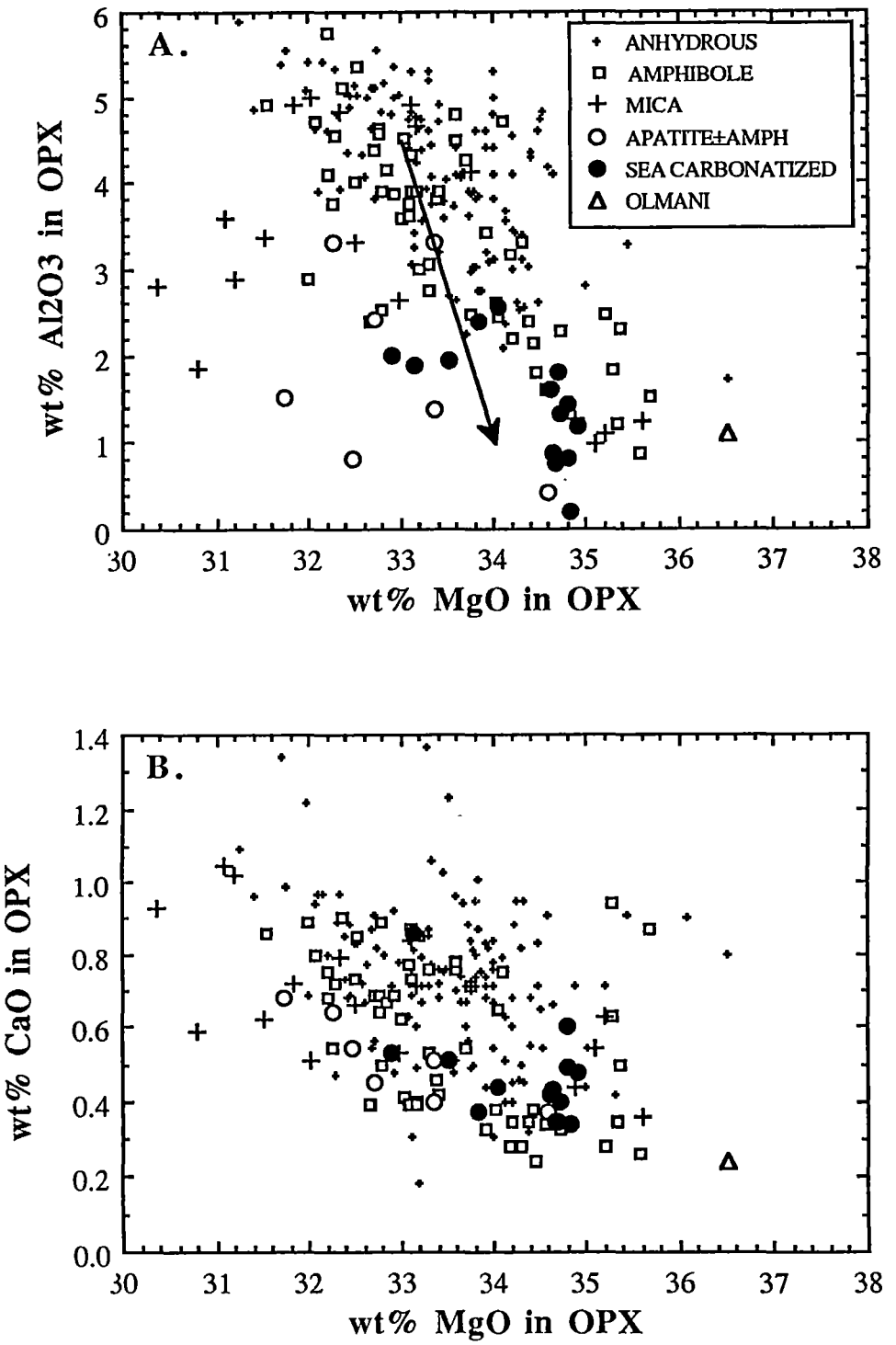

Figure 2.3.2: Plots against wt% MgO in opx grains in spinel peridotites of (A) Al_2O_3, and (B) CaO. This indicates that the carbonatized samples are low in Al_2O_3, but share CaO contents which are typical of other metasomatised and anhydrous peridotite xenoliths. The arrow on (A) is a vector indicating how a typical opx composition from a model anhydrous xenolith would vary on progressive loss of Mg-Tschermak's component, and suggests that compositions of the opx's from the SEA carbonatized suite are the result of such a process. Note also the low MgO content of opx's in many mica-bearing peridotites. Data sources as in figure 2.3.1.

The arrow shown on figure 2.3.2a indicates that the low Al_2O_3 and high MgO content of orthopyroxenes from the SEA carbonatized suite is consistent with a trend generated by partial removal of Mg-Tschermak's component from a model orthopyroxene composition typical of those found in anhydous peridotite xenoliths (33 wt% MgO; 4.5 wt% Al_2O_3).

2.3.4 Primary spinel

Primary spinel grains are enclosed within glassy patches in all of the xenoliths except sample 76987 (magnesian wehrlite) (table B3). Compositionally, these spinels are distinctive from those reported in many other spinel peridotite suites. As a group, they have unusually high atomic 100*Cr/(Cr+Al), ranging from 25.6 to 86.9, with most falling in the range 70-87. In general, spinels in the wehrlites have higher 100*Cr/(Cr+Al) than in the harzburgites or lherzolites (figure 2.3.3). The spinels are also unusual in having low 100*Mg/(Mg+Fe^{2+}) ranging from 38.3 to 71.6, with the wehrlites generally having lower values than lherzolites or harzburgites. 100*Fe^{3+}/$\sum$Fe is similar to spinels from other anhydrous and metasomatised peridotite xenoliths (figure 2.3.4). TiO_2 contents are also similar to those reported from other spinel peridotite xenoliths (figure 2.3.5), ranging from 0.06 to 0.34 wt% in the wehrlites, from 0.21 to 0.66 wt% in the lherzolites, and from 0.02 to 0.12 wt% in the harzburgites. The lherzolites with high-Ti spinels also contain high Ti-pargasite±phlogopite (samples 70987 and 71004), which is interpreted to be the result of a previous metasomatic event involving a basaltic melt, as distinct from a carbonatite melt. Primary spinel compositions are presented in table B3 (Appendix B).

On a plot of 100*Cr/(Cr+Al) vs. 100*Mg/(Mg+Fe^{2+}) (figure 2.3.3), spinels from this suite display some of the highest 100*Cr/(Cr+Al) and lowest 100*Mg/(Mg+Fe^{2+}) yet reported for spinels from peridotite xenoliths in continental settings. Spinel compositions from anhydrous peridotites define a partial melting trend (Dick and Bullen, 1984) on figure 2.3.3. However, the spinels from this suite have more extreme compositions than nearly all of these, suggesting that their compositions were not primarily controlled by previous partial melting event(s). The trend in spinel compositions exhibited by members of the SEA carbonatized suite could result from removal of some (Mg,Fe)Al_2O_4 component from an already refractory Cr-spinel composition.

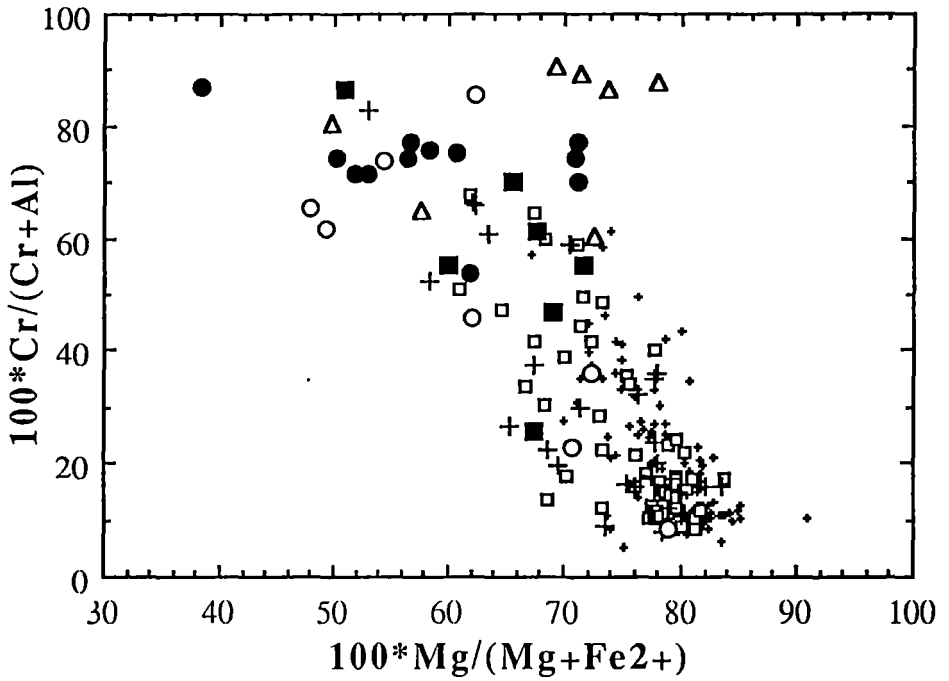

Figure 2.3.3: 100*Mg/(Mg+Fe^{2+}) vs. 100*Cr/(Cr+Al) for spinels from peridotites in data sources listed in figure 2.3.1, showing high 100*Cr/(Cr+Al) and low 100*Mg/(Mg+Fe^{2+}) of carbonatized suite. Symbols as in figure 2.3.4. The main trend exhibited by anhydrous, amphibole, and mica-bearing peridotites is believed to result from mineral/melt partitioning relationships (Dick and Bullen, 1984).

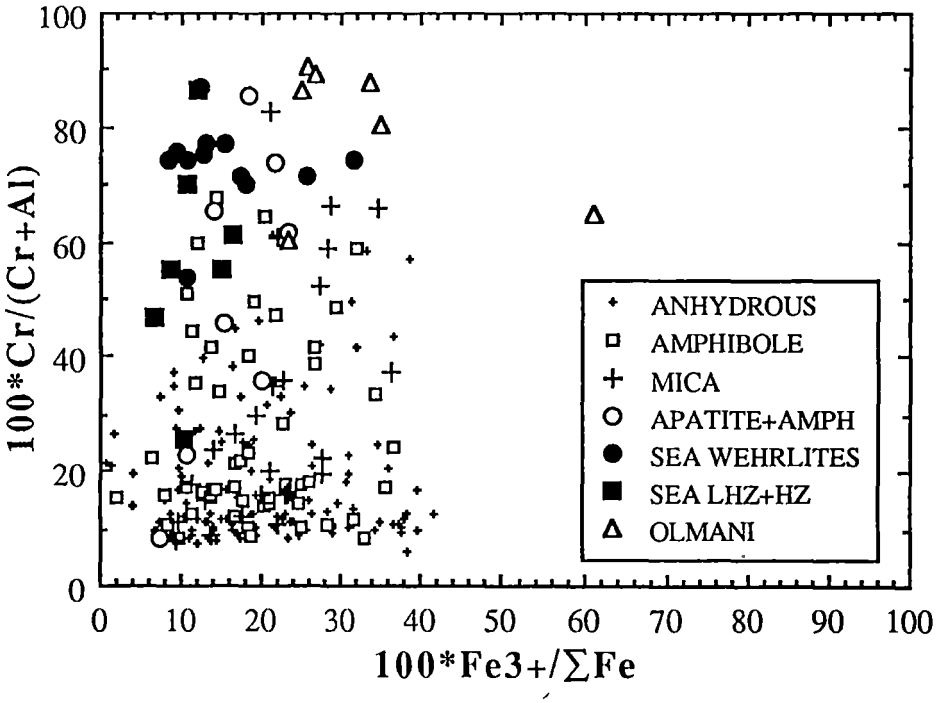

Figure 2.3.4: 100*Fe^{3+}/∑Fe vs. 100*Cr/(Cr+Al) for spinels from peridotites reported in data sources from figure 2.3.1, demonstrating that carbonatized suite have spinels with similar 100Fe^{3+}/∑Fe values to those from other peridotite xenoliths. Symbols as in figure 2.3.2.

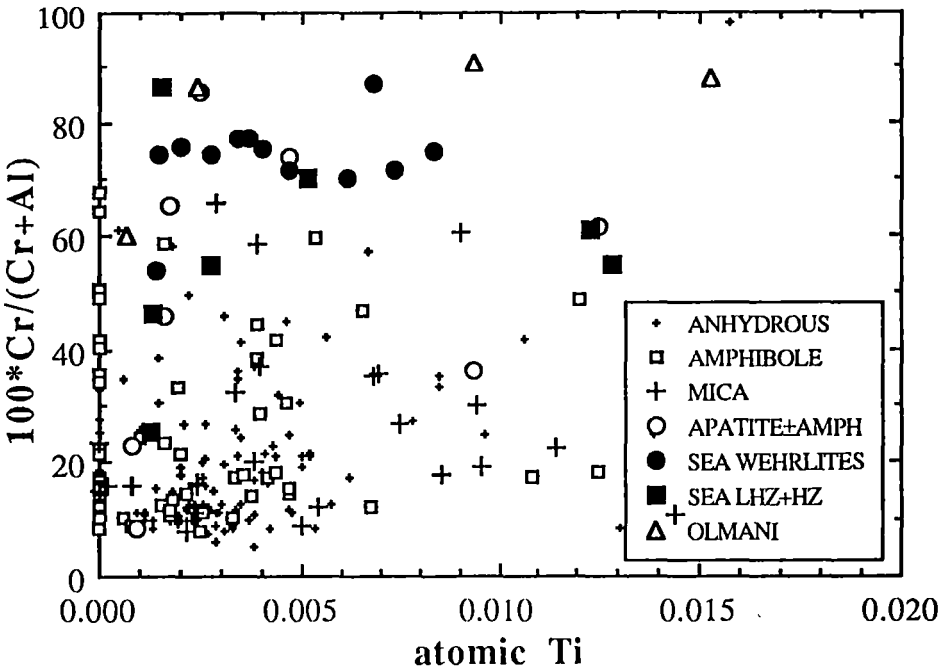

Figure 2.3.5 Atomic Ti vs. 100Cr/(Cr+Al) for spinels from database used in previous figures. Symbols as in figure 2.3.2. This illustrates that Ti contents of spinels in carbonatized peridotites are similar to most other xenoliths. Notable exceptions are many of the mica-bearing peridotites, which contain high-Ti spinels, consistent with their frequently cited bulk-rock Fe-Ti enrichment. The two high-Ti spinel-bearing carbonatized lherzolites also contain high-Ti amphibole±phlogopite, and are believed to have suffered basaltic metasomatism as well as carbonatite metasomatism.

This in turn suggests that the pre-metasomatic lithosphere was very refractory. As will be seen in Chapter 3, this is consistent with the postulated high bulk-rock MgO content of the pre-metasomatic lithosphere, as indicated by figures 3.3.1a-f.

2.3.5 Primary clinopyroxene

Frey and Green (1974), Frey and Prinz (1978), Galer and O'Nions (1989) and others have shown that clinopyroxene compositions in anhydrous mantle peridotites are essentially controlled by processes related to melt/residue equilibria. This results in systematic variations in compositions when plotted against wt% MgO. For example, Na_2O, Al_2O_3 and TiO_2 correlate negatively, whereas Cr_2O_3 correlates positively (figure 2.3.6a-g). Compositions of the annealed clinopyroxenes from the wehrlites in this suite are, however, quite distinctive, and are apparently controlled by other processes. They tend to be enriched in Na_2O, Cr_2O_3 and SiO_2, and depleted in Al_2O_3

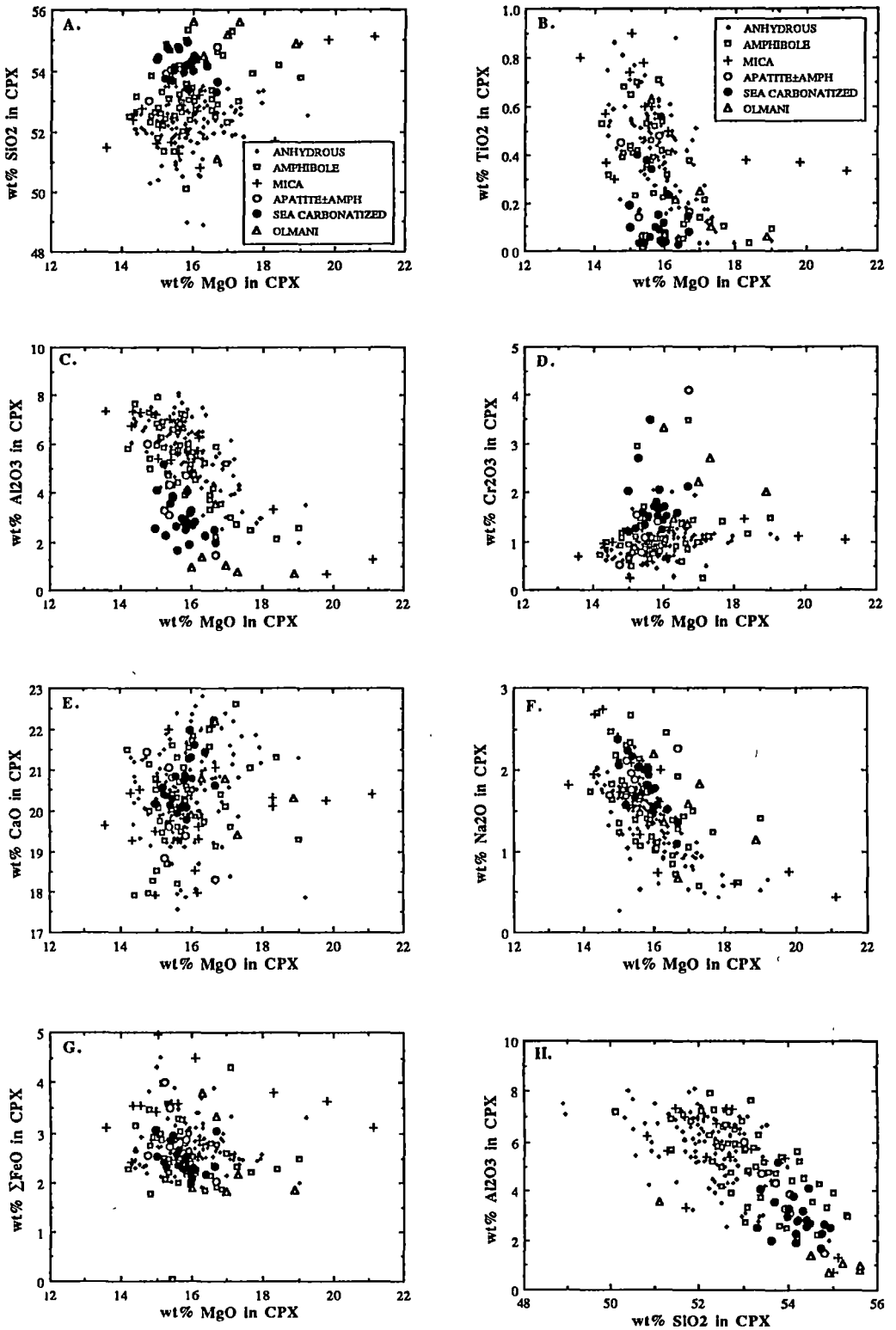

Figure 2.3.6: Plots against wt% MgO of (A) SiO_2, (B) TiO_2, (C) Al_2O_3, (D) Cr_2O_3, (E) CaO, (F) Na_2O, and (G) ΣFeO in cpx's from the database used in figure 2.3.1. Symbols as in figure 2.3.2. (H) Plot of SiO_2 vs Al_2O_3 for the same cpx database.

and TiO_2 for a given MgO content. These characteristics reflect unusually high abundances of the ureiite component in the samples (see table A4).

2.3.6 Phases rimming and replacing primary orthopyroxene

In lherzolite and harzburgite samples which illustrate the partial replacement of orthopyroxene, the mineral chemistry of the replacement phases is somewhat variable (table A5). Accurate microprobe analysis often proved difficult as the fine grain size of the replacement olivine or clinopyroxene grains frequently resulted in excitation of adjacent grains by the electron beam. However, olivine in the replacement rims is always more forsteritic than primary olivine from the same sample. For example, in sample 71008, olivine replacing orthopyroxene ranges from Fo_{91} to Fo_{92}, compared with the primary olivine with $Fo_{87.5}$. Similarly, in sample SH8, olivine replacing orthopyroxene has $Fo_{92.2}$ to $Fo_{93.5}$, compared with primary olivine at $Fo_{89.5}$. CaO contents of replacement olivines range from 0.02 to 1.04 wt% (mean 0.28 wt%), and are substantially higher than CaO in primary olivines (range 0.01 to 0.06 wt%; mean 0.04 wt%). Replacement clinopyroxene is also very variable in composition, even within one replacement rim. In general, however, replacement cpx is higher in MgO, Na_2O and SiO_2, and, lower in Al_2O_3 and TiO_2 (figure 2.3.7), than either metasomatic cpx in the wehrlites, or primary cpx's in anhydrous xenoliths from around the world. $100*Mg/(Mg+Fe^{2+})$ of replacement cpx is invariably higher than that of coexisting primary or annealed, metasomatic cpx.

A possible explanation is that they represent the product of reaction between the amphibole occurring in the xenoliths and the primary orthopyroxene. Lykins and Jenkins (1991) demonstrated experimentally that the reaction

2.1 $Na_2CaMg_4Al_3Si_6O_{22}(OH)_2 + 5MgSiO_3 =$
pargasite opx

$$CaMgSi_2O_6 + 4Mg_2SiO_4 + (NaAlSi_3O_8 + CaAl_2Si_2O_8) + H_2O$$
diopside forsterite plagioclase

controls pargasite stability in the presence of orthopyroxene at P<9 kbars. Isothermal decompression of a pargasite-bearing lherzolite or harzburgite assemblage during ascent in the host magma could result in reaction 2.1 occurring at low pressures,

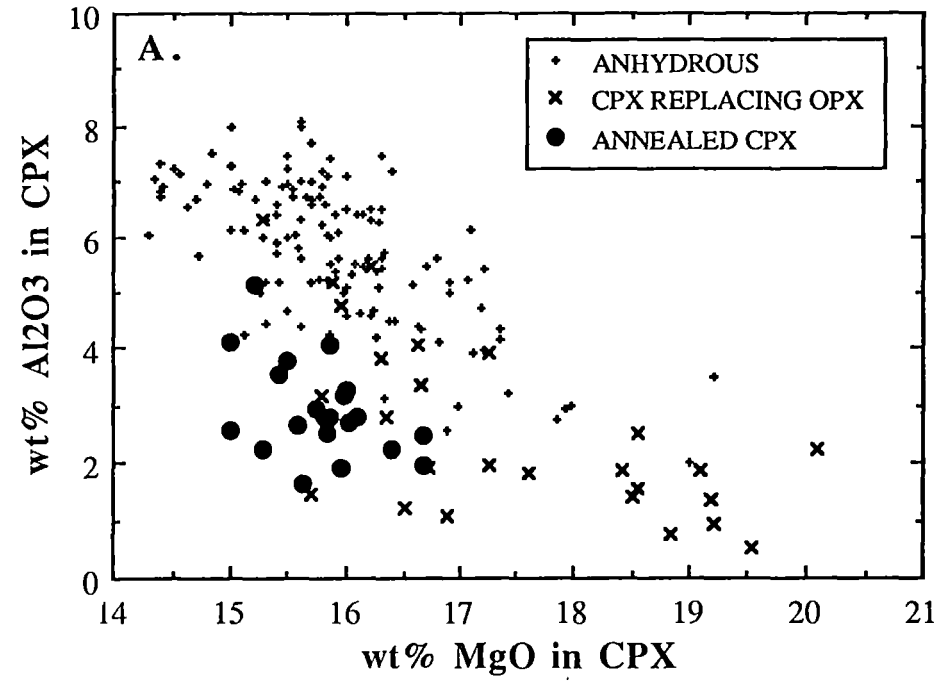

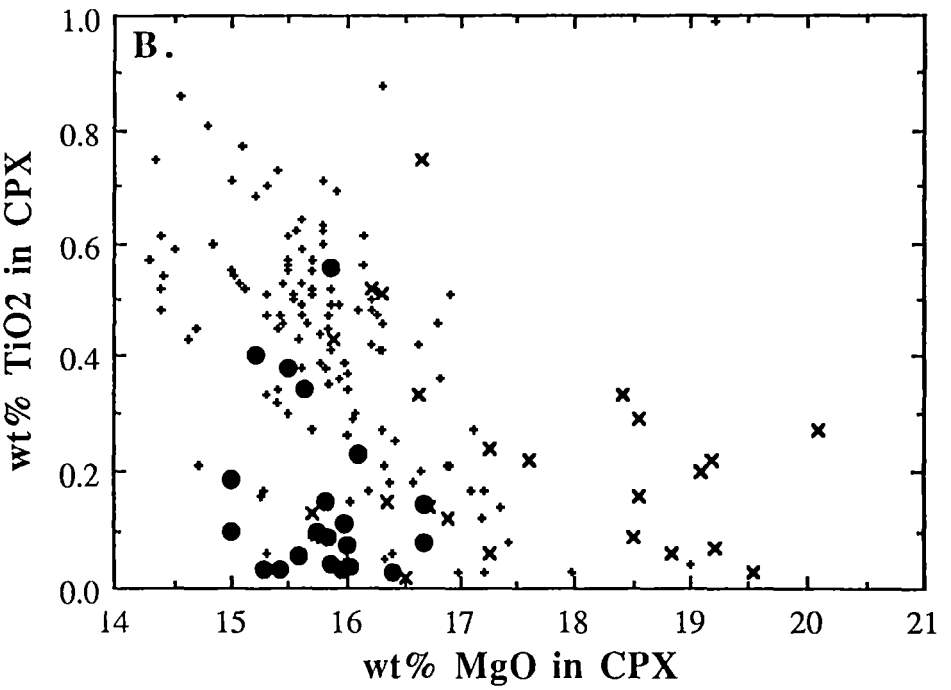

Figure 2.3.7: Plots against wt% MgO of (A) Al_2O_3 and (B) TiO_2 for clinopyroxene grains replacing orthopyroxene, compared with clinopyroxene from world-wide anhydrous xenoliths, and annealed clinopyroxenes in the SEA carbonatite metasomatised suite.

producing a rim of olivine+clinopyroxene where primary orthopyroxene was in contact with pargasitic amphibole. Plagioclase, which is not observed, is assumed to produce melt at the plagioclase + olivine + orthopyroxene + clinopyroxene + spinel eutectic.

However, the fact that fine-grained aggregates of olivine+clinopyroxene were observed frequently replacing orthopyroxene in the absence of amphibole-glass (see section 2.2), as well as the low Al_2O_3 content of the secondary clinopyroxene, suggest an alternative explanation that the orthopyroxene replacement rims represent arrested stages of the reaction opx + dol = cpx + ol + CO_2, between ascending dolomitic carbonatite melt and primary orthopyroxene at 15-20 kbars, as predicted by experimentally-determined pyrolite-COH phase relations (Wallace and Green, 1988; Falloon and Green, 1990).

Sample 76988 (an orthopyroxene-free magnesian wehrlite) contains poikilitic inclusions of olivine in large clinopyroxene grains. The olivines are approximately 1 mol% richer in forsterite than porphyroclastic or neoblastic olivine grains from the same sample (see table B1), and are believed to represent a further stage in the replacement of orthopyroxene than is preserved in the olivine+clinopyroxene replacement rims described above, that is, complete replacement of orthopyroxene, with only partial annealing and coarsening of a previously fine-grained olivine+clinopyroxene assemblage. The magnesian wehrlites are believed to represent the final stage of this process, in which annealing and textural equilibration is complete.

2.3.7 Apatite

Metasomatic apatites in this suite are halogen rich, containing from 1.14-4.83 wt% F and 0.26-2.36 wt% Cl. Atomic F/Cl values are invariably >1, ranging from 1.28 up to 18.38. An abundance of CO_2-rich fluid inclusions in apatite grains, which may have exsolved from the the apatite upon decompression during ascent of the xenoliths, as well as consistently low cation totals (table B7) suggests that significant hydroxyapatite and carbonate components are present as well. SrO varies from 0.49 to 2.90 wt%, with P_2O_5 and CaO contents range from 38.92 to 42.28 wt%, and 49.20 to 55.63 wt% respectively (see table B7).

Compositional variation between individual apatite grains within one sample is limited, as evident from the analyses presented in table B7. Similarly, multiple analyses of single grains proved them to be almost homogeneous. Many metasomatic apatite grains (eg; samples 76990 and 76987), however, have thin rims of clear, inclusion-free apatite where the grain edges are in contact with amphibole-derived glass (figure 2.2.6). These rims are compositionally distinct from the interior of the grain, having, most notably, a lower Sr content, and higher F/Cl values. In addition, in some samples, needles and laths of euhedral apatite can be observed in amphibole-decompression glass, often nucleating on pre-existing metasomatic apatite grains. Compositionally, these are similar to the inclusion free rims described above. Thus, these rims are considered to represent overgrowths of apatite deposited on pre-existing metasomatic apatite during quenching of the amphibole-derived glass.

2.3.8 Amphibole, phlogopite, internal glass and associated microphenocrysts

Relict amphibole is found in five of the xenoliths (71007 and 71000 are wehrlites, 71004 and 70987 are lherzolites, and 71006 is a harzburgite). Samples 71006, 71007 and 71000 contain low-Ti pargasite (TiO_2<1wt%), whereas 71004 and 70987 contain high-Ti pargasite (TiO_2>3wt%). In addition, minor phlogopite was observed in 71004 and 71007. Analyses of these phases are presented in table B8.

The glassy patches exhibit a large range of compositions, both within and between individual patches and between different samples. Table B9 contains average analyses from one or more glass patches in most of the samples in the suite. The range of these analyses is demonstrated by figure 2.3.8, in which various oxides are plotted against wt% MgO.

Secondary olivine microphenocrysts in the glass patches are usually 1-4 mol% richer in forsterite than primary olivine from the same sample (table B10). NiO contents are comparable (0.22-0.47 wt%). However, CaO contents are higher in the secondary olivine, typically around 0.22 wt%, compared with average of 0.03 wt% in primary olivines. 100*Mg/(Mg+$\sum$Fe) values are usually unzoned from rim to core. The olivine microphenocrysts are generally euhedral, although in some cases evidence of resorption is present.

Endmember compositional ranges in average secondary clinopyroxene grains are as follows; Wo 44.11 to 50.43 mol %; En 46.23 to 53.24 mol%; Fs 2.65 to 5.91, and

are comparable to primary clinopyroxenes from the suite (table B11). They are, however, generally less sodic, but more aluminous than coexisting primary clinopyroxenes.

Secondary spinels have generally higher $100*Mg/(Mg+Fe^{2+})$, lower $100*Cr/(Cr+Al)$ and higher $100*Fe^{3+}/\sum Fe$ than coexisting primary spinel (table B12). They are also substantially richer in TiO_2 (0.44 to 1.72 wt%).

Several lines of evidence suggest that the internal glass patches derive from decompression fusion of hydrous silicate phases, such as amphibole or phlogopite. For example, in all samples in which amphibole or phlogopite were found, the grains have rounded, embayed shapes, suggestive of partial melting. In addition these grains were invariably partially or completely surrounded by glass and associated secondary microphenocrysts. Sample 76992 (from Mt Noorat), the only composite xenolith in the suite, also provides textural evidence that the internal glass in these xenoliths derives from melting of a pre-existing phase. Mineralogically, this xenolith is a glass-bearing, spinel wehrlite assemblage. Part of the sample is well annealed, and unsheared and is similar in general characteristics to other wehrlites in the suite. This part of the xenolith, however, contacts sharply with a strongly foliated portion, in which the fabric is defined by elongation and alignment of clinopyroxene grains and primary spinel+glass patches (figure 2.3.9). Definition of the foliation by alignment of glass patches requires that the glass has replaced a sheared or foliated solid phase *in situ*, which was subsequently melted. It is believed that the prior phase was amphibole. The observations favour an origin for glass in these xenoliths which involves melting of a pre-existing solid phase, rather than an origin as a trapped intercumulus, or migratory melt.

Furthermore, the alkali element and Ti abundances of the glass (table B9) are dependent on the nature of the hydrous phase with which it is associated (Frey and Green, 1974). For example, in 71000, which contains low-Ti pargasite, the glass is relatively low in TiO_2 (average 0.86 wt%), and has a low K_2O/Na_2O value (average 0.35), consistent with melting of low-Ti amphibole (amphibole in 71000 has K_2O/Na_2O value of 0.30; table B8), rather than phlogopite and/or high-Ti amphibole. In contrast, glass in 70987, in which the hydrous silicate phase observed was high-Ti pargasite, has a similarly low K_2O/Na_2O (average 0.53, compared with value for relict amphibole of 0.35), but markedly higher TiO_2 (average 3.52 wt%). Glass in sample

71004, in which relict grains of both phlogopite and high-Ti pargasite were observed, has a higher K_2O/Na_2O (average 0.88), and high TiO_2 content (average 2.71 wt%), consistent with its derivation by mixing of melts of both amphibole and phlogopite.

Glass compositions in the majority of the remaining xenoliths (which contain no relict hydrous silicate phases) are consistent with an origin for the glass by melting of low-Ti amphibole (ie; low K_2O/Na_2O and low TiO_2). Exceptions are 70969 and 70972, in which glass compositions are more potassic (average K_2O/Na_2O values of 0.98 and 1.06 respectively), suggesting the presence of both phlogopite and amphibole before glass formation.

The glasses are chemically heterogeneous, both within and between samples, particularly with respect to MgO, SiO_2, Al_2O_3, FeO and CaO contents (table B9; figure 2.3.8). The ubiquitous presence of clinopyroxene and spinel, and frequent presence of olivine microphenocrysts within the glass patches suggest that varying degrees of crystallization of these phases may have exerted some control on glass compositions. In addition, reaction with adjacent primary phases such as spinel, olivine or pyroxenes may have modified the glasses. The unusually high P_2O_5 in many of these glasses (figure 2.3.10) suggests that metasomatic apatite may have contributed CaO and P_2O_5 components, and that many of the glasses may be saturated in apatite.

The phase relations of the system pargasite-H_2O-CO_2 have been determined experimentally to 8 kbar by Holloway (1973) and 9 kbar by Lykins and Jenkins (1991). Near isothermal transport of a pargasite-bearing xenolith at magmatic temperatures from lithospheric pressures to near surface conditions should result in melting of the hydrous phase. Partial crystallization, and quenching of the resultant liquid produced the crystalline assemblages observed in the glassy patches described above.

2.3.9 Carbonate

Regardless of its textural setting, carbonate is calcitic in composition, containing 52.25 to 57.14 wt% CaO (table B13). 100*Mg/(Mg+ΣFe) values for carbonate found as inclusions in glass or olivine (76995, 76993, 73797) are higher than coexisting primary phases, ranging from 95.5 to 99. However, vein carbonate in 73797 has a

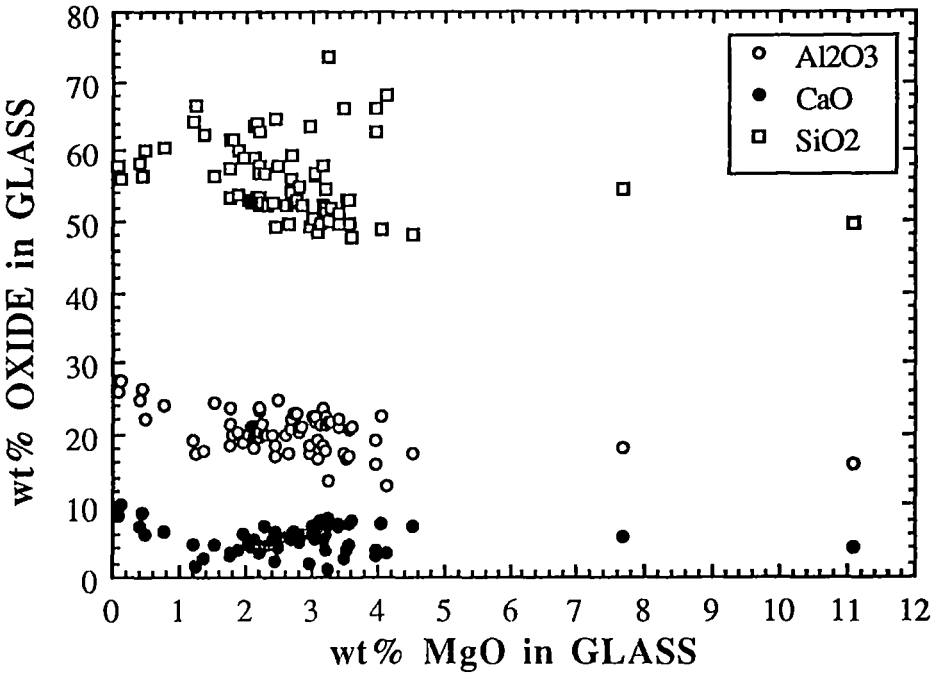

Figure 2.3.8: Plots against MgO of Al_2O_3, CaO and SiO_2 for average internal glass compositions from the SEA carbonatized suite, showing systematic variation probably related to metastable fractionation of sp+cpx±ol microphenocrysts on quenching of the glass. See table B9 for data.

distinctly lower 100*Mg/(Mg+$\sum$Fe) value of 88.3. The carbonate is essentially free of alkali components, TiO_2 and Al_2O_3 (except vein carbonate in 73797), but contains significant P_2O_5 (0.93 to 2.49 wt%).

Carbonate is very rare in mantle-derived xenoliths. However, calcitic carbonate has been reported from one other southeastern Australian spinel peridotite xenolith (O'Reilly and Griffin, 1988). Canil (1990) reported the results of a series of decompression experiments in the peridotite-CO_2 system, which demonstrated that the absence of carbonate in nearly all xenoliths (despite abundant evidence for its involvment in petrogenetic processes in the mantle; eg; Brey and Green, 1976), is due to decarbonation on ascent via the reaction enstatite + dolomite = forsterite + diopside + CO_2. Apparently, the only manner in which dolomitic carbonate in a peridotite xenolith can survive the rapid decompression associated with ascent to the surface, is if it is included within a phase which chemically shields it from interaction with orthopyroxene.

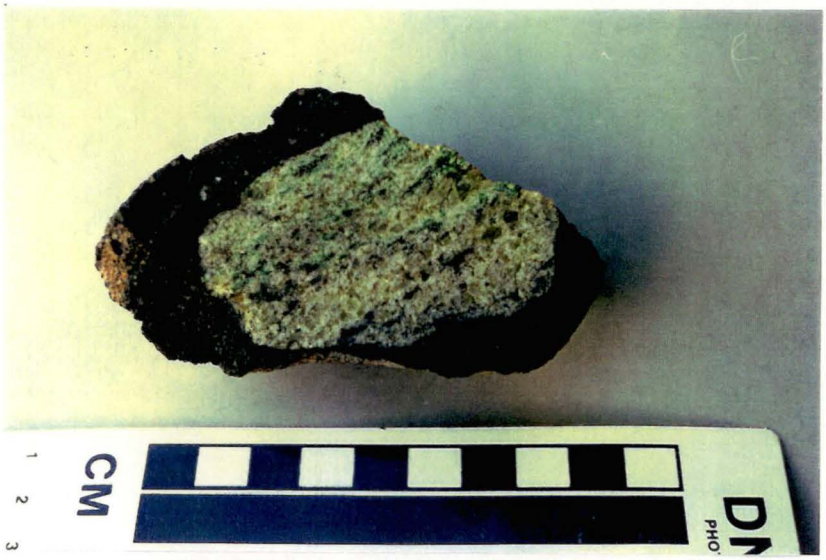

Figure 2.3.9: Sample 76992, showing foliation defined by elongation and alignment of apple-green clinopyroxene grains, and grey glassy patches. This suggests that the glass has replaced a previously foliated solid phase which subsequently melted. See text for further explanation.

The fact that, at least in samples 76995 and 76993, the carbonate is found only in association with orthopyroxene replacement textures and amphibole decompression glass, as well as the high Mg/(Mg+$\sum$Fe) values for the carbonate, tends to favour an origin associated with the metasomatic carbonatite, rather than low temperature remobilization or weathering effects. However, the latter cannot be precluded in the case of the vein carbonate in 73797, although the presence of carbonate as inclusions in olivine suggests a deep origin, rather than low pressure and low temperature veining. In samples 76995 and 76993, carbonate may be preserved in the process of reacting with primary orthopyroxene.

The reaction

2.1 $4MgSiO_3 + CaMg(CO_3)_2 = 2Mg_2SiO_4 + CaMgSi_2O_6 + 2CO_2$
enstatite dolomite forsterite diopside

was determined in PT space in the system CaO-MgO-SiO_2-CO_2 by Wyllie and Huang (1976). In addition, the reaction

2.2 $CaMgSi_2O_6 + 3CaMg(CO_3)_2 = 2Mg_2SiO_4 + 4CaCO_3 + 2CO_2$
diopside dolomite forsterite calcite

was bracketed experimentally by Käse and Metz (1980). Figure 2.3.11 indicates that these univariant reactions intersect, forming an invariant point at approximately 9 kbars and 830°C. Thus the reaction

2.3 $MgSiO_3 + CaMg(CO_3)_2 = Mg_2SiO_4 + CaCO_3 + CO_2$
enstatite dolomite forsterite calcite

will occur at pressures and temperatures below this. Therefore, dolomite which may remain stable in an orthoypyroxene-free wehrlite at pressures below reaction 2.1, will be converted to magnesian calcite on crossing this reaction during decompression associated with host magma eruption.

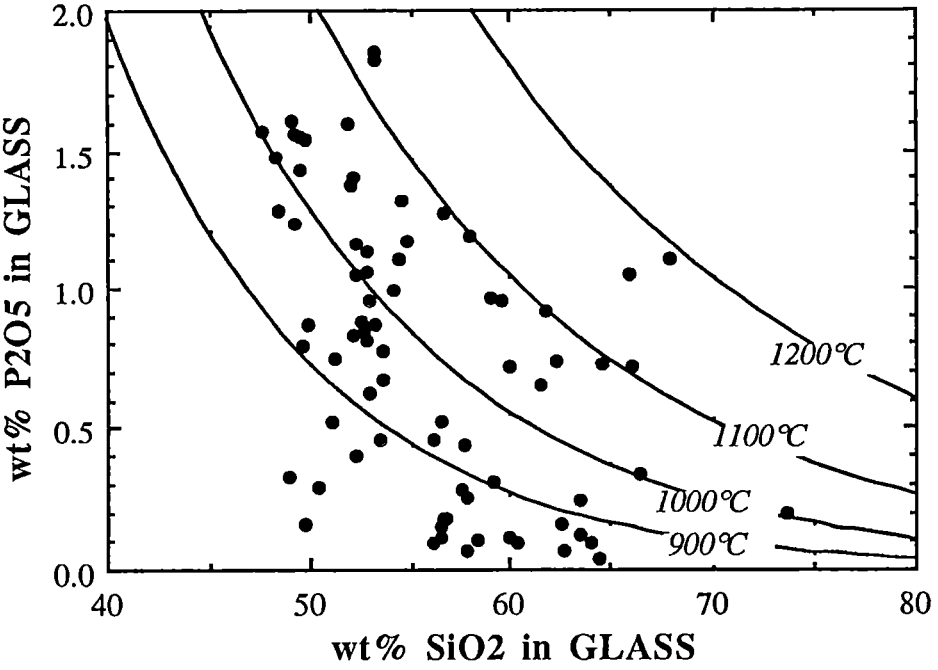

Figure 2.3.10: Plot of SiO_2 vs. P_2O_5 for average internal glass compositions from the SEA carbonatized suite. The curves are apatite saturation curves calculated using the relationship of Harrison and Watson (1984). Virtually all the glass analyses plot below the 1100°C saturation curve, implying that (1) some glasses have reached saturation in apatite components due to dissolution of metasomatic apatite by glass derived from decompression fusion of amphibole, and (2) the maximum T of eruption of the host magmas which transported the nodules to the surface was 1100°C.

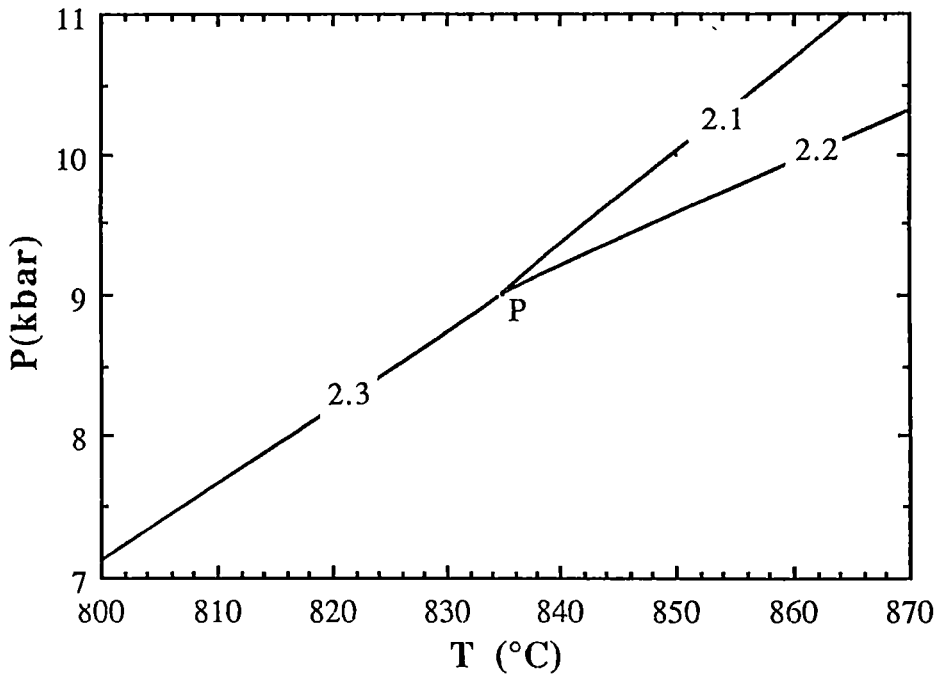

Figure 2.3.11: Reactions 2.1 (Wyllie and Huang, 1976) and 2.2 (Käse and Metz, 1980) plotted in PT space, and intersecting at invariant point P, to generate reaction 2.3. See text for further explanation.

2.4 Discussion

2.4.1 The case for carbonatite metasomatism

The petrographic and mineralogical characteritics of the suite as described in earlier sections agree very closely with the predicted (Green and Wallace, 1988) products of the metasomatic interaction of carbonatite melts with refractory lithosphere.

For example, the assemblage of highly forsteritic olivine and sodic, high $Mg/(Mg+Fe^{2+})$ clinopyroxene, coupled with the complete absence of orthopyroxene is a strikingly unusual characteristic of the wehrlites in this suite compared with other mantle-derived spinel peridotites. It is plausibly explained by interaction of lherzolitic or harzburgitic lithosphere with dolomitic carbonatite via the decarbonation reaction 2.1, resulting in complete replacement of primary orthopyroxene with forsteritic olivine and sodic Cr-diopsidic clinopyroxene (Green and Wallace, 1988; Chapter 1).

Furthermore, preservation of rims of forsteritic olivine and clinopyroxene unequivocally replacing primary orthopyroxene are considered to be further evidence of the occurrence of the above decarbonation reaction. Evidence of the presence of CO_2-rich decarbonation fluids is also preserved as fluid inclusions in metasomatic apatite, olivine, and clino- and orthopyroxene. The almost ubiquitous occurrence of accessory apatite and amphibole also conforms to the predictions of Green and Wallace (1988).

It is therefore considered that the orthopyroxene-free wehrlites from the suite represent the "end-product" of carbonatite metasomatism in which the primary orthopyroxene was reacted out of existence by influx of excess carbonatite. Rapid annealing, and partial or complete re-equilibration, removed direct evidence of the metasomatic decarbonation reaction, and resulted in production of the apatite+amphibole-bearing magnesian wehrlite suite. In the lherzolites and harzburgites, metasomatism was interrupted before exhaustion of orthopyroxene or carbonatite, by entrainment in the host magma, followed by rapid ascent to the surface, and quenching, resulting in preservation of olivine+clinopyroxene replacement textures on primary orthopyroxene.

2.4.2 Decarbonation reactions and carbonatite melt evolution

The low contents of Al_2O_3 in relict orthopyroxene grains in the harzburgites and lherzolites from this suite, as well as the low $100*Mg/(Mg+Fe^{2+})$ and high

100*Cr/(Cr+Al) from primary spinels (particularly those from the wehrlites), are consistent with decarbonation reactions between these primary lithospheric phases and sodium-bearing dolomitic carbonatite melt involving removal of (Mg,Fe)-Tschermak's component from orthopyroxene and $(Mg,Fe)Al_2O_4$ component from spinel. This has introduced diopsidic clinopyroxene with high Na_2O and Cr_2O_3, and low Al_2O_3 and TiO_2, into the assemblage. Possible end-member decarbonation reactions are as follows;

2.4 $4MgSiO_3 + CaMg(CO_3)_2 = 2Mg_2SiO_4 + CaMgSi_2O_6 + 2CO_2$
enstatite dolomite forsterite diopside

2.5 $[7MgSiO_3 + MgAl_2SiO_6] + Na_2CO_3 = 4Mg_2SiO_4 + 2NaAlSi_2O_6 + CO_2$
orthopyroxene sodium carbonate forsterite jadeite

2.6 $9MgSiO_3 + Mg(Cr,Al)_2O_4 + Na_2CO_3 = 5Mg_2SiO_4 + 2Na(Cr,Al)Si_2O_6 + CO_2$
enstatite spinel sodium carbonate forsterite jadeite-ureiite solid solution

Experimental evidence (Wallace and Green, 1988) suggests that in its source regions, the carbonatite formed in equilibrium with pargasitic amphibole. Partitioning of H_2O into this silicate phase would have resulted in low, but significant H_2O solubility in the carbonatite melt (estimated at 1-2 wt%; Wallace and Green, 1988). However, subsequent, shallower metasomatic decarbonation reactions between the ascending carbonatite and peridotite wall rock could have stabilized amphibole as the melt underwent open system decarbonation. A possible end-member decarbonation reaction is as follows;

2.7 $10MgSiO_3 + 3MgAl_2O_4 + 3CaMgSi_2O_6 + [Na_2CO_3 + Ca(OH)_2] =$
enstatite spinel diopside carbonatite melt components

$$2NaCa_2Mg_4Al_3Si_6O_{22}(OH)_2 + 4Mg_2SiO_4 + CO_2$$
pargasite forsterite

Precipitation of metasomatic apatite may be interpreted in terms of rapid evolution of the carbonatite melt, resulting in increasing P_2O_5 and halogen contents, until apatite saturation is achieved. Further evidence for such evolution of the carbonatite melt is

manifest in the rare occurrence of secondary orthopyroxene (figure 2.4.1), which rims some apatite grains, and forms delicate veinlets which invade and replace adjacent clinopyroxene and primary olivine (eg; 71004 and 71008). End-member reactions may be written in which primary forsterite, diopside, and [halogen+P_2O_5]-bearing carbonatite melt components react, producing secondary orthopyroxene and haloapatite components; for example

2.8 $9Mg_2SiO_4 + 9CaMgSi_2O_6 + [3P_2O_5 + CaX_2] = 27MgSiO_3 + 2\ Ca_5(PO_4)_3X$

primary olivine; diopside; carbonatite melt components; secondary orthopyroxene; haloapatite

where X=F, Cl etc. The Al_2O_3 content of the secondary orthopyroxene is lower than that of the relict, primary orthopyroxene. Otherwise, their compositions are broadly similar (table B2).

2.5 Summary

Based on the pyrolite-CO_2-H_2O phase relations presented by Wallace and Green (1988) and Falloon and Green (1990), and summarized in Chapter 1, as well as the petrographic and mineralogical evidence presented in this Chapter, a model for interaction of sodic, dolomitic carbonatite melt with refractory harzburgitic or lherzolitic lithosphere in presented.

An ascending carbonatite melt crosses the divariant decarbonation reaction opx + dol = ol + cpx + CO_2 at 15-20 kbar (Wallace and Green, 1988; Green and Wallace, 1988; Falloon and Green, 1990). A series of decarbonation reactions occurs between components in wall-rock phases and the carbonatite. The nett effect of these reactions is to react the enstatite and Mg-Tschermak's components from orthopyproxene, and $MgAl_2O_4$ components from spinel, with dolomitic and sodium carbonate components of the carbonatite, producing forsteritic olivine, and sodic Cr diopsidic clinopyroxene. These end-member reactions would be accompanied by release of abundant CO_2-rich fluid.

A small $Ca(OH)_2$ component in the carbonatite could result in stabilization of low-Ti pargastic amphibole. Evolution of the melt to high P_2O_5 and halogen content could result in precipitation of apatite, and in rare instances produce secondary

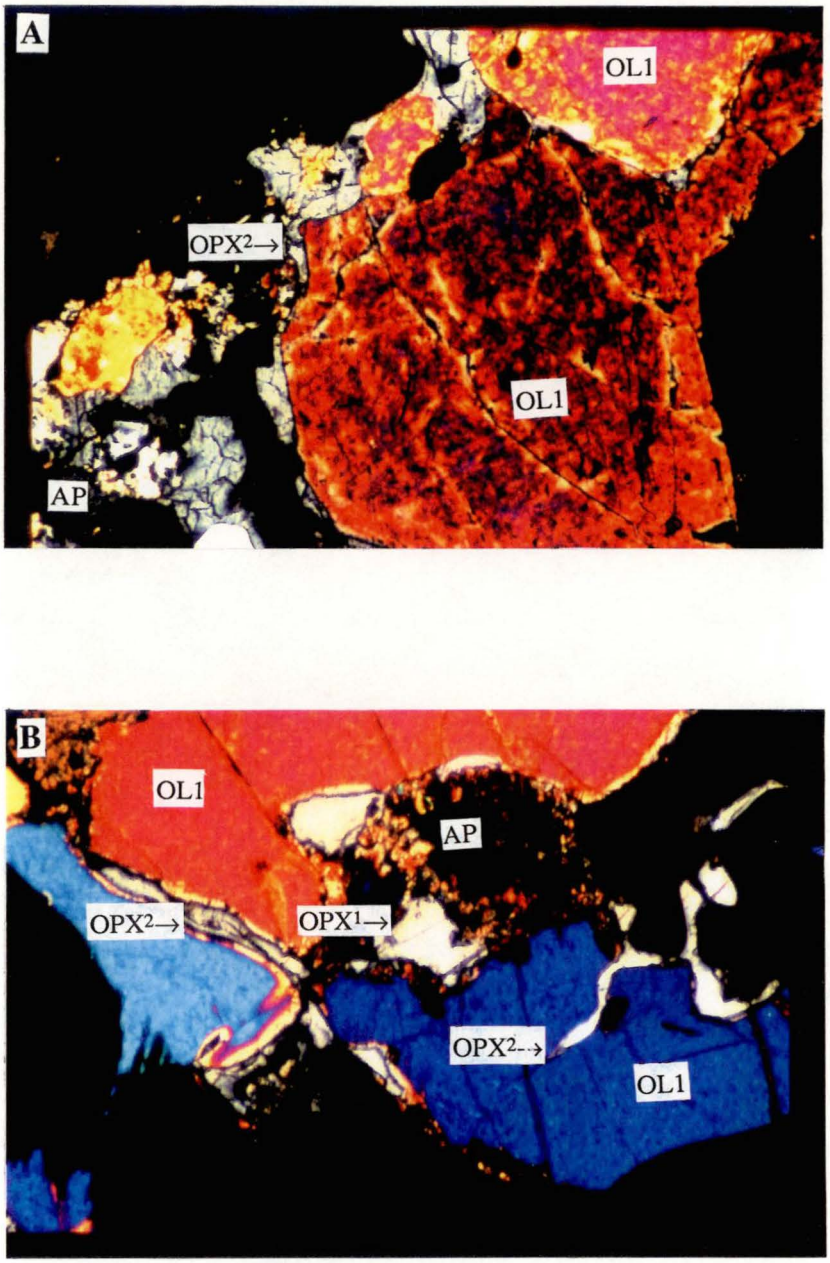

Figure 2.4.1: Secondary orthopyroxene (OPX^2) which rims and replaces primary olivine (OL^1) and clinopyroxene, and is associated with apatite (AP) in (A) sample 71004, and (B) sample 71008. This provides evidence of evolution of the carbonatite as described in the text. Note in 71008, the contrasting appearance of primary orthopyroxene (OPX^1), which is rimmed by a replacement assemblage of fine-grained olivine and clinopyroxene (magnification 50x for A and B).

orthopyroxene. Complete replacement of primary orthopyroxene by olivine and clinopyroxene, involving influx of excess carbonatite melt, followed by annealing, produced the wehrlite suite. Interruption of the decarbonation reaction by entrainment in the host magma resulted in preservation of textures indicative of the above reaction. Furthermore, exhaustion of the supply of carbonatite melt before elimination of orthopyroxene, followed by annealing, could conceivably produce anhydrous spinel lherzolites, in which slightly increased cpx/opx values are the only petrographic trace of carbonatite metasomatism.

CHAPTER 3

GEOCHEMICAL EVIDENCE FOR CARBONATITE METASOMATISM OF THE SOUTHEASTERN AUSTRALIAN LITHOSPHERE AS DISPLAYED IN SPINEL PERIDOTITE XENOLITHS

3.1 Aims of the chapter

The purposes of this chapter are firstly, to demonstrate that major, minor and trace element signatures, and isotopic systematics of a suite of SEA xenoliths are consistent with metasomatism by an ephemeral carbonatite melt, and secondly, to further develop the model for carbonatite metasomatic activity presented in Chapters 1 and 2, by establishing its relationship to other metasomatic styles in this part of the continental lithospheric mantle, and to the magmatic activity associated with eruption of the Newer Volcanics.

3.2 Analytical details

Central portions of the nodules described in Chapter 2 were cut out to minimize the effect of host contamination, and cleaned ultrasonically to remove fragments of the saw blade. These were then crushed in either an agate or tungsten-carbide ring mill. Major elements were determined by XRF using fused glass discs made from these powders. Na_2O was determined by atomic absorption spectroscopy (AAS). REE, and Hf, Ta, Th and Sc were determined by Instrumental Neutron Activation Analysis (INAA) at the Becquerel Laboratories (NSW). Other trace elements were determined by XRF using pressed powder pills. Isotopic analyses were performed at ANU by isotope dilution (ID). Analytical procedures are described in more detail in Appendix A.

3.3 Evidence from major element geochemistry for metasomatism by an ephemeral dolomitic carbonatite

Geochemical analyses of the nodules comprising this suite are presented in Appendix C. The major element geochemistry of that part of the lithosphere represented by these samples reflects the modal changes induced by the metasomatic decarbonation reactions described in Chapter 2. For example, replacement of orthopyroxene by clinopyroxene, and addition of apatite, has driven bulk-rock CaO/Al_2O_3 to unusually

high values (from 0.68 to 5.22 with average 2.62, compared with 0.95 for "average" subcontinental lithosphere of McDonough, 1990). Similarly, the presence of metasomatic pargasite and clinopyroxene with high jadeite+ureiite contents in the samples has resulted in unusually high bulk-rock Na_2O/Al_2O_3 values (0.11 to 0.71 with average 0.43, compared with the typical value of 0.11).

The presence of modal apatite results in high P_2O_5 contents (up to 0.77 wt%). Notably, sample 70965, an apatite-free, amphibole glass-bearing magnesian wehrlite, contains only 0.02 wt% P_2O_5.

Plots of oxide components vs. wt% MgO for a database which includes >300 spinel peridotite analyses from localities around the world yields systematic trends which are generally interpreted to be the result of basaltic or picritic melt extraction, as outlined in Chapter 1 (eg; Frey et al. 1985; Nickel and Green, 1984). Incompatible elements such as Al, Ca, Na and Ti, which partition more strongly into the melt phase during partial melting of peridotite, produce negative correlations, indicative of their progressive depletion in the residue with increasing amounts of melt extraction. On the other hand, compatible elements such as Ni are enriched in the residue on partial melting, resulting in positive correlations when plotted against wt% MgO. The suite described here exhibits mixing trends towards high CaO, P_2O_5, K_2O and Na_2O, and low SiO_2 and Al_2O_3 (figure 3.3.1a-f). For a given MgO content, these nodules contain up to 2.5 wt% more CaO, up to 0.7 wt% more P_2O_5, up to 0.7 wt% more Na_2O, and up to 0.06 wt% more K_2O than the average. On the other hand, SiO_2 and Al_2O_3 contents are as much as 2 and 1.5 wt% less than average, respectively. This suggests that there has been substantial addition of a component rich in CaO, P_2O_5, K_2O and Na_2O. The decreased wt% Al_2O_3 and SiO_2 reflect dilution of the pre-metasomatic Al_2O_3 and SiO_2 contents of the wall-rock by addition of a component which is very low in these oxides. This is consistent with a metasomatic process which involves absorption by refractory lithosphere of a dolomitic, low silica, phosphate-rich, sodic carbonatite melt, accompanied by substantial loss of CO_2-rich fluid. On the oxide vs. wt% MgO plots, each sample therefore can be located on a simple bulk mixing line between a refractory pre-metasomatic composition, and a sodic, dolomitic, carbonatite composition (figure 3.3.2). The experimental study (Wallace and Green, 1988), which defined the carbonatite melt composition, is supportive of an explanation for the observed geochemical characteristics by carbonatite metasomatism.

TiO_2 and Cr_2O_3 contents in the selected samples show different behaviour. For most samples, their abundances lie within the partial melting trends exhibited by a large

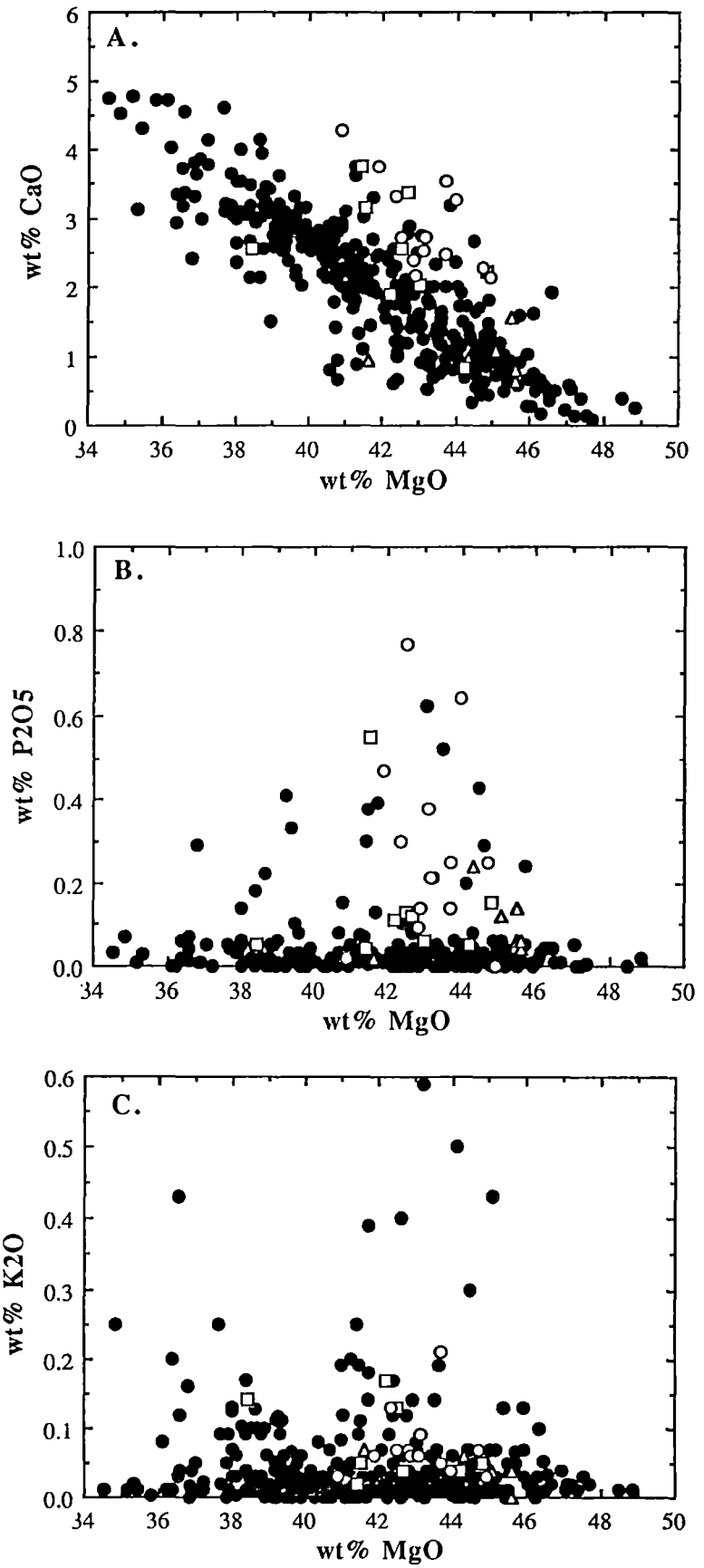

Figure 3.3.1: Plots against wt% MgO of (A) wt% CaO, (B) wt% P_2O_5, (C) wt% K_2O for >300 worldwide spinel peridotite xenoliths (filled circles), and the carbonatite-metasomatised suite (open symbols). Open circles are wehrlites, squares are lherzolites and triangles are harzburgites.

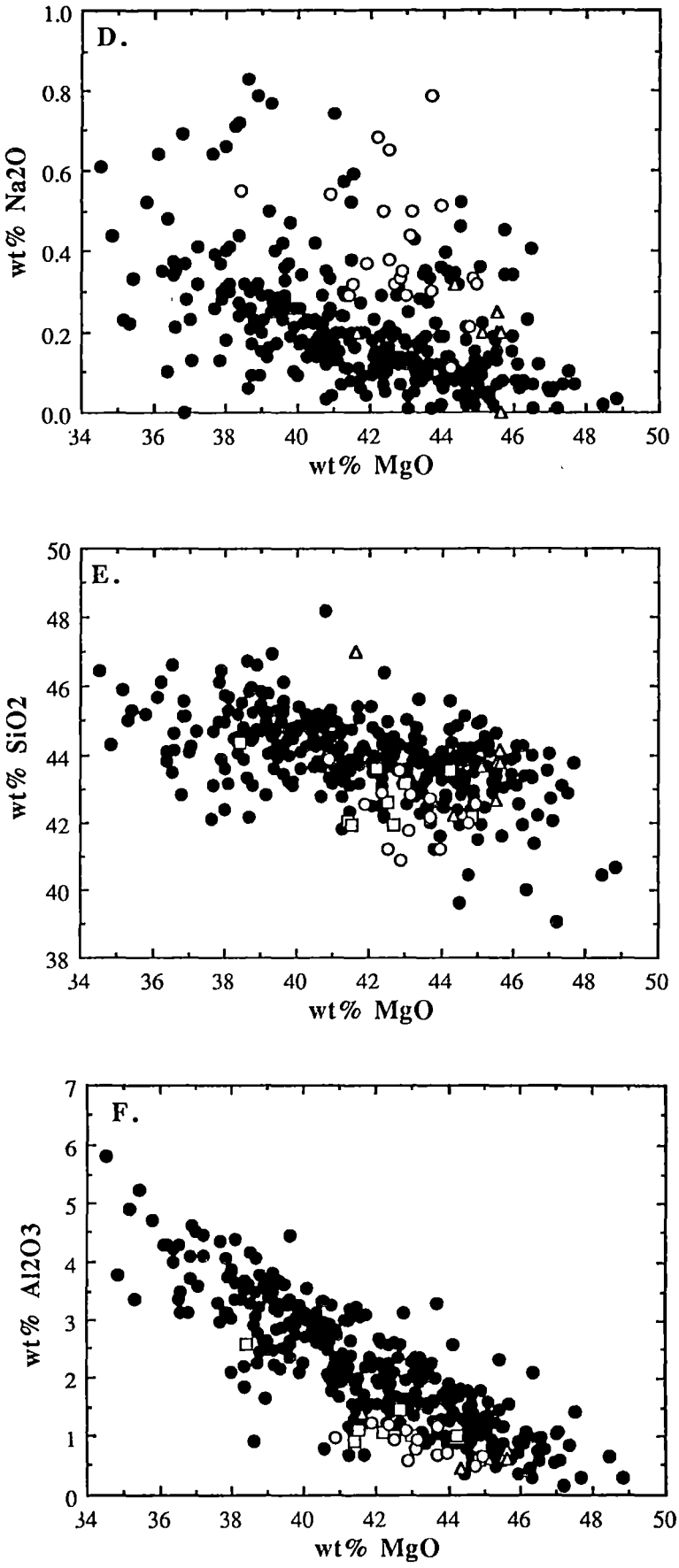

Figure 3.3.1 continued: Plots against wt% MgO of (D) wt% Na_2O, (E) wt% SiO_2 and (F) wt% Al_2O_3 for >300 worldwide spinel peridotite xenoliths (filled circles), and the carbonatite-metasomatised suite.

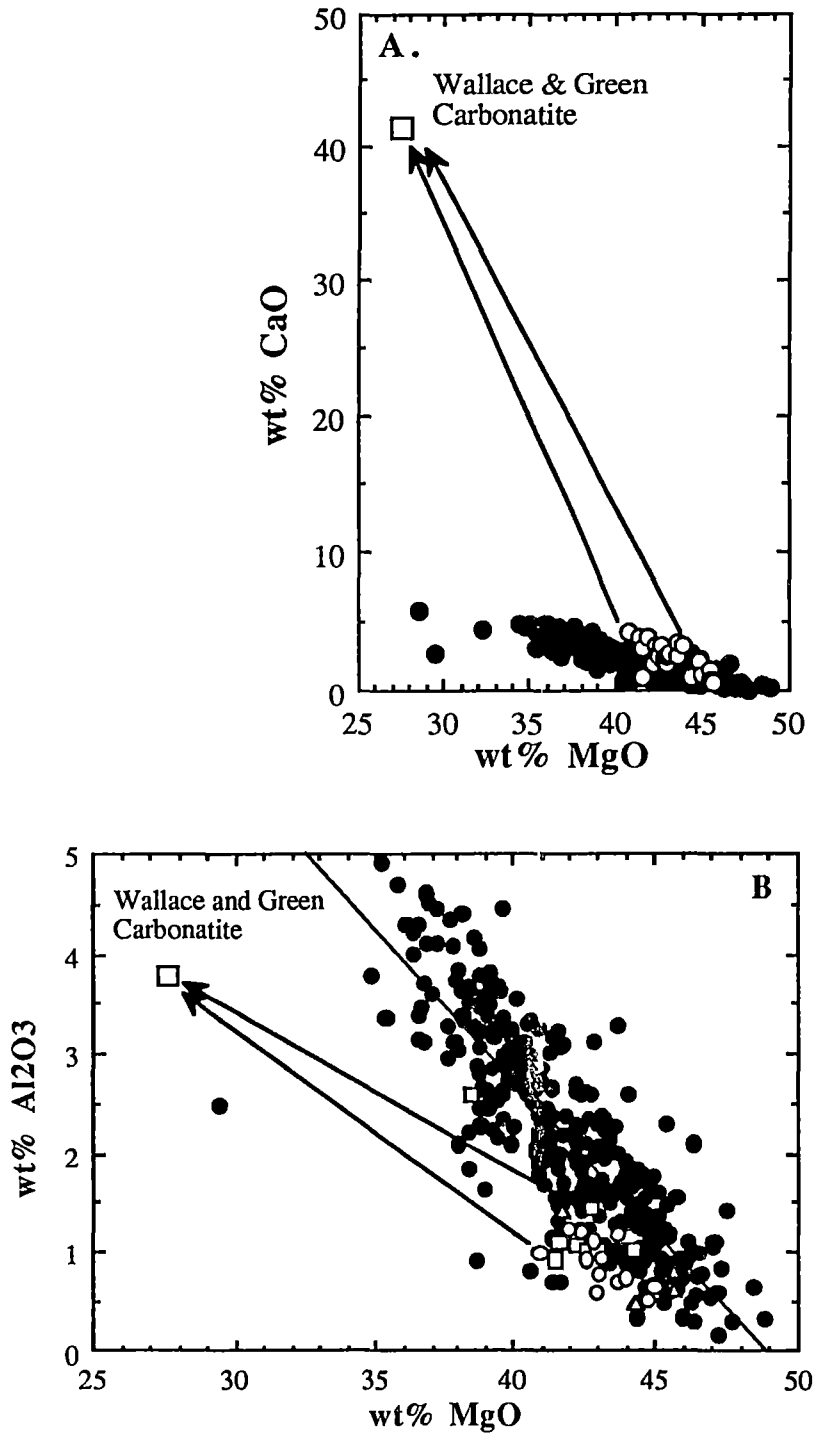

Figure 3.3.2: Plots of wt% MgO vs. wt% CaO (A) and Al_2O_3 (B) for spinel peridotite database used in fig. 3.3.1, extrapolated to demonstrate mixing relationship between refractory, pre-metasomatic peridotite lithosphere and the ephemeral carbonatite, to generate the carbonatized suite, resulting in CaO enrichment, and Al_2O_3 dilution.

number of world-wide peridotites (figure 3.3.3a and b), and appear to be unaffected by the carbonatite addition, suggesting that these components are not significantly enriched by addition of such a melt to the lithosphere. Lack of enrichment in TiO_2, despite enrichment in other incompatible minor elements (such as Na and K), appears to be a distinctive feature of this metasomatic style. In contrast, the Group 2 peridotite xenolith (GN24) reported by Stolz and Davies (1988) contained 0.26 wt% TiO_2, with modal high-Ti pargasite and mica. This was attributed to metasomatic interaction between lithospheric lherzolite and intrusive Cenozoic alkaline magmas related to the host Newer Volcanics. Samples 70987 and 71004 from this study also display Ti-enrichment (0.15 and 0.20 wt% TiO_2 respectively) and hence plot above the melt extraction trend on the MgO vs. TiO_2 plot (figure 3.3.3a). These elevated Ti-contents are due to the presence of high-Ti pargasite and minor phlogopite. It is believed that these samples have suffered metasomatism associated with intruding mafic silicate melts in addition to carbonatite metasomatism. This is explored further in a later section.

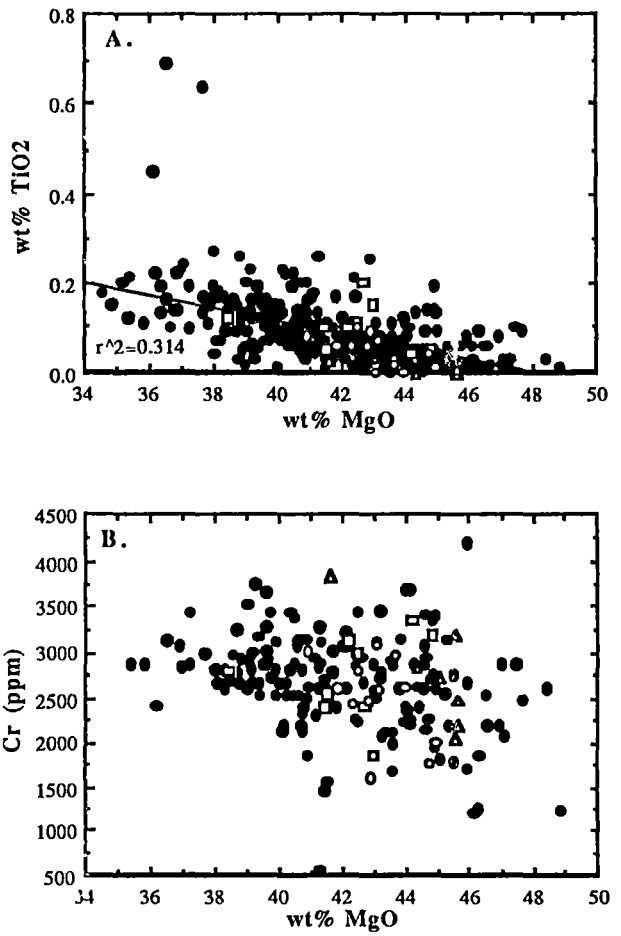

Figure 3.3.3: Plots against wt% MgO of (A) wt% TiO2 and (B) Cr (ppm) for worldwide spinel peridotite database used in fig. 3.3.1 and carbonatized suite. Symbols as in figure 3.3.1.

Bulk rock Mg#'s (Mg#=100*Mg/[Mg+ΣFe]) for the suite are typically magnesian, ranging from 86.8 to 91.4, similar values to those reported for other suites of mantle-derived peridotites (eg; Frey and Green, 1974; Frey and Prinz, 1978; Nickel and Green, 1984; Frey et al. 1985; Preβ et al. 1986; Chen et al. 1989; Galer and O'Nions, 1989; Fan and Hooper, 1989). The experimental carbonatite composition of Wallace and Green (1988) had an Mg# of 84.5, which is only slightly lower than typical lithospheric material, suggesting that Fe/Mg fractionation during addition of such a carbonatite melt to refractory lithospheric peridotite would be minimal (Green and Wallace, 1988). However, moderate FeO enrichment at a given MgO content is evident (particularly for the lherzolites and wehrlites) on a plot of wt% MgO vs. wt% FeO (figure 3.3.4) which includes the world-wide spinel peridotite database, and is consistent with the metasomatising carbonatite having Mg# around 78, assuming an MgO content similar to that of the Wallace and Green (1988) estimate (see chapter 4).

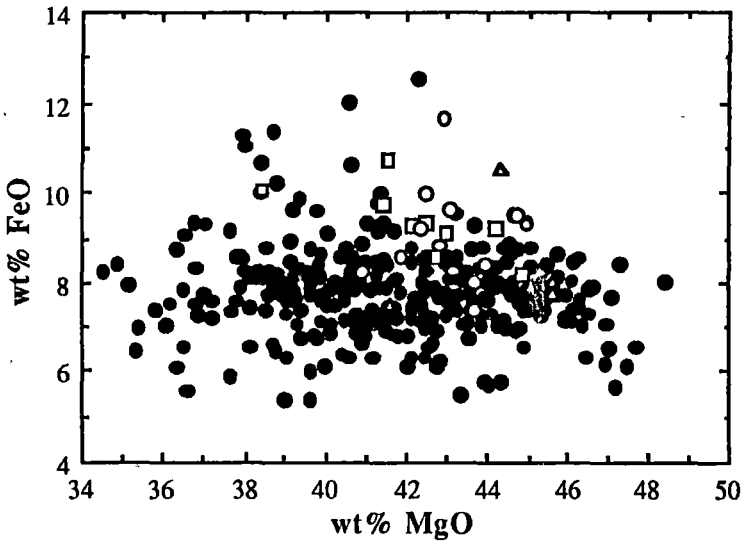

Figure 3.3.4: Plot of wt% MgO vs. wt% FeO for spinel peridotite database used in fig. 3.3.1, demonstrating moderate Fe-enrichment trend associated with carbonatite metasomatism. Symbols as in figure 3.3.1. This suggests that the metasomatic agent had Mg# less than that of typical refractory peridotite.

3.4 Trace element characteristics of carbonatite metasomatised peridotite.

3.4.1 Compatible trace elements - evidence of prior melt extraction, and a non-cumulate origin for the magnesian wehrlites.

Plots against MgO of Ni, Cr and V for a suite of world-wide spinel peridotite xenoliths also reflect basaltic melt extraction events in a similar manner to major elements. For example, Ni shows a well-constrained positive trend, reflecting its highly compatible

nature in silicate melt-peridotite equilibria (figure 3.4.1). Cr has a somewhat scattered trend with a near horizontal slope, suggesting a bulk K_d of approximately 1 during partial melting of a peridotite source (figure 3.3.4b). In both cases, however, the suite of nodules being described here plots within the melt extraction trend, suggesting that, along with Ti, carbonatite melts are incapable of causing significant enrichment in Ni, Cr or V. The abundances of these elements in the nodules reflect an earlier (MORB?) extraction event.

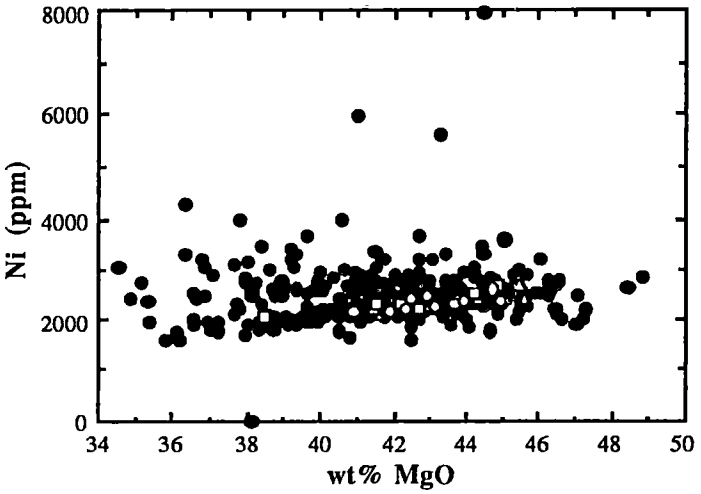

Figure 3.4.1: Plot of wt% MgO vs. Ni (ppm) for worldwide spinel peridotite database used in figure 3.3.1. Symbols are those used in figure 3.3.1.

Compatible trace element variations (such as Ni) can be used to demonstrate an origin for this suite which involves partial melting of the lithosphere, rather than high pressure fractional crystallization and accumulation of olivine and clinopyroxene from a mafic magma. This is of particular importance for the wehrlites, as many examples of wehrlites derived from high pressure crystallization of mafic melts have been reported from the southeastern Australian region (Ellis, 1976; Griffin et al. 1984; Griffin et al. 1988). Frey and Green (1974), Frey and Prinz (1978) and Frey et al. (1985) have all modelled Ni variation in a lherzolitic residue of 1-30% partial melting, and in a cumulate derived from 1-30% fractional crystallization of olivine from a basalt magma. The range of Ni abundances produced in the solid (residue or cumulate) as each of these processes proceeds is distinctive. For example, as shown by Frey and Green (1974), crystallization of 1-30% olivine from a basaltic liquid which initially contained 2000 ppm Ni, assuming $K_d^{Ol/Ni} = 10$, produces a variation in the ratio of Ni content in the cumulate to initial Ni content in the melt (C_s/C_o) from 10 (0% crystallization) to 3.3 (30% crystallization). In other words the Ni content in a suite of olivine dominated xenoliths derived by 1-30% olivine fractional crystallization from basaltic melt should vary by a factor of three. On the other hand, 1-30% fractional

melting of a lherzolite source will change C_s/C_o (now the ratio of Ni content in the residue to the initial, primitive Ni content) only slightly, from 1 to 1.38 (27.5% variation). Similar results were obtained for modelling involving equilibrium crystallization and melting. The wehrlites under consideration here have a limited range of Ni contents (2135 to 2599 ppm, ie. 18% variation) consistent with a residual origin, rather than origin by cumulate processes. Ni variation is similar to that exhibited by other suites of xenoliths which have been demonstrated to represent residues after partial melting events [eg. group I nodules from the San Carlos Volcanic Field of Frey and Prinz (1978); Ronda peridotite of Frey et al. (1985)].

Green (1970, 1973) demonstrated that *ca.* 1-30% partial melting of lherzolite will produce only a small change in Mg# of the residue, from 89 to 92. However, 1-30% fractional crystallization of olivine from an olivine tholeiite magma changes the liquidus olivine forsterite content substantially, from 90 to 87.5 for 10% crystallization, 90 to 83 (20%) and 90 to 70 (30%). Olivines in this suite are consistently forsteritic, ranging from 88 to 91, typical of other xenolith populations which have been shown to be residues of partial melting events (eg; the Ronda peridotite of Frey et al. 1985). In contrast, the clearly cumulate wehrlite inclusions described by Ellis (1976) have olivine Fo contents from 61 to 80 mol%.

3.4.2 Incompatible trace elements

The incompatible trace element patterns of these nodules are characterised by substantial to extreme enrichment above Primitive Mantle estimates (Sun and McDonough, 1989), and some distinctive inter-element fractionations. Using wt% MgO as the abscissa, the abundances of incompatible trace elements in these xenoliths may be compared with >300 other world-wide nodules. This suite displays enrichment in Zr, Nb, Sr, Y, LREE and HREE, and Th (figure 3.4.2a-d). A primitive mantle normalized "spidergram" (figure 3.4.3) for representatives of this suite, indicates strong fractionations in Ba/Th, K/La, Th/Nb, Na/Zr, Zr/Hf and Ti/Eu.

The nodules display strong but variable LREE enrichment and fractionation of LREE from HREE (figure 3.4.4a-c). Primitive mantle normalized (Sun and McDonough, 1989) La contents range from 3.32 to 66.23. Normalized $[La/Yb]_{PM}$ ranges from 12.6 to 65.3. Plots of LREE against P_2O_5 content reveal well-constrained positive correlations, suggesting strong apatite control on the abundances of these elements (figure 3.4.5). This can also be seen by comparing the REE plot of apatite-bearing wehrlites (eg; 71001 and 70972) with that of sample 70965, which is an apatite-free,

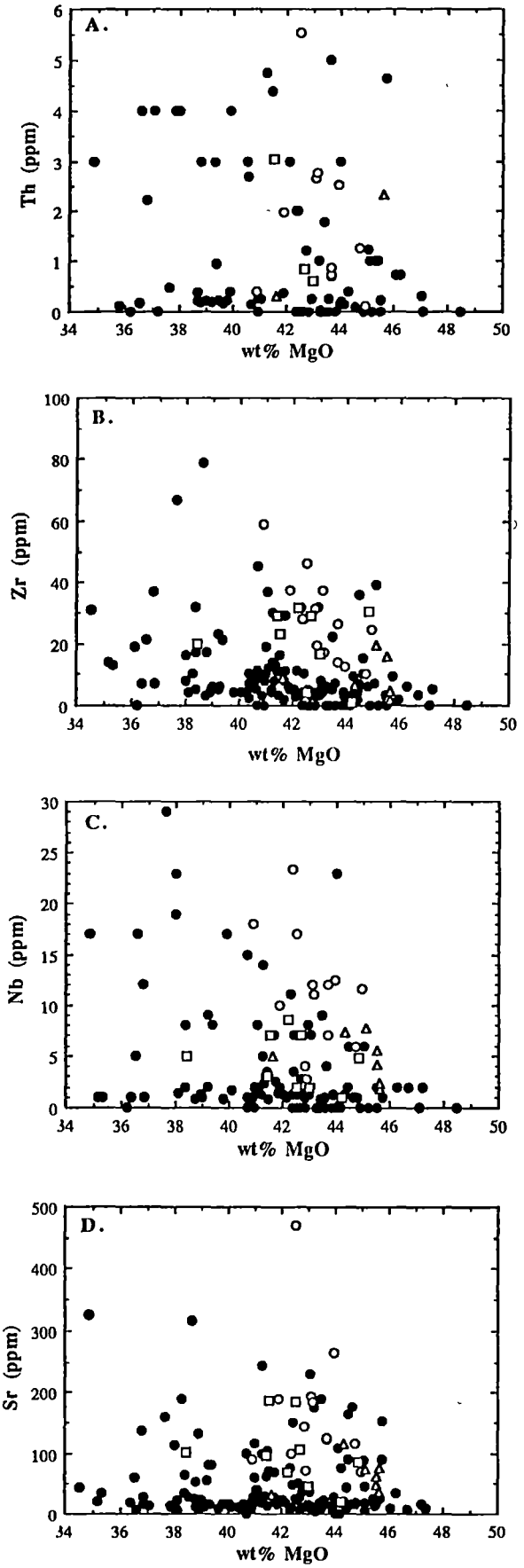

Figure 3.4.2: Plots against wt% MgO of (A) Th, (B) Zr, (C) Nb and (D) Sr comparing carbonatized wehrlites (open circles), lherzolites (open squares) and harzburgites (open triangles) with spinel peridotites from around the world (filled circles). These plots demonstrate strong enrichments of carbonatite-metasomatised suite in these trace elements.

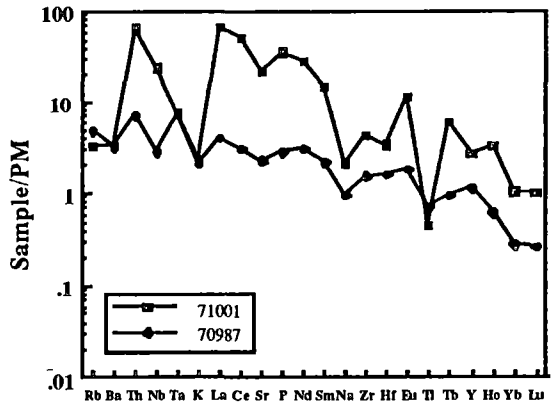

Figure 3.4.3: Primitive mantle-normalized (Sun and McDonough, 1989) spidergram for two samples which span the range of trace element enrichments exhibited by the suite. Sample 70987 has a low modal apatite content compared with 71001, demonstrating the control on abundances of LREE, Sr, P and Th exerted by apatite. Note also strong fractionations (particularly evident for 71001) in ratios such as Ba/Th, Nb/Th, Na/Zr, K/La, Zr/Hf and Ti/Eu. Note that Ta is <LLD in both cases.See text for further discussion.

magnesian wehrlite (figure 3.4.4a). Sample 70965 displays an unusual flattening of the segment from La to Tb, imposing a concave downwards character to the plot. For example, for 70965, $[La/Tb]_{PM}$ is 0.91, but $[Tb/Yb]_{PM}$ is 3.66. The HREE segment of the curve, however, is similar to that of the apatite-bearing wehrlites. This pattern is similar to apatite-free magnesian wehrlites and clinopyroxene-bearing dunite nodules from Olmani, Tanzania, (Rudnick et al. 1993), which have also been attributed to carbonatite metasomatism (figure 3.4.4d), and to clinopyroxene separates from several previously reported SEA apatite + amphibole bearing xenoliths (eg; GN2 and GN20 of Stolz and Davies, 1988), and is consistent with formation of clinopyroxene in equilibrium with a phase strongly enriched in LREE, such as apatite.

REE plots of clinopyroxene separates obtained from samples 71000 (apatite-bearing wehrlite) and 71008 (apatite-bearing lherzolite) essentially parallel that of 70965 at higher absolute abundances (figure 3.4.4e), suggesting that clinopyroxene is a significant control on HREE contents, and that the absence of apatite from 70965 is responsible for its unusual "LREE-flattened" pattern. Data are presented in table 3.1.

Sweeney et al. (1992) have demonstrated experimentally that garnet in equilibrium with carbonatite melt at 30kbar will fractionate LREE and HREE, resulting in high LREE/HREE values in the melt. For example, partition coefficients between carbonatite melt and garnet at 33 kbar, and 1000°C were 0.30 for Ce ad 18.5 for Lu (Sweeney et al. 1992). These carbonatite trace element characteristics would be

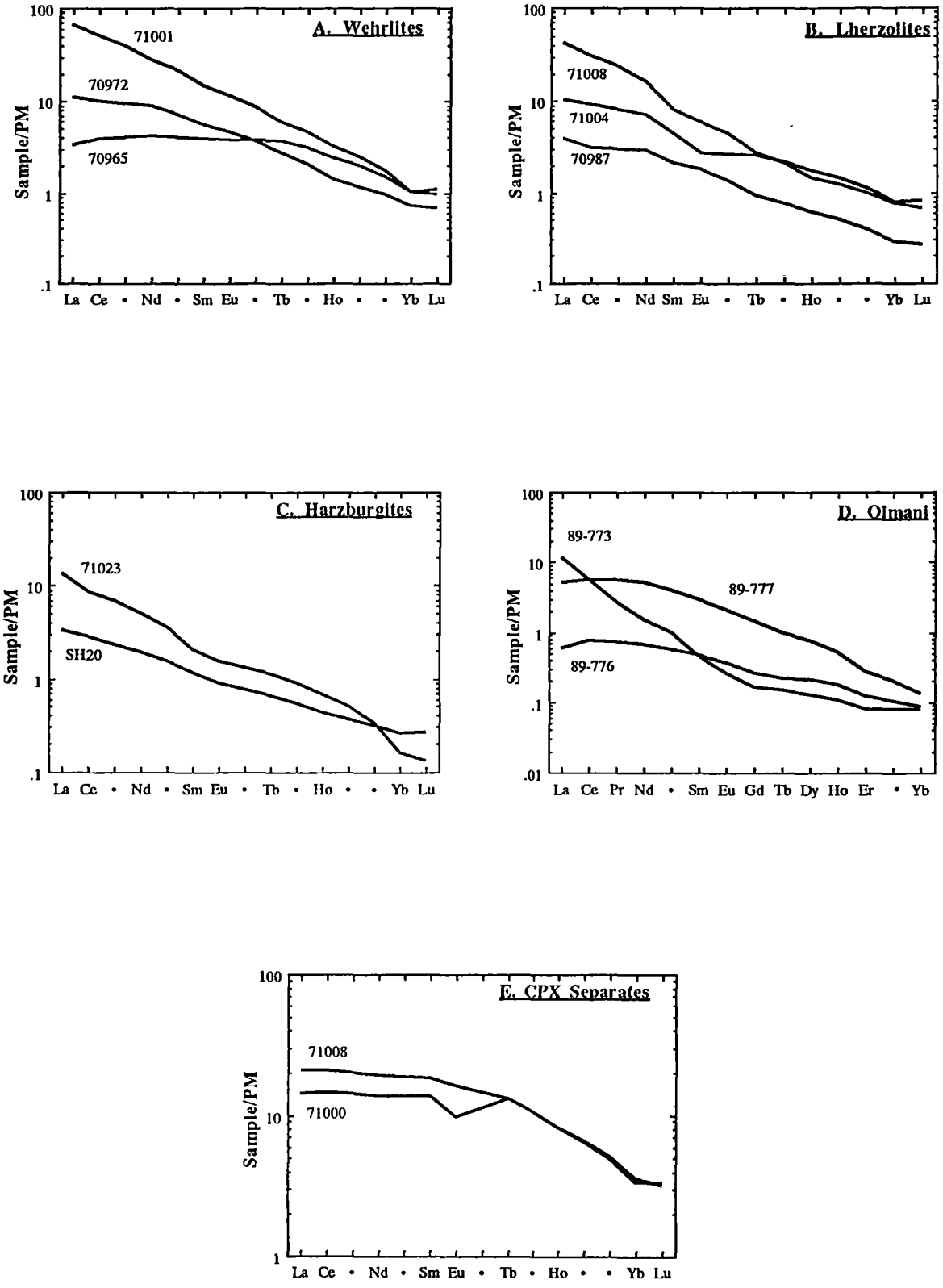

Figure 3.4.4: Primitive mantle-normalized (Sun and McDonough, 1989) REE plots of (A) representative magnesian wehrlites. 71001 has abundant apatite, 70972 has less, and 70965 has no modal apatite. 71001 and 70965 nearly span the range of abundances exhibited by the remainder of the wehrlites in the carbonatized suite, (B) three representative lherzolites, (C) two representative harzburgites from the carbonatized suite, (D) samples from the Olmani suite (Rudnick et al. 1993) which are also believed to interacted with carbonatite melt. 89-773 contains accessory monazite. 89-777 contains minor apatite associated with glassy vugs, and 89-776 is a clinopyroxene dunite. Note similarity of the patterns for 89-777 and 89-776 to that of 70965, (E) clinopyroxene separates from 71008 and 71000. Data in table 3.1. Note similarity in form of patterns to 70965, 89-777 and 89-776.

Table 3.1: Trace element analyses of clinopyroxene separates from 71000 and 71008, determined by INAA.

Sample	71000	71008
La	9.72	14.40
Ce	26.00	37.20
Nd	18.4	26.00
Sm	6.04	8.05
Eu	1.62	2.70
Tb	<1.40	<1.42
Ho	1.33	<1.33
Yb	1.78	1.67
Lu	0.24	0.25
Hf	3.28	1.56
Sc	37.20	44.00
Ta	<1.70	<1.60
Th	3.34	<1.10

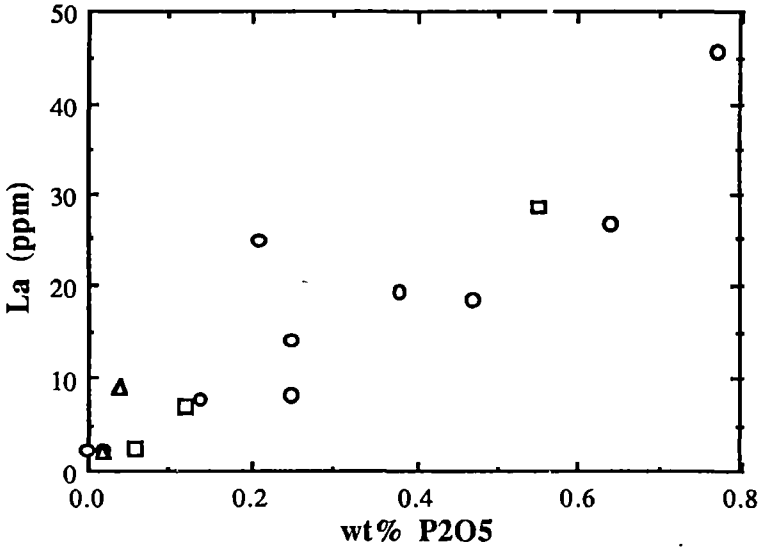

Figure 3.4.5: Plot of wt% P2O5 vs La (ppm) for carbonatized peridotite suite, demonstrating strong control exerted by modal apatite on LREE abundances. Symbols as for figure 3.3.1.

superimposed on depleted lithosphere when the ascending melt metasomatizes it at 15-20 kbar. Therefore, the steeply-fractionated REE patterns are established as a characteristic of the carbonatite melt itself, and suggest involvement of residual garnet in the carbonatite's source regions.

Abundances of Sr and Th are also strongly controlled by apatite modal abundance (as measured by bulk wt% P_2O_5). This is clearly indicated by excellent positive correlations of these trace elements plotted against P_2O_5 content (figure 3.4.6a and b).

As mentioned in section 3.3, Ti abundances appear to be unaffected by carbonatite metasomatism, resulting in a distinctive decoupling of LILE enrichment from Ti abundances. For example, Ti/Eu values are low, ranging from 100 to 500. This contrasts with estimates of the primitive mantle Ti/Eu value of 7700 (Sun and McDonough, 1989). Similarly, Zr/Hf values are strongly fractionated, ranging from 34 to 102 (mean = 62), compared with the primitive mantle value of 36. The implications of these observations are discussed more fully in section 3.5.

3.5 Discussion

3.5.1 The case for carbonatite metasomatism

The preservation of textures indicative of strain in most of the nodules in this suite (Chapter 2), the consistently high bulk-rock Mg/(Mg+$\sum$Fe), and the range of Ni abundances (section 3.4) preclude an origin for the magnesian wehrlites as high pressure cumulates from crystallization of mafic magmas in the lithosphere. The unusually high Ca/Al and Na/Al values are coupled with petrographic and mineralogical evidence for the reactions predicted by decarbonation interaction between lithospheric wall-rock phases such as orthopyroxene and spinel (Chapter 2), and dolomitic carbonatite melt. The observations are consistent with a model in which simple bulk mixing of refractory lherzolitic or harzburgitic lithosphere and a low-Al_2O_3, LILE-enriched, sodic dolomitic carbonatite in the manner described by Green and Wallace (1988) has produced the observed major and minor element compositions in the carbonatized suite.

Thus, the inferred sequence of events requires the existence of original refractory lherzolite or harzburgite (component A of Frey and Green, 1974). Comparatively recent influx of carbonatite melt resulted in decarbonation reactions and conversion of

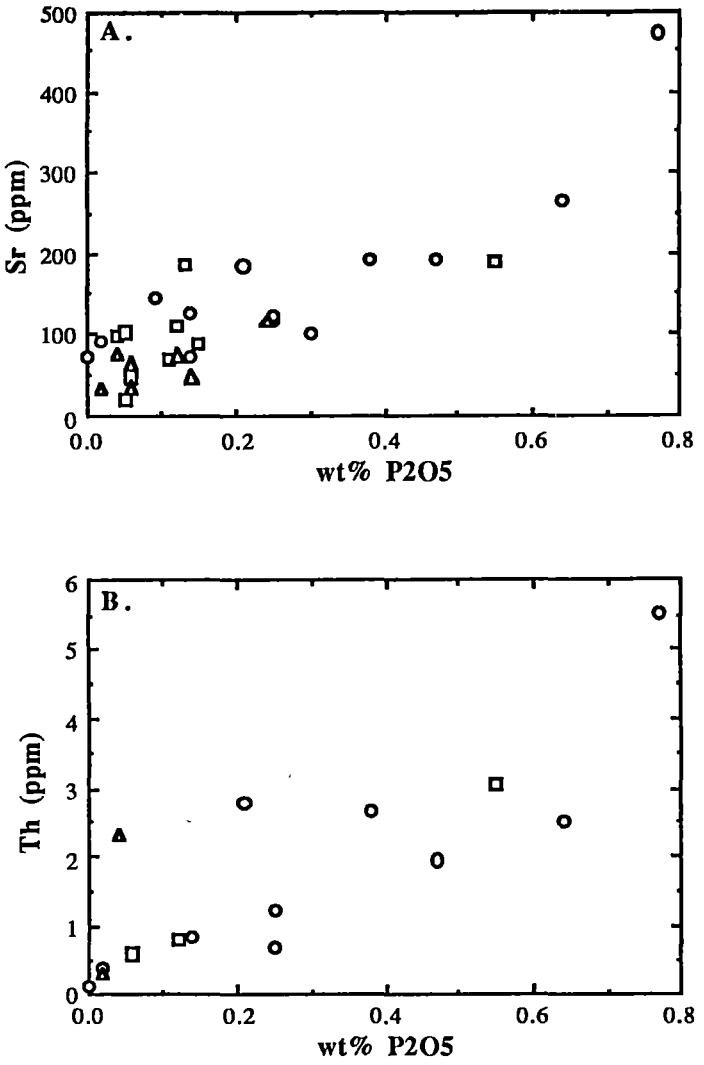

Figure 3.4.6: Plots of wt% P_2O_5 vs (A) Sr (ppm) and (B) Th (ppm) for carbonatized suite. The strong positive correlation demonstrate strong apatite control on the abundances of these elements. Symbols are those used in figure 3.3.1

component A to a LILE- and CaO-enriched, Al_2O_3-depleted composition. Annealing produced a texturally-equilibrated olivine + clinopyroxene + Cr-spinel + low-Ti pargasite ± residual orthopyroxene + apatite assemblage. In some cases, the metasomatic event was interrupted before annealing, by entrainment in the host basanite, resulting in preservation of penetrative olivine + clinopyroxene replacement rims and olivine + clinopyroxene veins associated with relict orthopyroxene. Finally, ascent in the host magma resulted in decompression melting of pargasite or phlogopite.

The "end-product" of carbonatite metasomatism of the lithosphere is an apatite-bearing, orthopyroxene-free magnesian wehrlite assemblage. Such assemblages have been reported previously (Nickel and Green, 1984) but their origin has been attributed

to cumulate processes. For example, Nickel and Green (1984) considered five nodules (their group B) to be of cumulate origin from a basaltic liquid. Re-examination of these samples (held in the Geology Department, University of Tasmania) has revealed that the three most refractory (bulk Mg# = 88.5-90.3) members of the group (BME-18, BME-51 and BME-135) share the petrographic, mineralogical and geochemical characteristics of lithosphere which has undergone carbonatite metasomatism. For example, they are apatite bearing wehrlites (olivine + clinopyroxene ± low-Ti pargasite ± Cr-spinel ± orthopyroxene + apatite). Sample BME-18 contains minor relict orthopyroxene which is clearly being replaced by olivine+clinopyroxene. Primary olivine is Fo_{88-90}, and is consistent with a residual mantle origin, although olivines from other members of group B have lower Fo contents, consistent with cumulate origin. Clinopyroxenes are sodic (see figure 3.5.1). Bulk rock chemistry is also consistent, with CaO/Al_2O_3 values ranging from 2.3 to 2.9, and Na_2O/Al_2O_3 from 0.44 to 0.49. Trace element data are not available. Re-examination of the five xenoliths of Nickel and Green's group B, suggests that some ultramafic xenoliths previously attributed to cumulate processes may in fact have formed as a result of interaction of lithosphere with an ephemeral carbonatite melt.

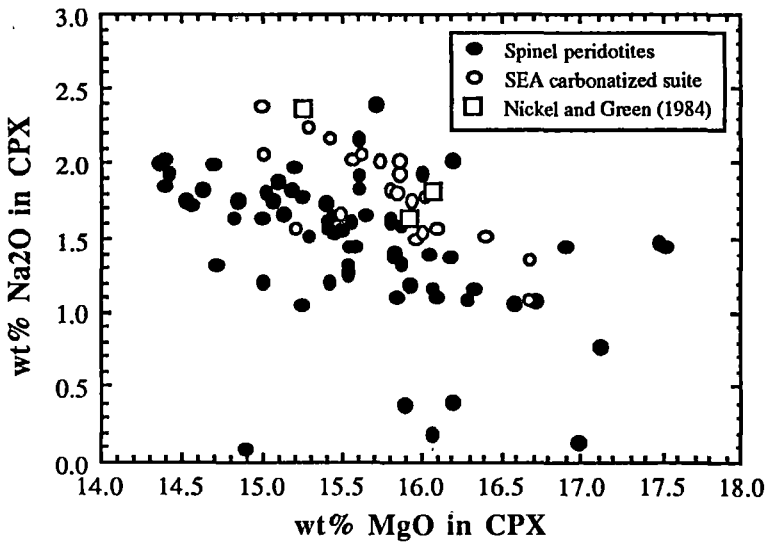

Figure 3.5.1; Plot of wt% MgO vs wt% Na_2O for clinopyroxenes in spinel peridotite xenoliths from a variety of locations, the SEA carbonatized suite, and three wehrlites (BME-18, BME-51 and BME-135) attributed by Nickel and Green (1984) to cumulate processes. Clinopyroxene compositions in the latter group are markedly similar to those of the carbonatized suite, suggesting that these may also be the result of carbonatite metasomatism (see text). Data sources are from Frey and Prinz (1978), Nickel and Green (1984), Preß et al. (1986), Fan and Hooper (1989), Galer and O'Nions (1989) and table B4 (Appendix B).

Apatite+amphibole-bearing lherzolite nodules are relatively common in Western Victorian volcanic centres (for examples, see Frey and Green, 1974; O'Reilly and Griffin, 1988; Nickel and Green, 1984; Stolz and Davies, 1988). However, descriptions of olivine+clinopyroxene replacement rims around relict orthopyroxene have only been reported (Frey and Green, 1974) in one sample (2700). Again, it is possible that these nodules are the product of metasomatism of the lithosphere by a carbonatite melt (see later). Exhaustion of the metasomatising carbonatite before complete replacement of orthopyroxene, with subsequent annealing, could produce a texturally-equilibrated assemblage of olivine + orthopyroxene + clinopyroxene + amphibole + apatite + spinel. This would result in nodules in which direct evidence of interaction with carbonatite melt (that is olivine+clinopyroxene replacement rims on orthopyroxene) has been obliterated during annealing. The relationship of other, previously reported, apatite-bearing SEA peridotite xenoliths to those described herein, is explored more fully in following sections.

3.5.2 Estimates of the composition of the carbonatite melt

Wallace and Green (1988) demonstrated that their primary experimental carbonatite had a sodic dolomitic composition, with Mg# of 84.5, and significant P_2O_5 and K_2O (see table 1 of Wallace and Green, 1988). Assuming that carbonatite metasomatism involves simple bulk mixing of the major and minor element components of this melt with refractory lithosphere (ie; an ephemeral metasomatic style; Green and Wallace, 1988), then constraints can be placed on the major element composition of the metasomatic carbonatite.

Compared to a worldwide suite of >300 spinel peridotite xenoliths (figure 3.3.1), the carbonatite-metasomatised suite defines a trend towards unusually high CaO contents for a given MgO content (figure 3.3.1a). Each carbonatized sample can be placed on a mixing line (figure 3.3.2) between a refractory, pre-metasomatic composition (along the mantle trend), and a dolomitic carbonatite composition assumed, in figure 3.3.2 to match the experimental carbonatite of Wallace and Green (1988). Similar plots against MgO of Na_2O, Al_2O_3, and SiO_2 (figures 3.3.1d-f) indicate that the metasomatising carbonatite was enriched in Na_2O, but low in Al_2O_3 and SiO_2, consistent with the experimental estimate of Wallace and Green (1988).

If the pre-metasomatic composition of each wehrlite is assumed to lie on the least squares regression line through the 'normal' spinel lherzolite partial melting trends on figures 3.3.1a and 3.3.2, then addition of 1 - 6% carbonatite can generate the compositions of the carbonatized suite. This agrees with experimental estimates of the

% carbonatite involved (see Chapter 4). Below, these percentages, established from the major element abundances, are used to estimate approximate trace element abundances in the carbonatite.

Table 3.2: Details of mineralogy and data sources used throughout this chapter. Samples marked "*" are magnesian wehrlites.

Mineralogy	Source	Sample Numbers
Anhydrous peridotites	1	DR9894; BMS1; LE14B; LE16B; NT13B
	2	BM20; GN14; GN13
Amphibole±Glass bearing peridotites	1	DR9955; WGBM5; DR9708; DR11311; WGBM2; SBM1; DR9740; BM70; WGBM1; WGBM15
	3	SL5; SL3; SL1; SL7; SL4
	4,5	2604; 84402; 2642; 2769; 85168; BM134; 2669; 2728; 2730; 2736
Apatite+amphibole bearing peridotites	1	SGN1; DR9933; DR11020; DR11308; BM650; BM654; BM655
	2	GN2; GN3; GN20; GN6; GN5; GN8
	4,5	2700
Mica+amphibole bearing peridotites	1	WGBM14; LE15B; WGBM16; DR9741; BM630
	2	GN24
	3,4	SL2; SL6; 2640
	5	84413; 84438
Carbonatized peridotites	6	70956*; 70969*; 70972*; 70987; 71000*; 71001*; 71004; 71008; 2631* 76989*; 76990*; 76991*; 76995; 71023

Sources:
1. O'Reilly and Griffin, 1988
2. Stolz and Davies, 1988
3. Chen et. al. 1989
4. Frey and Green, 1974
5. McDonough and McCulloch, 1987
6. Appendix C, herein

Sr and Nd abundances for the majority of published analyses of SEA spinel peridotites are well correlated (see table 3.2 for data sources, and fig 3.5.2; McDonough and McCulloch, 1987). If, as assumed, the Sr and Nd contents of the carbonatized suite result from mixing between a depleted peridotite composition and 1 - 6% carbonatite, a range of suitable carbonatite compositions car be calculated. Sample NT13B (a LILE-depleted, anhydrous xenolith described by O'Reilly and Griffin, 1988) has a representative pre-metasomatic composition (Sr = 7.08 ppm; Nd = 0.489 ppm), with MgO and CaO abundances close to the spinel lherzolite regression line in figure 3.3.1a. The calculated carbonatite compositions have 1457 - 7361 ppm Sr (av. 3324 ppm), and 90 - 655 ppm Nd (av. 353 ppm). These abundances fall within the range for natural, eruptive carbonatites from a variety of localities (Nelson et al., 1988; W.

Taylor, unpublished data), but are substantially more enriched than any lava from the Newer Volcanics (figure 3.5.2).

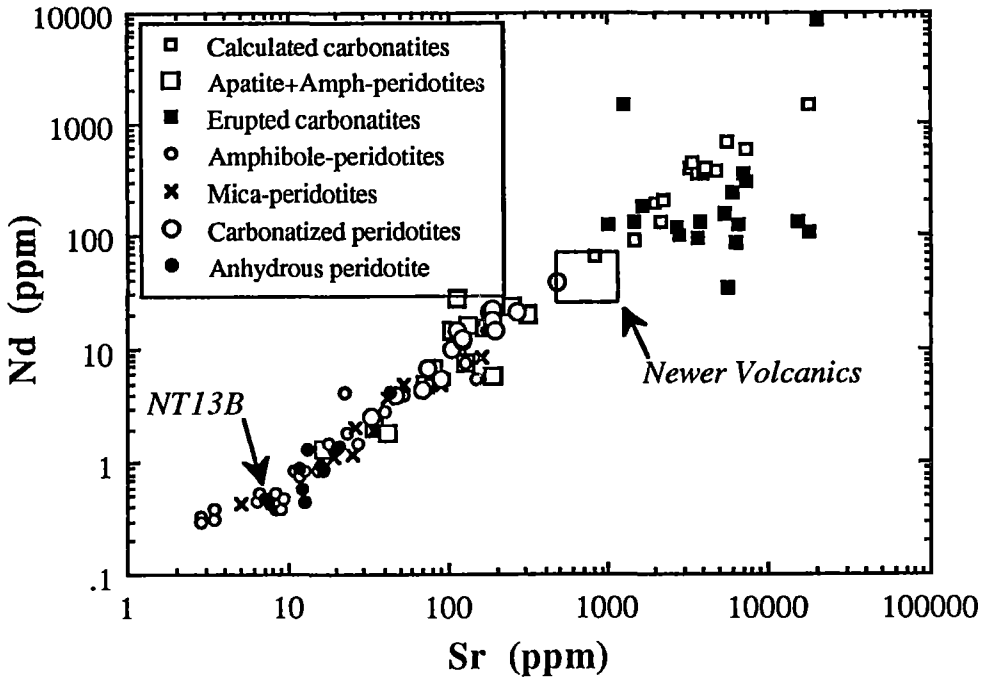

Figure 3.5.2: Sr vs. Nd for a range of SEA peridotite xenoliths. Data sources are given in table 4.1. NT13B (O'Reilly and Griffin, 1988) is representative of pre-metasomatic lithosphere. See text for further explanation.

Depleted and metasomatised spinel peridotite xenoliths generally have unfractionated Zr/Hf values of around 36, similar to estimates of primitive mantle (Jochum et al. 1986; Sun and McDonough, 1989), ocean island basalts (OIB), MORB, and island arc basalts (IAB). However, the carbonatized peridotite suite exhibits a positive inter-element correlation and unusually high Zr/Hf values (34 to 102, av. 62). Also, many natural carbonatites have high Zr/Hf. For example, the Mt Weld carbonatite in the Yilgarn region (W. Australia) has an average Zr/Hf = 116 (W. Taylor, unpublished data). Many of the carbonatites reported by Nelson et al. (1988) have similarly high values. Assuming that the Zr and Hf contents of the carbonatized suite are the result of mixing of the carbonatite and depleted pre-metasomatic lithosphere, the calculated carbonatite composition ranges from 158 - 1611 ppm Zr, and 2 - 34 ppm Hf, matching the range for natural carbonatites (figure 3.5.3).

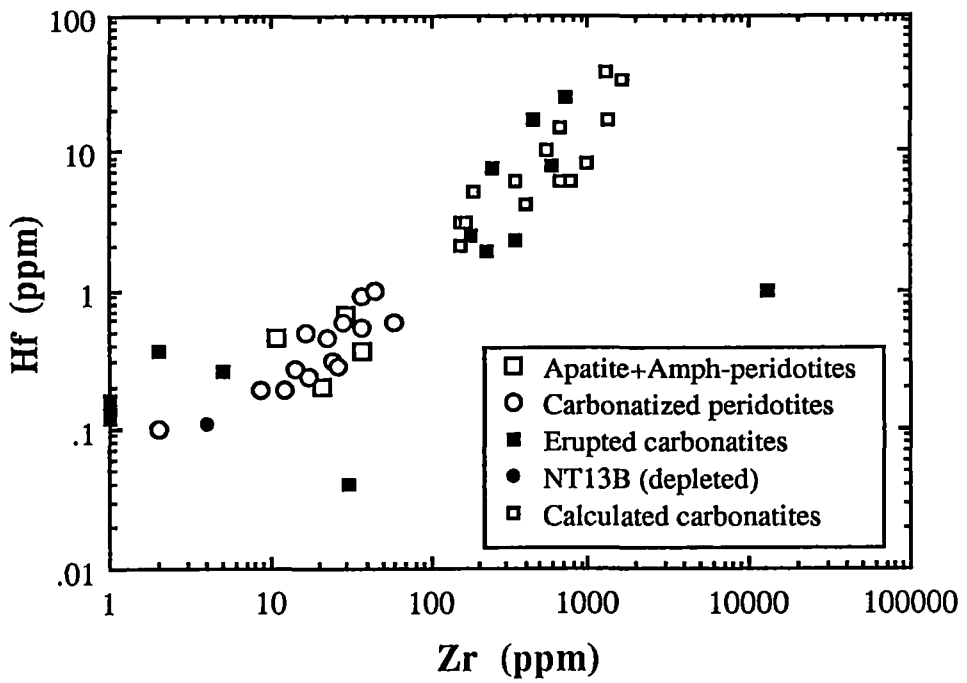

Figure 3.5.3: Plot of Zr vs. Hf for a range of SEA peridotite xenoliths. See text for further explanation.

Therefore, in summary, the major and trace element compositions of the SEA carbonatized xenolith suite are consistent with absorption by refractory peridotite, of 1-6% of a Na_2O-enriched, dolomitic melt, with low Al_2O_3 and SiO_2. The melt would be strongly enriched in LILE, with strongly fractionated Zr/Hf values.

3.5.3 Relationship with other metasomatic styles represented in the SEA lithosphere

Southeastern Australian type I mantle-derived xenoliths (Frey and Prinz, 1978) display a wide variety of metasomatic mineralogies, and variable degrees of trace element enrichment. In the following section this variation is briefly reviewed, with the aim of establishing possible relationships between carbonatite metasomatism and other metasomatic styles represented in the SEA lithopshere.

Many SEA peridotite xenolith samples are anhydrous (olivine + orthopyroxene + clinopyroxene + spinel assemblages). Others contain pargasitic amphibole, often associated with glassy patches derived from low pressure melting of hydrous phases (pargasite±phlogopite) on ascent of the nodule to the surface (Frey and Green, 1974). In some xenoliths, replacement of amphibole by glass is complete. Many amphibole- or glass-bearing xenoliths are LREE-enriched. For example, $(La/Yb)_{PM}$ (normalized to primitive mantle of Sun and McDonough, 1989) of sample SL5 (Chen et al., 1989) is 14.2. Sample WGBN15 (O'Reilly and Griffin, 1988) has $(La/Yb)_{PM}$ of 7.7. Other

amphibole±glass-bearing xenoliths have near-chondritic or depleted REE contents. Sample 2642 (Frey and Green, 1974), with 2 modal% amphibole, has $(La/Yb)_{PM}$ of 0.83. Similarly, anhydrous xenoliths may have depleted or enriched REE patterns. Samples DR9894 and BM20 (O'Reilly and Griffin, 1988) have $(La/Yb)_{PM}$ of 0.47 and 2.4 respectively. The majority of anhydrous, or amphibole±glass-bearing samples have chondritic Ti/Eu (7740±2250) and Zr/Hf values (≈36).

The presence of mica±amphibole in many xenoliths is correlated with enriched Rb, Ba, K and Ti relative to other metasomatic styles, but retention of near-chondritic Ti/Eu and Zr/Hf values. Apatite-bearing xenoliths invariably also contain low-Ti pargasite, are strongly enriched in LREE, Th, Sr, P, Nb and Ta, and display unusually fractionated Ti/Eu (200 - 2000) and Zr/Hf (36 - 100) values. The carbonatite metasomatised wehrlites, lherzolites and harzburgites described herein have trace element patterns very similar to other, previously reported apatite±low-Ti pargasite-bearing xenoliths (for an example, see figure 4 of Yaxley et al. 1991).

3.5.4 Isotopic ratios in metasomatised xenoliths

Figure 3.5.4 shows published Nd-Sr isotopic data for representative populations of the above groups. Xenoliths with different metasomatic styles and trace element patterns appear to have distinctive isotopic characteristics. For example, most anhydrous nodules display depleted signatures (high $^{143}Nd/^{144}Nd$ [0.512512-0.512974] and low $^{87}Sr/^{86}Sr$ [0.703347-704775]), reflecting a previous melting event. In contrast, the amphibole-bearing group displays a large range in Nd-Sr isotopic compositions, extending from very depleted to very enriched values.

The mica-bearing samples are more restricted in isotopic composition, with $^{143}Nd/^{144}Nd$ = 0.512549-0.512853 and $^{87}Sr/^{86}Sr$ = 0.704031-0.706241. Interestingly, of the metasomatised nodules, the apatite+amphibole-bearing group define a relatively restricted field in $^{87}Sr/^{86}Sr$ vs. $^{143}Nd/^{144}Nd$ space. It extends from values close to Bulk Earth (BE) towards slightly more enriched values, partially overlapping with the previous two fields. The narrow isotopic composition of apatite-bearing nodules has been noted previously by Griffin et al. (1988) and Stolz and Davies (1988), and is also distinct from that of the host Victorian Pliocene to Recent Newer Volcanics. Interestingly, isotopic analyses from the carbonatized suite (table 3.3) plot within or very close to the apatite+amphibole-bearing group (figure 3.5.4).

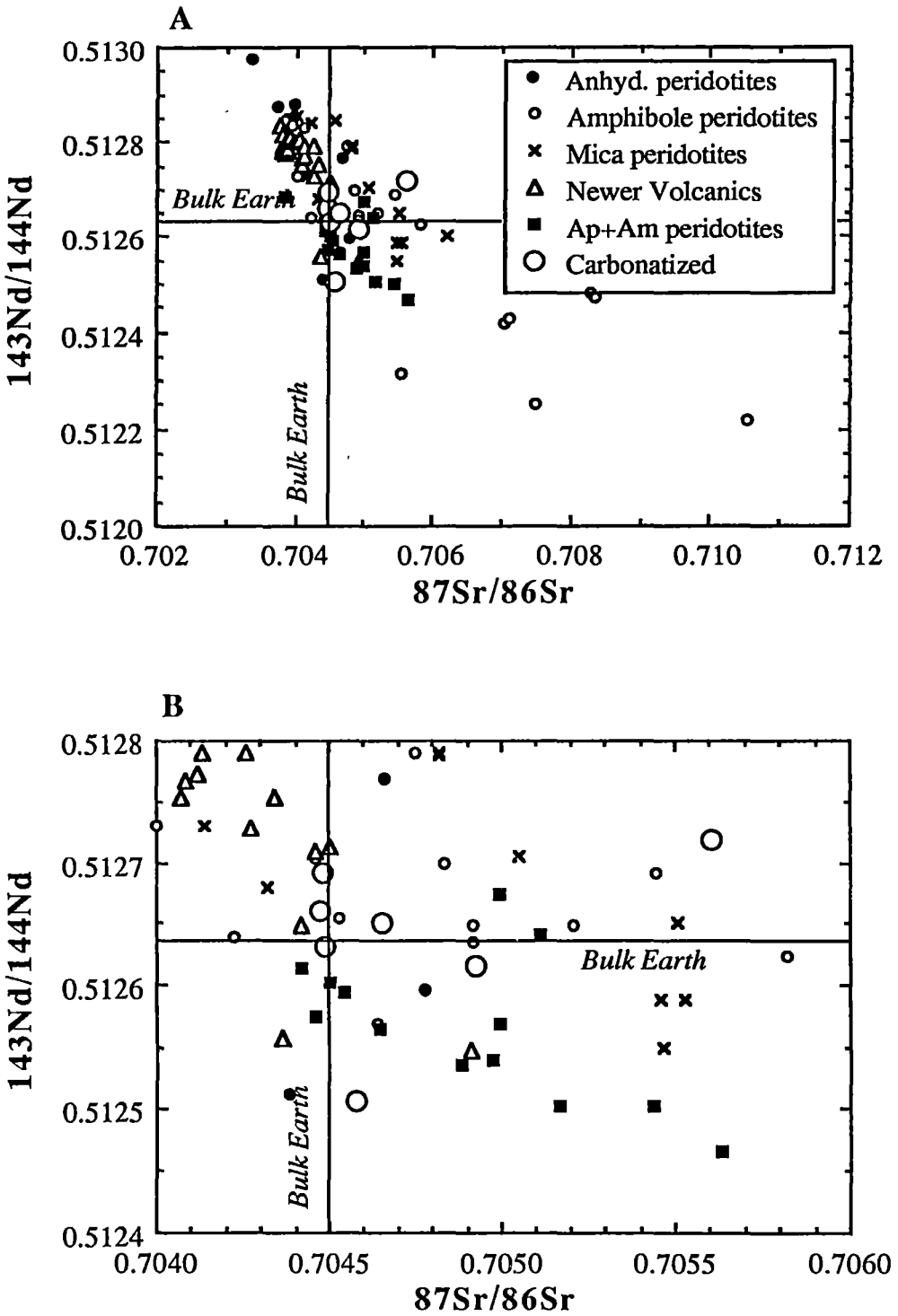

Figure 3.5.4: Plots of $^{87}Sr/^{86}Sr$ vs. $^{143}Nd/^{144}Nd$ for SEA spinel peridotite xenoliths. Data sources listed in Table 3.2, except for carbonatized suite, which is listed in Table 3.3, and Newer Volcanics data, which is from McDonough et al. (1985). (A) Showing all available data (B) Closer view of Sr-Nd isotopic space around bulk earth, illustrating similarity in carbonatized and apatite+amphibole-bearing suites. See text for further explanation.

Table 3.3: Sr and Nd isotopic data obtained by isotope dilution from the carbonatized suite. Sample numbers followed by AP and CPX refer to separates of apatite and clinopyroxene respectively. All other quoted values are whole-rock measurements. Details of isotopic analysis are presented in appendix A.

SAMPLE	Sr (ppm)	$^{87}Sr/^{86}Sr$	Sm(ppm)	Nd(ppm)	$^{143}Nd/^{144}Nd$
71001		0.704483	6.5548	39.695	0.512631
			6.5521	39.693	0.512618
76995		0.705605	0.46921	1.8831	0.512713
				1.8826	0.512722
70965		0.704574	1.147	6.533	0.512504
		0.704572		6.533	0.512507
2631		0.704908	3.1233	19.8152	0.512616
		0.704935			
76989		0.704479	3.7056	24.247	0.512692
			3.7081		
			3.7041		
71008	185	0.70447	3.31	22.1	0.51266
71008AP	9407	0.70450	171	1317	0.51266
71008CPX	385	0.70464	11.1	52.9	0.51264
71000	192	0.70456	3.00	18.3	0.51265
71000AP	11474	0.70450	138	1035	0.51264
71000CPX	383	0.70488	4.88	22.4	0.51266

Mica±amphibole metasomatism may be related to intrusion of mafic melts into the lithosphere (Stolz and Davies, 1988; O'Reilly and Griffin, 1988). The latter authors, and O'Reilly et al. (1991) have rationalized trace element patterns in SEA xenoliths in terms of a model for metasomatism in which lherzolite wall-rock acts as a "chromatographic column" (Bodinier et al. 1987; Navon and Stolper, 1987). Fluids expelled from crystallizing mafic dykes and veins intrude refractory lithospheric wall-rock and evolve as they permeate from the dyke margin into pristine wall-rock, resulting in zones of progressively changing metasomatic style.

However, the source of metasomatic fluids involved in apatite+amphibole metasomatism remains unclear (Stolz and Davies, 1988; Griffin et al. 1988; O'Reilly et al. 1991). Stolz and Davies (1988) suggested that this fluid/melt derived from a deeper source, with an isotopic signature like BE. Alternatively, the similarity of its isotopic characteristic with BE may reflect an "averaging" effect as the fluid/melt moved through and interacted with isotopically heterogeneous lithosphere composed of variously metasomatised Cr-diopside lherzolite and Al-augite peridotites (Griffin et al. 1988; O'Reilly et al. 1991). In the next section, it is demonstrated (a) that the

with a carbonatite melt, in the manner proposed by Green and Wallace (1988) and demonstrated by Yaxley et al. (1991), and (b) that the Sr and REE-enriched nature of the carbonatite results in complete overprinting of any pre-metasomatic, lithospheric signature, suggesting that the Sr-Nd isotopic composition of the apatite+amphibole-bearing and carbonatized groups directly reflects that of the metasomatic carbonatite.

3.5.5 The nature of the agent of apatite+amphibole addition

A key feature of the geochemistry of the nodules produced by carbonatite metasomatism is a distinctive decoupling of substantial LILE enrichment from Ti abundance, consistent with the prediction that metasomatic carbonatite melts would not produce significant Ti enrichment.

Depleted, anhydrous nodules interpreted as residues after basaltic melt extraction (eg: Frey et al. 1985; Jochum et al. 1989) generally have unfractionated Ti/Eu values (McDonough and Frey, 1990), similar to the Primitive Mantle estimate of 7740 (Sun and McDonough, 1989). This is due to similar partitioning behaviour of Ti and Eu between mafic silicate melts and peridotite residue (figure 3.5.5). Thus, partial melting of peridotite is not expected to substantially fractionate Ti and Eu. Similarly, it is unlikely that metasomatism involving addition of undersaturated basaltic melts to refractory lithosphere will cause fractionation between Ti and Eu, as the K_d's involved are similar to the partial melting case. This is supported by the fact that nodules bearing petrographic evidence of metasomatism by basaltic melts (ie; modal mica±high Ti-amphibole) have Ti/Eu values similar to Primitive Mantle (eg; Kurat et al. 1980; Stolz and Davies, 1988; O'Reilly and Griffin, 1988; Yaxley et al. 1991), despite their overall LILE enrichment (figure 3.5.5). On the other hand, metasomatised nodules containing modal apatite+low-Ti pargasitic amphibole display systematically lower Ti/Eu values at similar absolute Ti abundances (Frey and Prinz, 1978; Stolz and Davies, 1988; O'Reilly and Griffin, 1988), comparable with Ti/Eu values of the carbonatite metasomatised wehrlites. This suggests that the metasomatic processes involved are capable of fractionating Ti and Eu, as has been pointed out by McDonough and Frey (1990).

An ephemeral carbonatite melt is a possible candidate for the metasomatic agent in this case, as it is unlikely to transport significant Ti but is strongly enriched in all REE, including Eu. This is supported by experimental K_d determinations made by Sweeney et al. (1992). Ti is strongly compatible with garnet and amphibole (K_d's>1) when they are in equilibrium with a dolomitic carbonatite melt at PT conditions appropriate to the source regions of primary carbonatites (Wallace and Green, 1988). Migration of

carbonatite melt into overlying lithosphere, and absorption of such a melt in this region, will lower Ti/Eu values, without substantially altering absolute Ti abundances.

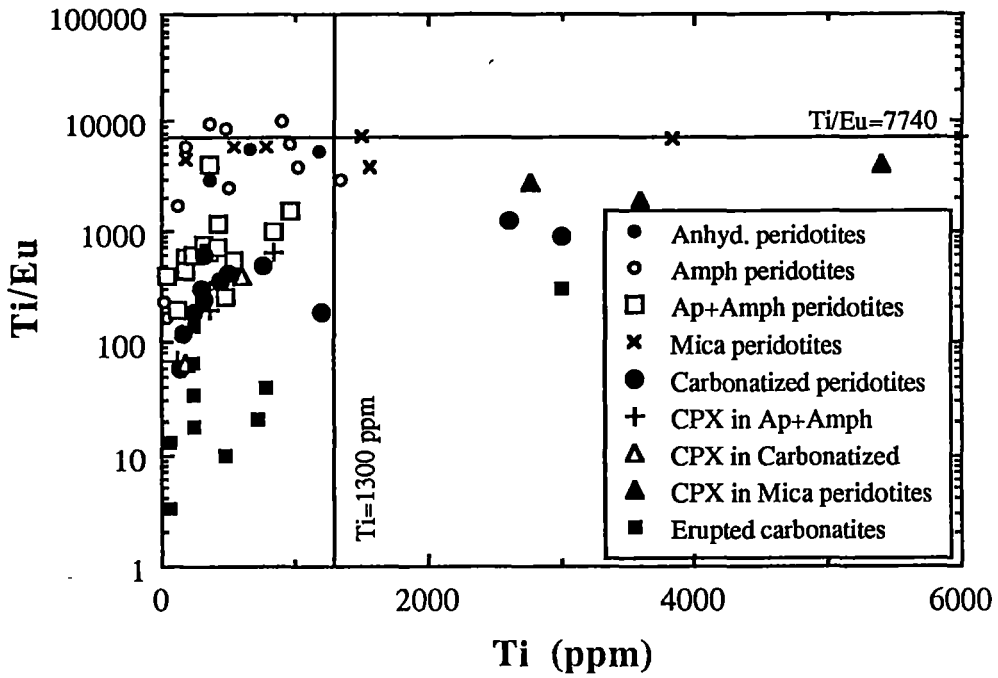

Figure 3.5.5: Ti vs. Ti/Eu for SEA spinel peridotite xenoliths. Data sources listed in table 3.2. See text for further explanation.

Most apatite+amphibole-bearing xenoliths from the literature have slightly higher Ti/Eu than the magnesian wehrlites described herein. In addition, clinopyroxene separates from 71008 and 71000, and from other apatite+amphibole xenoliths (group 3 of Stolz and Davies, 1988) plot within the field defined by low-Ti amphibole±apatite bearing nodules (figure 3.5.5). This suggests that the low Ti/Eu value is a primary feature of the carbonatite melt, and not simply dependent on addition of varying amounts of apatite (and therefore Eu) to a lithosphere containing a range of Ti abundances. The Ti/Eu values of the carbonatized wehrlites, and the apatite+amphibole suite are the result of mixing between depleted peridotite with Primitive Mantle Ti/Eu values and an end-member composition with low Ti/Eu and low absolute Ti abundance. The higher bulk-rock Ti/Eu values of the apatite+amphibole suite presumably reflects addition of less carbonatite to the pre-metasomatic lithosphere than in the case of the wehrlites. Importantly, eruptive carbonatites reported from several continents (Nelson et al. 1988; W. Taylor, unpubl. data) have Ti/Eu values <2400, and generally low Ti abundances (figure 3.5.5).

Thus, it is proposed that the apatite+amphibole-bearing group of nodules were metasomatised by a carbonatite melt, in a similar manner to the suite described earlier

in this chapter, and by Yaxley et al. (1991). Most of the apatite+amphibole group retain orthopyroxene, and olivine+clinopyroxene replacement rims have not been reported (except in sample 2700, by Frey and Green, 1974). However, exhaustion of the carbonatite before complete consumption of primary wall-rock orthopyroxene, with subsequent annealing, could remove this direct evidence of carbonatite interaction (section 3.5.1).

Figure 3.5.5 also demonstrates that the metasomatic agent responsible for mica or amphibole addition (without apatite) to the lithosphere, has not fractionated Ti/Eu, as this xenolith suite plots close to Primitive Mantle over a range of Ti contents. Nickel and Green (1984) attributed formation of amphibole to near isochemical (in terms of major and minor elements) metasomatism by reaction of hydrous fluids with primary clinopyroxene and spinel. This could be accompanied by addition of large ion lithophile elements (including LREE), transported in H_2O-rich fluid.

Trace element patterns (fig 3.4.3) in carbonatized peridotites are consistent with the experimental constraints on primary carbonatite genesis. For example, depleted Ba, Rb, K and Ti, and fractionated LREE/HREE in the carbonatized peridotites suggest that phlogopite and garnet were in equilibrium with the carbonatite in its source regions. Sweeney et al. (1992) showed experimentally that K and Ti are strongly retained by phlogopite (and less strongly by pargasitic amphibole), and that garnet in equilibrium with carbonatite melt at 30kbar will fractionate REE, resulting in high melt LREE/HREE values. For example, K_d's between carbonatite melt and garnet at 33 kbar and 1000°C are 0.30 for Ce and 18.5 for Lu (Sweeney et al. 1992). These carbonatite trace element characteristics will be superimposed on depleted lithosphere if the ascending melt metasomatizes it at around 20kbar. Thus, the trace element geochemistry of the carbonatized suite of spinel peridotite xenoliths is consistent with absorption by depleted lithosphere of a carbonatite derived from a garnet + phlogopite ± amphibole bearing source.

3.5.6 A model for carbonatite metasomatism

This chapter is concerned with carbonatite melt existing in the upper mantle, and reacting with overlying lherzolite because of decarbonation reactions intersected during ascent of the melt towards the surface. Accepting the foregoing arguments that the magnesian wehrlites and related xenoliths do show the effects of metasomatism by ephemeral carbonatite melts, then the origin of such melts may be addressed. Carbonatite melts in the upper mantle at 20-30 kbar depths are believed to form by a number of different processes:

• Liquid immiscibility from a carbonated silicate melt (Koster van Groos and Wyllie, 1966). However, Baker and Wyllie (1990) have shown that this is unlikely at pressures greater than 20 kbar. The experimental phase relations of Wallace and Green (1988) require that the metasomatic interaction between peridotite lithosphere and carbonatite melt occurs at around 20 kbar. Therefore the carbonatite melt must be generated at P>20 kbar.

• Carbonatite genesis could have involved low degrees of melting of carbonated, phlogopite±pargasite-bearing lherzolite in the garnet stability field, as demonstrated experimentally by Wallace and Green (1988) and Falloon and Green (1990). A "cool" or shield geotherm would require depths of around 100 km for a magnesitic carbonatite to form in equilibrium with phlogopite-bearing garnet peridotite (Falloon and Green, 1990). A hotter geotherm could generate dolomitic carbonatite as a primary melt in the pargasite±phlogopite stability field. Higher temperature geotherms are possible as a result of heating of the lithosphere during magmatic activity associated with eruption of both the Older and Newer Volcanics of Victoria.

• Carbonated, undersaturated mafic silicate melts ascending from depths >90km in the asthenosphere will crystallize pargasite±phlogopite as they enter the experimentally-constrained carbonatite melt stability PT window (Wallace and Green, 1988), producing pargasite±phlogopite-enriched garnet lherzolite or harzburgite as the silicate melt component reacts with the mantle wall-rock. Carbonate originally dissolved in the silicate melt forms a residual, highly evolved sodic, dolomitic carbonatite melt [or a magnesite-rich carbonatite at higher pressures (P>25kbar)]. If the melt were magnesitic, partial re-equilibration on ascent at low melt fractions would drive the melt composition towards sodic dolomite, due to interaction with diopside and jadeite components in wall-rock clinopyroxene (Green and Wallace, 1988; Wallace and Green, 1988). The carbonatite melt will be poor in Rb, K, Ti and Ba (since these are retained in hydrous silicate phases in the 20-30 kbar interval), and enriched in REE, with high La/Yb, and low Ti/Eu values. Sr abundances will be 1500 - 7400 ppm, Nd 90 - 650 ppm, Zr 160 to 1611 ppm, and Hf from 2 to 30 ppm. The Sr-Nd isotopic signature of the carbonatite will reflect that of the crystallizing undersaturated silicate melt.

A carbonatite melt may segregate at very low melt fractions (≥0.02%, Hunter and MacKenzie, 1988) and may ascend rapidly and pervasively through the isotopically and geochemically heterogeneous lithosphere. At depths corresponding to ≈20 kbar pressure, the melt enters a PT regime in which carbonate is unstable in contact with orthopyroxene-bearing lherzolite, being replaced instead by CO_2-rich fluid. The major and trace element components of the carbonatite are absorbed by the lithosphere during

a series of end-member decarbonation reactions which replace wall-rock orthopyroxene with forsteritic olivine and sodic clinopyroxene (Green and Wallace, 1988; Chapter 2). The extreme abundance of Sr and Nd in the carbonatite swamps any pre-metasomatic isotopic signature, resulting in overprinting of a fairly restricted isotopic composition onto the lithosphere at this level (figure 3.5.4). This is illustrated by simple mass balance calculations. An estimate of the mode of sample 71008 was made by least squares mixing calculations using its bulk (Appendix C) and mineral compositions (Appendix B). The clinopyroxene mode was found to be 12.98% and apatite 1.40% (Σr^2=0.16; d=0.40). This was used to perform mass balance calculations for Sr and Nd using the elemental abundances in each phase and the bulk rock (table 3.3). This indicated that apatite and clinopyroxene account for 71.2 and 27.0% respectively of Sr, and 72.8 and 27.0% respectively of Nd in the bulk sample. This, coupled with the observation that the isotopic composition of apatite and clinopyroxene separates from each of samples 71000 and 71008 are within analytical error of the bulk-rock values (table 3.3) supports the contention that the Sr-Nd isotopic signature of the carbonatized nodules is virtually identical to that of the metasomatising carbonatite.

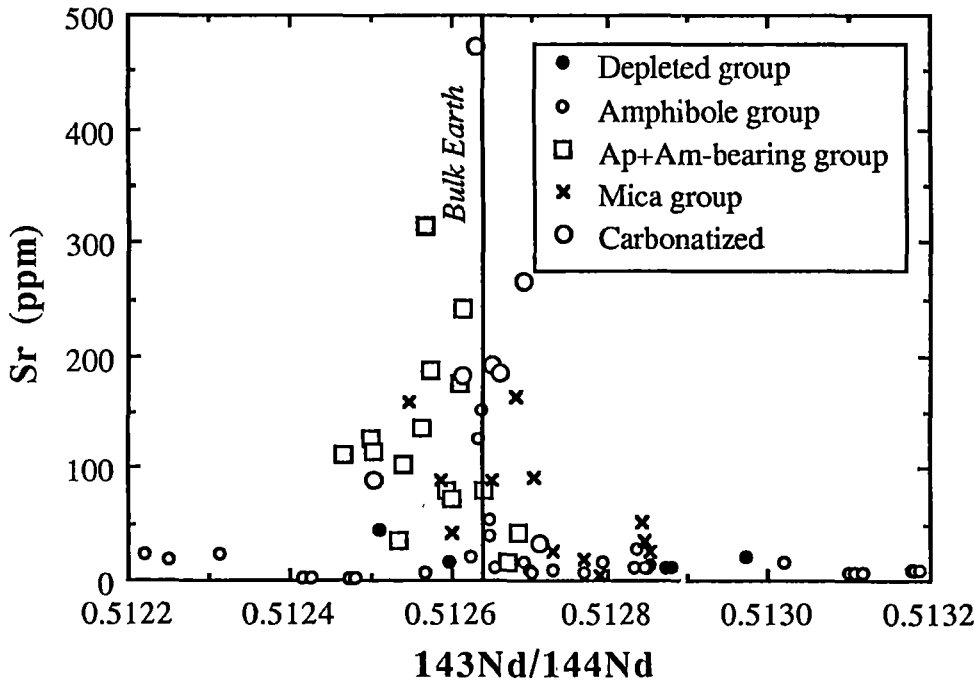

Figure 3.5.6: $^{143}Nd/^{144}Nd$ vs. Sr for SEA peridotite xenoliths. Data sources given in table 3.2. This illustrates that apatite-bearing nodules have bulk earth-like Nd-isotopic signatures and very high absolute Sr contents, similar to the carbonatized suite, and provides evidence that the metasomatising carbonatite responsible for apatite deposition has swamped the bulk-rock isotopic characteristics. See text for further explanation.

Furthermore, figure 3.5.6 illustrates that many of the nodules from SEA which have $^{143}Nd/^{144}Nd$ similar to the carbonatized suite described herein (and similar to estimates of bulk-earth) are of the apatite+low-Ti pargasite bearing type, and are also strongly enriched in Sr, compared with other anhydrous or metasomatised nodules.

Evolution of the carbonatite melt leads to low-Ti pargasite and apatite deposition. If the carbonatite flux was sufficiently high, complete or near complete replacement of primary orthopyroxene occurs. Subsequent annealing results in production of apatite+amphibole spinel wehrlite. Interruption of the metasomatic process by entrainment in an invading silicate magma from deeper levels, leads to preservation of textures indicative of olivine+clinopyroxene replacement of orthopyroxene. Exhaustion of the supply of carbonatite melt before elimination of orthopyroxene, with subsequent annealing, produces the apatite+amphibole suite of xenoliths in which orthopyroxene replacement textures are no longer preserved. Furthermore, parts of the lithosphere that suffered partial replacement of orthopyroxene, but without apatite+amphibole deposition, will anneal, producing LILE enriched, anhydrous, or "cryptically metasomatised" peridotite (see section 3.5.7).

The Tertiary volcanics of southeastern Australia contain a range of mafic compositions (Frey et al. 1978; Irving and Green, 1976) from olivine tholeiites, through alkali olivine basalts and basanites, to olivine melilitites. The role of dissolved carbonate in their petrogenesis has been demonstrated (Brey and Green, 1976; Frey et al. 1978). Episodic tapping of a larger melt fraction (≥5% melt) from 50 to 100 km follows, and may overlap with, a period in which small melt fractions (carbonated olivine melilitites to olivine-rich basanites) from deeper levels (≥90 km) were generated, and either erupted, or reacted within the lithosphere in the manner described above. These produce derivative carbonatite magmas, and mantle metasomatism due to reaction of the carbonatitic magmas at depths of 60 to 70 km.

3.5.7 How important is carbonatite metasomatism?

Recent studies have provided evidence for a similar style of carbonatitic metasomatism in the lithosphere under the Kaapvaal craton in southern Africa (Rudnick et al. 1992; Rudnick et al. 1993) and the Saharan Basin (Dautria et al. 1992). The Kaapvaal xenolith suite was sampled from the ankaramitic Olmani cinder cone in Tanzania, and consists mostly of clinopyroxene-bearing, orthopyroxene-absent dunites, as well as a wehrlite and a harzburgite. The orthopyroxene-free, olivine+clinopyroxene assemblage bears a striking similarity with the SEA magnesian wehrlites. However, the Olmani suite is distinct from the SEA suite in that the former samples are generally

free of hydrous phases, with the exception of minor apatite-bearing glass-lined vugs in some of the dunites and the wehrlite. The harzburgite contains no clinopyroxene, but minor monazite was observed as oval inclusions in extremely refractory olivine (Fo_{94}).

The Olmani suite shares many of the geochemical characteristics of the SEA suite, such as high Ca/Al (1.75 to 10.8), enrichment in LREE, low Ti/Eu and high Zr/Hf values. However, there are important differences as well. Figure 3.5.7 is a plot of wt% MgO vs. wt % CaO for ≈300 world-wide spinel peridotites, the SEA carbonatized suite, and the Olmani samples. Whereas the compositions of the SEA suite appear consistent with bulk mixing with a dolomitic melt, the compositions of the Olmani suite are suggestive of mixing with a few % of a CaO-bearing magnesitic carbonatite. Such a carbonatite melt may have interacted with extremely refractory lithosphere via the reaction

$$\text{magnesite} + \text{enstatite} = \text{forsterite} + CO_2$$

(Newton and Sharp, 1975; Brey et al. 1983). Any dolomitic component in the melt would react in the manner described by Green and Wallace (1988), via the reaction

$$\text{enstatite} + \text{dolomite} = \text{forsterite} + \text{diopside} + CO_2$$

The nett effect of these two reactions would be to increase the Fo content of the primary olivine, and to replace any orthopyroxene with clinopyroxene, resulting in the highly magnesian clinopyroxene-dunite assemblages observed.

Genesis of carbonatite melt with a magnesitic, as opposed to dolomitic composition, may be possible at P≥25 kbar (Falloon and Green, 1990), as sub-solidus carbonate is magnesitic in the pyrolite-CO_2-H_2O system at these higher pressures.

The Saharan xenolith suite, described by Dautri et al. (1992), is from In Teria, Algeria, and is hosted by Quaternary melilititic volcanics. The suite consists of harzburgites and dunites which retain preserved textural evidence of replacement of primary orthopyroxene by a fine-grained assemblage of olivine and clinopyroxene, similar to the lherzolites and harzburgites described in Chapter 2. In addition, they have high Ca/Al values, and strong enrichment in LREE. Several of the samples have low Ti/Eu values (samples 1, 4, 5, 6 and 7).

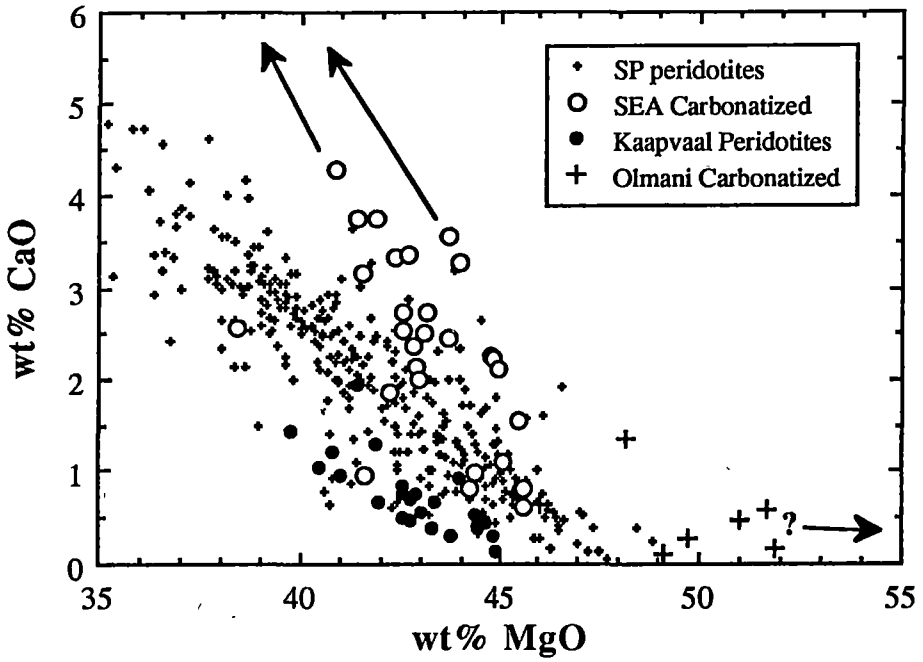

Figure 3.5.7: Plot of wt% MgO vs. wt% CaO for ≈300 spinel peridotite xenoliths, the SEA and Olmani carbonatized suites (Rudnick et al. 1993), and Kaapvaal garnet peridotites from Boyd and Mertzman (1987). Arrows to high Ca/Mg from SEA suite are mixing lines between pre-metasomatic peridotite and dolomitic carbonatite melt. The "?" arrow is possible mixing line between highly refractory lithosphere and Ca-magnesite carbonatite composition, to generate the Olmani suite. Garnet peridotites are included to illustrate highly refractory nature of Kaapvaal lithosphere.

The Saharan suite have been subjected to two successive metasomatic stages (Dautria et al. 1992). The first involved interaction with undersaturated silicate melts, and resulted in addition of Ti-rich amphibole and Ti-rich phlogopite to the lithosphere. The second stage was the result of influx of a carbonatite melt into the lithosphere at ≈20 kbar, and produced the replacement textures on primary orthopyroxene grains.

The recognition of carbonatite metasomatism in several different localities raises the question of its overall importance to the trace element budget of the upper mantle. It clearly has at least local importance in continental intra-plate volcanic settings. In addition, Dupuy et al. (1992) have demonstrated that many intra-plate volcanic rocks (including oceanic examples) have unusually elevated Zr/Hf values, and have also argued for a carbonatite component in the source regions of these magmas. Furthermore, Green and Wallace (1988) originally suggested that carbonatitic melts may be responsible for the enrichment observed in cryptically metasomatised nodules (Dawson, 1984). Baker and Wyllie (1992) have demonstrated that the Ce/Yb and P/Ti values of anhydrous, cryptically metasomatised spinel peridoite xenoliths can be

explained using dolomitic carbonatite as the metasomatic agent. For example, addition of <0.5 wt% dolomitic carbonatite with Ce/Yb≥400 to depleted peridotite can create the enrichment levels observed in cryptically metasomatised spinel peridotite xenoliths. In addition, Hunter and MacKenzie (1989) have shown that carbonate melts can segregate from olivine-dominated residues at very low melt fractions, whereas CO_2-rich fluids (often proposed as agents of cryptic metasomatism) cannot (see Chapter 4). Furthermore, addition of clinopyroxene to an olivine matrix can inhibit the mobility of small fractions of silicate melt (Toramaru and Fufii, 1986). If this also applies to carbonate melts, it may explain the frequently observed inverse correlation between refractoriness of xenolith compositions (measured, for example, by bulk CaO content), and trace element enrichment (Frey and Green, 1974; Baker and Wyllie, 1992). The more refractory, (ie; more olivine-rich) parts of the lithosphere may allow greater access of carbonatite melt, and therefore greater levels of trace element enrichment. This would result in the inverse correlation between CaO content and LILE enrichment observed in figure 3.5.8 and also by Frey and Green (1974) and Baker and Wyllie (1992).

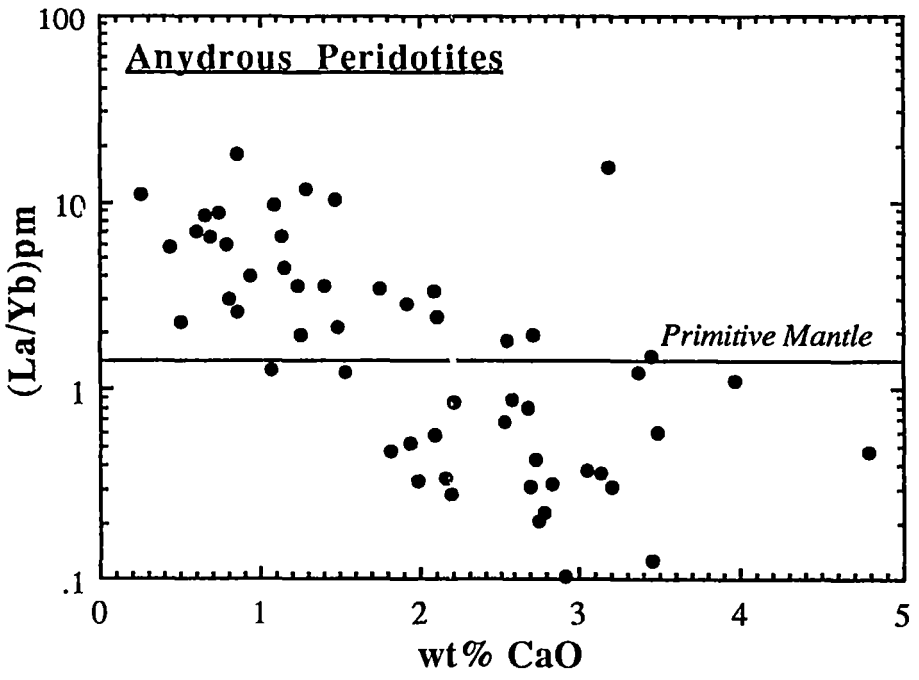

Figure 3.5.8: Plot of wt% CaO vs. La/Yb normalized to Primitive Mantle of Sun and McDonough (1989), for anydrous spinel peridotite xenoliths, demonstrating that the most refractory xenoliths in terms of major element geochemistry, are the most enriched in terms of LILE abundances. See text for further explanation. Data sources are from BVSP (1981), Dupuy et al. (1987), Kurat et al. (1980), O'Reilly and Griffin (1988), Ottonello (1980), Song and Frey (1989), Stosch and Lugmair (1986) and Xue et al. (1990).

3.6 Conclusions

(1) The unusual major element characteristics of the SEA suite of apatite+pargasite-bearing magnesian wehrlites, lherzolites and harzburgites [high Ca/Al, Na/Al, enriched P_2O_5, "typical" mantle Mg/(Mg+ΣFe)'s etc] are consistent with mixing between refractory harzburgitic or lherzolitic lithosphere and dolomitic carbonatite, accompanied by release of CO_2-rich fluid.

(2) The inferred metasomatism creates moderate to extreme enrichment in LILE, particularly LREE, Sr, and Th, unusually low Ti/Eu and high Zr/Hf values, and high $[La/Yb]_{PM}$. Most of the LREE, Sr and P enrichment is hosted by accessory apatite. LILE enrichment is decoupled from Ti abundances, which appear to be unaffected by carbonatite metasomatism.

(3) Complete elimination of orthopyroxene by reaction between pre-metasomatic lithosphere and the ascending carbonatite, followed by rapid annealing, has produced the magnesian wehrlites. Interruption of the metasomatic process by entrainment in the host magma has resulted in preservation of textures indicative of replacement of primary orthopyroxene by forsteritic olivine + Na-rich clinopyroxene, according to the metasomatic reaction orthopyroxene + dolomitic melt = clinopyroxene + olivine + CO_2.

(4) Some wehrlite xenoliths from SEA, previously attributed to cumulate processes, may in fact be the product of carbonatitic metasomatism.

(5) Assuming that carbonatite metasomatism of the lithosphere occurs by simple bulk mixing between refractory lherzolitic or harzburgitic lithosphere and dolomitic melt (Green and Wallace, 1988), then mixing-trends in major element geochemistry exhibited by the SEA magnesian wehrlite suite require the addition of 1-6% dolomitic carbonatite.

(6) This constrains the carbonatite to having trace element abundances within the following ranges: 1460-7360 ppm Sr, 90-660 ppm Nd, 160-1600 ppm Zr and 2-34 ppm Hf.

(7) Certain trace element fractionations within peridotite xenoliths characterize carbonatite metasomatism. For example, Zr/Hf values are high, whereas Ti/Eu is low. In addition, carbonatized nodules have strongly fractionated LREE/HREE, have high

Nb/Ta values, and are depleted in Ba and Rb. This implies the presence of garnet±phlogopite in the carbonatite source regions.

(8) Peridotite xenoliths from the SEA lithosphere exhibit a range of metasomatic styles, including anhydrous or variably LREE-enriched amphibole±glass-bearing types, mica±high-Ti pargasite-bearing types, and apatite±low-Ti-pargasite-bearing types. Based on trace element and Sr-Nd isotopic considerations, it is considered that the apatite+low-Ti pargasite nodules were also metasomatised by a carbonatite melt.

(9) A model for carbonatite metasomatism is proposed, in which carbonated, undersaturated mafic silicate melts (eg; olivine melilitites) ascend from the asthenosphere into the stability field in which carbonatite melt exists in equilibrium with amphibole-bearing garnet peridotite. Crystallization of phlogopite±amphibole from this melt results in evolution of the residual melt to sodic dolomitic carbonatite melt at low P, or possibly magnesitic carbonatite melt at high pressures. The carbonatite melt can ascend at low melt fractions, and will interact with the lithosphere at 15-20 kbar, in the manner described by Green and Wallace (1988) and in Chapter 2. The trace element and isotopic characteristics of the influxing carbonate melt will be imposed onto the lithosphere at this level.

(10) Carbonatite metasomatism has been recently reported from several other locations, suggesting that it may be at least of local importance in regions exhibiting intra-plate volcanism. In addition, it may also be capable of producing trace element enrichment observed in some anhydrous or "cryptically" metasomatised peridotite xenoliths.

CHAPTER 4

EXPERIMENTAL REVERSALS OF NATURAL METASOMATIC PROCESSES INVOLVING EPHEMERAL CARBONATITE MELTS - IMPLICATIONS FOR MANTLE PROCESSES

4.1 Introduction

Most carbonatitic magmas are believed to have their source regions in the Earth's mantle. This conclusion is largely based on studies of the isotopic compositions of carbonatites in systems such as C, O, Sr, Nd and Pb (Deines and Gold, 1973; Sheppard and Dawson, 1975; Nelson, et. al. 1988). However, a number of petrogenetic models have been invoked for their formation. For example, carbonatites may be the result of (1) liquid-liquid immiscibility (Koster van Groos and Wyllie, 1966; Freestone and Hamilton, 1980; Kjarsgaard and Hamilton, 1988; 1989) from undersaturated silicate melts (nephelinites), (2) primary melting of carbonated peridotite mantle (Lancelot and Allegre, 1974; Dawson, 1962; Twyman and Gittins, 1985; 1987; Wallace and Green, 1988; Thibault, et al. 1992), or (3) evolution of carbonated, undersaturated silicate melts during fractional crystallization (Donaldson and Dawson, 1978; Rankin and LeBas, 1974; LeBas, 1977; 1987).

The experimental discovery by Wallace and Green (1988) of a stability field of sodic, dolomitic carbonatite melt in equilibrium with pargasite-bearing Hawaiian pyrolite supports the possibility that at least some erupted carbonatites (eg; the natro-carbonatites of Oldoinyo Lengai) may have evolved from low degree primary carbonatitic melts (Wallace and Green, 1988; Sweeney et al. 1992). Such melts may also be extremely effective agents of metasomatism in the lithosphere (Green and Wallace, 1988; Chapters 2 and 3). Previous chapters have presented a model for carbonatite metasomatism in the SEA lithosphere, based on mineralogical and geochemical evidence. The purposes of this chapter are (1) to present evidence deduced from high pressure experiments using peridotite compositions, for involvement of primary carbonatites in mantle metasomatism, (2) to assess the relationship between primary carbonatite melts and those erupted at the Earth's surface, and (3) to briefly examine the implications for intraplate volcanic activity, of large fluid fluxes associated with carbonatite metasomatism in the lithosphere.

4.2 Experimental reversals of the natural carbonatite metasomatic process

4.2.1 Introduction

In order to test the model for carbonatite metasomatism presented in Chapters 2 and 3, a series of high pressure experiments was performed. These aimed to demonstrate that the compositions of two of the southeastern Australian magnesian wehrlite (orthopyroxene absent) nodules described in Chapters 2 and 3 are consistent with the metasomatic addition of an ephemeral sodic dolomitic melt to an orthopyroxene-bearing spinel peridotite assemblage, resulting in decarbonation and replacement of orthopyroxene by clinopyroxene. This was achieved by effectively reversing the natural metasomatic process, by running hydrous (≈0.5 wt% H_2O), synthetic compositions equivalent to those of 71001 and 70965 (minus 40% olivine) (Appendix C) in the presence of 1, 5 or 7 wt% CO_2, at a range of PT conditions which span the carbonatite melt field in the fluid undersaturated pyrolite-CO_2-H_2O system (Wallace and Green, 1988). This produced carbonatite melt in equilibrium with harzburgite or lherzolite residue, and allowed estimates of the composition of the postulated natural, metasomatizing carbonatite to be made. Implicit in this approach is an assumption that apart from fugutive CO_2 (or possibly H_2O), the pre-existing lherzolite has acted as a "sponge" towards the postulated carbonatite. This is one limiting scenario to a spectrum in which a "wall-rock reaction" component of metasomatism requires knowledge of partitioning relationships between carbonatite melts and mantle lherzolite minerals (olivine, orthopyroxene, clinopyroxene, spinel, garnet, amphibole, phlogopite, apatite).

4.3 Experimental Details

4.3.1 Choice and preparation of starting materials

The compositions of samples 71001 and 70965 were chosen for the experimental investigation. Both fulfill the carbonatite metasomatic characteristics described previously, but they also exhibit significant differences in their geochemistry. For example, 70965 has a significantly higher CaO/Al_2O_3 (4.38 cf 2.96) at similar Al_2O_3 contents, but slightly lower Na_2O/Al_2O_3 (0.55 cf. 0.71). P_2O_5 content is much higher in 71001 (0.77 wt% cf. 0.02 wt%) and this is reflected in the modal apatite contents of the natural assemblages; 70965 is free of detectable modal apatite, whereas GENMIX least squares mixing calculations performed using the whole-rock and mineral compositions of nodule 71001 indicate an apatite content of 2.2 modal %.

Synthetic amphibole-bearing wehrlites with the same compositions as samples 71001 and 70965 (-40% olivine of ambient mol% forsterite) were prepared from high purity oxides and carbonates which were ground under AR quality acetone for several hours to ensure homogeneity. These starting mixes were fired in 100mg aliquants for 48 hours with excess water at 15 kbar and 925°C (sub-solidus), producing an olivine + clinopyroxene + pargasite + Cr-spinel + apatite assemblage (71001), and an olivine + clinopyroxene + pargasite + Cr-spinel assemblage (70965). No orthopyroxene was detected in either composition. Determinations of phase compositions enabled the calculation of modal proportions (table 4.1). Examination of powdered run material suspended in immersion oils under transmitted light, and of polished sections under the SEM and electron microprobe confirmed the modal analyses. Excess water was observed bubbling from the pierced capsules after synthesis runs. Run material was ground to <10μm under acetone, and then dried for several hours at 400°C in argon. Least squares mixing calculations on the whole-rock, and mineral phase compositions of the synthetic wehrlites revealed an amphibole content of 19.8%, and an apatite content of 3.12% in composition 71001. Assuming stoichiometric water in these two hydrous phases, then the bulk water content of 71001 is approximately 0.5 wt%. The 70965 composition contains 0.4 wt% H_2O. 70965 contains substantially higher modal clinopyroxene (22.7% cf. 5.4% in 71001) reflecting its greater CaO content and Ca/Al value. The bulk and modal compositions are presented in table 4.1.

4.3.2 Experimental runs

Aliquants of the synthetic wehrlites, together with sufficient silver oxalate ($Ag_2C_2O_4$) to decompose to 1, 5 or 7 wt% CO_2 (total mass around 15mg) were loaded into welded 2.2mm outside diameter (OD) $Ag_{75}Pd_{25}$ or $Ag_{70}Pd_{30}$ capsules. A small disc of pre-fractured San Carlos olivine [100*Mg/(Mg+ΣFe)=89] was placed near the top of the capsule, to trap any melt as inclusions. In some runs, a layer of coarsely crushed San Carlos olivine was used in the same manner. A sketch of the capsule configuration is presented in figure 4.3.1. The base of the capsule was maintained at T<100°C during welding to minimize premature decomposition of the $Ag_2C_2O_4$. The small capsule was surrounded by natural magnesite in a welded 3.5mm OD $Ag_{50}Pd_{50}$ or Pt outer capsule.

The buffering reaction (magnesite-periclase-graphite; MPG),

4.1 $MgCO_3 = MgO + C + O_2$

ensured carbonate stability during runs by maintaining $fO_2 \approx$EMOG (Eggler and Baker, 1982).

Experiments were run in a 0.5 inch diameter high pressure piston-cylinder apparatus at the University of Tasmania. NaCl or NaCl-pyrex assemblies were used with graphite heaters. No pressure correction was applied. Pressures are accurate to ±1 kbar.

Table 4.1: Bulk compositions (weighed in) for starting mixes used in these experiments. Modal proportions were determined by least squares mixing of bulk and individual phase compositions.

	71001	70965
SiO_2	41.50	45.89
TiO_2	0.17	0.13
Al_2O_3	1.55	1.65
ΣFeO	9.70	7.35
Cr_2O_3	0.76	0.86
MnO	0.30	0.25
MgO	38.93	35.51
CaO	4.59	7.21
Na_2O	1.10	0.91
K_2O	0.12	0.05
P_2O_5	1.30	0.03
NiO	-	0.02
TOTAL	100.00	99.85
100*Mg/(Mg+ΣFe)	87.74	89.60
olivine	70.87	55.77
cpx	5.35	22.72
spinel	0.84	0.11
amphibole	19.82	21.40
apatite	3.12	0.00
Σr^2	0.12	0.68
distance	0.35	0.83

Temperature was controlled to an accuracy of ±10°C, and precision of ±1°C with a $Pt/Pt_{90}Rh_{10}$ thermocouple attached to a Eurotherm 818P solid-state contoller. Run times varied from 2 to 168 hours.

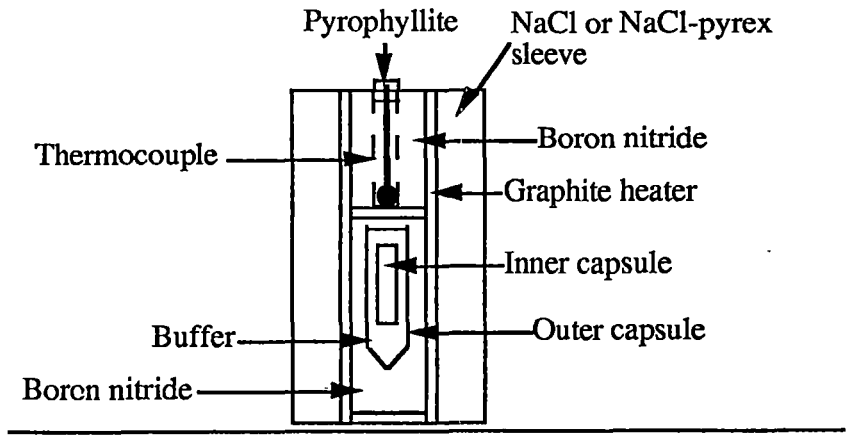

Figure 4.3.1: Diagram showing capsule assembly used in these experiments. Note the double capsule arrangement, in which a small, inner capsule fabricated from $Ag_{75}Pd_{25}$ is surrounded by magnesite buffer, which is contained in a Pt or $Ag_{50}Pd_{50}$ outer capsule. The outer capsule is surrounded by boron nitride, which is the pressure-transmitting medium. Heating is provided by the graphite heater, and the entire assembly is surrounded by a NaCl or NaCl/pyrex sleeve. Thermocouple was made of $Pt/Pt_{90}Rh_{10}$. Entire assembly is 1/2" in diameter.

4.3.3 Analytical details

Run products and residual buffer material were examined optically under immersion oils of accurately known refractive index (RI) in order to identify phases and to ensure that buffer exhaustion had not occurred. Run material was mounted in epoxy and polished in water-free oils to prevent dissolution of any carbonate phases (Wallace and Green, 1988). These mounts were used during Scanning Electron Microspcopy (SEM) on a Phillips 505 SEM, and electron probe microanalysis. In addition, unpolished fragments of run material from a couple of the runs were examined under the SEM to check for loss of quench phases during polishing.

Electron probe microanalyses were performed at the University of Tasmania on a Cameca SX50 electron microprobe which was calibrated using natural mineral standards. Data was processed using PAP data reduction. Count times were 10 to 30 seconds on peaks, and 5 to 15 seconds on background, depending on the element's concentration. An accelerating voltage of 15kV, and beam currents of 10 (carbonate analyses) or 20nA (silicates+spinel+apatite analyses) were used.

Phase equilibration in runs appears to have been achieved, based on reproducibility of mulitple analyses of silicate phases. Fe loss was minimized by the use of $Ag_{75}Pd_{25}$ or

$Ag_{70}Pd_{30}$ capsules. Its absence was confirmed by lack of zoning in olivine grains, and by reasonable atomic 100*Mg/(Mg+ΣFe) values of phases and bulk compositions.

4.4 Experimental Results

4.4.1 Solidus position

Details of run conditions, and phases detected in each run are presented in table 4.2 , with representative microprobe analyses in tables D1 to D5 (Appendix D).

Although the exact position of the solidus was not determined for these compositions, the sub- or super-solidus position of each run was delineated using the following criteria;

(1) Super-solidus runs contained carbonate with distinctive quench textures comprised of acicular to tabular dolomite, and delicate needles of (Na,Mg)-carbonate. Carbonate in sub-solidus runs did not display quench-like textures.

(2) Amphibole and amphibole+apatite were present in sub-solidus runs for compositions 70965 and 71001 respectively. No runs using 70965 contained detectable apatite, and amphibole and apatite were missing from all super-solidus runs using both compositions.

4.4.2 Silicate, spinel and apatite mineralogy

The experimental runs produced carbonate-bearing harzburgitic (71001) or lherzolitic (70965) assemblages. Despite its abundance in the amphibole-wehrlite starting material, clinopyroxene was absent in all runs using composition 71001, but was ubiquitous in 70965 runs. Euhedral lathes of pargasitic amphibole were present in runs at 900°C for both compositions, but were not detected in super-solidus runs at T>900°C in either composition. Orthopyroxene was present in all CO_2-bearing runs, despite being absent in the starting compositions.

Olivine compositions (table D1) ranged from $Fo_{87.9-88.4}$ (composition 71001) and $Fo_{89.3-90.3}$ (composition 70965). No systematic increase in Fo content was observed when crossing the solidus into the carbonate melt field, consistent with the observations of Wallace and Green (1988), and Thibault et al. (1992). Similarly, the atomic 100*Mg/(Mg+ΣFe) in orthopyroxene in 71001, and orthopyroxene and clinopyroxene in 70965 did not increase systematically with temperature (tables D2

Table 4.2: Summary of runs and products. Wt% CO_2 quoted on a "weighed-in" basis, and represents maximum values due to possible minor decomposition of $Ag_2C_2O_4$ on welding. Abbreviations: OL = olivine; OPX = orthopyroxene; CPX = clinopyroxene; AP = apatite; AM = amphibole; SP = spinel; MAG = sub-solidus magnesitic carbonate; DOL = sub-solidus dolomitic carbonate; CBTE = quenched carbonate melt; GL = quenched silicate melt (glass). Runs at 15 kbar were synthesis runs.

Run Number	*P(kbar)*	*T(°C)*	*Run time (hrs)*	*CO2 (wt%)*	*Phases*
Composition 71001					
T-3149	15	925	48	0.00	OL+CPX+AM+AP+SP
T-3301	22	900	117	0.97	OL+OPX+CPX+AM+AP+SP+MAG
T-3172	22	900	48	4.31	OL+OPX+CPX+AM+AP+SP+MAG
T-3170	22	1000	24	5.28	OL+OPX+SP+CBTE
T-3690	22	1000	168	5.00	OL+OPX+SP+CBTE
T-3197	22	1050	24	5.09	OL+OPX+SP+CBTE
T-3491	22	1070	25	4.43	OL+OPX+SP+CBTE
T-3188	22	1100	2	7.24	OL+OPX+GL
Composition 70965					
T-3309	15	925	48	0.00	OL+CPX+AM+SP
T-3482	22	900	120	1.06	OL+OPX+CPX+AM+SP+DOL
T-3315	22	900	116	4.60	OL+OPX+CPX+AM+SP+DOL
T-3627	22	1000	168	5.00	OL+OPX+CPX+SP+CBTE
T-3447	22	1000	25	4.49	OL+OPX+CPX+SP+CBTE
T-3560	22	1050	160	5.00	OL+OPX+CPX+SP+CBTE
T-3327	22	1050	24	4.50	OL+OPX+CPX+SP+CBTE
T-3586	22	1050	60	10.00	OL+OPX+CPX+SP+CBTE
T-3469	22	1070	24	4.43	OL+OPX+CPX+SP+CBTE
T-3336	22	1150	2	4.92	OL+OPX+CPX+GL

and D3). In most cases, pyroxene 100*Mg/(Mg+ΣFe) values were slightly higher than Fo contents in co-existing olivines.

The presence of orthopyroxene+carbonate melt in runs at 1000°C or more, suggests that reversal of the postulated metasomatic reaction orthopyroxene + dolomitic melt = olivine + clinopyroxene + CO_2-rich fluid, has occurred. In 71001, clinopyroxene was eliminated in supersolidus runs, suggesting that CO_2 was in excess. The retention of clinopyroxene in 70965 supersolidus runs suggests that the pre-metasomatic rock was lherzolite, or that 5 or even 7wt% CO_2 was not sufficient to completely reverse the process if the precursor rock was harzburgite. This is supported by the presence of spheroidal vapour holes in 71001 run material (figure 4.4.1a), which were absent in 70965 runs. It is also consistent with the much higher Ca/Al value of 70965 compared with 71001, despite the former's lack of modal apatite.

In Chapter 2, a series of carbonatite metasomatic end-member reactions between sodic dolomitic melt and lithospheric wall rock phases was proposed on the basis of the mineral chemistry of phases in the nodules comprising the SEA carbonatized suite;

2.4 $4MgSiO_3 + CaMg(CO_3)_2 = 2Mg_2SiO_4 + CaMgSi_2O_6 + 2CO_2$
enstatite dolomite forsterite diopside

2.5 $[7MgSiO_3 + MgAl_2SiO_6] + Na_2CO_3 = 4Mg_2SiO_4 + 2NaAlSi_2O_6 + CO_2$
opx sodium carbonate forsterite jadeite

2.6 $9MgSiO_3 + Mg(Cr,Al)_2O_4 + Na_2CO_3 = 5Mg_2SiO_4 + 2Na(Cr,Al)Si_2O_6 + CO_2$
enstatite spinel sodium carbonate forsterite jadeite-ureiite solid solution

2.7 $10MgSiO_3 + 3MgAl_2O_4 + 3CaMgSi_2O_6 + [Na_2CO_3 + Ca(OH)_2] =$
enstatite spinel diopside carbonatite melt components

$2NaCa_2Mg_4Al_3Si_6O_{22}(OH)_2 + 4Mg_2SiO_4 + CO_2$
pargasite forsterite

The nett effect of these is to remove enstatite and Mg-Tschermak's components from orthopyroxene, and $MgAl_2O_4$ component from spinel, replacing them with diopside, jadeite and ureiite components in clinopyroxene, and forsterite in olivine. These reactions are accompanied by the release of CO_2-rich fluid during interaction of lherzolitic or harzburgitic lithosphere with carbonatite melt. Al_2O_3 and CaO contents in orthopyroxene in equilibrium with carbonatite melt using both compositions are higher than in the subsolidus runs, consistent with reversal of the metasomatic reactions (2.4-

Figure 4.4.1: Back-scattered electron images of (A) run T-3690 showing abundant quench needles of (Na,Mg)-carbonate, and spheroidal vesicles indicating the presence of an abundant fluid phase, (B) closer view of patch of quenched carbonatite melt in T-3690, showing delicate needles of (Na,Mg)-carbonate, and white, tabular dolomite grains, and (C) carbonate melt trapped as an inclusion in layer of coarsely crushed San Carlos olivine in run T-3586, displaying clear quench texture. Scale bar is 0.1mm in A, and 10µm in B and C.

2.7 above) involving enstatite and Mg-Tschermak's components in orthopyroxene (table D2).

Amphibole was found in all subsolidus runs for both starting mix compositions as tabular grains up to 10 μm in length. It has a rather unusual edenitic composition, rather than being pargasitic, due mainly to low Al content (table D4). For example, in 71001 runs, amphibole was Al-deficient, containing no octahedral Al (Al^6), and only about 1.2 Al^4 cations per 8 oxygen anions. In runs using 70965, amphibole contained about 0.8 Al^6 cations per 8 oxygen anions, and similar levels of Al^4 to those in 71001 runs. The amphibole compositions in the experimental study of Wallace (1989) were pargasitic, being richer in Al, but generally poorer in Na. The low Al amphibole compositions in this study probably reflect the low whole-rock Al_2O_3 content of the 71001 and 70965 compositions (table 4.1).

Amphibole was not detected in any supersolidus runs. This is probably due to complete or near complete reversal of the metasomatic end-member reaction (2.7) above. In 71001 supersolidus runs, the absence of clinopyroxene suggests the presence of excess CO_2. This means that equilibrium (2.7) would have been forced to favour the carbonation reaction until elimination of amphibole. In 70965 compositions, in which clinopyroxene is still present in supersolidus runs, the presence of minor amphibole is a possibilty. However, none was detected after extensive examination under the microprobe.

Apatite was abundant in the 71001 starting composition, and in subsolidus runs using that composition (T-3172 and T-3301). However, it was absent from all 71001 runs at T≥1000°C. Apatite was not detected in either the 70965 synthesis run, or in any experimental runs using this composition. Apatite compositions were difficult to determine quantitatively because of the small grain size. However, in addition to CaO and P_2O_5, it contained minor FeO and MgO (≈1.2 and 1.5 wt% respectively).

Cr-spinel grains were detected in most runs, but were generally too small (1-2 microns) for accurate microprobe analysis. Semi-quantitative analysis of spinels from run T-3469 indicated a high atomic 100*Cr/(Cr+Al) value (≈61).

4.4.3 Carbonate compositions

Carbonate was detected in all runs at T<1100°C. In runs at 900°C, tiny, interstitial crystals of carbonate material were clearly recognizable. In runs at PT conditions within the carbonate melt stability field of Wallace and Green (1988), the carbonate

displayed distinctive quench textures. Carbonate was not found in runs T-3188 and T-3336.

Sub-solidus carbonate compositions varied between the different starting compositions at identical PT conditions. For example, subsolidus runs using 71001 (T-3301 and T-3172) contained abundant interstitial Ca-bearing magnesitic carbonate with 100*Mg/(Mg+ΣFe) = 92.2 (T-3301) and 91.7 (T-3172). However, in the subsolidus run using the 70965 composition (T-3315), carbonate had a magnesian dolomite composition, with Mg/(Mg+Fe) = 91.0, and atomic Ca/(Ca+Mg) of 0.47 (table D5).

The presence of subsolidus magnesitic carbonate in 71001 runs at 22 kbars contrasts with other studies in the peridotite-CO_2-H_2O system (eg; Wallace and Green, 1988), in which dolomite was found. However, subsolidus magnesite is compatible with the absence of diopsidic pyroxene; the reaction magnesite + diopside = enstatite + dolomite thus being irrelevant.

Supersolidus carbonate proved extremely difficult to analyse directly by electron microprobe. This was due in part to the nature of its quench aggregates. Backscattered SEM analysis of unpolished fragments of run material (T-3690 and T-3627) revealed the presence of tiny, tabular, mid-grey dolomitic crystals [100*Mg/(Mg+ΣFe) = 79], and spectacular quench growth of a (Na+Mg)-carbonate phase [100*Mg/(Mg+ΣFe) = 77; figure 4.4.1b]. Microprobe analyses of these phases are presented in table D5. Despite careful impregnation of run material with epoxy before polishing, and the use of water-free polishing oils, it proved impossible to prevent mechanical loss of the delicate Na-rich needles. This resulted in most analyses of carbonate quench being dolomitic with unreasonably low Na-contents.

In addition, carbonate melt inclusions were not detected in the San Carlos olivine (discs, or coarsely crushed layers) included in the 71001 runs. Carbonate melt appeared to be distributed along grain boundaries, forming 2-3 μm pools at grain-boundary triple junctions. This made microprobe analysis without contamination from surrounding phases difficult. Most 70965 runs did succeed in trapping some interstitial melt as inclusions in layers of crushed olivine (figure 4.4.1c). This is presumably because all (5%) CO_2 was consumed in the 70965 runs, producing ≈10% melt. In the 71001 runs, CO_2 was in excess, and insufficient melt was produced to form inclusions. In either case, however, apparent loss of a Na-rich phase could not be prevented. For these reasons, a quantitative microprobe analysis of the composition

of carbonate melt was difficult to obtain. However, the similarity in nature and composition of quench carbonate phases in these experiments with those of Wallace and Green (1988) support a sodic dolomitic composition with relatively high 100*Mg/(Mg+ΣFe). Representative analyses of supersolidus carbonate phases are presented in table D5.

Runs at 1050°C using the 70965 composition (T-3560 and T-3586) produced unusual melt compositions, with higher SiO_2, Al_2O_3 and TiO_2 than melts in 1000°C runs (table D5). The T-3560 melt has a 100*Mg/(Mg+ΣFe) value of 70.52, more akin to that of primary silicate melts, than carbonatitic melts. It is believed that these melts are transitional between dolomitic carbonatite and undersaturated silicate melts, and that 1050°C at 22 kbars lies very close to the amphibole-out curve for the 70965 composition. However, T-3197 (71001 at 1050°C) produced dolomitic carbonatite melt with 100*Mg/(Mg+ΣFe) = 90, and is therefore within the carbonate melt field.

The composition of the melt phase produced at 1000°C using the 70965 starting composition was estimated by employing a "normative" calculation. The following procedure and assumptions were made. All Na_2O and K_2O were assigned, along with appropriate CO_2, to alkali carbonate components of the melt. P_2O_5, and stoichiometric CaO and H_2O were assigned to hydroxyapatite in the melt. The balance of CO_2 was assigned to calcite and Fe-bearing dolomite components of the melt, the ratio of calcite to dolomite being determined using Ca/(Mg+Fe) value of the Wallace and Green (1988) composition (CM1). A small amount of SiO_2 (3 wt% to match CM1), MgO, FeO and CaO was allocated on an equimolar basis to forsterite (Fo_{90}) and diopside [100*Mg/(Mg+ΣFe)=90], as carbonatite melt components. All Cr_2O_3 was assigned to spinel, along with sufficient Al_2O_3 to give Cr/(Cr+Al) of 60. TiO_2 was assigned to ilmenite, and the balance of Al_2O_3 (along with MgO and SiO_2) to Mg-Tschermak's molecule. The balance of CaO was assigned to diopside, along with MgO, FeO and SiO_2 [100*Mg/(Mg+ΣFe)=90], and the remainder of MgO, FeO and SiO_2 were incorporated in olivine and enstatite. This procedure produced a sodic, dolomitic composition (CM2 in table D5) very similar to CM1 of Wallace and Green (1988), with a high atomic 100*Mg/(Mg+ΣFe) of 83.7 (cf. 84.5 for CM1), 5.4 wt% Na_2O (assuming 50% CO_2), and an atomic Ca/(Mg+Fe) value of 1.1 (cf. 0.9 for CM1).

An estimate of the melt's composition was also made based on Na partitioning between clinopyroxene and melt. The experiments of Wallace and Green (1988) revealed a $K_d^{cbte/cpx}$(Na) at 22 kbars and 1000°C of 9.69. Clinopyroxene in equilibrium with carbonate melt in run T-3447 (70965+5% CO_2 at 2.2 GPa and

1000°C) contains 1 wt% Na_2O, suggesting that the carbonatite melt would contain 9.7 wt% Na2O. Given this information, and the compositions of the (Na,Mg)-carbonate and dolomite quench phases, the relative proportions of these two quench phases can be estimated [44.7% (Na,Mg)-carbonate+55.3% dolomite]. Addition of the two quench phases in these proportions again produced a sodic dolomitic composition, similar to that of Wallace and Green (1988), with high P, and low Ti and Al contents (CM3 in table D5). A distinction from the Wallace and Green (1988) composition is the lower 100*Mg/(Mg+ΣFe) [78 cf. 84.5].

4.5 Discussion

4.5.1 Implications of experimental investigation for CO_2-rich fluid distribution in the lithosphere

The experiments outlined above demonstrate that the compositions of the magnesian wehrlite suite described in Chapters 2 and 3 are consistent with metasomatic absorption of sodic dolomitic melt by refractory lithosphere at around 20 kbars and 1000°C. They also imply that very substantial CO_2-rich fluid fluxes could be generated during carbonatite metasomatism. For example, 7 wt% CO_2 was insufficient to eliminate clinopyroxene from composition 70965, although $\leq$5 wt% achieved this for 71001. Nevertheless, it appears that fluid fluxes in excess of 5 wt% CO_2 are feasible. This could result in fracturing of the overlying lithosphere, particularly in the light of recent experimental data which suggests that CO_2-rich fluids are unlikely to be able to migrate along grain-boundaries in an olivine-dominated matrix, and would accumulate at intergranular triple-points until the porosity exceeded 6-8% (Hunter and MacKenzie, 1988). At porosities >6-8%, fracturing would occur. This would allow easy access of subsequent mafic silicate magmas to the upper lithosphere, or surface, and increase the chances of entrainment of mantle xenoliths into those magmas. In addition, any adjacent magma batches would become saturated in CO_2-rich fluid, which would be exsolved on crystallization at lower pressures. Fluid flux resulting from carbonatite metasomatism may also have a role in driving explosive alkali basalt eruptions in an intra-plate volcanic setting (Bailey, 1987).

4.5.2 The role of carbonatites in intra-plate volcanism

Erupted carbonatites occur in continental settings, often associated with volcanism involving highly undersaturated silicate melts (nephelinites, kimberlites, lamproites etc). They have also been reported from oceanic intra-plate settings such as Cape Verde and the Canary Islands (Allegre et al. 1971; Silva et al. 1981; Barrera et al. 1981; Nelson et al. 1988). In addition, Nelson et al. (1988) and Dupuy et al. (1992)

recently proposed an involvement for carbonatite components in the source regions of many OIBs. Below a model is proposed which aims to show how the carbonatitic component could be incorporated into intraplate volcanics.

Upwelling partially molten asthenosphere, or ascending asthenospheric diapirs (figure 4.5.1) could enter the stability field of dolomitic carbonatite in equilibrium with amphibole (Wallace and Green 1988), and crystallize amphibole+clinopyroxene, evolving to the intergranular sodic, dolomitic carbonatite melt. This highly enriched and mobile melt fraction could segregate and ascend to around 20 kbars. If it crossed the solidus of the peridotite-CO_2-H_2O system at pressures greater than the decarbonation reaction opx + dol = cpx + ol + CO_2, it would create enriched dolomitic peridotite. Alternatively, it could intersect the solidus at lower pressures than the decarbonation reaction, and metasomatise the lithosphere in the manner described in Chapters 2 and 3 and by Green and Wallace (1988). This would lead to formation of a zone of amphibole+apatite-bearing olivine wehrlite at around 60 km depth. Decarbonation accompanying this process would be substantial (see section 4.5.1), and could cause fracturing and disruption of the lithosphere above this region. Subsequent carbonatite melts would migrate into these fractures, and interact with wall rock, driving it towards wehrlite, and allowing further ascent of later carbonatite magmas. Decarbonation accompanying metasomatism of the wall-rock would propagate the fracture system towards shallower levels in the lithosphere. Carbonatites ascending through this fracture system, could undergo further decarbonation reactions. For example, the reaction dolomite + 3cpx = 2fo + 4calcite + 2CO_2 (Wyllie and Huang, 1976) would increase the calcite component in the melt and may modify it towards a suitable parent to erupted calcitic carbonatite (sövite) (Sweeney et al. 1992). Alternatively, a magnesite component could be introduced into the melt via the reaction opx + dolomite = cpx + 2magnesite (Sweeney et al. 1992). Eruption of the carbonatite to the surface may sometimes occur as a result of continued propagation of the fracture system to shallower levels in the lithosphere. Crustal decarbonation (Sweeney et al. 1992) may generate alkali-rich fenitizing fluids.

Subsequent mafic silicate melts, derived from the asthenosphere may ascend through the metasomatized region and the fracture zones created by interactions between the lithosphere and the carbonatites, and have their compositions modified as well. For example, many intraplate volcanics have unusually fractionated Zr/Hf values (Dupuy et al. 1992) despite the similarity of melt-residue partition co-efficients for these two elements in basalt-peridotite equilibria. High Zr/Hf appears to be a characteristic otherwise confined to erupted carbonatites (eg; Nelson et al. 1988) or carbonatite

metasomatised peridotite xenoliths (Chapter 3; Rudnick et al. 1993). Assimilation of metasomatic clinopyroxene (derived from carbonatite metasomatism) by primitve mafic melts may drive their compositons towards ankaramites (eg; Barsdell and Berry, 1988).

4.6 Conclusions

(1) Experiments in the system Hawaiian pyrolite+CO_2+H_2O have identified a stability field for carbonatite melt+pargasitic amphibole, and have characterized it as having a sodic dolomitic nature. This implies that carbonatites may be generated as low degree primary melts of carbonated peridotite, or by evolution of carbonated undersaturated silicate melts which crystallize amphibole±phlogopite in reaction with lherzolite wall-rock in the carbonatite melt stability field.

(2) Such carbonatites may have an extensive role in metasomatism of the lithosphere in both continental and oceanic settings, as a result of decarbonation of the ascending carbonatite at 15-20 kbars. This may drive refractory lherzolite or harzburgite lithosphere towards amphibole+apatite-bearing olivine wehrlite, with high Ca/Al, Na/Al and Zr/Hf, and elevated LILE abundances without concomitant Ti enrichment.

(3) Experimental reversals performed on synthetic compositions matching those of two of the carbonatite-metasomatised peridotite nodules described in Chapters 2 and 3, support the interpretation that the metasomatic phase is an ephemeral sodic dolomitic carbonatite melt, and imply that very large CO_2-rich fluid fluxes would be released from the metasomatised volumes of the lithosphere.

(4) Such large fluid fluxes may cause fracturing of the lithosphere in regions above zones of carbonatite metasomatism, allowing rapid migration of subsequent carbonatitic magmas. Metasomatism of wall-rock by interaction with carbonatites may result in modification of the melts towards suitable parental compositions for erupted carbonatites. In addition, subsequent plume-derived intraplate volcanics may suffer modification of their trace element characteristics by wall-rock reaction as they ascend through the metasomatised region (eg; increased Zr/Hf).

CHAPTER 5

AN EXPERIMENTAL INVESTIGATION OF CARBONATE STABILITY AT HIGH PRESSURES IN A HYDROUS BASALT+$CaCO_3$ SYSTEM

5.1 Introduction

Veins, fractures and vesicles containing pure calcitic carbonate, as well as other low-T alteration minerals, have frequently been reported in altered ocean floor basalts either dredged, or recovered from drill cores from various localities around the Earth's ocean basins (eg; Richardson et al. 1980; Baragar et al. 1977; Hart and Staudigel, 1978; Alt et al. 1986). Subduction of such altered, carbonate-bearing basalts provides a plausible mechanism for recycling carbonate back into the Earth's mantle, where it is believed to contribute to a large variety of petrogenetic processes, including diamond formation, asthenospheric melting of peridotite to produce highly undersaturated meliltitites and related magmas (Brey and Green, 1975; 1976), formation of carbonatite melts and kimberlites, and carbonatite or CO_2-rich fluid metasomatism (see earlier chapters, and O'Reilly and Griffin, 1988) etc.

To assess the contribution to, and role of, subducted carbonate in the Earth's carbon cycle, it is important to understand the behaviour of calcitic carbonate at high pressures and temperatures in a basaltic system. The occurrence, in some eclogite facies rocks, of apparently primary calcitic carbonate (sometimes as pseudomorphs after aragonite) coexisting with high pressure minerals such as garnet, omphacitic clinopyroxene and occasionally quartz pseudomorphs after coesite (eg; Klapova, 1990; Wang and Liou, 1991; Wang et al. 1992), suggests that carbonate can survive burial to depths corresponding to eclogite facies pressure-temperature conditions without decarbonation or melting (see Chapter 6).

For these reasons, a series of MPG-buffered experiments (buffer described in Chapter 4) in a hydrous basalt+$CaCO_3$ system were performed at pressures from 15 to 35 kbars, and temperatures from 700 to 1000°C. These experiments aimed to assess the stability of calcitic carbonate under the pressure-temperature conditions imposed on altered, carbonate-bearing ocean floor basalts carried in the subducted slab to depths of up to 120 km.

5.2 Choice and preparation of starting composition

The basalt composition (GA1) used in these experiments is listed in table 5.1, and represents an average of 53 analyses of altered ocean floor basalts, and greenschists from ophiolites and the Franciscan terrane, western USA (data sources in caption for table 5.1). GA1 is very similar to the estimate of altered ocean floor basalt made by Gill (1981), which was an average of all DSDP basement samples from Legs 1-29 (Hart, 1976). GA1 is also compared with the range of analyses of >80 fresh primitive MORB glasses (data sources cited by Falloon and Green, 1987, in their figure 4) in table 5.1. The most significant differences are the more evolved character of GA1 (resulting from inclusion of whole-rock data, rather than primitve glasses, in its calculation), and the higher Na_2O/CaO value of GA1 compared with the primitve MORB glasses (0.4 cf. 0.13-0.20 respectively). This probably reflects replacement of Ca-rich plagioclase by albite during low temperature hydrothermal alteration (albitization) of the basalts from which GA1 was calculated.

Table 5.1: Composition GA1 used in these experiments, compared with altered ocean floor basalt composition estimated by Gill (1981), and range of primitive, unaltered MORB glasses reported by Falloon and Green (1987). Data sources used in calculating GA1 are Alt and Emmerman (1985), Aumento and Loncarevic (1969), Bailey et al. (1964), Cann (1969), Coish et al. (1982), Dietrich et al (1978), Hekinian (1982), Hekinian and Aumento (1973), Humphris and Thompson (1978), Melson and Van Andel (1966) and Pearce (1975).

	GA1	Gill (1981)	Primitive Glasses Minimum	Maximum
SiO_2	50.35	50.61	48.20	51.64
TiO_2	1.49	1.80	0.50	1.30
Al_2O_3	16.53	16.20	15.50	17.62
ΣFeO	9.83	10.06	7.30	9.40
MnO	0.17	-	0.09	0.25
MgO	7.94	6.99	8.10	10.70
CaO	9.60	10.17	11.23	13.57
Na_2O	3.49	2.96	1.42	2.71
K_2O	0.44	0.92	0.01	0.32
P_2O_5	0.16	0.29	0.03	0.14
TOTAL	100.00	100.00	-	-
FeO/Fe_2O_3	2.27	1.14		
$Mg/(Mg+\Sigma Fe)$	59.00	55.32	68.00	73.00

The GA1 starting mix was made using high purity oxides of Si, Ti, Al, Fe^{3+}, Mn, and Mg, and carbonates of Na, K and Ca. P was added as calcium pyrophosphate

($Ca_2P_2O_7$). These were mixed, and mechanically ground in an agate mortar under AR grade acetone for several hours to ensure homogeneity and a fine enough grain size to allow reasonable equilibration times during subsequent synthesis runs. The homogenized starting mix was pelletized, and fired at 950°C overnight in a Pt crucible in air, in order to determine ignition loss. It was then crushed, and Fe^{2+} was added as synthetically prepared pure fayalite. Further grinding rehomogenized the mix, which was then dried in Ar at 400-450°C for several hours, and henceforth stored in a dessicator.

Garnet amphibolite was synthesised from the starting mix composition by sealing ≈100mg of the starting mix, along with 7.5 wt% H_2O (added with a microsyringe), in a $Ag_{50}Pd_{50}$ large diameter capsule [outside diameter (OD) = 3.5mm], which was arc welded shut. The capsule was kept cool (T<100°C) during welding by immersion in water-soaked tissue paper. The seal was tested by weighing before and after heating in an oven to 120°C. The prepared capsule was then fired at 20 kbar and 700°C in a 0.5 inch piston cylinder apparatus at the University of Tasmania, producing a garnet+amphibole assemblage. Minor quartz and rutile were also present.

5.3 Details of experimental runs

Aliquants of GA1 garnet amphibolite were mechanically blended (without acetone) with 3 or 10wt% AR $CaCO_3$, 10wt% pure natural magnesite, or 5wt% $CaCO_3$ + 5wt% $MgCO_3$. In some experiments carbonate was completely excluded. Samples of approximately 15mg of the resultant mixtures were loaded into 2.2mm OD $Ag_{75}Pd_{25}$ or $Ag_{50}Pd_{50}$ capsules. These were sealed shut by arc welding, and loaded in 3.5mm OD $Ag_{50}Pd_{50}$ or Pt capules. The inner capsule was surrounded by natural magnesite buffer (MGP) which ensured carbonate stability by maintaining fO_2≈EMOG (Eggler and Baker, 1982; see also Chapter 4). A diagram of capsule configuration is provided in figure 4.1.1.

The experimental runs were performed in a 0.5 inch high-pressure piston-cylinder apparatus at the University of Tasmania, using NaCl or NaCl-pyrex sleeves, and boron nitride as the pressure transmitting medium. Heating was provided by a graphite heater, and the run temperature was controlled by a $Pt/Pt_{90}Rh_{10}$ thermocouple attached to a Eurotherm 818P controller. Pressures are accurate to ±1 kbar, and temperature was controlled to an accuracy of ±10°C, and a precision of ±1°C. Run times varied from 3 to 200 hours.

5.4 Analytical details

Details of optical, SEM and electron microprobe analyses of run materials are described in Chapter 4 (section 4.3.3) and Appendix A .

5.5 Experimental results

5.5.1 Phase relations

Table 5.2 contains details of all runs, including the phase assemblages produced. Phase relations for the GA1+10% calcite runs are summarized in figure 5.5.1. Back-scattered electron images of typical run products are presented in figure 5.5.2.

Runs at T<750°C tended to be fine-grained, and, in some cases, difficult to probe. However, products from runs at T≥750°C were well crystallized. Garnet usually formed large, euhedral crystals which were up to 30μm across in some runs. These grains invariably contained abundant, irregularly shaped "poikilitic" inclusions of omphacite, which in some cases (eg; T-3551) occupied up to ≈50 vol% of the grain (figure 5.5.2a). Care was taken to avoid these inclusions during microprobe analysis of the garnet grains, to minimize "contamination" of the analysis.

Clinopyroxene and amphibole formed euhedral to subhedral, usually tabular grains, which were finer grained (5-15μm long) than co-existing garnet. Primary grains were distinguishable from quench phases largely on the basis of grain-size (quench material was extremely fine), their tabular form, and their more magnesian compositions.

Carbonate tended to occur as irregularly shaped grains which were typically ≈10-20μm across (figure 5.5.2b and c). Rutile occurred as rare, rounded grains which were too fine-grained for accurate microprobe analysis (<3μm).

The positions of the solidus and other major phase boundaries were not bracketed precisely. Interstitial glass (including abundant very fine-grained needles of quenched amphibole and clinopyroxene) was detected in all runs at T>700°C. Runs conducted at 700°C (T-3230 and T-3805) did not contain detectable glass, were finer grained than higher temperature runs, and also contained minor quartz (or coesite at 30 kbar). These garnet ± amphibole ± clinopyroxene + carbonate + rutile + quartz/coesite assemblages are therefore interpreted to be sub-solidus. On the other hand, runs T-3821, T-3819 and T-3237 and (750°C and 15, 25 and 30 kbar respectively) contained

Table 5.2: Summary of run conditions and phases detected. Abbreviations; Ga=garnet, Cpx=clinopyroxene, Am=amphibole, CC=calcitic carbonate, Dol=dolomitic carbonate, Mag=magnesitic carbonate, Gl=glass (including quench phases), Rt=rutile. Parentheses around a phase indicate that it was present in trace quantities.

Run Number	*T(°C)*	*P(kbar)*	*% carbonate*	*Run time (hrs)*	*Phases*
T-3821	750	15	10% calcite	96	Ga+(Cpx)+Am+CC+Gl+Rt
T-3812	850	15	10% calcite	5	Am+Cpx+Gl
T-3605	1000	15	10% calcite	5	Am+Cpx+Gl
T-3230	700	20	10% calcite	166	Ga+Am+CC+Rt+Qz
T-3734	850	20	none	4	Ga+Am+Cpx+Gl+Rt
T-3736	850	20	3% calcite	24	Ga+Am+Cpx+Gl+Rt
T-3212	850	20	10% calcite	8	Ga+Cpx+Am+Gl+CC+Rt
T-3221	950	20	10% calcite	5	Ga+Cpx+(Am)+Gl
T-3237	750	25	10% calcite	166	Ga+Cpx+(Am)+Dol+Gl+Rt
T-3210	850	25	10% calcite	3	Ga+Cpx+Gl+CC+Rt
T-3228	950	25	10% calcite	6	Ga+Cpx+Gl+CC
T-3551	1000	27	10% calcite	5	Ga+Cpx+Gl+CC+Rt
T-3805	700	30	10% calcite	200	Ga+Cpx+Dol+Cs+Rt
T-3811	850	30	10% calcite	7	Ga+Cpx+CC+Gl+Rt
T-3818	850	30	10% magnesite	6	Ga+Cpx+Mag+Gl+Rt
T-3782	900	30	none	49	Ga+Cpx+Gl+Rt
T-3780	900	30	10% calcite	48	Ga+Cpx+Gl+CC+Rt
T-3817	900	30	5% mag + 5% cc	6	Ga+Cpx+Dol(?)+Gl+Rt
T-3794	900	30	10% magnesite	49	Ga+(Cpx)+Gl+Mag+Rt
T-3819	750	35	10% calcite	73	Ga+Cpx+Dol+Gl+Rt

Figure 5.5.1: Phase diagram constructed from the results of GA1+10% calcite runs. Shaded portions of each box indicate the presence of the phase indicated in the key. Note that all runs contained clinopyroxene, except the one at 20 kbar and 700°C. Numbers next to boxes refer to K_d for Ca/Mg partitioning between carbonate and co-existing garnet, defined and discussed in section 5.6. Dashed lines are phase boundaries, as indicated. Solid curved line is model geotherm for upper part of descending basaltic oceanic crust from Oxburgh and Turcotte (1976). Solid straight lines are calcite-aragonite and aragonite+Mg-calcite-aragonite+dolomite phase transitions from Irving and Wyllie (1975).

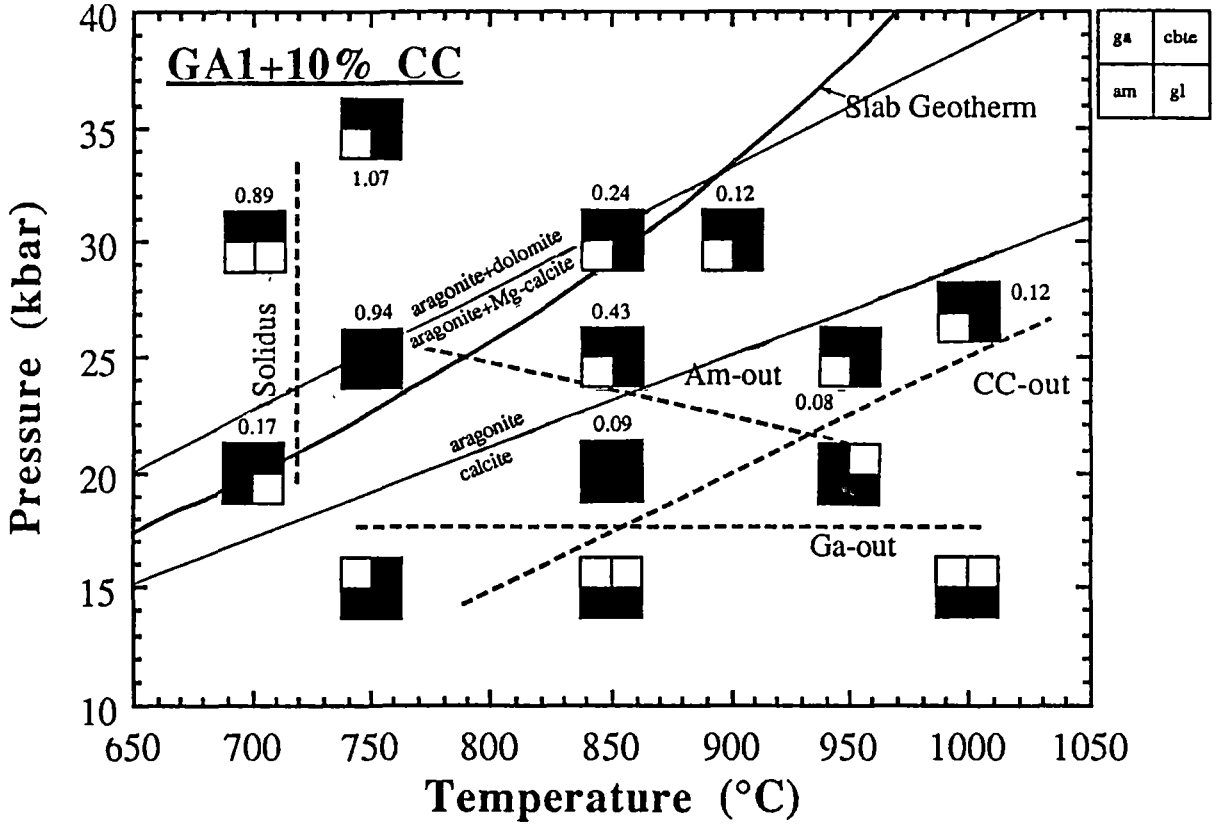

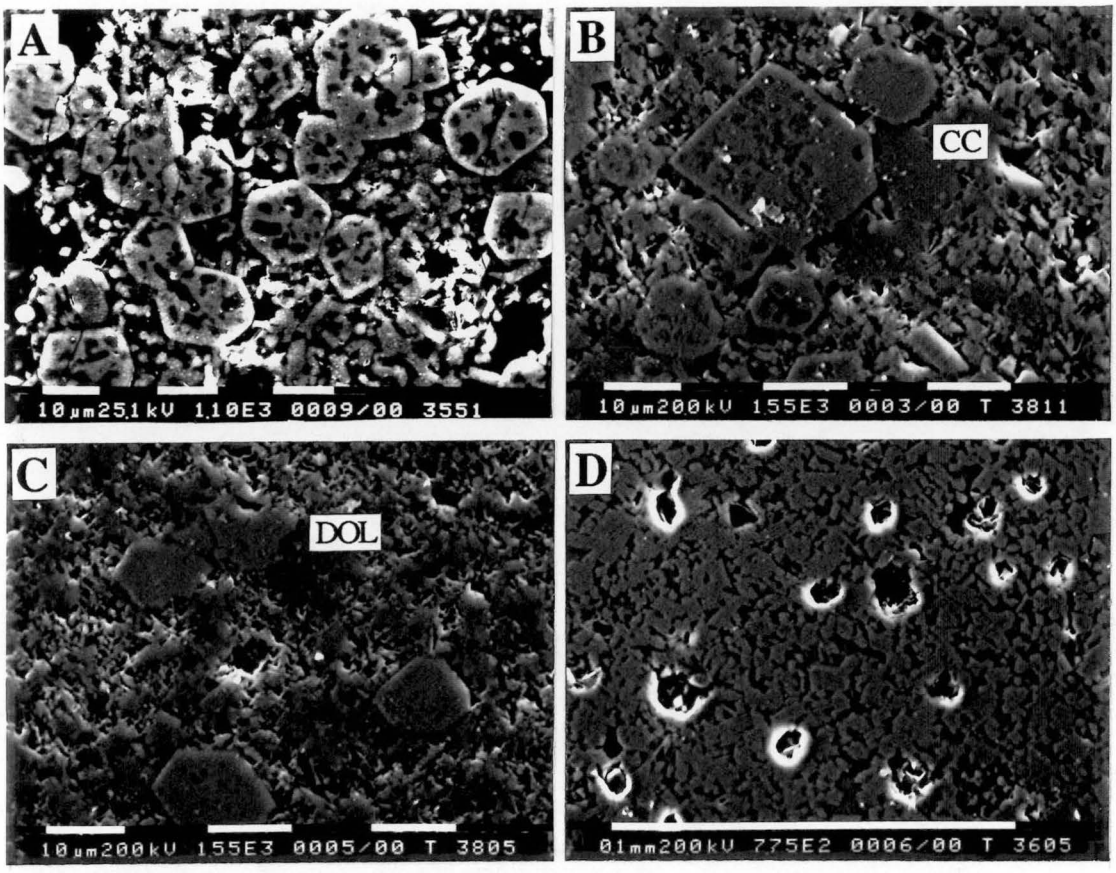

Figure 5.5.2: Back-scattered electron images of products of 4 GA1+10% calcite runs. (A) is run T-3551 (27 kbar/1000°C) showing abundant poikilitic clinopyroxene inclusions in euhedral garnet grains. Finer, tabular grains are clinopyroxene. Interstitial melt is also present. (B) is run T-3811 (30 kbar/850°C), showing a large calcitic carbonate (CC) grain in contact with, and to the right of the large, square garnet grain near the centre of the image, (C) is run T-3805 showing dolomitic carbonate (DOL), sub- to euhedral garnets and fine-grained clinopyroxene. Note the finer-grained nature of this run compared with T-3811 (B), indicative of the sub-solidus nature of T-3805. (C) is run T-3605 (15 kbar/1000°C) showing tabular amphibole and clinopyroxene grains, with interstitial melt. Note also the abundant vesicles, indicating the presence of a CO_2-rich fluid formed as a result of decarbonation of the calcite in this run. Scale bar is 10µm long in A, B and C, and 0.1mm in D.

minor glass, and no free silica. These, and all other runs at T>750°C are interpreted as super-solidus.

All super-solidus runs, as well as run T-3805 (30kbar, 700°C) contained omphacitic clinopyroxene. Minor amphibole was detected in grain mounts made from run material from T-3237 (25kbar, 750°C) and T-3221 (20kbar, 950°C), although it was not detected with the microprobe. However, amphibole was absent from T-3210 (25kbar, 850°C), suggesting that the amphibole-out curve has negative slope in PT space, running from slightly above 25 kbar at 750°C, to slightly above 20 kbar at 950°C. In runs containing both omphacite and amphibole, the ratio of omphacite to amphibole appeared to increase with temperature (degree of melting).

Garnet was detected in all runs at P>15 kbar. Garnet-out therefore lies between 15 and 20 kbar, over the temperature interval 850-1000°C, in broad agreement with previous determinations of the phase relations of water-saturated basaltic compositions (TH Green, 1982).

Residual carbonate was found in all GA1+10% calcite runs except T-3812 (15 kbar, 850°C), T-3605 (15 kbar, 1000°C) and T-3221 (20 kbar, 950°C), bracketing carbonate-out to having a positive slope in PT space, as indicated on figure 5.5.1. Runs at T>calcite-out contained abundant spheroidal holes, indicative of the presence of several vol% of a CO_2-rich fluid phase (figure 5.5.2d), as a result of decarbonation of the calcite. Run T-3736 (20 kbar, 850°C), which was run with only 3wt% calcite contained no detectable residual carbonate, indicating some CO_2 solubility in the co-existing melt. Carbonate was not detected in run T-3817 (GA1+5% calcite + 5% magnesite). The reason for this is unclear. Irving and Wyllie (1975) determined the phase relations of the join $CaCO_3$-$MgCO_3$ at 30 kbar in an anhydrous system. A 50/50 calcite+magnesite mixture would produce a carbonate melt with molar Ca/Mg of ≈60/40 at a liquid peritectic at about 1300°C. The hydrous nature of the system considered here may have resulted in lowering of the solidus temperature, and melting of the calcite+magnesite mixture included in run T-3817.

Very minor quantities of rutile were detected in all GA1+10% calcite and GA1+10% magnesite runs which contained residual carbonate. It was absent from runs with higher degrees of melting at lower pressures (T-3221, T-3605, T-3812), suggesting that rutile-out also has positive slope in PT space, approximately coincident with CC-out on figure 5.5.1. Rutile was also present in the two GA1+0% calcite runs (T-3734

and T-3782), the GA1+3% calcite run (T-3736) and the GA1+5% magnesite + 5% calcite run (T-3817).

In low temperature runs (750°C), glass was distributed in small melt pools at grain boundary intersections. Higher degrees of melting resulted in a continuous grain boundary network of melt, with residual garnet+clinopyroxene. This is illustrated in figure 5.5.3a and b, which are potassium K_α X-ray maps of runs T-3819 (35 kbar and 750°C) and T-3780 (30 kbar and 900°C). In some high temperature runs, minor segregation of melt towards the top of the capsule was observed. Reliable melt compositions proved difficult to determine because of modification by quench overgrowth onto residual primary phases (figure 5.5.3). A few examples of melt compositions are presented in table E5 (although they should be considered estimates only). Near solidus melts are dacitic, and progressively become basaltic with increasing temperature at given pressure (eg; compare compositions for T-3237, T-3210 and T-3228 in table E5). This is broadly consistent with previous experimental melting studies of hydrous basalt compositions (eg; TH Green, 1982). Thus, these runs contain residual carbonate in equilibrium with high silica melts. This contrasts with melting behaviour in the peridotite+CO_2+H_2O system, where free silica is absent, and carbonate becomes the lowest temperature melt fraction (Wallace and Green, 1988).

5.5.2 Variations in mineral chemistry with pressure, temperature and % carbonate

Phase compositions for each run are presented in tables E1 to E5 (Appendix E). Reasonable equilibration of runs was achieved, based on inter- and intra-grain homogeneity of phases. Fe-loss was minimized by the use of $Ag_{75}Pd_{25}$ capsules where possible, and was checked on the electron microprobe by broad beam area scans of run products.

Clinopyroxene compositions (table E1) were generally omphacitic, containing between 6.3 and 35.2 mol% jadeite, 55.0 and 74.8 mol% diopside+hedenbergite, 2.22 and 19.50 mol% Ca-Tschermak's and minor Ca-Ti-Tschermak's ($CaTiAl_2O_6$) components (figure 5.5.4). Aegirine (Aeg) was absent in all cases. Clinopyroxene compositions vary systematically with changes in temperature. For example, in GA1+10% calcite runs, $100*Mg/(Mg+Fe^{2+})$ increases with increasing temperature (figure 5.5.5a) at given pressure, with the exception of T-3230 and T-3212 (20kbars, 700 and 850°C respectively). However, there does not appear to be any systematic variation in $100*Mg/(Mg+Fe^{2+})$ of clinopyroxene with pressure at constant temperature.

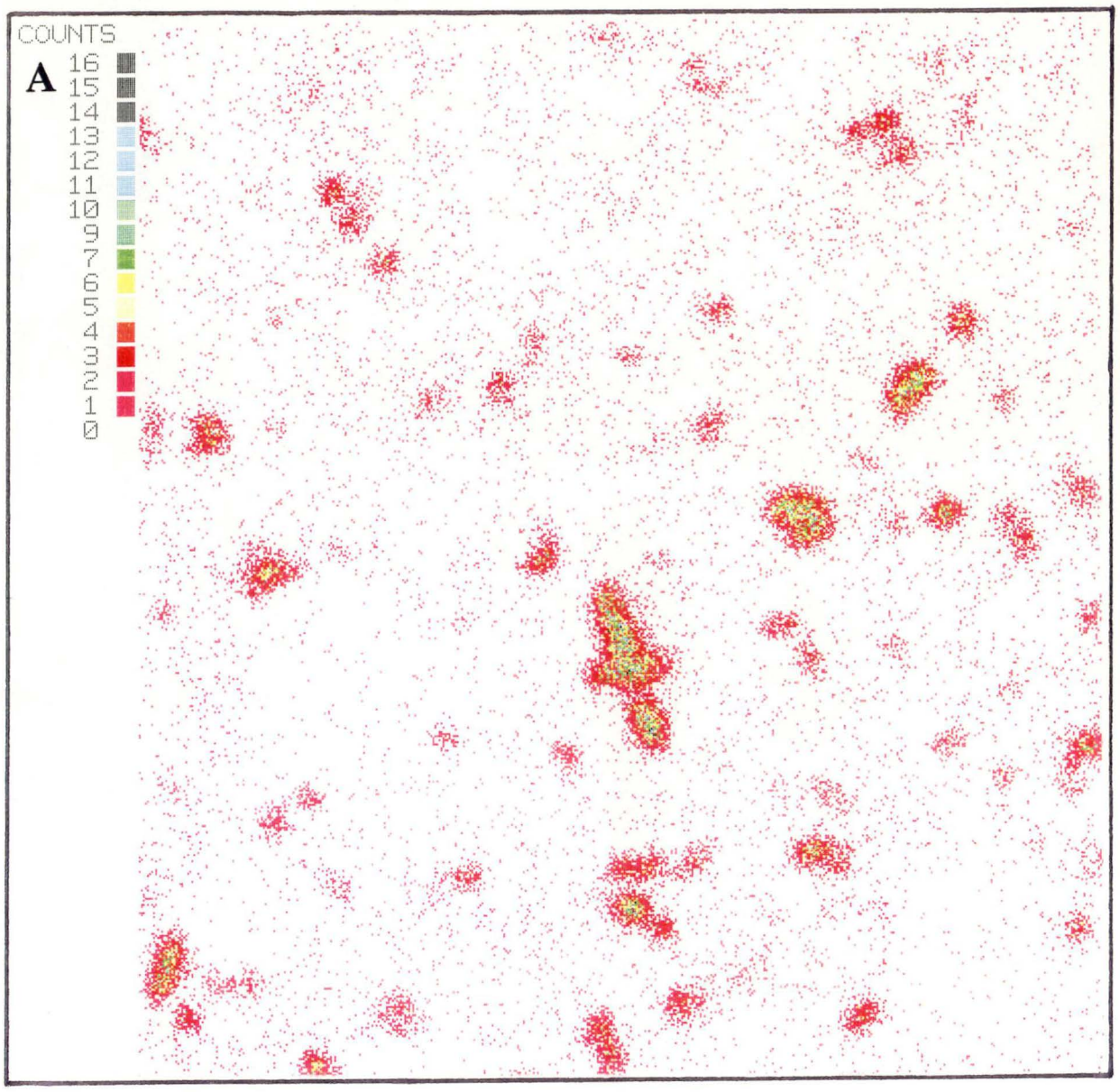

Figure 5.5.3a: X-ray map of potassium K_α peak of run T-3780 (GA1+10% calcite at 35 kbar and 750°C). The images were recorded using Cameca ADV CIPP image acquisition and processing software package on a Cameca SX50 electron microprobe (Central Science Laboratory, University of Tasmania). Image resolution is 512x512 pixels at 1200x magnification. Accelerating voltage was 15 kV, beam current was 40 nA, and pixel counting time was 10 milliseconds. Colour scale for counts/second is displayed on edge of map. Melt is confined to isolated interstitial pools. Some of the larger pools display increased K concentration (yellow and green areas) near centre of pool compared with rims (pink-red areas), indicating overgrowth of amphibole or clinopyroxene on adjacent primary phases during quenching, and concentration of K in residual melt.

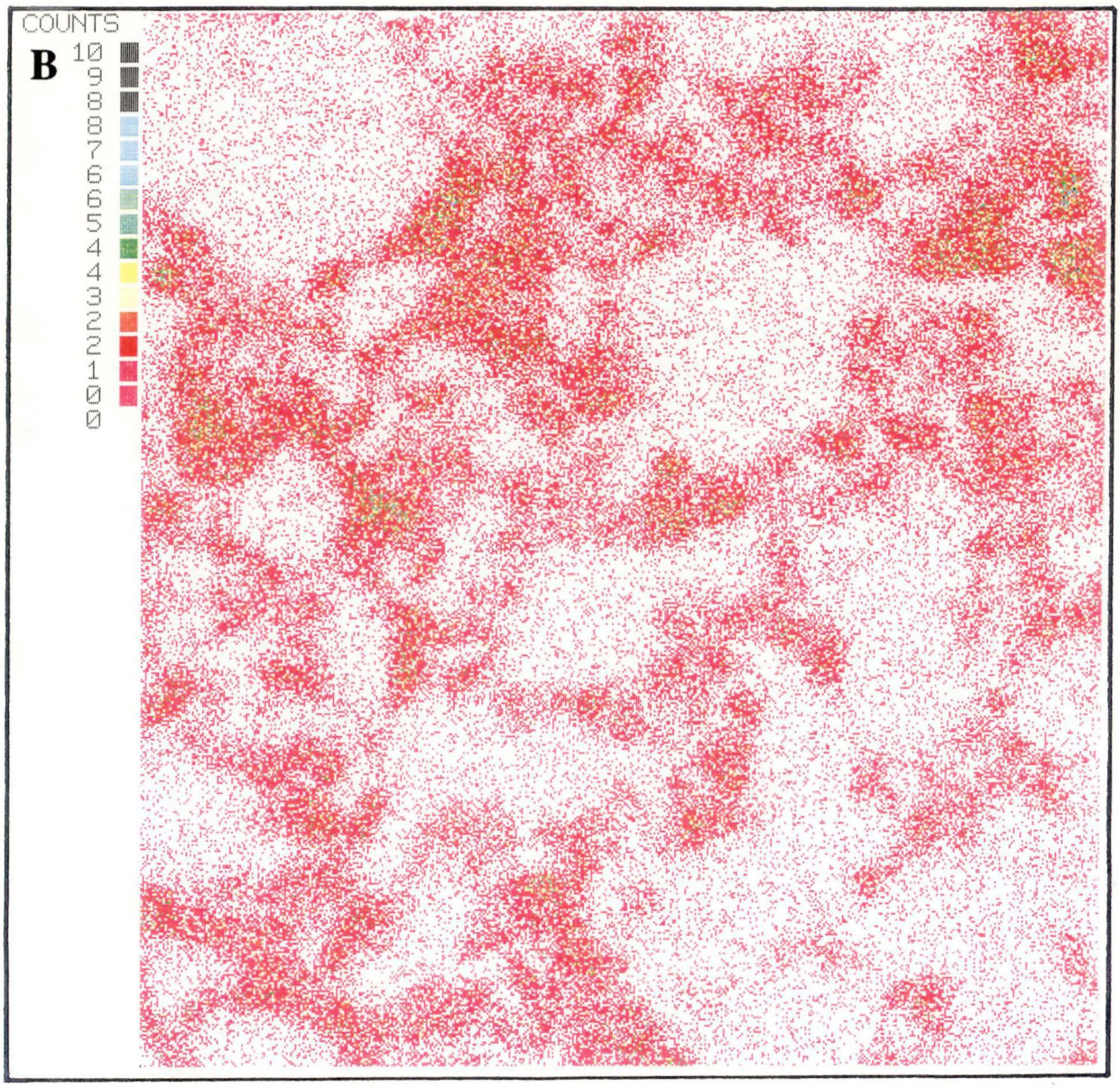

Figure 5.5.3b: X-ray map of potassium K_α peak of run T-3819 (GA1+10% calcite at 30 kbar and 900°C). The areas of low (background) K concentration are primary garnet and clinopyroxene grains, with most melt concentrated into a partially continuous intergranular network. Many of the melt pools have higher K concentrations in the centre compared with the rim, as in the previous map. The image was acquired under the same operating conditions as outlined in caption for figure 5.5.3a. Note, however, that colour scale for counts/second is slightly different to that in figure 5.5.3a.

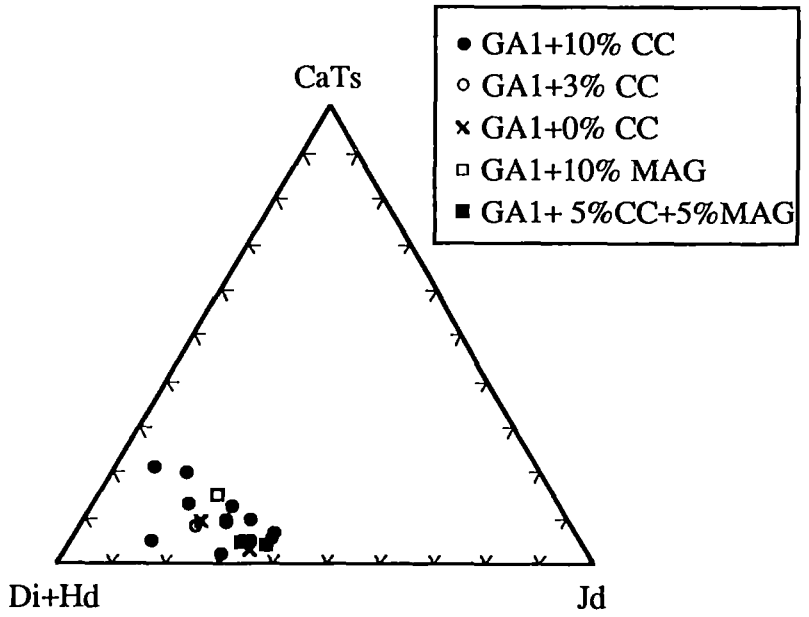

Figure 5.5.4: Clinopyroxene compositions in experimental runs plotted in jadeite (Jd)-Diopside+Hedenbergite (Di+Hd)-Ca-Tschermaks component (CaTs) compositional space.

Jadeite contents were calculated following the method of Mysen and Griffin (1973). These generally decrease with increasing temperature at constant pressure (figure 5.3.5b), with the exception of two 30 kbar runs (T-3805 and T-3811 at 700 and 850°C respectively). At T≥850°C, jadeite increases with increasing pressure. This relationship is disrupted at lower temperatures by the unexpectedly low jadeite content in clinopyroxene from run T-3805.

The Ca-Tschermak's component in clinopyroxene also increases systematically with increasing temperature (figure 5.3.5c). Variation with increasing pressure is somewhat non-systematic, although, at T≥850°C the higher pressure runs contain lower mol% Ca-Tschermak's component.

At constant PT conditions, increasing the amount of calcite in the run results in decreasing $100*Mg/(Mg+Fe^{2+})$ in coexisting clinopyroxene. This is demonstrated by three runs at 20 kbar and 850°C, with 0, 3 and 10wt% calcite (T-3734, T-3736 and T-3212 respectively), in which $100*Mg/(Mg+Fe^{2+})$ changes from 68.6 to 66.0 to 62.9. Two runs at 30 kbar and 900°C containing 0 and 10 wt% calcite (T-3782 and T-3780 respectively) exhibited similar behaviour, with $100*Mg/(Mg+Fe^{2+})$ varying from 77.90 to 76.39. Jadeite and Ca-Tschermak's contents do not appear to vary systematically with varying % calcite.

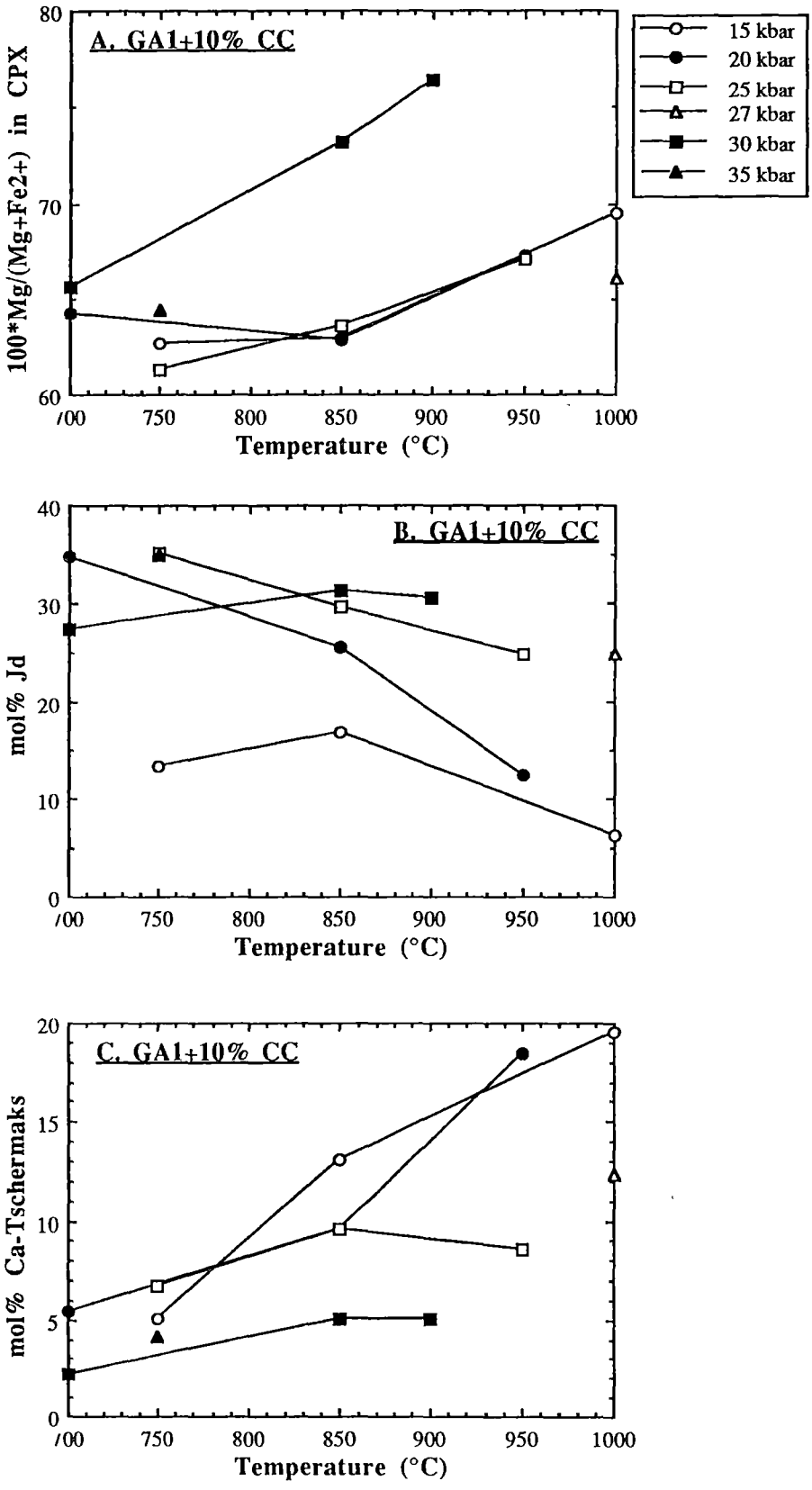

Figure 5.5.5: Variation in clinopyroxene compositions in GA1+10% calcite runs, with temperature and pressure. (a) is 100*Mg/(Mg+Fe^{2+}), (b) is jadeite and (c) is Ca-Tschermak's component. See text for further explanation.

Garnets range in grossular content from 22.00 to 44.02 mol% in runs containing 10% calcite (table E2). Pyrope in these runs varies from 18.11 to 49.56 mol%, with almandine varying from 28.44 to 51.07 mol% (figure 5.5.6). Spessartine and andradite components are small, and are not considered further. Representative garnet compositions are presented in table E2.

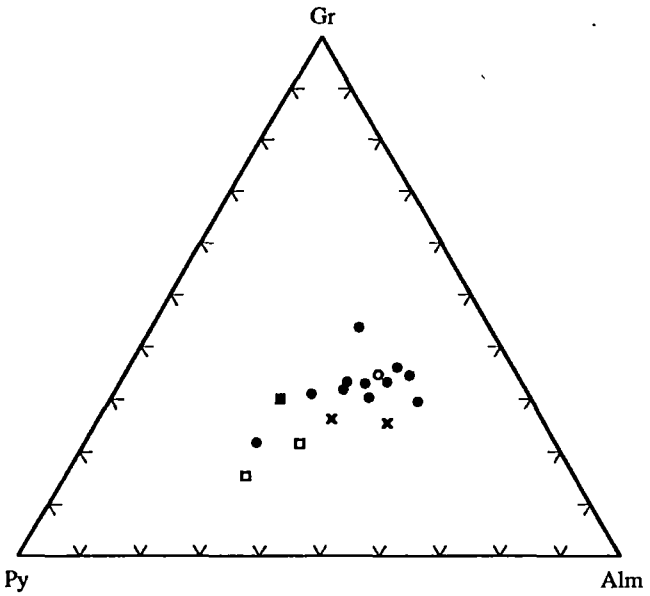

Figure 5.5.6: Garnet compositions from the experiments, plotted in grossular (Gr)-pyrope (Py)-almandine (Alm) space. Symbols as for figure 5.5.4.

Generally, pyrope increases, and almandine decreases with increasing run temperature at a given pressure (figure 5.5.7a and b). However, run T-3230 did not fit these patterns, having an unusally magnesian composition. This run was extremely fine-grained, and garnet was very rare, with the result that the composition listed in table E2 was based on a single microprobe analysis. This analysis may represent an overlap with amphibole or clinopyroxene, resulting in a more magnesian composition. Apart from this run, grossular contents were generally fairly constant with increasing temperature (figure 5.5.7). An exception to this is run T-3221, in which grossular is markedly higher (44.02 mol%) compared with other runs. Notably, this was the only garnet-bearing run at T>calcite-out. With increasing pressure, at low temperatures (750°C), grossular increased (compare T-3237 with T-3819). However, this trend reversed at 850 and 950°C, where it decreased with increasing pressure.

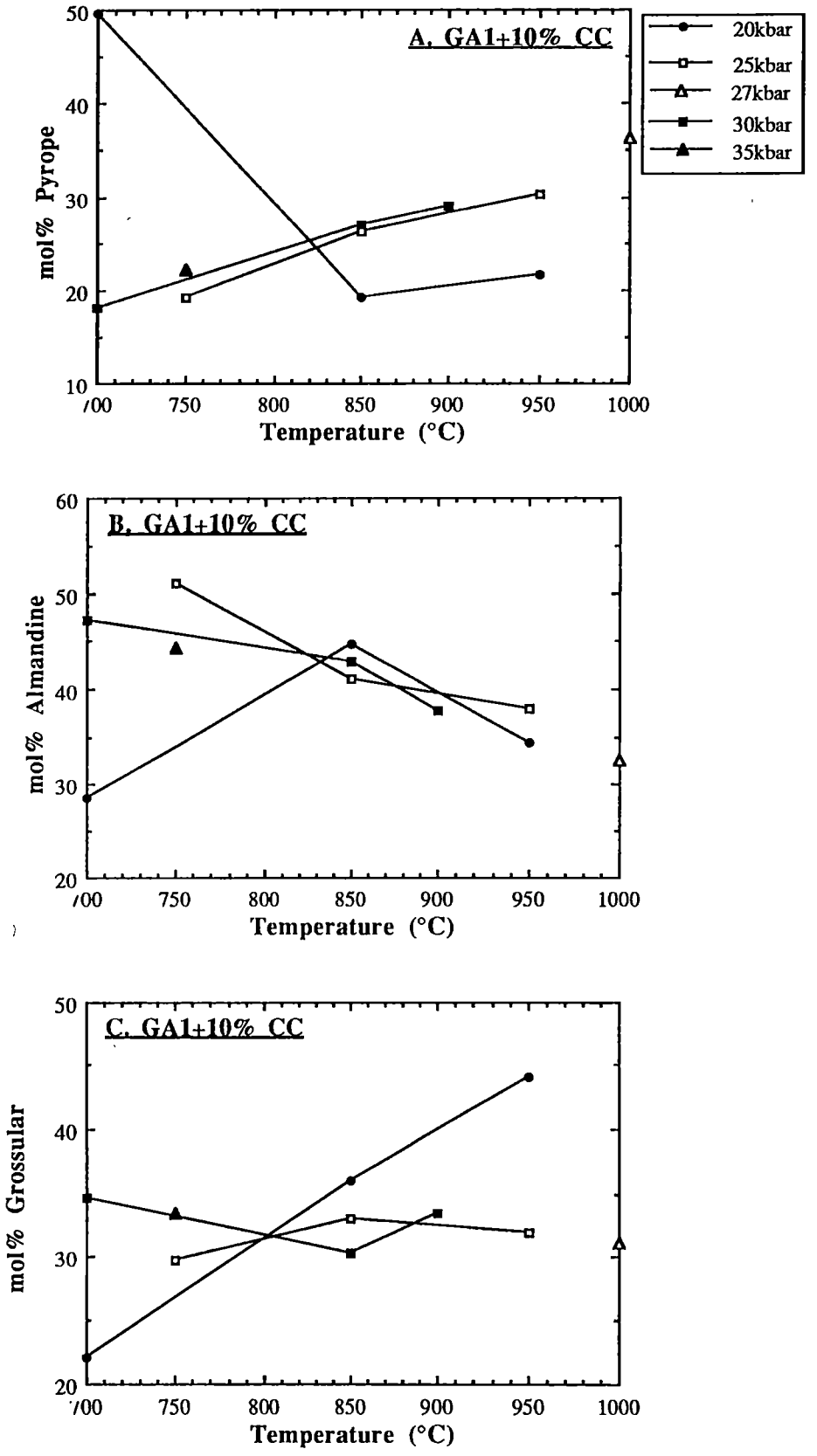

Figure 5.5.7: Variation in garnet compositions in GA1+10% calcite runs, with temperature and pressure. (a) is pyrope, (b) is almandine and (c) is grossular. See text for further explanation.

Garnet compositions also depended systematically on the % calcite added to the run. Increasing % calcite resulted in increasing grossular, and decreasing pyrope. This is evident in runs T-3734, T-3736 and T-3212, which were all run at 20 kbar and 850°C, with 0, 3 and 10 wt% calcite respectively. This pattern is also evident for runs T-3782 and T-3780, run at 30kbar and 900°C, with 0 and 10 wt% calcite respectively (figure 5.5.8).

Addition of magnesite to the runs resulted in more pyrope-rich, grossular-poor garnets than calcite-bearing runs at identical PT conditions. For example, runs T-3811 (10% calcite) and T-3818 (10% magnesite) were both run at 30 kbar and 850°C, and had garnet with compositions $Gr_{30.2}Py_{27.0}Alm_{42.8}$ and $Gr_{21.5}Py_{42.5}Alm_{36.0}$ respectively. Furthermore, T-3780 (10% calcite), T-3817 (5% calcite+5% magnesite) and T-3794 (10% magnesite) were all run at 30 kbar and 900°C, and contained garnet with systematically increasing pyrope and decreasing grossular. The compositions were $Gr_{33.4}Py_{29.0}Alm_{37.6}$, $Gr_{30.0}Py_{41.7}Alm_{28.4}$ and $Gr_{15.5}Py_{54.4}Alm_{30.1}$ respectively.

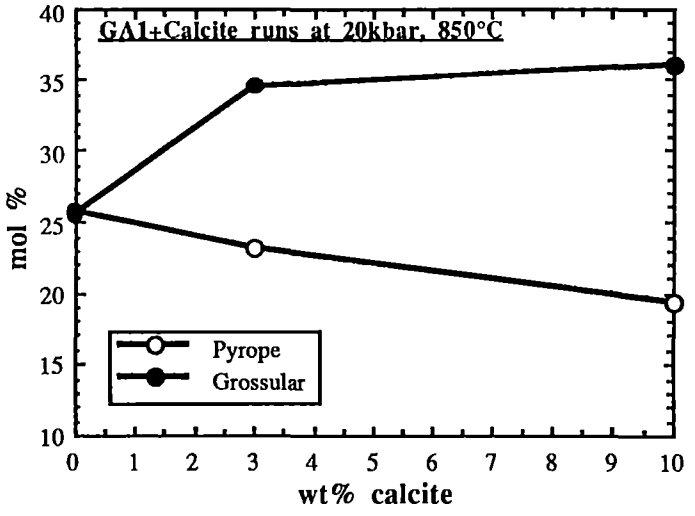

Figure 5.5.8: Plot of wt% calcite in run vs. mol % grossular and pyrope in co-existing garnet at 20kbar, 850°C, demonstrating that increasing the amount of calcite results in higher grossular, and lower pyrope at constant PT conditions. A similar relationship is observed in runs at 30kbar and 900°C, which contained 0 and 10 wt% calcite (T-3782 and T-3780 respectively).

Carbonate was found in all runs except T-3817, T-3812, T-3605 and T-3221. Representative compositions are presented in table E3. It occurred as irregularly shaped grains up to 10μm across. In runs at PT conditions close to the calcite-out curve, the carbonate composition was (Fe,Mg)-bearing calcite (table E3). In the four carbonate-bearing GA1+10% calcite runs closest to calcite-out, Ca/(Ca+Mg+Fe) decreased systematically with increasing pressure and temperature, varying from

0.979 at 15 kbar and 750°C (T-3821) down to 0.87 at 27 kbar and 1000°C (T-3551) (figure 5.5.9).

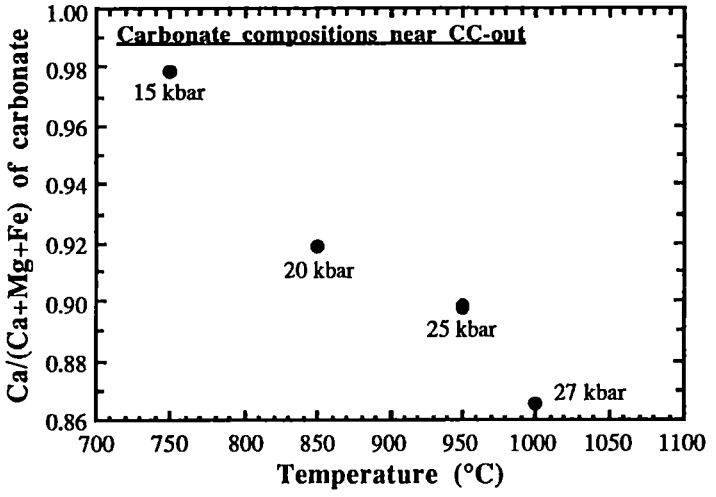

Figure 5.5.9: Temperature vs. Ca/(Ca+Mg+Fe) of carbonate in runs at PT conditions near CC-out (figure 5.5.1), demonstrating systematic decrease in Ca/(Ca+Mg+Fe) with increasing pressure and temperature.

However, at higher pressures and lower temperatures, Ca/(Ca+Mg+Fe) for residual calcite decreases. This is illustrated in the ternary diagram in figure 5.5.10, in which carbonate compositions are plotted in terms of the end-member components calcite, magnesite and siderite. Stability of Fe-bearing dolomite is favoured at low temperatures and higher pressures. For example, runs T-3819 (35 kbar, 750°C), T-3805 (30 kbar, 700°C) and T-3237 (25 kbar, 750°C) contain residual carbonate which is close to an Fe-bearing dolomite composition [Ca/(Mg+Fe) = 1.08, 1.43 and 1.13 respectively]. Changing conditions to lower pressures or higher temperatures rapidly stabilizes more calcitic carbonate.

The residual equilibrium carbonate compositions determined in this study are consistent with calcite-magnesite phase relations as determined by Irving and Wyllie (1975). From a series of isobaric phase diagrams on the $CaCO_3$-$MgCO_3$ join at pressures of 15, 25 and 30kbar [figures 6B and 7 of Irving and Wyllie (1975)], the boundary between aragonite+dolomite (at higher pressure) and aragonite+magnesian calcite (at lower pressure) can be constructed, and is included on figure 5.5.1. The three dolomite-bearing runs in the GA1+10% calcite system (T-3237, T-3819 and T-3805) plot on or above this boundary. The positive slope of the boundary is consistent with the observed stabilization of dolomite at high pressures and low temperatures. Below this boundary carbonate compositions are magnesian calcites. The solid solution observed between Ca and Mg-rich carbonate end-members in these

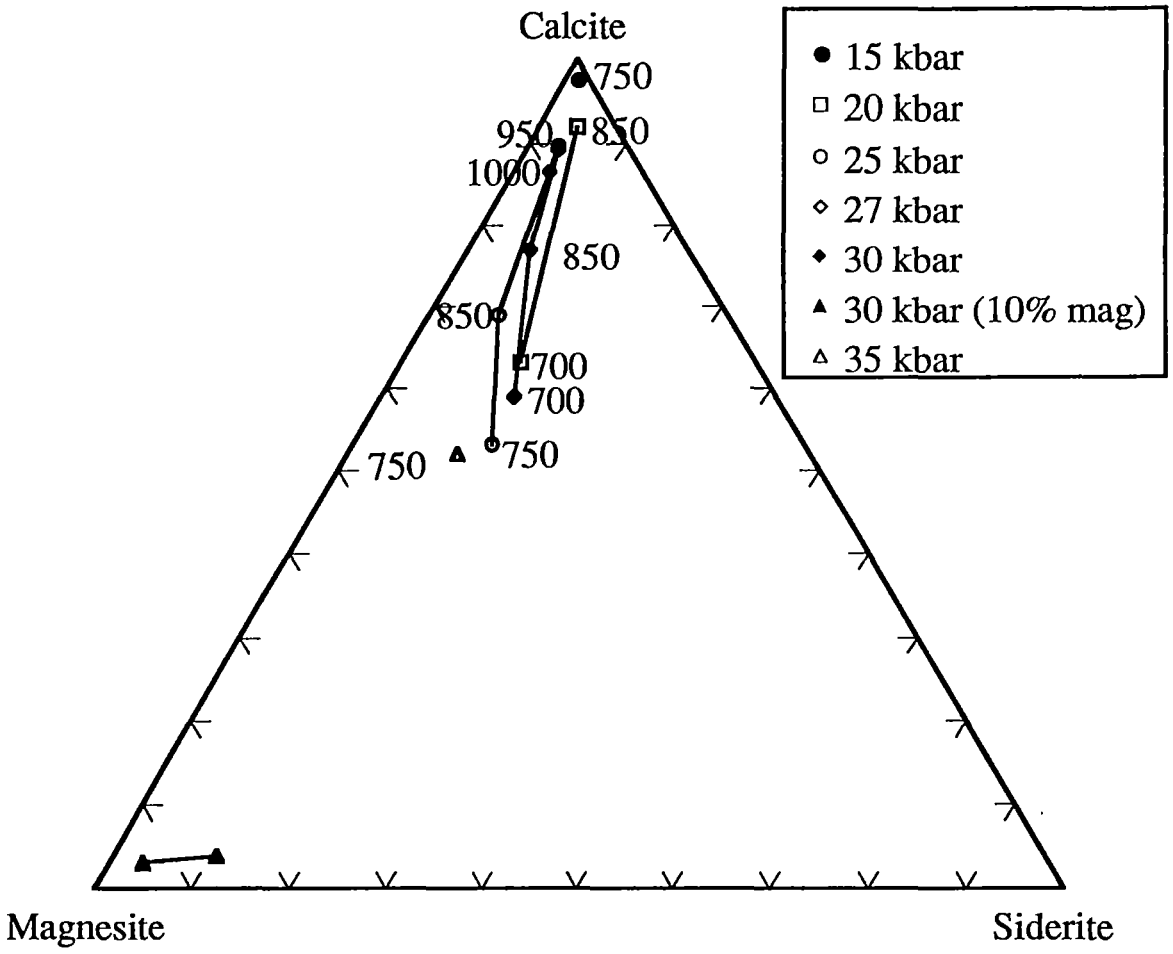

Figure 5.5.10: Ternary plot of Ca-Mg-Fe for carbonate compositions in the GA1+10% calcite or magnesite runs, indicating that dolomite is stabilized by low temperatures and high pressures. Tie-lines join isobaric runs. Numbers are run temperatures (°C).

experiments has extended calcite stability into the aragonite phase field for the pure $CaCO_3$ system. The phase transition between calcite and aragonite in the pure $CaCO_3$ system is also included on figure 5.5.1 and is sub-parallel to calcite-out. This means that the carbonates plotted in figure 5.5.9 are calcites rather than aragonites.

Amphiboles are calcic-amphiboles, and include edenite, magnesio-hornblende and ferroan pargasite, using the classification of Leake (1978). Mineral chemistry (table E4) appears to be controlled by the degree of partial melting present in the run, as well as the presence or absence of carbonate. For example, comparison of isobaric GA1+10% calcite runs (T-3230 with T-3212, and T-3812 with T-3605) reveals decreasing Na_2O and increasing $100*Mg/(Mg+Fe^{2+})$ with increasing temperature. With the addition of calcite to the run at identical PT conditions, amphibole compositions exhibit minor, but systematic increases in CaO, resulting in the variation

from magnesio-hornblende to edenite (compare T-3734, T-3736 and T-3212, all run at 20 kbar, 850°C with 0, 3 and 10 wt% $CaCO_3$ respectively).

5.6 Garnet-carbonate exchange reactions

Runs conducted at identical PT conditions with increasing amounts of calcite result in a systematic increase in grossular and decrease in pyrope components in co-existing garnet, as described above (figure 5.5.8). This, coupled with the tendency of residual carbonate compositions to vary from calcite to Fe-bearing dolomite with increasing pressure and decreasing temperature (figure 5.5.10), suggests that an exchange reaction between calcite and garnet is occurring

5.1 $Mg_3Al_2Si_3O_{12} + 6CaCO_3 = Ca_3Al_2Si_3O_{12} + 3CaMg(CO_3)_2$
pyrope calcite grossular dolomite

The pressure-temperature dependence of this equilibrium is illustrated by the variation of the partition coefficient

$$K_d = (Ca/Mg)_{ga}/(Ca/Mg)_{cbte}$$

(where ga=garnet and cbte=coexisting carbonate). K_d values for GA1+10% calcite runs are presented in table 5.3. In addition, they have been included on figure 5.5.1. High K_d values are favoured by low temperatures and high pressures. For example, in low pressure, high temperature runs close to the calcite-out curve (figure 5.5.1), K_d values are less than 0.13, but runs at 25-35 kbar and 700-750°C have K_d>0.8. This suggests that subduction of relatively cool, calcitic carbonate-bearing basaltic oceanic crust may result in conversion of the carbonate to dolomite at depths corresponding to pressures >25kbar.

Run T-3794 was run with 10% magnesite (pure $MgCO_3$) rather than calcite at 900°C and 30 kbar. The residual carbonate was magnesitic but contained significant CaO and FeO contents. The garnet co-existing with this magnesitic carbonate has a composition $Gr_{15.1}Py_{53.1}Alm_{31.8}$, and is clearly more pyrope-rich than in the equivalent calcite-bearing run (T-3780; $Gr_{33.4}Py_{29.0}Alm_{37.6}$), or the carbonate free run (T-3782; $Gr_{26.2}Py_{35.0}Alm_{38.8}$). In terms of Ca, Mg and Fe partitioning between coexisting garnet, clinopyroxene and carbonate, there is clearly compositional control in that for a given CO_3^{2-} content, a magnesian composition will have grossular-poor garnet coexisting with magnesite, and a Ca-rich composition will have grossular-rich garnet

coexisiting with calcite. Intermediate compositions would be expected to have dolomite, but the minimum melting composition in $CaCO_3$-$MgCO_3$ (Irving and Wyllie, 1975) may have eliminated dolomite in run T-3817, in the presence of H_2O.

Comparison of garnet and co-existing carbonate compositions between T-3794 and T-3818 (GA1+10% magnesite at 30kbar, 850°C) suggests that increasing temperature at constant pressure results in higher pyrope and lower grossular in garnet, and higher calcite and lower magnesite in carbonate. The reconnaissance data on pressure-temperature and bulk composition effects show that a further pressure-temperature dependent exchange reaction

5.2 $Mg_3Al_2Si_3O_{12} + 3CaMg(CO_3)_2 = Ca_3Al_2Si_3O_{12} + 6MgCO_3$
pyrope dolomite grossular magnesite

must also be considered in analyzing mineral stability and composition relationships.

Table 5.3: Variation of K_d with temperature in GA1+10% calcite runs.

P (kbar)	T (°C)	K_d
35	750	1.07
30	700	0.89
	850	0.24
	900	0.12
27	1000	0.12
25	750	0.94
	850	0.43
	950	0.08
20	700	0.17
	850	0.09

5.7 Dependence of equilibrium carbonate composition on bulk composition

Figure 5.7.1 illustrates some dependence of the equilibrium carbonate composition on bulk chemistry. Runs at 30 kbar and 900°C were conducted with no carbonate (T-3782), 10wt% calcite (T-3780), 5wt% calcite+5wt% magnesite (T-3817) and 10wt%

magnesite (T-3794). Figure 5.7.1 displays vectors which indicate the change in bulk composition of the runs with addition of the various carbonate components. Garnet + clinopyroxene ± carbonate compositions are also plotted, with coexisting phases joined by tie-lines. The three-phase field defined by T-3780 phases includes the GA1+10wt% calcite bulk composition. However, the GA1+10wt% magnesite bulk composition lies just outside the three-phase field defined by T-3794 garnet, clinopyroxene and magnesite compositions, consistent with the presence of a more Fe-rich melt phase. The tie-line joining clinopyroxene and garnet in the carbonate-free run (T-3782) should lie on the more magnesian side of the GA1 bulk composition if melt is the only additional Ca+Mg+Fe-bearing phase present. However, this is not the case, and may indicate the presence of another (undetected), low-Ca phase, such as phengite.

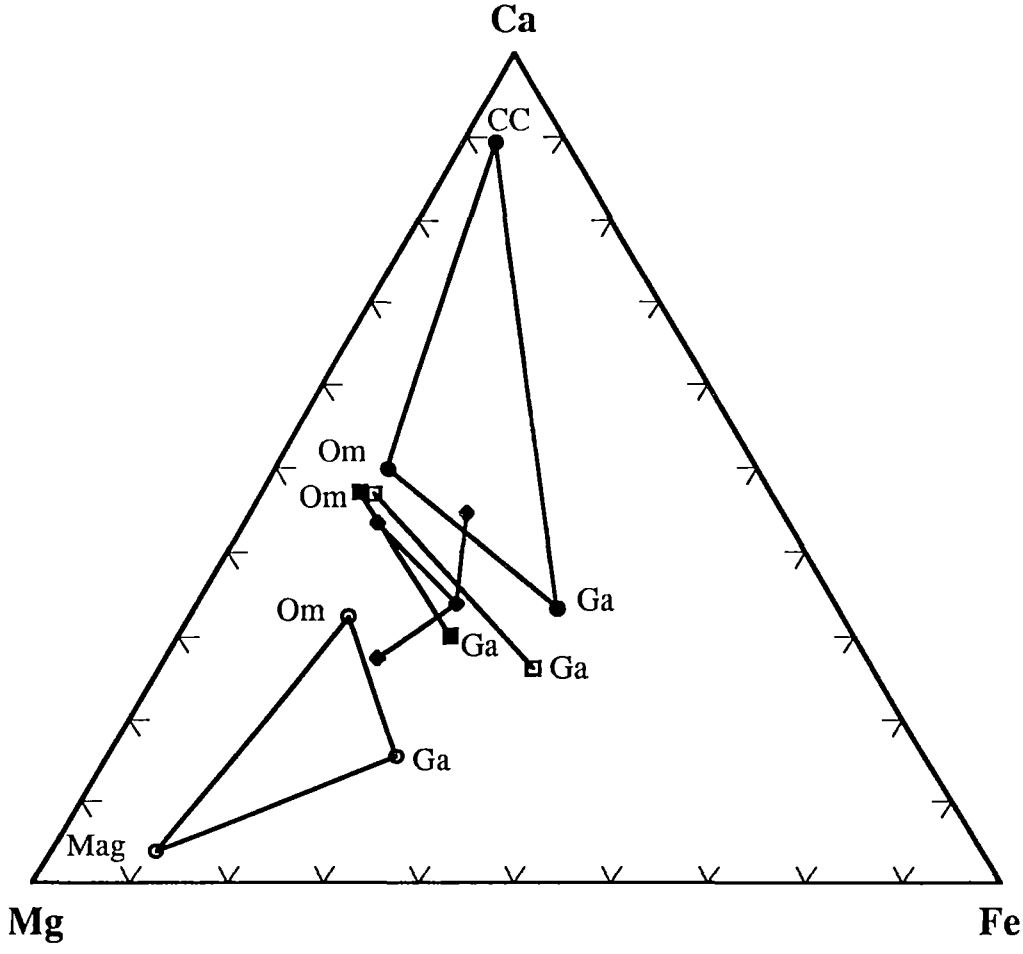

Figure 5.7.1: Ternary plot in Ca-Mg-Fe space of coexisting garnet (Ga), omphacitic clinopyroxene (Om) and carbonate (CC=calcite or Mag=magnesite) for runs conducted at 30kbar and 900°C. Filled circles are T-3780 (GA1+10% CC), open circles are T-3794 (GA1+10% Mag), open squares are T-3782 (GA1+0% CC), filled squares are T-3817 (GA1+5% CC + 5% Mag). Of the four diamonds, the middle one is GA1 bulk composition, the most calcic is GA1+10% CC, the most magnesian is GA1+10% Mag, and the diamond with the lowest Fe content in GA1+5% Mag +5% CC. See text for further explanation.

Substitution of calcite by magnesite in the runs shifts the equilibrium carbonate composition from Mg-bearing calcite in the former case, to Ca-bearing magnesite in the latter. In addition, garnet and clinopyroxene compositions are more magnesian in the magnesite-bearing run. Similar results are observed in runs containing either 10wt% calcite or magnesite at 30kbar and 850°C. Furthermore, in the 30kbar, 900°C runs the GA1+5% calcite+5% magnesite run contains clinopyroxene and garnet compositions which lie between those of the GA1+10% calcite and GA1+10% magnesite runs in Ca-Mg-Fe ternary space. This may indicate the existence of a compositional divide between phase fields for calcite and magnesite in Ca-Mg-Fe ternary space, with GA1 bulk composition lying close to, or on it.

It is therefore considered that higher pressure runs in the GA1+10wt% calcite system (for example, at P>>35kbars and temperatures close to the solidus) would not be likely to result in magnesite stability. A compositional shift towards more magnesian bulk-rock chemistry would be necessary.

5.8 Discussion

5.8.1 Evidence from natural rocks that carbonate can survive subduction

The results of the experimental study described above allow constraints to be placed on the behaviour of subducted carbonate. Numerous attempts have been made to model the thermal structure within subducting oceanic slabs, and have yielded rather model dependent results (eg; Oxburgh and Turcotte, 1970, 1976; Toksöz et al. 1971, 1973; Helfrich et al. 1989). Nevertheless, it appears that temperatures high enough to cause decarbonation of subducted calcitic carbonate are unlikely to be reached near the upper surface of the slab, which is likely to be the hottest part (figure 5.5.1). Thus, the residual nature of calcitic carbonate, to even quite high degrees of melting in the hydrous basalt+$CaCO_3$ system examined above, suggests that much subducted carbonate will survive without decarbonation or melting to a least 35 kbars, and almost certainly to much higher pressures.

Evidence exists from natural eclogites in crustal high pressure metamorphic terranes that supports the hypothesis that carbonate can survive transport to very high pressures in basaltic systems. Klapova (1990) has described a suite of eclogites from the Saxothuringicum metamorphic complex in the Czech Republic. Several of these samples, which achieved peak metamorphism at around 14 kbar and 650°C, contain primary carbonate, which displays petrographic and mineralogical evidence of the

occurrence of reaction 5.1 in a natural system. These samples are described in some detail in Chapter 6.

Furthermore, Wang et al. (1989; 1990; 1992) and Wang and Liou (1991) have described calcite+dolomite-bearing eclogites and other high-pressure metamorphic rocks from the Dabie Mountains in central China. The Dabie Mountains are a fault-bounded collisional terrane in central China. Regional metamorphism of this terrane is believed to have resulted from collision between the Sino-Korean and Yangtze Cratons during the Triassic. Continental thickening associated with this event resulted in high pressure regional metamorphism. The terrane contains gneisses, schists, marble, amphibolites and minor ultramafic blocks, as well as eclogite blocks and boudins. The eclogites contain quartz inclusions in garnet and omphacite. In some cases, the quartz inclusions are believed to be pseudomorphs after coesite, on the basis of radial fractures in the host mineral, around the inclusions (Wang et al. 1989; 1990; Okay et al. 1989). These are believed to have formed as a result of dilation of the inclusion during retrograde conversion of coesite to quartz, and indicate a minimum peak metamorphic pressure of 28 kbar (Bohlen and Boettcher, 1982) in the northern part of the complex. Calcite inclusions in garnet from a marble have also been observed. Radial cracking in the host mineral grain suggests that the calcite is a pseudomorph after aragonite. Calcite and minor dolomite with compositions $Ca_{0.95}Mg_{0.02}Fe_{0.02}Mn_{0.01}CO_3$ and $Ca_{0.47}Mg_{0.42}Fe_{0.11}CO_3$ respectively, have also been found as matrix minerals in coesite-bearing eclogites (Wang et al. 1992). These observations strongly support an ultra-high pressure origin for these carbonate-bearing rocks. In addition, quartz pseudomorphs after coesite have been discovered in garnet grains from marble, phengite schist and biotite gneisses which host the eclogitic boudins and blocks in this complex, suggesting cogenetic metamorphism of the discrete eclogites bodies and their host country rock, rather than solid-state tectonic introduction of previously metamorphosed high-pressure eclogites into lower grade country rocks.

5.8.2 The ultimate fate of subducted carbonate

The ultimate fate of carbonate which survives subduction to P>35kbar, may, in part, depend on redox processes in the deeper upper mantle. At present, broad consensus concerning the oxidation state of the mantle has yet to be reached. However, application of recent calibrations of the spinel-olivine Fe/Mg exchange oygen geobarometer (Ballhaus et al. 1990; 1991) suggest that significant large scale variations in mantle fO_2 do exist, and may be correlated with particular tectonic settings. For example, spinels in arc-related magmas and their cumulates yield fO_2

values between 1 and 3 log units above FMQ (Ballhaus et al. 1990). This contrasts with MORB and related abyssal peridotites, which indicate more reduced conditions (FMQ-1 log unit to FMQ+2 log units). However, fO_2 barometer calibrations have thus far only been relevant to the spinel stability field, meaning that understanding of oxygen fugacity levels in the deeper garnet stability field is limited (future oxygen barometers may be developed which depend on Fe^{2+}/Fe^{3+} values in garnet; Harley and Odling, 1991). For these reasons, it is appropriate to consider the behaviour of subducted carbonate under both oxidising and reducing conditions. For example, if mantle fO_2 were ≈IW+1 or 2 log units, then dolomitic carbonate could reduce to graphite (or diamond at higher pressures) co-existing with a water rich fluid (Taylor, 1985; 1986; Green et al. 1987). At lower fO_2's (≈IW) a CH_4>H_2O fluid would be produced.

Garnet-hosted microdiamonds have been reported in at least two crustal, ultra-high pressure metamorphic terranes (Kokchetav terrane in northern Kazakhstan, Sobolev and Shatsky, 1990; Tien-Shan in China, Tagiri and Bakirov, 1990). However, formation of these diamonds was attributed to deposition as methane-rich fluids underwent oxidation at P≥40 kbar and T>900-1000°C. On the other hand, production of diamond by reduction of subducted carbonate in at least some cases is supported by the recent discovery of carbonate infra-red absorption in an eclogitic diamond from the Roberts Victor kimberlite in South Africa (WR Taylor, pers. comm.). This particular diamond sample is believed to have grown at 50 kbar and 1000-1100°C (based on the degree of nitrogen aggregation in the diamond). The calcitic compostion is consistent with that of the equilibrium carbonate composition in the higher temperature experiments reported here (eg; T-3780, T-3551). Influx of a methane-rich fluid, or a low fO_2 melt, into a more oxidized, carbonate-bearing eclogite body, may have resulted in partial reduction of calcitic carbonate to diamond.

Alternatively, it may be possible that an internal redox process (fluid absent?) could occur, in which carbonate could oxidise Fe^{2+} in co-existing garnet, resulting in lower almandine, and increased andradite components in the garnet, and co-existing graphite or diamond. However the broad range of carbon isotopic compositions exhibited by diamonds of the eclogite paragenesis ($\partial^{13}C$ from +5 to -34.4; Sobolev et al. 1979) indicates the involvement of a variety of isotopically different fluids or melts in diamond formation. In addition, high andradite contents are unknown in mantle-derived garnets.

In the oxidised scenario, carbonate may convert to dolomite or magnesite by exchange between grossular and pyrope contents of eclogitic garnet as it was subducted to greater depths. Ringwood (1991) has proposed a model for subduction whereby the mafic component of the subducted slab accumulates at the 650km discontinuity, eventually forming a laterally extensive garnetite layer. This layer may also incorporate stable carbonate if fO_2 is sufficiently elevated. Partial melting of the garnetite layer would be likely at ambient temperatures (≈1600°C), resulting in metasomatism and refertilization of the overlying peridotite layer, which originally derived from subducted, depleted sub-oceanic lithosphere. In this way, originally subducted carbonate could be transfered from the garnetite layer into the peridotite layer. This enriched, carbonated peridotite layer may then act as source material for intraplate basaltic volcanics and kimberlites, both of which are associated with significant CO_2-rich volatile activity. Mantle convection below the garnetite layer, which acts as a thermal barrier, could trigger ascent of carbonated plumes or diapirs from the enriched peridotite layer immediately overlying the garnetite. The entrained carbonate could then be involved in shallower metasomatic events (such as those described in previous chapters) or in petrogenesis of undersaturated silicate melts (eg; olivine melilitites; Brey and Green, 1976), kimberlites, carbonatites etc.

5.9 Conclusions

(1) Calcite is a low temperature alteration mineral which is very commonly reported in vugs and veins in ocean floor basalts. Subduction of this carbonate has the potential to contribute to the Earth's carbon cycle.

(2) The phase relations for a hydrous basalt + calcite system are determined from 15-35 kbar, 700-1000°C, and indicate that (a) at low pressures and high temperatures (eg; T≥850°C at 15 kbar) calcite decarbonates, and (b) at higher pressures carbonate is stable as a residual phase in the presence of significant degrees of partial melting yielding a high SiO_2 melt phase. This suggests that much subducted carbonate can survive subduction to depths corresponding to pressures of at least 35 kbar.

(3) With increasing pressure at low temperature (T≤750°C) calcite undergoes an exchange reaction with coexisting garnet (pyrope + calcite = grossular + dolomite), resulting in dolomite being stable in equilibrium with grossular-rich garnet at P≥25 kbar. However, increasing temperature rapidly stabilizes calcitic carbonate, even at high pressures. Addition of magnesite to the basalt composition, rather than calcite,

stabilizes Ca-magnesite at 30 kbar and 900°C. This is attributed to the reaction pyrope + dolomite = grossular + magnesite.

(4) The ultimate fate of subducted carbonate may depend on redox conditions in the deeper upper mantle. Influx of low fO_2 fluids or melts into carbonate-bearing eclogite bodies may initiate reduction of carbonate to graphite or diamond. Alternatively, if fO_2 remains sufficiently high, subducted carbonate may be entrained within the garnetite layer (formerly subducted oceanic crust) at the 650km discontinuity, where it may ultimately be incorporated into the source regions of kimberlites, and intraplate volcanics.

CHAPTER 6

CARBONATE-BEARING ECLOGITES FROM THE SAXOTHURINGICUM, CZECH REPUBLIC - NATURAL EVIDENCE FOR CARBONATE STABILITY UNDER ECLOGITE FACIES CONDITIONS

6.1 Introduction

The eclogites of the Czech part of the Krusné hory Mountains (the Erzgebirge) constitute part of the Saxothuringicum unit of the Central European Variscan Orogenic Belt. The Erzgebirge crystalline complex has been generally metamorphosed under amphibolite facies conditions. However, the eclogites bodies represent high pressure units which were either (1) tectonically emplaced to higher crustal levels, being formerly derived from subducted oceanic crust (Behr et al. 1965; Frischbutter, 1990), or (2) are coherent members of the country rock, which were metamorphosed syntectonically with the country rock (Krentz, 1982; Krentz et al. 1990), but have not suffered retrogression to amphibolite.

Klapova (1990) described eclogites from this region in detail, including several samples which contain carbonate, which, on textural grounds, constitutes part of the primary eclogitic assemblage. The purpose of this chapter is to demonstrate that the textures and mineral chemical variation exhibited by these primary carbonate-bearing eclogites constitute a record of prograde and/or retrograde metamorphic histories for these rocks. The previous chapter provides experimental information which may be used in interpretation of the mineral reactions observed. Conversely, the natural rock data are useful in designing a continuation of the reconnaissance experimental study.

6.2 General Petrography of Krusné hory eclogites

Klapova (1985a, 1985b, 1990) recognised the successive crystallization of three assemblages in the eclogites of the Krusné hory Mountains, denoted as the pre-eclogite, eclogite and post-eclogite stages.

Pre-eclogitic phases are predominantly preserved as randomly arranged, frequently euhedral, minute inclusions in garnet. Mineral phases present include rutile, sulfide minerals, quartz, amphibole I, white mica, clinozoisite and zoisite. Carbonate occurs as inclusions in garnet in sample C960 (see below). In many cases, the inclusions in

garnet are confined to the core regions, with an idioblastic inclusion-free rim, suggesting two stages of garnet growth. The first stage probably involved rapid syntectonic growth of the cores, trapping pre-eclogitic phases as inclusions, and was followed by slower post-tectonic growth of the rims. Garnets usually show prograde chemical zoning, ie; increasing Mg/Fe from core to rim (Raheim and Green, 1974; Ellis and Green, 1979).

The eclogite stage of the development of these samples is characterized by assemblages including the following phases; omphacitic clinopyroxene, garnet, quartz, rutile, kyanite, and occasionally paragonite. In addition, amphibole II, zoisite and phengite crystallized subsequent to attainment of peak, metamorphic conditions. Application of garnet-clinopyroxene geothermometry, and geobarometry based on jadeite content in omphacite (Droop, 1983; Holland, 1980; Wells, 1979; Ellis and Green, 1979; Ganguly, 1979) by Klapova (1990), established minimum pressure and temperature estimates for peak equilibration conditions of 650±40°C and 13-15±1 kbars for the Krusné hory eclogites.

The post-eclogite assemblage represents retrograde replacement or partial replacement of eclogite phases. This has resulted in a spectrum of samples which display all degrees of retrogression from completely unaltered, to completely amphibolitized examples. Retrograde effects typically involve development of symplectites (clinopyroxene + plagioclase or amphibole + plagioclase) on the margins of omphacite grains, and development of kelyphitic rims on garnet. In some case replacement of garnet is complete. The detailed mineralogy of the post-eclogite stage has been described by Klapova (1988). The textures and compositional relationships among the carbonates will be interpreted within this broad framework of prograde, peak and retrograde reactions.

6.3 Descriptions of carbonate in eclogite samples

The carbonate-bearing eclogites which comprise the focus of this chapter include samples H323, K670, C960, H321, H324, and D521 (table 6.1). Of these, C960, K670 and H321 were described by Klapova (1990). The remainder have not previously been reported. Below is a brief description of the petrography of each sample, emphasizing the textural settings and compositions of the carbonate phases present. In the following descriptions, numbers prefixed by the letter "C" refer to particular carbonate grains or clusters of grains, and spatially associated phases on the thin section of the sample in question. Representative microprobe analyses of the

individual grains can therefore be identified with reference to these numbers in the data tables in Appendix F.

Table 6.1: Samples numbers relevant to this chapter. Catalogue numbers refer to collection at the Geology Department, University of Tasmania.

Field Number	Catalogue Number
H323	78137
K670	78138
C960	78139
H321	78140
H324	78141
D521	78142

6.3.1 Sample H323

This sample contains abundant small euhedral garnet grains, the cores of which are cloudy with very fine-grained inclusions. Patches of fine-grained quartz, abundant white mica, omphacitic clinopyroxene, and minor rutile and amphibole are also present.

Carbonate occurs in a number of textural settings and mineral associations. For example, inclusions of carbonate in omphacite (figure 6.3.1) invariably contain a volumetrically dominant core of magnesite, surrounded by a thin rim of dolomite in contact with the surrounding clinopyroxene (C3). Typical analyses are presented in table F1. In patch C3, magnesite core contains 0.29wt% CaO, and has an 100*Mg/(Mg+ΣFe) of 85. The surrounding dolomite has 100*Mg/(Mg+ΣFe) of 83.8.

Calcite is also present in the sample, in patch C4. In this case, an omphacite grain includes an irregularly shaped piece of calcite [100*Mg/(Mg+ΣFe) = 57.5], which is partially rimmed by dolomite [100*Mg/(Mg+ΣFe) = 86.59]. On the basis of Fe/Mg partitioning between the pyroxenes and carbonates observed in these rocks and in the experimental studies (Chapter 5), it is inferred that the included calcite is relict from a pre-eclogitic assemblage.

Similarly, in patch C1, a calcite core with 100*Mg/(Mg+ΣFe) = 26.6 is considered to be relict with a prograde zoning to 100*Mg/(Mg+ΣFe) = 78.7 in contact with magnesite with 100*Mg/(Mg+ΣFe) = 85.2. This magnesite has a dolomite

[100*Mg/(Mg+ΣFe) = 83.1] rim against silicate phases. There is some variation in 100*Mg/(Mg+ΣFe) between magnesite in different patches (81.5 to 85.2), providing further evidence for incomplete equilibration of prograde assemblages on hand specimen or thin section scale.

6.3.2 Sample K670

This is a garnet + clinopyroxene + phengite + quartz assemblage, with spectacular evidence of post-eclogite deformation. Garnet cores are rich in inclusions of pre-eclogite facies phases. Carbonate occurs typically as cores of Fe-bearing magnesite surrounded by rims of Fe-dolomite, in contact with euhedral garnet grains (figure 6.3.2). 100Mg/(Mg+ΣFe) varies from 80.5 to 83.3 in magnesite, and 84.7 to 86.6 in dolomite. Magnesite contains up to 0.51 wt% CaO. The variation in associated garnet compositions are described below.

6.3.3 Sample C960

This sample was described in detail by Klapova (1991) as an assemblage consisting of 43% omphacite, 27% garnet, 20% zoisite, 4% amphibole, 3% mica and traces of rutile and carbonate. Garnets are euhedral, and contain cores filled with angular inclusions of quartz, amphibole, clinopyroxene and rarely zoisite or carbonate. Clear, inclusion-free rims on the garnet typically constitute <25% of the width of the grain. Some garnet grains have inclusion free cores, surrounded by a zone of inclusions, which is in turn surrounded by a clear rim. Zoisite also occurs as large acicular grains with predominantly quartz inclusions, which follow the fabric defined by matrix quartz and other phases. Mica is patchily distributed as irregularly shaped to tabular grains. The matrix is defined by quartz, which defines a foliation wrapping around garnets. Large omphacitic clinopyroxene and amphibole grains, and minor rutile are also present.

Carbonate occurs in three textural settings. Calcitic veins cross-cut the fabric of the sample, occasionally traversing garnet grains. Close to these veins, calcite also occurs in disseminated patches in the groundmass. Calcite also occurs as discrete inclusions within garnet grains, or occasionally as discrete grains adjacent to garnet. No petrographically distinct rims were found on these calcite inclusions or grains, although the calcite compositions are variable. For example, vein calcite typically has 100*Mg/(Mg+ΣFe) from 47 to 74. MnO content ranges from 0.06 to 0.19 wt%, and FeO is consistently around 0.4 wt%. Patchy calcite, however, contains 0.31 to 0.55 wt% MnO, 0.95 to 1.21 wt% FeO, and has a range in 100*Mg/(Mg+ΣFe) of 34 to 42. A traverse across a calcite inclusion in garnet reveals a variation in MgO of 1.58 wt% on the rim, to 9.62 wt% in the core. MnO varies from 0.23 to 0.0 wt%

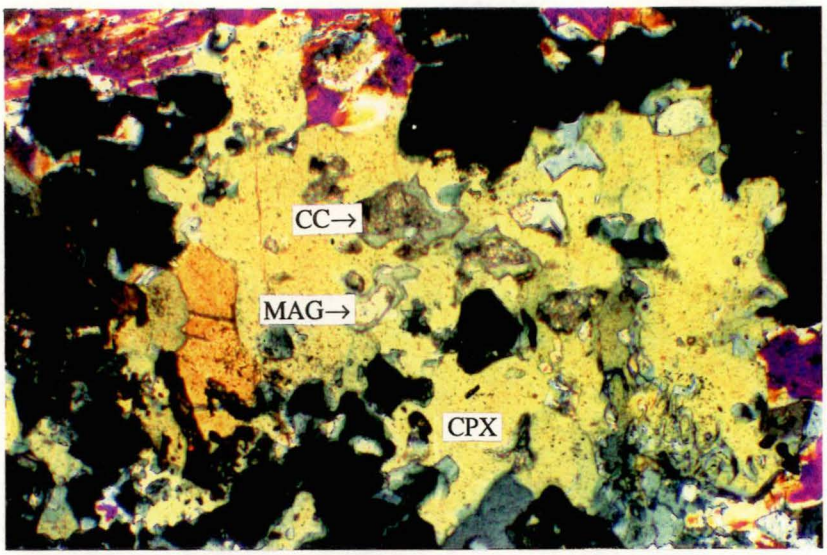

Figure 6.3.1: Photomicrograph of sample H323 at 50x magnification under crossed nicols, showing carbonate patches included in large, irregularly shaped omphacite grain (CPX). The carbonate patches contain a core of calcite±magnesite (CC, MAG) partially or completely surrounded by a thin rim of dolomite in contact with the clinopyroxene.

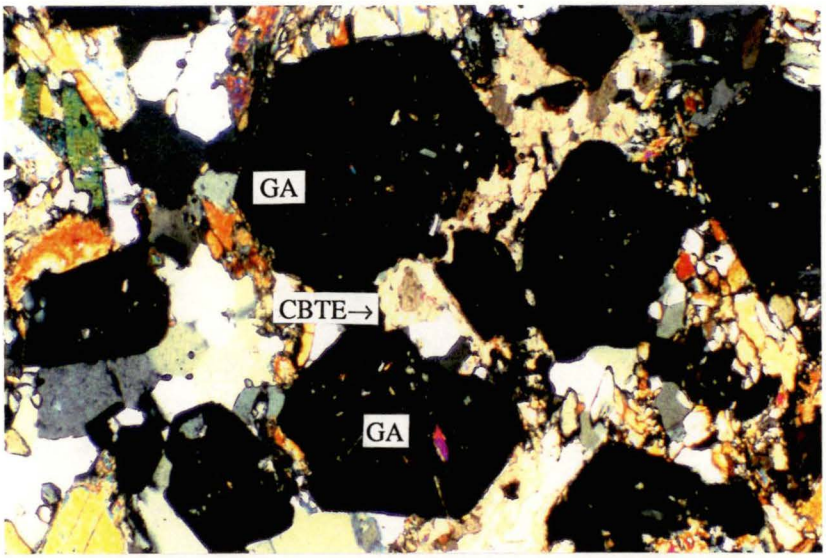

Figure 6.3.2: Photomicrograph of sample K670 at 50x magnification under crossed nicols. A patch of carbonate (CBTE; centre) lies between three isotropic euhedral garnet (GA) grains. The carbonate assemblage contains a core of magnesite (brown) surrounded by lighter rim of dolomite.

rim to core. 100*Mg/(Mg+ΣFe) of calcite in inclusions was typically in the range 79.7 to 83.0.

Use of textural relationships and Fe/Mg partitioning leads to the conclusion that calcite veinlets [100*Mg/(Mg+ΣFe) = 47 to 74] and patches [100*Mg/(Mg+ΣFe) = 34 to 42] are not in equilibrium with garnet or omphacite. However, calcite inclusions in garnet have 100*Mg/(Mg+ΣFe) = 79.7 to 83.0 and are inferred to have equilibrated with garnet on a prograde path, and partially readjusted on a retrograde path. This aspect is considered again in the discussion of garnet compositions. It is noted that C960 does not contain detectable magnesite or dolomite.

6.3.4 Sample H321

H321 contains 40% omphacitic clinopyroxene, 15% garnet, 30% amphibole, 8% carbonate and minor rutile, quartz and mica (Klapova, 1990). Carbonate is typically associated with garnet, and usually consists of relict calcite cores which have been nearly completely replaced by magnesite (figure 6.3.3a-c). This entire calcite+magnesite assemblage is in turn surrounded by thin dolomite rims. 100*Mg/(Mg+ΣFe) is typically 81.6 to 83.6 for magnesite, and 81.7 to 84.9 for dolomite. Calcite has 100*Mg/(Mg+ΣFe) of 67.5 to 76.3. CaO content in magnesite varies from 0.39 to 3.28 wt%.

In this sample also, the low 100*Mg/(Mg+ΣFe) of calcite, its increase towards magnesite and dolomite, and the textural relationships suggest that calcite is a relict, pre-eclogitic phase, but in this bulk composition the high pressure assemblage is garnet+magnesite, instead of garnet+calcite for the included carbonate of C960.

6.3.5 Sample H324

This is a zoisite eclogite, which contains abundant idiomorphic garnet grains, some of which some of which display evidence of minor breakdown on the rims, abundant annealed quartz, and large areas which have undergone secondary alteration to post-eclogitic amphibole+plagioclase. Tabular grains of zoisite and mica are also present, as well as irregularly shaped amphibole and clinopyroxene grains. Minor rutile, pyrite, apatite and perovskite were also detected.

Carbonate occurs as calcite inclusions within quartz, which appear to have no reaction relationship with the host. In this setting, the calcite is virtually pure $CaCO_3$, and probably constitutes part of the pre-metamorphic assemblage. In addition, calcite+dolomite inclusions are present within and adjacent to amphibole grains. In

Figure 6.3.3: A, B and C are photomicrographs of sample H321, showing carbonate patches, usually associated with small euhedral isotropic garnet grains. In (A) (magnification 50x), a large core of magnesite (MAG) is completely surrounded by a thin dolomite rim (DOL). In (B) (100x magnification) relict calcite (CC) is almost completely replaced by magnesite, which is in turn surrounded by a thin rim of dolomite. In (C) (magnification 50x), calcite is again partially replaced by magnesite, with the entire assemblage being rimmed by dolomite.

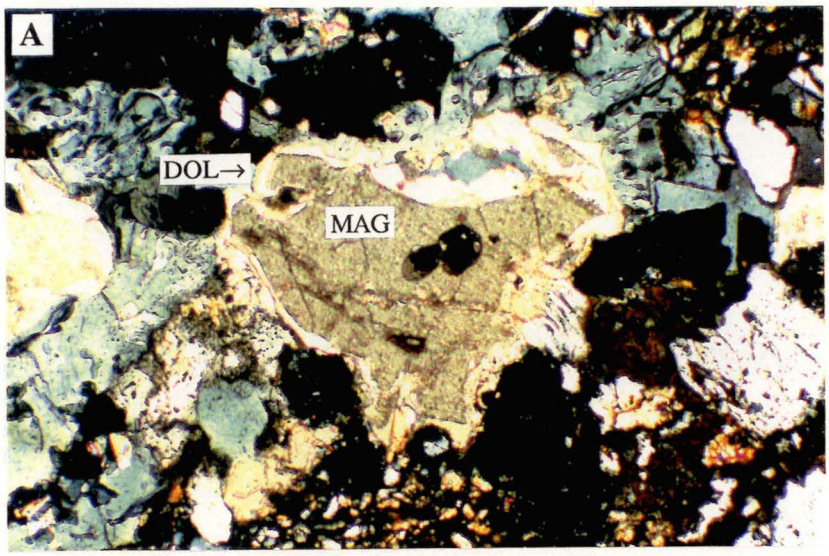
A
DOL→
MAG

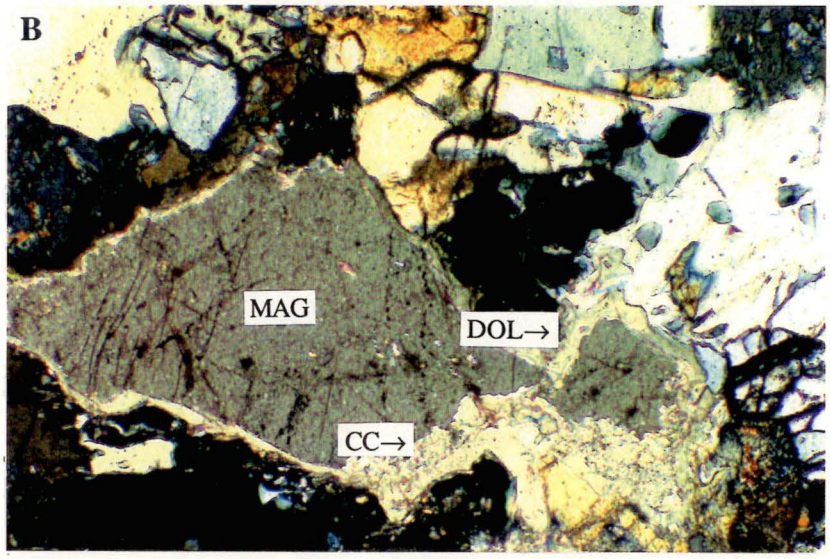
B
MAG
DOL→
CC→

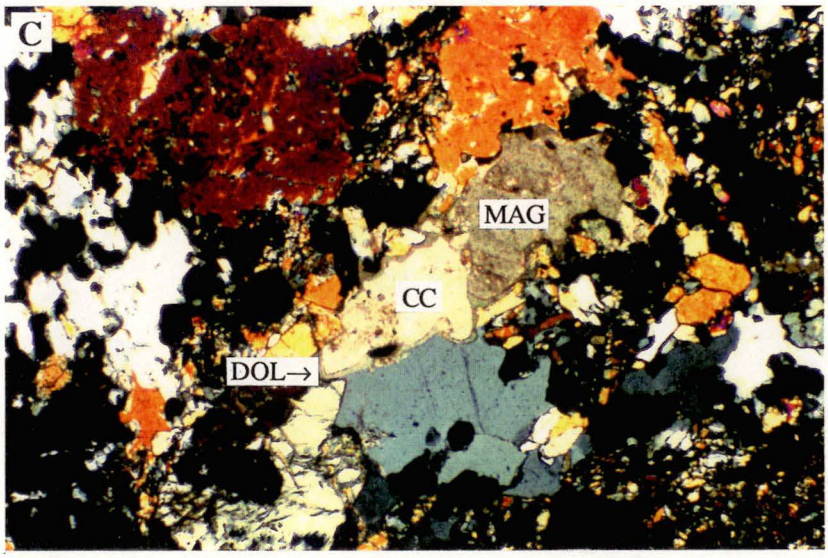
C
MAG
CC
DOL→

many of these patches magnesian calcite has formed thin, poorly developed rims on dolomite. Calcite in this situation has 100*Mg/(Mg+∑Fe) from 69.5 to 82.5. The dolomite cores have 100*Mg/(Mg+∑Fe) from 84.2 to 88.6.

6.3.6 Sample D521

This sample is another zoisite eclogite, most of which consists of very fine grained matrix of albite + amphibole. Large garnets (3-4 mm) with inclusion-rich cores are breaking down, producing kelyphytic rims of omphacite and opaque minerals. Zoisite, white mica and omphacitic clinopyroxene grains, and occasional patches of relict, fine-grained annealed quartz are also present.

Carbonate is abundant, and is frequently associated with garnet. Usually two carbonate phases are present; dolomite forms cores with rims of calcite. In some cases, the textural relationships are more complex, although the two phases are always present together. Similar carbonate patches are found associated with zoisite and amphibole. 100*Mg/(Mg+∑Fe) for the calcite rims is typically around 82.45, and 84.2 for the dolomitic cores.

The contrast in 100*Mg/(Mg+∑Fe) between calcite formed as thin rims on dolomite and with 100*Mg/(Mg+∑Fe) > 80, and the variable patches of calcite interpreted as pre-eclogitic phases, is very marked. The rims of calcite on dolomite, and of dolomite on magnesite are interpreted as similar retrograde effects on differing bulk compositions.

6.4 Evidence for prograde and retrograde garnet+carbonate reactions

6.4.1 Introduction

The basalt+carbonate experiments described in Chapter 5 indicate the existence of a series of exchange reactions between garnet components and carbonate. In the GA1+calcite system, increasing pressure at constant temperature favoured the reaction pyrope + calcite = grossular + dolomite. In addition, there is a bulk compositional effect such that magnesian compositions have magnesite+pyrope-rich garnet. It is also inferred that increasing pressure in more magnesian compositions will replace pyrope+dolomite with magnesite+grossular. These reactions are analogous to the reaction enstatite + dolomite = diopside + magnesite in lherzolite systems (Brey et al. 1983). It is believed that the carbonate textures displayed by the eclogites described in this Chapter represent preserved evidence for the occurrence of

these reactions during complex metamorphic histories involving prograde and retrograde variations in pressure and temperature.

The reconnaissance experimental study, and the observations on corona/reaction textures in the rocks allow construction of a model to explain compositional zoning, textures and phase assemblages in terms of a particular metamorphic PT trajectory. The chemical and textural relations among carbonates, pyroxenes and garnet may be schematically represented as in figure 6.4.1, noting that the solid solution limits for all phases are strongly temperature and pressure dependent, and that Fe/Mg partitioning is such that garnet is enriched in Fe, particularly at lower temperatures.

At a given PT (say 750°C, 30 kbar), a range of bulk compositions from calcite-bearing skarns (eclogite facies) to magnesite-bearing garnet lherzolites may occur with basaltic compositions being represented by dolomite-bearing eclogites (Ca-rich compositions) or magnesite-bearing eclogites and enstatite-eclogites (figure 6.4.2). The schematic figure 6.4.2 is drawn for pressures above the enstatite + dolomite = diopside + magnesite reaction (Brey et al. 1983). At lower pressures, the three phase fields will alter such that a dolomite eclogite, with grossular-rich garnet, representing composition A (figure 6.4.3) will be replaced by calcite-bearing eclogite/granulite, with garnet of lower grossular content. Similarly, a less calcic bulk composition B (figure 6.4.3), represented by magnesite-bearing eclogite at high pressure, will be replaced by dolomite-bearing eclogite/granulite, also with lower grossular content in garnet.

In the following sections, the carbonates with reaction rims and compositional zoning of garnet will be interpreted within this conceptual framework.

6.4.2 Garnet zoning and carbonate reaction rims

In attempting to interpret the compositions and textures of the rocks, is it inferred that Fe-rich calcite cores in carbonate patches are relict, but may approach equilibrium with (non-rim) compositions of neighbouring garnet if they show increasing $100*Mg/(Mg+\Sigma Fe)$ and $(Mg,Fe)CO_3$ contents. It is further inferred that the large magnesite cores (H323, H321, K670) and large dolomite cores (D521, H324) represent a "peak" metamorphism and approached, or reached equilibrium with *core* compositions of garnet, omphacitic clinopyroxene, and other "eclogite" phases appropriate to their bulk-rock chemical compositions. It is inferred that the rims of calcite on dolomite, and of dolomite on magnesite represent a further stage on the PT path, probably still within eclogite facies conditions, since some rims are

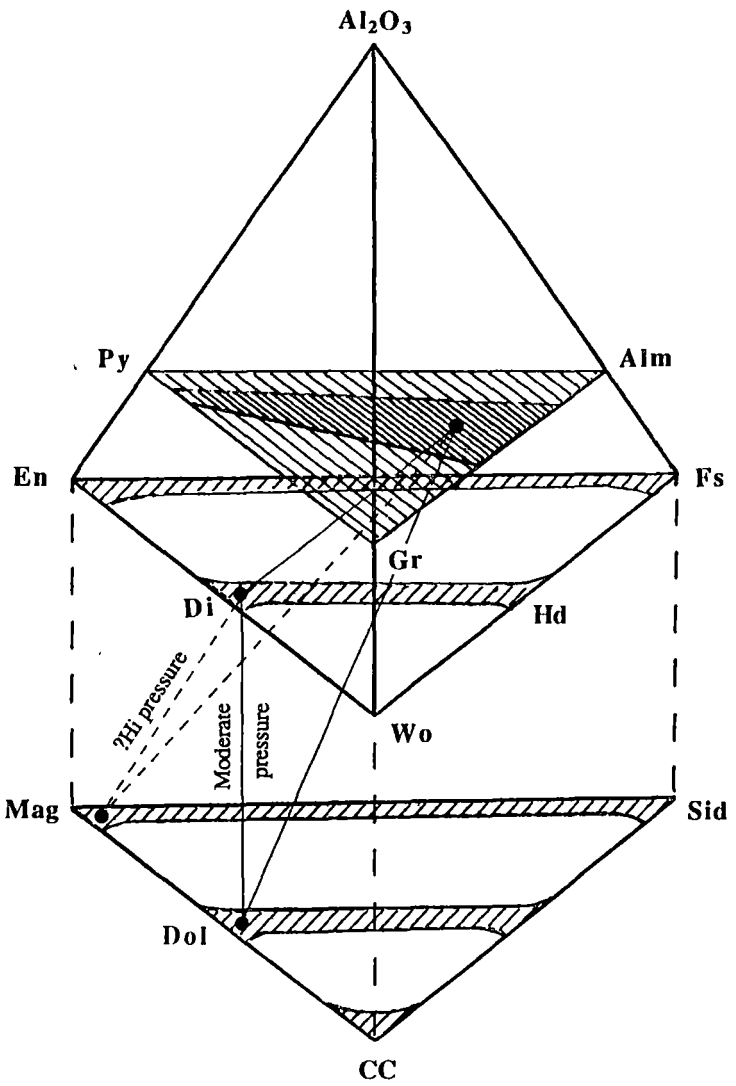

Figure 6.4.1: Schematic representation of reaction relationships in basalt+carbonate system. Thin solid line and dashed line are tie-lines joining equilibrium phase assemblages (filled circles) at moderate, and high pressures respectively. Note that solid solution (light cross-hatching) limits are strongly pressure and temperature dependent. Region of heavy cross-hatching represents range of basaltic compositions.

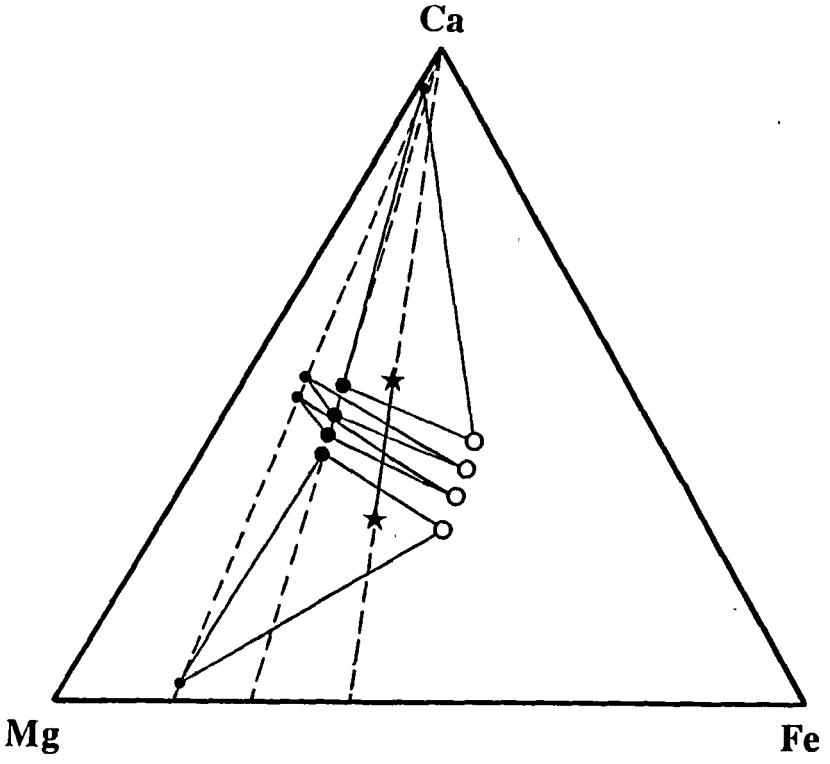

Figure 6.4.2: Schematic ternary plot in Ca-Mg-Fe space, illustrating the effect that bulk composition has on equilibrium phase compositions in basalt+carbonate system. This applies to pressures greater than the reaction enstatite + dolomite = diopside + magnesite (Brey et al. 1983). A range of basaltic compositions (constant Fe/Mg) is indicated by the line between the two stars. Open circles represent garnet compositions, larger filled circles are clinopyroxene compositions and smaller filled circles are carbonate compositions. A bulk composition corresponding to the more calcic star would contain the assemblage grossular-rich garnet+diopside+calcite (as indicated by the three-phase field which surrounds that bulk composition), whereas the more magnesian star would be an assemblage of grossular-poor garnet+diopside+magnesite. This low Ca bulk composition is transitional to peridotitic compositions, which would contain very low grossular garnet (4-6 wt% CaO) + orthopyroxene + clinopyroxene + magnesite. Bulk compositions in the middle of the range between the stars would contain assemblages of garnet+diopside+dolomite, as indicated.

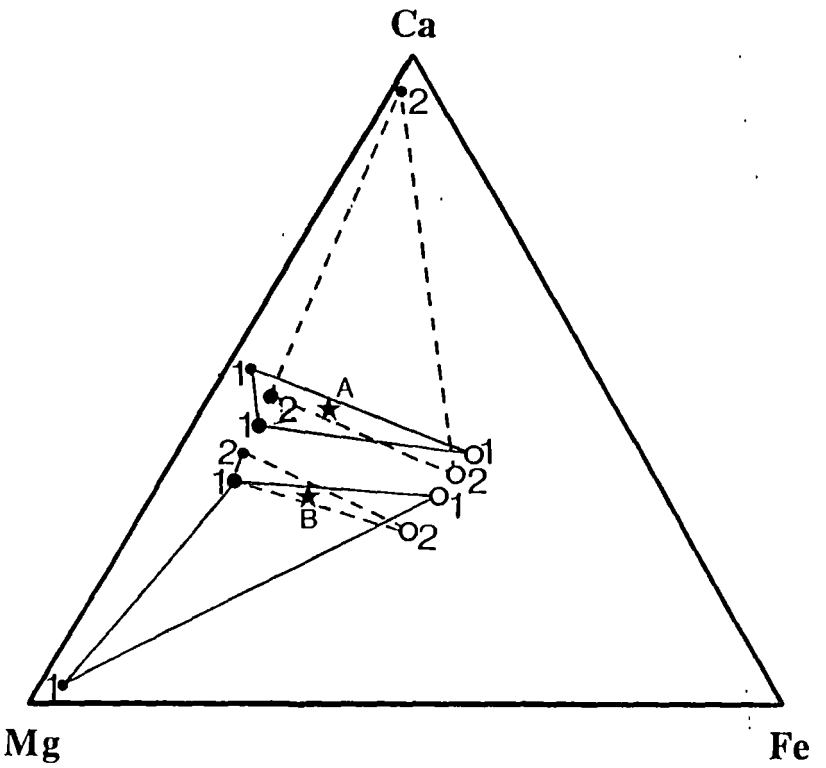

Figure 6.4.3: Schematic ternary plot in Ca-Mg-Fe space, illustrating the effect that decreasing pressure has on equilibrium assemblages. Symbols indicating phase compositions are same as in figure 6.4.2. A bulk composition A would, at high pressures, have a stable assemblage defined by the three phase field labelled 1 which includes A (ie; dolomite + diopside$_1$ + grossular-rich garnet). At lower pressures and higher temperatures, the stable assemblage (defined by 3 phase field labelled 2) becomes calcite + diopside$_2$ + garnet. For the more magnesian bulk composition B, the high pressure, lower temperature assemblage magnesite + diopside$_1$ + garnet (labelled 1) would be replaced at lower pressures and higher temperatures by the assemblage dolomite + diopside$_2$ + lower grossular garnet (labelled 2).

developed against omphacite. In attempting to deduce PT conditions for this stage, the compositions of immediately adjacent garnet and carbonate are used, the garnet exhibiting compositional zoning (decreasing grossular content, and changing 100*Mg/(Mg+ΣFe)) towards the carbonate.

Further alteration to amphibole-rich assemblages related to breakdown of garnet and omphacite, is associated with veins and patches of calcite in C960. No attempt is made to deduce the PT conditions for this sample as neither garnet nor omphacite appear stable in this assemblage.

6.4.3 Peak metamorphism

The dolomite cores and inferred garnet (non-rim)-dolomite pairs in H324 and D521 are used. In H324, garnet has a composition around $Gr_{25}Py_{20}Alm_{55}$ near to dolomite (ie; outside the rim reaction effect). In D521, the garnets analysed (patches C1, C4) are very low in grossular ($Gr_{12-14}Py_{33-23}Alm_{54-64}$) and are anomalous in relation to other assemblages.

There are magnesite cores and inferred garnet-magnesite pairs in H323 and H321. Minimum grossular contents ($Gr_{20-23}Py_{25-20}Alm_{53-55}$) in the cores of garnets increase slightly towards the carbonate, but then drop adjacent to the thin dolomite reaction rim (figures 6.4.4a-c). In K670, higher grossular content ($Gr_{25}Py_{15-10}Alm_{60-65}$) occurs in a more almandine-rich garnet and again decreases at the rim against dolomite (figure 6.4.5).

In C960, calcite included in garnet is inferred to range from the relict, pre-metamorphic composition towards a magnesian calcite [100*Mg/(Mg+ΣFe) = 83; $Ca_{69}Mg_{26}Fe_5$] immediately adjacent to garnet. This garnet (patch C4; figure 6.4.6a) has maximum grossular ($Gr_{32}Py_{18}Alm_{50}$) amongst all analysed samples and again shows zoning with depletion of grossular at the carbonate rim. Garnet elsewhere in sample C960 (patch C5; figure 6.4.6b) has $Gr_{22-25}Py_{35}Alm_{40-45}$ with a slight increase in grossular against calcite (100*Mg/(Mg+ΣFe) = 36-47). Only in sample H321 does relict calcite approach 100*Mg/(Mg+ΣFe) = 80 and in this sample also, the most grossular-rich garnet occurs close to this calcite. The most grossular-rich garnet is again $Gr_{30}Py_{20}Alm_{50}$.

Taken together, the "peak" metamorphic conditions illustrated by H321, H323, H324, K670 and C960 define garnet/carbonate relationships in which magnesite,

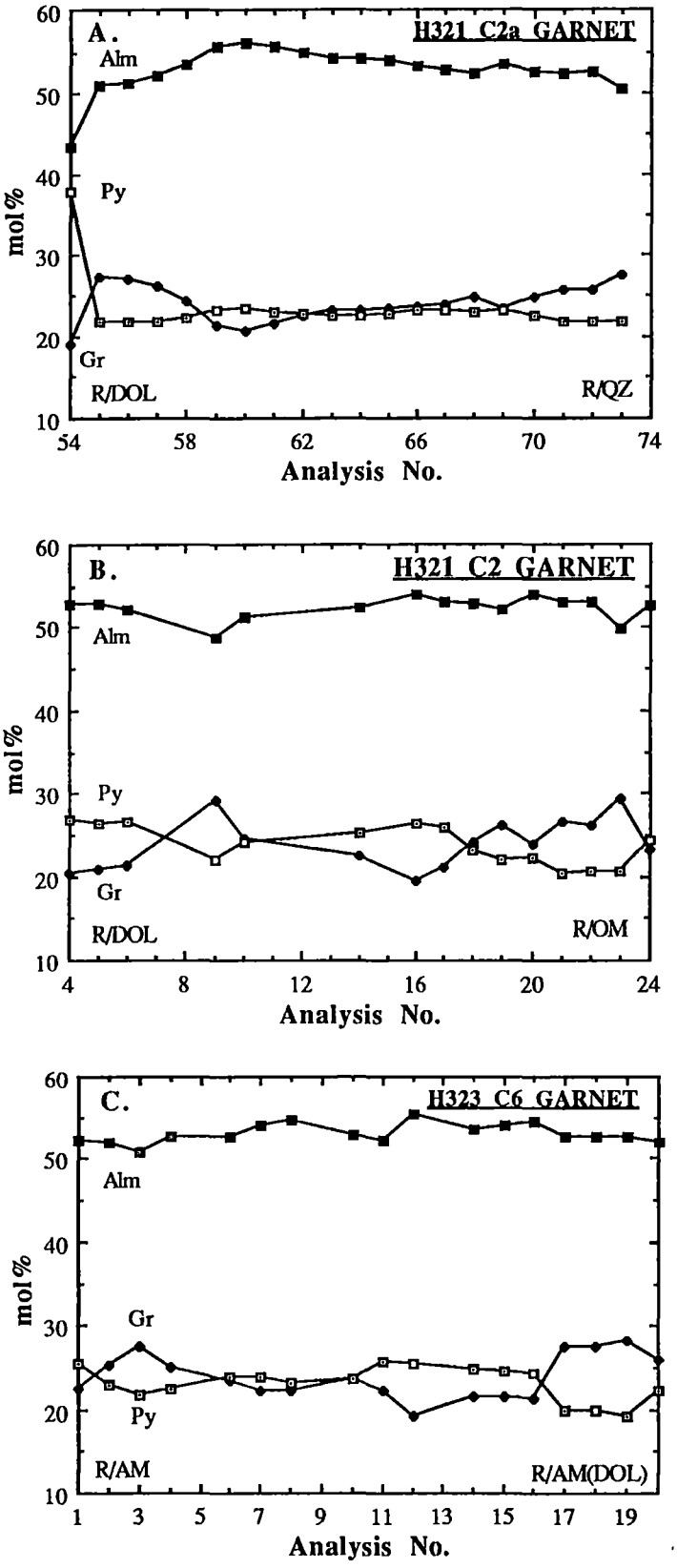

Figure 6.4.4: Compositional profiles for garnet grains from (A) sample H321, patch C2a), (B) sample H321, patch C2, and (C) sample H323, patch C6. In each case, successive analyses are evenly spaced. See text for explanation.

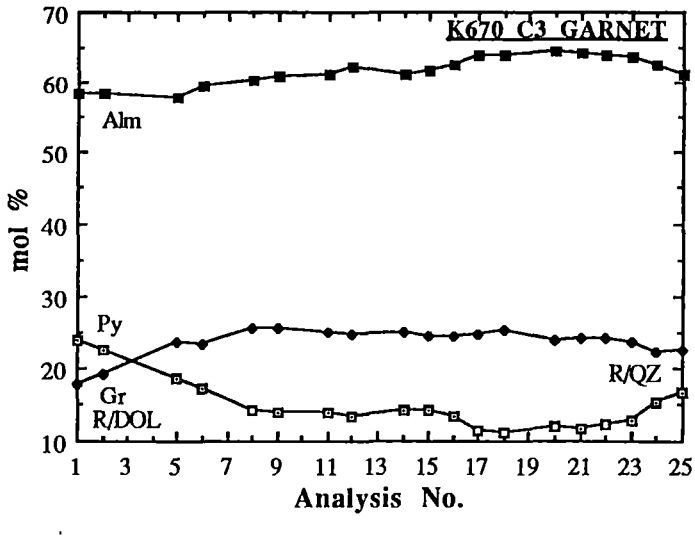

Figure 6.4.5: Compositional profiles for garnet grains from sample K670 patch C3. Successive analyses are evenly spaced. See text for explanation.

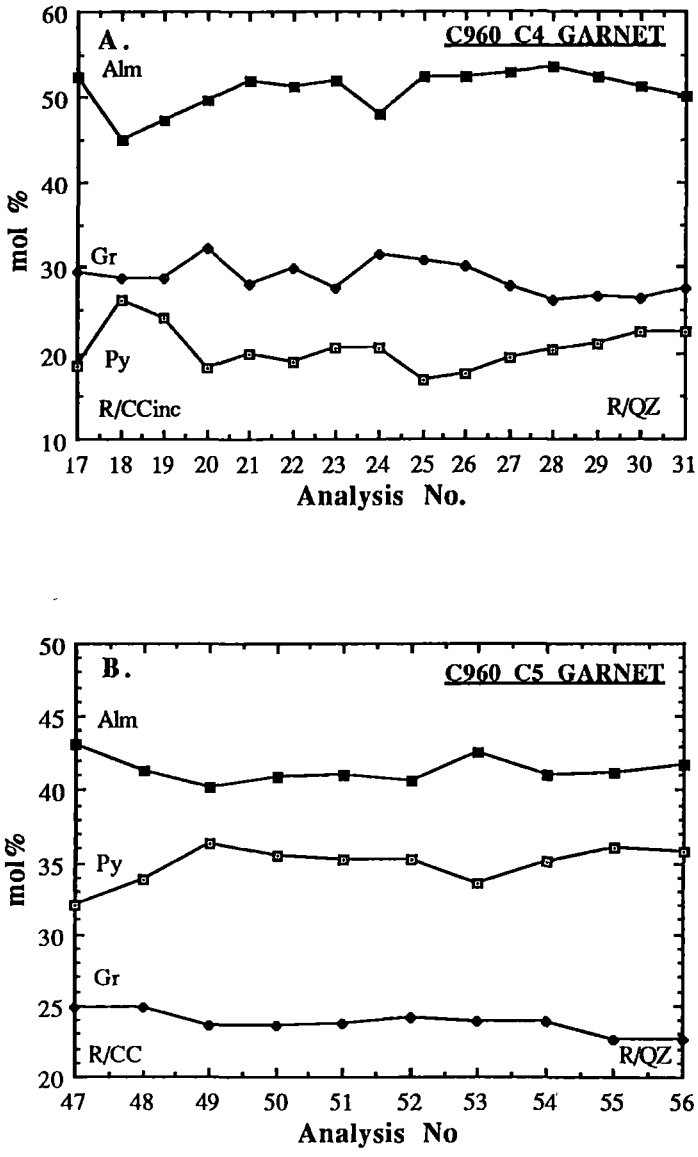

Figure 6.4.6: Compositional profiles for garnet grains from sample C960, (A) patch C4 and (B) patch C5. In each case, successive analyses are evenly spaced. See text for explanation.

dolomite and magnesian calcite coexist with increasingly grossular-rich garnet ($Gr_{20} \rightarrow Gr_{30}$) with fairly constant Fe/Mg values.

These relationships are illustrated graphically in figure 6.4.7 where they are compared with carbonate-garnet pairs from experiments at 20-35 kbar and 700-850°C.

6.4.4 Stage 2 metamorphism

The calcite rims on dolomite in H324 and D521, and the dolomite rims on magnesite in H321, H323 and K670 are attributed to this stage. The dolomite rims on magnesite have slightly lower 100*Mg/(Mg+$\sum$Fe) than the dolomite cores of the peak metamorphic assemblages. In addition, garnets adjacent to the dolomite rims move to lower grossular contents and higher 100*Mg/(Mg+$\sum$Fe). This is particularly marked for K670 (figure 6.4.5). In H321, garnet/magnesite cores have lower Fe/Mg values in garnet coexisting with similar magnesite to that in K670, possibly implying higher temperature for the H321 assemblage than K670. Again the replacement of magnesite by dolomite and zoning of garnet to lower grossular content and higher pyrope content (figure 6.4.4a and b), is inferred to be a response to a temperature increase at high pressure.

The calcite rims on H324 and D521 are not easy to interpret although in the projection in figure 6.4.8 they illustrate crossing tie-lines. In D521, the zoning of garnet to high 100*Mg/(Mg+$\sum$Fe) (pyrope content) is consistent with temperature increase, but in H324 there is little change in Fe/Mg, and only a small drop in grossular content of the garnet adjacent to the calcite rim.

6.4.5 Retrogressive alteration

All sample show some development of hydrous phases replacing garnet and omphacite particularly, but samples H324 and D521 are the most severely altered, with advanced development of kelyphite on garnet and the appearance of amphibole+albite, indicating relatively low pressures. These effects make interpretation of compositional zoning in phases very difficult, as missing rims are possible. The carbonate of this assemblage is calcite with moderate to low 100*Mg/(Mg+$\sum$Fe).

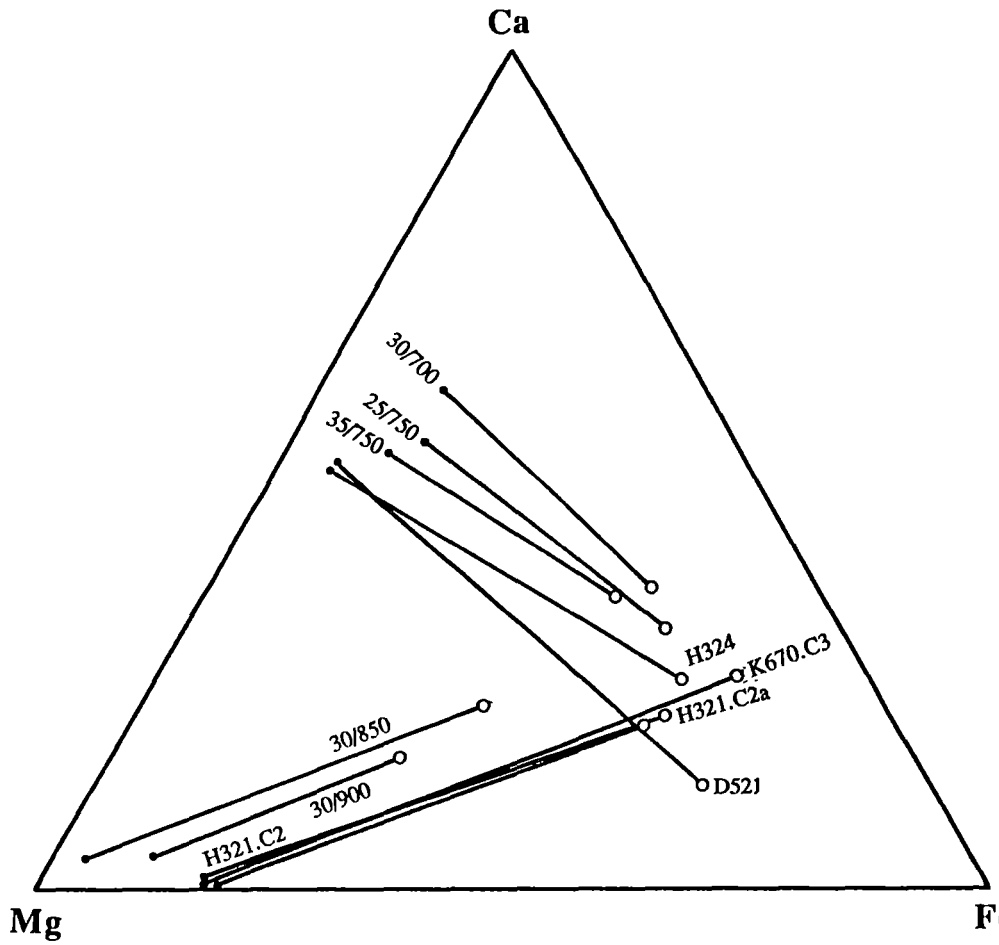

Figure 6.4.7a: Ternary plot in Ca-Mg-Fe space illustrating garnet-carbonate relationships in GA1+10% calcite experiments from 25-35 kbar, and 700-750°C, and GA1+10% magnesite experiments at 30 kbars, and 850 and 900°C (Chapter 5). These are compared with magnesite cores and inferred garnet "peak" compositions (cores) in samples H321 and K670, and with dolomite cores and inferred garnet "peak" compositions in D521 and H324. Open circles are garnet, filled circles are carbonate. See text for explanation.

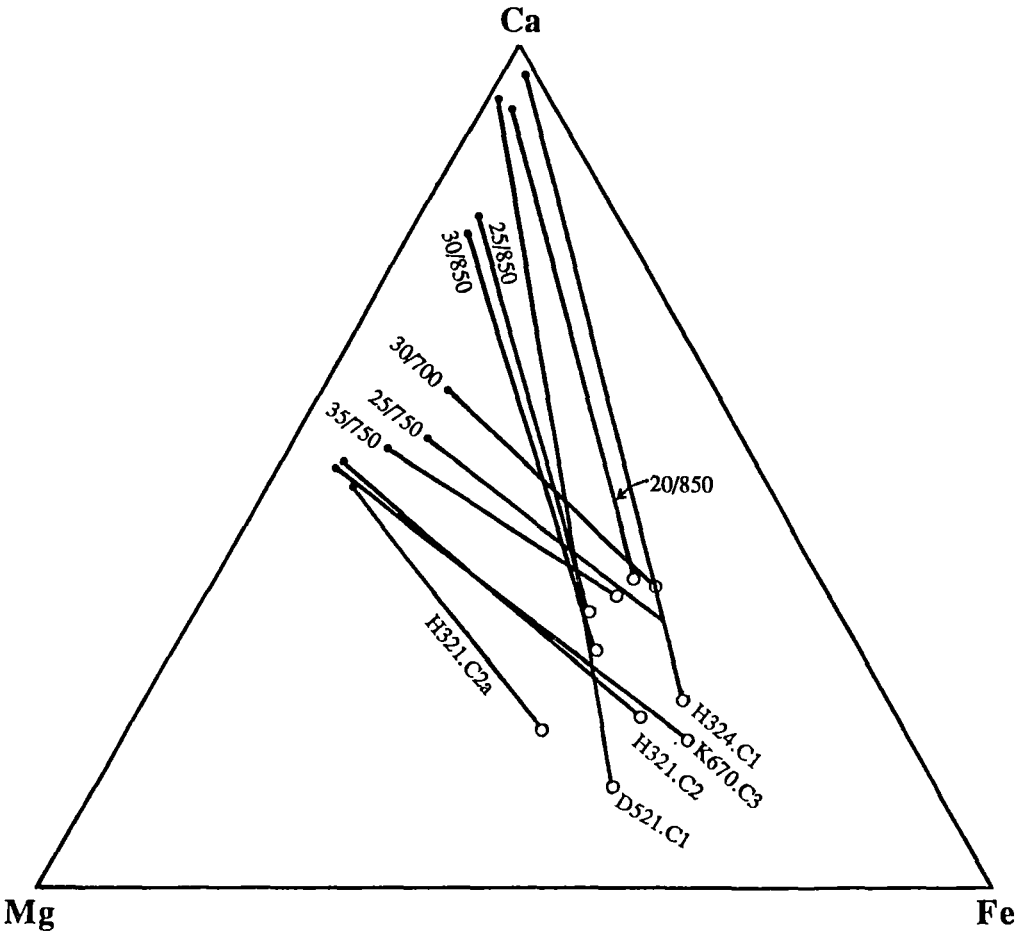

Figure 6.4.7b: Ternary plot in Ca-Mg-Fe space illustrating garnet-carbonate relationships in GA1+10% calcite experiments from 20-35 kbar, and 700-850°C (Chapter 5). These are compared with dolomite rims and garnet rims in contact with dolomite in samples H321 and K670, and calcite rims and garnet in contact with calcite in samples D521 and H324. These assemblages are interpreted as representing stage 2 metamorphism. Symbols as in figure 6.4.7a. See text for further explanation.

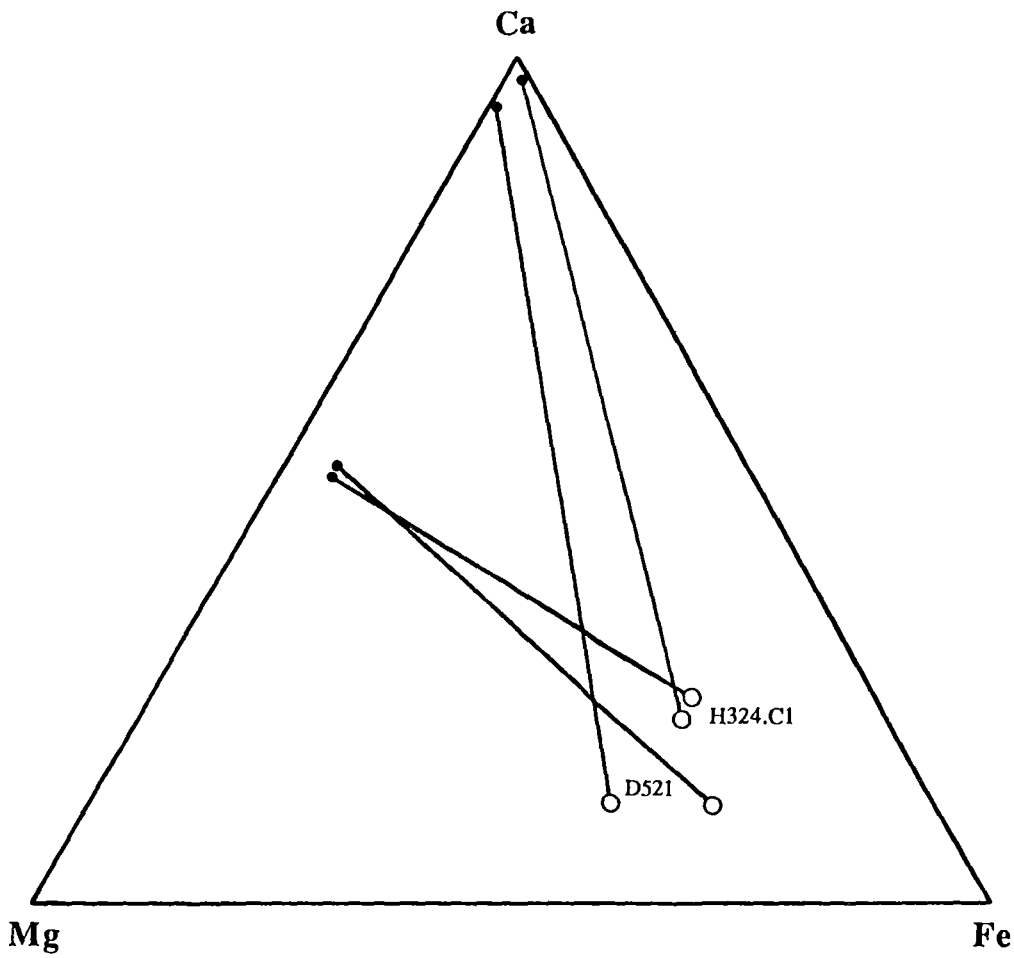

Figure 6.4.8: Garnet (open circles) and carbonate (filled circles) compositions for D521 and H324. Tie lines connect dolomite cores with inferred "peak" garnet core compositions, and calcite rims with garnet rim compositions in contact with calcite. Note the crossing tie lines. See text for further explanation.

6.5 Comparison of experimentally-determined phase assemblages with those of the Bohemian eclogites

In comparing experimental and natural phase assemblages it is assumed that a decrease in K_d' [where $K_d' = (Fe/Mg)_{ga}/(Fe/Mg)_{cbte}$] is indicative of a decrease in temperature. This is clearly illustrated in the experiments with magnesite (30 kbar, 850 and 900°C) and calcite (25 kbar, 850-1000°C) and may be inferred for dolomite. Similarly, lower temperatures will result in a decrease in mutual solid solution between the carbonates and, most probably, in a decrease in grossular content of garnet. However, a greater effect in the grossular content of garnet is exerted by pressure with an increase in both pyrope and grossular from 25 to 35 kbar at 750°C.

The garnet/dolomite pairs crystallized experimentally at 25 kbar, 750°C, have lower K_d' than the peak metamorphic garnet/dolomite pairs (figure 6.4.7a). In addition, the garnets of the natural rocks have lower grossular content (≈25 mol% rather than 30 mol%). Similarly, the garnet/magnesite pairs crystallized at 30 kbar, 850°C and 900°C have more magnesian magnesites with high $CaCO_3$ solid solution, and have much more pyrope-rich garnets than the natural garnet-magnesite associations (figure 6.4.7a).

It is therefore inferred that the "peak metamorphic" assemblages crystallized at P≤25 kbar and temperatures of 650-700°C.

The rim reaction of magnesite + grossular-rich garnet (core) to dolomite + pyrope-rich garnet (rim) is attributed to a temperature increase. Similarities in K_d' and carbonate solid solutions suggest that temperatures of around 750°C were attained, at pressures of about 25 kbar or slightly less, by samples H321, and possibly H323 and H324 as well. Sample K670 may not have reached temperatures quite as high as this (figure 6.4.7b).

If temperatures of 750°C at 20-25 kbar were reached, then in the presence of carbonate and amphibole, incipient melting would be anticipated (given a solidus temperature for GA1 between 700 and 750°C; Chapter 5). Although carbonate would remain refractory, the melt phase would be a sodic, siliceous melt. The presence of quartz and blue amphibole±zoisite±paragonite+rutile(II) pegmatoid patches associated with boudinage in eclogite (Klapova, 1990, and pers. comm.) is compatible with incipient melting under these conditions.

The calcite rims on dolomite may indicate decompression and pressures <20 kbar given that the grossular content of garnets in the natural rocks are lower than those in the experimental study at P≥20 kbar.

6.6 PT history of the eclogites

The current incomplete understanding of the complexities of eclogite+carbonate systems described in Chapter 5 preclude accurate calibration of the reactions between garnet and carbonates as geothermometers or barometers at this stage. More experiments at lower temperatures (650-750°C), using a variety of bulk compositions would be necessary. Of particular value for application to this suite of carbonated eclogites would be GA1+magnesite experiments at a range of pressures and near-solidus temperatures.

In the preceding section, it was argued that a prograde PT path through a low temperature regime attained a condition near 25 kbar, 650-700°C at which the eclogites approached equilibrium. Inclusions of relict phases in garnet particularly, and including calcite, preserve a fragmentary record of this PT path. The eclogites experienced heating, under approximately isobaric conditions to ≈750°C with partial reaction of magnesite to dolomite, where it was in contact with grossular-rich garnet. This was also accompanied by incipient melting with development of minor alkali-rich siliceous melt in the eclogite horizons. A greater degree of melting in non-eclogitic country rocks would be expected, and it may have been that the degree of melting was sufficient to destabilize the subduction regime, leading to uplift and decompression, and hydration reactions. The natural rocks provide an excellent parallel to the experimental study in that they demonstrate the stability of carbonate in the subduction regime, and their behaviour as refractory phases during initial partial melting.

However, the ability to interpret the detail of the solid-solid reactions and equilibria between carbonates, garnet and pyroxene will require detailed experimental study aimed at unravelling the effects of temperature, pressure and bulk composition.

Broad constraints can also be placed on the PT evolution of these samples by considering the Ca-Mg partitioning relationships (K_d as defined in Chapter 5, rather than K_d') between garnet, and dolomite and calcite. Table 6.2 lists K_d determinations based on the data used in constructing the tie-lines in figures 6.4.7 and 6.4.8.

Table 6.2: Ca-Mg partitioning data between garnet and dolomite, and garnet and calcite in the Czech eclogites. Abbreviations; ga=garnet; dol=dolomite; cc=calcite.

Sample	K_d*(ga-dol)*	K_d*(ga-cc)*
H324.C1	1.29	0.0135
D521.C1	0.438	0.0209
K670.C3	0.662	-
H321.C2a	0.464	0.0328
H321.C2	0.653	0.0490

This data tends to support the tie-line data above (figure 6.4.7). For example, when compared with the experimental K_d values on figure 5.5.1, the high K_d for H324 is indicative of a high pressure for peak equilibration, such as P>25 kbar at T≈750°C. K_d for the remainder of the samples are consistent with pressures between 20 and 30 kbar at temperatures of around 750°C or less.

On the other hand, the K_d calculated for garnet-calcite pairs are all very low, suggesting lower pressures and higher temperatures. This is consistent with the retrograde nature of the calcite rims on dolomite in H324 and D521.

For example, those samples in which calcite rims on higher pressure carbonate phases are absent, have probably remained at relatively low temperatures throughout their metamorphic history. Samples H323, H321 and K670, which record complete or near-complete replacement of relict primary calcite by magnesite may have been metamorphosed along a prograde PT path towards high pressures (possibly in excess of 25 kbar) at relatively low temperatures (less than 750°C). The dolomite rims formed on these samples indicates a path towards higher temperature and low pressure. Further decompression at high temperatures (T>750°C) may have produced calcite rather than dolomite on the rims of the carbonate assemblages in some samples.

To be consistent with the phase relations of the GA1+calcite or magnesite systems, as delineated in Chapter 5, those samples which exhibit calcite rims on dolomite cores (H324 and D521) must have evolved along clockwise PT paths. Rapid transport to high pressures (possibly P>25kbar) at relatively low temperatures (650-700°C) resulted in almost complete conversion of primary calcite (?) to dolomite in equilibrium with garnet. This was followed by a relatively short heating event which increased temperatures to 750°C, at similar or slightly lower pressures, resulting in stabilization of calcite on the rims of the dolomite.

This compares with K670 and H321, in which magnesite±calcite cores are rimmed by dolomite. These samples have been transported to high pressures, and relatively low temperatures, resulting in partial or complete conversion of primary calcite to magnesite. The presence of magnesite rather than dolomite as the high pressure carbonate phase is related to bulk-compositional variation between samples, rather than attainment of significantly higher peak pressure compared with dolomite+calcite-bearing samples (figure 6.4.2). K670 and H321 also experienced a near isobaric heating event to 750°C, producing dolomite rims on magnesite. They then followed a low temperature retrograde path to lower pressures in order to maintain dolomite stability rather than calcite, on the rims of the magnesite±calcite assemblages.

6.7 Conclusions

(1) The experimental study described in Chapter 5 has demonstrated that carbonate is stable to P>35 kbar in subduction setting. However, there are clearly complex reactions to be studied, the nature of which depend on bulk chemical composition, and whether aragonite, dolomite or magnesite is the stable carbonate phase at P>30kbar, 700-900°C.

(2) The possibility exists that Ca/Mg partitioning in dolomite-garnet or dolomite-clinopyroxene pairs could be used to calibrate a geobarometer, providing the effect of variations in Fe/Mg can be understood.

(3) The carbonated eclogites from the Czech Republic provide natural-rock analogues of the experiments, demonstrating carbonate stability in an eclogitic assemblage in the presence of partial melting to produce siliceous melts.

(4) Subduction of rocks in the region may have reached 25 kbar at 650-700°C, and was followed by an isobaric heating event, destabilization and uplift with attendant retrogression, presumably associated with nappe-type emplacement.

CHAPTER 7

CRUST-MANTLE CARBON RECYCLING AND ITS ROLE IN PETROGENESIS

Much effort has been directed at understanding the role of trace quantities of volatile components (chiefly in the CHO-system) in magma genesis within the Earth's mantle. In particular, the extent to which such volatiles (especially CO_2) are recycled between crust and mantle has excited substantial recent interest. The experimental and natural rock evidence described in previous chapters provide important constraints on the nature of these processes, particularly in relation to intra-plate magmatism.

That many samples of altered ocean-floor basalt contain veins and vesicles containing secondary calcitic carbonate (Richarson et al. 1980; Baragar et al. 1977; Hart and Staudigel, 1978; Alt et al. 1986; Staudigel et al. 1989) suggests that subduction of such carbonate may be a viable mechanism for carbon recycling (Hauri et al. 1993; Trull et al. 1993; Zhang and Zindler, 1993). A necessary condition for the viability of such models, however, is that carbonate phases are stable under PT conditions appropriate to a subducting slab. This was demonstrated in Chapter 5 where it was shown that most model geotherms for the subducting slab (for example, that of Oxburgh and Turcotte, 1976) traverse the experimentally-delineated eclogite+residual carbonate stability field, suggesting that secondary calcitic carbonate in a typical ocean-floor basalt can survive subduction to at least 35kbar and probably to much higher pressures, even in the presence of a significant partial melt fraction, and to temperatures of >1000°C at ≥27kbar (figure 5.5.1).

This conclusion is supported by the occasional occurrence of primary carbonate in high-pressure metamorphic rocks. A variety of carbonate compositions and textures from the suite of carbonated eclogites from the Czech part of the Saxothuringicum described in Chapter 6 provide a natural example of the stability of carbonate under eclogite-facies conditions.

In addition, recent papers have demonstrated that recycling of carbon into the mantle can explain the abundances and isotopic characteristics of volatile species in basalts and fluid inclusions from mantle xenoliths. For example, Zhang and Zindler (1993) concluded, on the basis of studies of the quantities of He and Ar in the degassed mantle, and the observed outgassing ratios of CO_2/He at mid-ocean ridges, that 72±10% of the total degassable CO_2 present in the primitive Earth, is still resident in the mantle. This is

strong, independent evidence for recycling of CO_2 back into the Earth's mantle via subduction. Furthermore, the study of Trull et al. (1993) suggested from a study of carbon and helium isotopic ratios in ultramafic xenoliths from hot-spot localities (Loihi-Hawaii, Réunion and Kerguelen) that the (shallower) MORB mantle source does not require a recycled contribution to its CO_2 budget, but that the (deeper) OIB mantle source does.

Further support is lent to the concept of subduction-related carbon-recycling by a recent study of four mantle xenoliths from ocean islands associated with the Samoan and Macdonald hot spots (two each from Savai'i and Tubuai; Hauri et al. 1993). These xenoliths contain primary olivine + orthopyroxene assemblages, and secondary clinopyroxene + spinel ± apatite ± glass. The secondary assemblages were interpreted to be the result of interaction between primary lithospheric material and carbonatite melts, in a manner similar to that described in Chapters 2 and 3. This interpretation is supported by trace element patterns (in particular the strong enrichment of LREE over Ti) obtained from constituent phases, which strongly resemble the patterns reported for the Victorian wehrlites in Chapter 3, and the carbonatite-metasomatised peridotites described by Rudnick et al. (1993) and Dautria et al. (1992). Thus, based on these petrographic and geochemical observations, Hauri et al. (1993) proposed metasomatism of the lithosphere underlying the MacDonald and Samoan hot-spots by carbonatite melts.

The two Samoan xenoliths have extreme isotopic compositions which are characteristic of the EMII mantle source (very high $^{87}Sr/^{86}Sr$, and low $^{143}Nd/^{144}Nd$). On the other hand the Tubuai xenoliths have isotopic signatures similar to the HIMU mantle component (low $^{87}Sr/^{86}Sr$, high $^{206}Pb/^{204}Pb$). Because the Sr-Nd-Pb budgets of the xenoliths are dominated by the metasomatising carbonatite, the extreme isotopic compositions of the xenoliths directly reflect those of the carbonatite. This suggests in turn the presence, in the carbonatite source regions, of recycled, carbonated oceanic crust, and Hauri et al. (1993) have linked the HIMU signature with the altered mafic oceanic crust, and the EMII signature with recycled sediment. The authors finally note that "The association of these recycled isotopic signatures with carbonatite metasomatism indicates that some mechanism must exist to transport CO_2 ... through subduction zones and into the convecting mantle."

Thus, several independent lines of evidence (isotopic and trace element data from natural carbonatized xenoliths; studies of noble gas and carbon abundances and isotopic compositions in xenoliths and basaltic melts; high pressure experimental evidence as described in Chapter 5; studies of primary carbonate in high pressure metamorphic rocks

which also bear evidence of partial melting, as described in Chapter 6) strongly suggest that recycling of carbon through subduction is both a viable and important process.

The ultimate fate of carbonate which survives subduction to P>35kbar depends on mantle redox conditions, about which consensus has yet to be reached. Because of the relative PT effects on oxygen buffers based on C-C-O or carbon in carbonates, and those based on $Fe^{2+} \rightarrow Fe^{3+}$ or $Fe \rightarrow Fe^{2+}$ reactions, increasing pressure may redistribute oxygen in a carbonated eclogite so that the higher pressure assemblages contain carbonate with garnet and omphacite with low Fe^{3+} contents. At lower pressures, a graphite-bearing eclogite with $NaFe^{3+}Si_2O_6$ (acmite) and $Ca_3Fe^{3+}{}_2Si_3O_{12}$ (andradite) components will be the equivalent assemblage at constant oxygen content. If, for example, fO_2 conditions were between IW+1 and IW+2 log units, then subducted dolomitic or magnesitic carbonate (fO_2>IW+3 log units) could reduce to graphite/diamond co-existing with a H_2O-rich fluid (Luth, 1993; Taylor, 1985; Taylor and Green, 1986; Green et al. 1987; Green et al. 1993). Garnet-hosted microdiamonds from ultra-high pressure metamorphic terranes in Kazakhstan (Sobolev and Shatsky, 1990) and Tien-Shan (Tagiri and Bakirov, 1990), or eclogitic diamonds in kimberlite may be witnesses of such processes.

The postulated redox contrast between fragments of subducted crust and surrounding reduced mantle may also act as a site for melting. If the Earth is still degassing volatile species in the C-H-O system, then reduced CH_4+H_2O fluids may reduce carbonate in eclogite in the manner described in the last paragraph, producing diamond, and a water-rich fluid. Fluxing of surrounding mantle and recycled crustal material with these H_2O-rich fluids may lower the solidii below ambient temperatures and hence induce "redox" melting. These primitive melts may be rich in volatiles, and will bear isotopic and trace element characteristics of their mixed source, namely components related to recycled oceanic crust, and components derived from mantle peridotite (Green et al. 1993).

Evidence for involvement of recycled oceanic crust (including sediment) has been cited in studies of intra-plate volcanic products. For example, Gerlach et al. (1988) proposed that many of the isotopic, and major and trace element characteristics of magmas erupted onto the Cape Verde archipelago could be explained by variable degrees of melting of a heterogeneous mantle consisting of depleted mantle (DM component) and recycled oceanic crust (HIMU component). Furthermore, Dupuy et al. (1993) have recently shown that many intraplate basaltic rocks have elevated Zr/Hf values (>36, the chondritic value) and have explained this in terms of carbonatitic metasomatism of the basaltic source regions, on the basis that many natural carbonatites have fractionated Zr/Hf values.

Melts generated at redox interfaces within the upper mantle or transition zone under "hot-spots" may ascend, either entrained in plumes or diapirs, or by percolation flow. At depths corresponding to pressures of ≈30 kbar the carbonated melts will enter the pargasitic amphibole+carbonatite melt stability field (Wallace and Green, 1988; Falloon and Green, 1990), and crystallize amphibole ± phlogopite ± clinopyroxene. The residual melt will evolve to carbonatite, with extreme enrichments in REE and Sr, high Zr/Hf, and low Ti/Eu values, which can segregate at low melt fractions, ascending rapidly to depths of 15-20 kbar, where a series of decarbonation reactions with lithospheric wall-rock phases will drive the lherzolitic or harzburgitic lithosphere towards apatite+amphibole-bearing spinel wehrlite. Cryptic metasomatism may also result from minor replacement of primary orthopyroxene by fine-grained assemblages of olivine+clinopyroxene, which could rapidly anneal to an equilibrated texture. Significant release of CO_2-rich fluid could cause fracturing of the lithosphere, allowing easier ascent of subsequent volatile-charged silicate, or even carbonatite melts (see Chapter 4), and facilitating entrainment of metasomatised lithospheric fragments in those melts.

Mantle metasomatism by carbonatite melts, over longer times, may convert a significant lithospheric volume (layer) to olivine-rich wehrlite, with the fugitive CO_2 largely lost from the system. If lithospheric melting of this region occurs in a later geodynamic cycle (eg; re-activation in the mantle wedge overlying a subduction zone) then the wehrlite may act as a source composition for distinctive magmas, ie; melts in equilibrium with olivine + clinopyroxene ± spinel, and not in equilibrium with orthopyroxene.

In this study, high pressure - high temperature experimental techniques and geochemical and petrological studies of natural mantle samples have been used to explore some of the significant processes which come into play in carbon recycling and mantle interaction with C-H-O fluids. The studies have revealed promising lines of further investigation.

REFERENCES

ALLEGRE CJ, PINEAU F, BERNAT M and JAVOY M, 1971: Geochemical evidence for the occurrence of carbonatites on the Cape Verde and Canary Islands: Nature 233, 103.

ALT JC and EMMERMAN R, 1985: Geochemistry of hydrothermally altered basalts: DSDP hole 504B, leg 83: Init. Rep. DSDP 83, 249-262.

ALT JC, HONNOREZ J, LAVERNE C and EMMERMAN R, 1986: Hydrothermal alteration of a 1 km section through the upper oceanic crust, Deep Sea Drilling Project Hole 504B: Mineralogy, chemistry, and evolution of seawater-basalt interactions: J. Geophys. Res. 91, 10,309-10,335.

ANDERSON T, O'REILLY SY and GRIFFIN WL, 1984: The trapped fluid phase in upper mantle xenoliths from Victoria, Australia: implications for mantle metasomatism: Contrib. Mineral. Petrol. 88, 72-85.

AUMENTO F and LONCAREVIC B, 1969: The Mid-Atlantic Ridge near 45°N. III. Bald Mountain: Can. J. Earth Sci. 6, 11-24.

BAILEY DK, 1982: Mantle metasomatism - continuing chemical change within the Earth: Nature 296, 525-530.

BAILEY DK, 1987: Mantle metasomatism - perspective and prospect, in FITTON, JG and UPTON, BGJ (eds): Alkaline Igneous Rocks: Oxford, Blackwell, pp 1-14.

BAILEY EH, IRWIN WP and JONES DL, 1964: Fransiscan and related rocks, and their significance in the geology of western California: Calif. Div. Mines and Geology Bull. 183, 177p.

BAKER MB and WYLLIE PJ 1992: High-pressure apatite solubility in carbonate-rich liquids: implications for mantle metasomatism: Geochim. Cosmochim. Acta 56, 3409-3422.

BAKER MB, and WYLLIE PJ, 1990: Liquid immiscibility in a nephelinite-carbonate system at 25kbar and implications for carbonatite origin: Nature 346, 168-170.

BALLHAUS C, BERRY RF and GREEN DH, 1990: Oxygen fugacity controls in the Earth's upper mantle: Nature 349, 437-440.

BALLHAUS C, BERRY RF and GREEN DH, 1991: High pressure experimental calibration of the olivine-orthopyroxene-spinel oxygen barometer: implications for the oxidation state of the upper mantle: Contrib. Mineral. Petrol. 107, 27-40.

BARAGAR WRA, PLANT AG, PRINGLE GJ and SCHAU M, 1977: Petrology and alteration of selected units of Mid-Atlantic Ridge basalts sampled from sites 332 and 335, DSDP: Can. J. Earth. Sci. 14, 837-874.

BARRERA JL, FERNANDEZ SANTIN S, FUSTER JM and IBARROLA E, 1981: Ijolitas-sienitas-carbonatitas de los macizos del norte del complejo plutonico basal de Fuerteventura (Islas Canarias): Bol. Geol. Min. (Madrid) 92, 309-321.

BARSDELL M and BERRY RF, 1988: Origin and evolution of primitive island arc ankaramites from western Epi, Vanuatu: J. Petrol. 31, 747-777.

BASALTIC VOLCANISM STUDY PROJECT, 1981: Basaltic volcanism on the terrestial planets: Pergamon Press, Inc. New York, 1286pp.

BEHR HJ, FRITSCH E and MANSFELD L, 1965: Die Granulite von Zöblitz im Erzgebirge als Beispiel für Granulitbildung in die freichenden Scherhorizonten: Krystalinikum 3, 7-29.

BODINIER JL, DUPUY C, DOSTAL J and BERLET C, 1987: Distribution of trace transition elements in olivine and pyroxenes from ultramafic xenoliths: application of microprobe analysis: Am. Mineral. 72, 902-913.

BODINIER JL, VASSEUR G, VERNIERES J, DUPUY C and FABRIES J, 1990: Mechanisms of mantle metasomatism: Evidence from the Lherz orogenic peridotite: J. Petrol. 31, 597-628.

BOHLEN SR and BOETTCHER AL, 1982: The quartz-coesite transformation: a pressure determination and the effects of other components: J. Geophys. Res. 87, 7073-7078.

BOYD FR and MERTZMAN SA, 1987: Composition and structure of the Kaapvaal lithosphere, southern Africa, in MYSEN BO (ed): Magmatic processes: physicochemical principles: Geochem. Soc. Spec. Publ. 1, 13-24.

BRENAN JM and WATSON EB, 1988: Fluids in the lithosphere. 2: Experimental constraints on CO_2-transport in dunite and quartzite at elevated P-T conditions with implications for mantle and crustal decarbonation processes: Earth Planet. Sci. Lett. 91, 141-158.

BREY G and GREEN DH, 1975: The role of CO_2 in the genesis of olivine melilitite: Contrib. Mineral. Petrol. 49, 93-103.

BREY G and GREEN DH, 1976: Solubility of CO_2 in olivine melilitite at high pressures, and the role of CO_2 in the Earth's upper mantle: Contrib. Mineral. Petrol. 55, 271-230.

BREY G, BRICE WR, ELLIS DJ, GREEN DH, HARRIS KL and RYABCHIKOV ID, 1983: Pyroxene-carbonate reactions in the upper mantle: Earth Planet. Sci. 62, 63-74.

BROWN GM, PINSENT RH and COISY P, 1980: The petrology of spinel peridotite xenoliths from the Massif Central, France: Am. J. Sci. 280A, 471-496.

CANIL D, 1990: Experimental study bearing on the absence of carbonate in mantle-derived xenoliths: Geology 18, 1011-1013.

CANIL D, and SCARFE CM, 1989: Origin of phlogopite in mantle xenoliths from Kostal Lake, Wells Gray Park, British Columbia: J. Petrol. 30, 1159-1179.

CANN JR, 1969: Spilites from the Carlsberg Ridge, Indian Ocean: J. Petrol. 10, 1-19.

CHEN CY, FREY FA and SONG Y, 1989: Evolution of the upper mantle beneath southeast Australia: geochemical evidence from peridotite xenoliths in Mt Leura basanite: Earth Planet. Sci. Lett. 93, 195-209.

COISH RA, HICKEY R and FREY FA, 1982: Rare earth element geochemistry of the Betts Cove ophiolite, Newfoundland: complexities in ophiolite formation: Geochim. Cosmochim. Acta 46, 2117-2134.

COLEMAN RG and LANPHERE MA, 1971: Distribution and age of high-grade blueschists, associated eclogites, and amphibolites from Oregon and California: Geol. Soc. Am. Bull. 82, 2397-2412.

CONTICELLO S and PECCERILLO A, 1990: Petrological significance of high-pressure ultramafic xenoliths from ultrapotassic rocks of Central Italy: Lithos 24, 305-322.

DAUTRIA JM, DUPUY C, TAKHERIST D and DOSTAL J, (1992): Carbonate metasomatism in the lithospheric mantle: peridotitic xenoliths from a melilititic district of the Sahara basin: Contrib. Mineral. Petrol. 111, 37-52.

DAWSON JB, 1962: The geology of Oldoinyo Lengai: Bulletin Volcanologique 24, 349-387.

DAWSON JB, 1984: Contrasting types of upper mantle metasomatism, in KORNPROBST J (ed): Kimberlites II: the mantle and crust-mantle relationships: Amsterdam, Elsevier, pp289-294.

DEINES P and GOLD DP, 1973: The isotopic composition of carbonatite and kimberlite carbonates and their bearing on the isotopic composition of deep-seated carbon: Geochim. Cosmochim. Acta 37, 1709-1733.

DEITRICH V, EMMERMAN R, OBERHANSLI R and PUCHELT M, 1978: Geochemistry of basaltic and gabbroic rocks from West Mariana Basin and Marian Trench: Earth Planet. Sci. Lett. 39, 127-144.

DICK HJB and BULLEN T, 1984: Chromian spinel as a petrographic indicator in abyssal and alpine-type peridotites and spatially associated lavas: Contrib. Mineral. Petrol. 86, 54-76.

DONALDSON CH and DAWSON JB, 1978: Skeletal crystallization and residua; glass compositions in a cellular alkalic pyroxenite nodule from Oldoinyo Lengai: implications for evolution of alkalic carbonatite lavas: Contrib. Mineral. Petrol. 67, 139-149.

DOSTAL J and CAPREDI S, 1976: Uranium in spinel peridotite inclusions in basalts from Sardinia: Contrib. Mineral. Petrol. 54, 245-254.

DROOP GTR, 1983: Pre-alpine eclogites in the Pennine Basement Complex of the Eastern Alps: J. Metamorphic Geol. 1, 3-12.

DUPUY C, DOSTAL J, BODINIER JL, 1987: Geochemistry of spinel peridotite inclusions in basalts from Sardinia: Mineral. Mag. 51, 561-568.

DUPUY C, LIOTARD JM and DOSTAL J, 1992: Zr/Hf fractionation in intraplate basaltic rocks: carbonate metasomatism in the mantle source: Geochim. Cosmochim. Acta 56, 2417-2424.

EGGLER DH and BAKER DR, 1982: Reduced volatiles in the system C-O-H: Implications to mantle melting, fluid formation, and diamond genesis, in AKIMOTO S and MANGHNANI MH (eds): High-pressure research in geophysics: Tokyo Centre for Academic Publications, pp237-250.

EGGLER DH, 1978: The effect of CO_2 upon partial melting of peridotite in the system Na_2O-CaO-Al_2O_3-MgO-SiO_2-CO_2 to 35 kb, with an analysis of melting in a peridotite-H_2O-CO_2 system: Am. J. Sci. 278, 305-343.

EGGLER DH, 1987: Solubility of major and trace elements in mantle metasomatic fluids: experimental constraints, in MENZIES MA and HAWKESWORTH CJ (eds): Mantle metasomatism: London, Academic Press, pp21-41.

ELLIS DJ and GREEN DH, 1979; An experimental study on the effect of Ca upon garnet-clinopyroxene Fe-Mg exchange equilibria: Contr. Mineral. Petrol. 71, 13-22.

ELLIS DJ, 1976: High pressure cognate inclusions in the Newer Volcanics of Victoria: Contrib. Mineral. Petrol. 58, 149-180.

FALLOON TJ and GREEN DH, 1987: Anhydrous partial melting of MORB pyrolite and other peridotite compositions at 10 kbar: implications for the origin of primitive MORB glasses: Mineral. Petrol. 37, 181-219.

FALLOON TJ and GREEN DH, 1989: The solidus of carbonated fertile peridotite: Earth Planet. Sci. Lett. 94, 364-370.

FALLOON TJ and GREEN DH, 1990: Solidus of carbonated fertile peridotite under fluid saturated conditions: Geology 18, 195-199.

FAN Q, and HOOPER PR, 1989: The mineral chemistry of ultramafic xenoliths of Eastern China: implications for upper mantle composition and paleogeotherms: J. Petrol. 30, 1117-1158.

FINNERTY AA and BOYD FR, 1987: Thermobarometry for garnet peridotites: basis for the determination of thermal and compositional structure of the upper mantle, in NIXON PH (ed): Mantle xenoliths: John Wiley, New York, pp 381-402.

FREESTONE IC and HAMILTON DL, 1980: The role of liquid immiscibility in the genesis of carbonatites: an experimental study: Contrib. Mineral. Petrol. 73, 105-117.

FREY FA and GREEN DH, 1974: The mineralogy, geochemistry and origin of lherzolite inclusions in Victorian basanites: Geochim. Cosmochim. Acta 38, 1023-1059.

FREY FA and PRINZ M, 1978: Ultramafic inclusions from San Carlos, Arizona: Petrologic and geochemical data bearing on their petrogenesis: Earth Planet. Sci. Lett. 38, 129-176.

FREY FA, GREEN DH and ROY SD, 1978: Integrated models of basalt petrogenesis: a study of quartz tholeiites to olivine melilitites from southeastern Australia utilizing geochemical and experimental petrological data: J. Petrol. 19, 463-513.

FREY FA, SUEN CJ and STOCKMAN HW, 1985: The Ronda high temperature peridotite: geochemistry and petrogenesis: Geochim. Cosmochim. Acta 49, 2469-2491.

FRISCHBUTTER A, (1990): Prävariszische Granitoide der Fichtelgebirgisch-Erzgebirgischen Antiklinalzone und ihre Beduetung für die Krustenenwicklung am Nordrand des Böhmischen Masivs: Veröffentl Zentralinst Physik Erde, Potsdam 69, pp153.

GALER SJG and O'NIONS RK, 1989: Chemical and isotopic studies of ultramafic inclusions from the San Carlos Volcanic Field, Arizon: a bearing on their petrogenesis: J. Petrol. 30, 1033-1064.

GANGULY J, 1979: Garnet and clinopyroxene solid solutions and geothermometry based on Fe-Mg distribution coefficient: Geochim. Cosmochim. Acta 43, 1021-1029.

GERLACH DC, CLIFF RA, DAVIES GR, NORRY M and HOGSON N, 1988: Magma sources of the Cape Verdes archipelago: Isotopic and trace element constraints: Geochim. Cosmochim. Acta 52, 2979-2992.

GILL J, 1981: Orogenic andesites and plate tectonics: Springer Velag, Berlin, 390pp.

GREEN DH and WALLACE ME, 1988: Mantle metasomatism by ephemeral carbonatite melts: Nature 336, 459-462.

GREEN DH, 1970: Compositions of basaltic magmas as indicators of conditions of origin: application to oceanic volcanism: Royal Soc. Philos. Trans. 268, 707-721.

GREEN DH, 1973: Conditions of melting of basanite magma from garnet peridotite: Earth Planet. Sci. Lett. 17, 456-465.

GREEN DH, 1990: The role of oxidation-reduction and C-H-O fluids in determining melting conditions and magma compositions in the upper mantle: Proc. Indian Acad. Sci. 99, 153-165.

GREEN DH, FALLOON TJ and TAYLOR WR, 1987: Mantle-derived magmas - roles of variable source peridotite and variable C-H-O fluid compositions, in MYSEN, BO (ed): Magmatic processes: physicochemical principles: Geol. Soc. Spec. Publ 1, 139-154.

GREEN DH, EGGINS SM and YAXLEY GM, 1993: Mantle dynamics - the other carbon cycle: Nature 365, 210-211.

GREEN TH, 1982: Anatexis of mafic crust and high pressure crystallization of andesite, in THORPE, RS (ed): Andesites: John Wiley and Sons, pp 465-487.

GRIFFIN WL, O'REILLY SY and STABEL A, 1988: Mantle metasomatism beneath western Victoria, Australia: II. Isotope geochemistry of Cr-diopside lherzolites and Al-augite pyroxenites: Geochim. Cosmochim. Acta 52, 449-459.

GRIFFIN WL, WASS SY and HOLLIS JD, 1984: Ultramafic xenoliths from Bullenmerri and Gnotuk maars, Victoria: petrology of a subcontinental crust-mantle transition: J. Petrol. 25, 53-87.

HARLEY SL, and ODLING NWA, 1990: Reducing mantle redox options: Nature 348, p394.

HARRISON TM and WATSON EB, 1984: The behaviour of apatite during crustal anatexis: equilibrium and kinetic considerations: Geochim. Cosmochim. Acta 48, 1467-1477.

HART SR 1976: Chemical variance in deep ocean basalts: Init. Rep. DSDP 34, 301-336.

HART SR and STAUDIGEL H, 1978: Oceanic crust: age of hydrothermal alteration: Geophys. Res. Lett. 5, 1009-1012

HAURI EH, SHIMUZU N, DIEU JJ and HART, SR, 1993: Evidence for hot-spot related carbonatite metasomatism in the oceanic upper mantle: Nature 365, 221-227.

HEKINIAN D and AUMENTO F, 1973: Rocks from the Gibbs Fracture Zone and the Minia Seamount near 53°N in the Atlantic Ocean: Mar. Geol. 14, 47-72.

HEKINIAN R, 1982: Petrology of the ocean floor: Amsterdam, Elsevier 393pp.

HELFRICH GR, STEIN S, and WOOD BJ, 1989: Subduction zone thermal structure and mineralogy and their relationship to seismic wave reflectons and conversions at the slab/mantle interface: J. Geophys. Res. 94, 753-763.

HOLLAND TJB, 1980: The reaction albite = jadeite + quartz determined experimentally in the range 600-1200°C: Am. Mineral. 65, 129-134.

HOLLOWAY JR, 1973: The system pargasite-H_2O-CO_2: a model for melting of anhydrous mineral with a mixed volatile fluid: I. Experimental results to 8 kbar: Geochim. Cosmochim. Acta 37, 651-666.

HUMPHRIS SE and THOMPSON G, 1978: Hydrothermal alteration of oceanic basalts by seawater: Geochim. Cosmochim. Acta 42, 107-125.

HUNTER RH and MacKENZIE D, 1988: The equilibrium geometry of carbonate melts in rocks of mantle composition: Earth Planet. Sci. Lett. 92, 347-356.

IRVING AJ and GREEN DH 1976: Geochemistry and petrogenesis of the Newer Basalts of Victoria and South Australia: J. Geol. Soc. Aust. 21, 45-66.

IRVING AJ and WYLLIE PJ, 1975: Subsolidus and melting relationships for calcite, magnesite and the join $CaCO_3$-$MgCO_3$ to 36 kb: Geochim. Cosmochim. Acta. 39, 35-53.

IRVING AJ, 1980: Petrology and geochemistry of composite ultramafic xenoliths in alkali basalts and implications for magmatic processes within the mantle: Am. J. Sci. 280, 389-426.

JAQUES AL and GREEN DH, 1980: Anhydrous melting of peridotite at 0-15 Kb pressure and the genesis of tholeiitic basalts: Contrib. Mineral. Petrol. 73, 287-310.

JOCHUM KP, McDONOUGH WF, PALME H and SPETTEL B, 1986: Compositional constraints on the continental lithospheric mantle from trace elements in spinel peridotite xenoliths: Nature 340, 548-550.

JOHNSON RW, 1989: Intraplate volcanism in eastern Australia and New Zealand: Cambridge University Press, Cambridge, 408pp.

KÄSE H-R and METZ P, 1980: Experimental investigation of the metamorphism of siliceous dolomites IV. Equilibrium data for the reaction 1 diopside + 3 dolomite = 2 forsterite + 4 calcite + $2CO_2$: Contrib. Mineral. Petrol. 73, 151-159.

KEMPTON PD, MENZIES MA and DUGGAN MA, 1984: Petrography, petrology and geochemistry of xenoliths and megacrysts from the Geronimo Volcanic Field, southeastern Arizona, in KORNPROBST J (ed): Kimberlites II: The mantle and crust-mantle relationships: Amsterdam, Elsevier, 71-83.

KJARSGAARD BA and HAMILTON DL, 1988: Liquid immiscibility and the origin of alkali-poor carbonatites: Mineral. Mag. 52, 43-56.

KJARSGAARD BA and HAMILTON DL, 1989: The genesis of carbonatites by immiscibility, in BELL, KD, (ed): Carbonatites: genesis and evolution Unwin Hyman, London, pp388-404.

KLAPOVA H, 1985a: Petrology and geochemistry of eclogites from the Krusné hory area, Erzgebirge Mts., NW Bohemia: Terra Cognita 4, p5.

KLAPOVA H, 1985b: Metmorfitcheskaya evolyuciya eklogitov Ercgebirge (severo-zapadnaya Bogemiya, CSSR): Bull Acad. Sci. GSSR 118,369-372.

KLAPOVA H, 1988: Retrográdní premena krusnohorskych eklogitu: Vest. Ustr. Ust. geol. 63, 1010.

KLAPOVA H, 1990: Eclogites of the Bohemian part of the Saxothuringicum: Rozpr. Cesk. Akad. Ved. Rada. Mate. Prir. Ved. 100, 1-86.

KLEEMAN JD, GREEN DH and LOVERING JF, 1969: Uranium distribution in ultramafic inclusions from Victorian basalts: Earth Planet. Sci. Lett. 5, 449-458.

KOSTER VAN GROOS AF, and WYLLIE PJ, 1966: Liquid immiscibility in the system Na_2O-Al_2O_3-SiO_2-CO_2 at pressures to 1 kilobar: Am. J. Sci. 264, 234-255.

KRENTZ O, 1982: Zum Charakter der Metamorphose und zur Altersstellung pelitischer Metamorphite des westlichen Erzgebirge: Dr rer nat thesis Bergakademie Freiberg, pp176.

KRENTZ O, THOMAS R and WIEDEMANN R, 1990: Aussagen zur Regional metamorphose des mettleren und westlichen Erzgebirges mit Hilfe thermobarometischer Einschlußuntersuchungen: Z. Geol. Wiss 18, 315-326.

KURAT G, EMBEY-ISZTIN A, KRACHER A and SCHARBERT HG, 1991: The upper mantle beneath Kapfenstein and the Transdanubian Volcanic Region, E Austria and W Hungary: a comparison: Mineral. and Petrol. 44, 21-38.

KURAT G, PALME H, SPETTEL B, BADDEHAUSEN H, HOEMEISTER H, PALME C and WÄNKE H, 1980: Geochemistry of ultramafic xenoliths from Kapfenstein, Austria: evidence for a variety of upper mantle processes: Geochim. Cosmochim. Acta 44, 45-60.

LANCELOT JR and ALLEGRE CJ, 1974: Origin of carbonatitic magma in light of the Pb-U-Th isotope system: Earth Planet. Sci. Lett. 22, 233-238.

LEAKE BE, 1978: Nomenclature of amphiboles: Am. Mineral. 63, 1023-1052.

LEBAS MJ, 1977: Carbonatite-nephelinite volcanism: an African case history: London, Wiley Interscience.

LEBAS MJ, 1987: Nephelinites and carbonatites, in FITTON, JG and UPTON, BGJ, (eds): Alkaline Igneous Rocks, Oxford, Blackwell, pp 53-84.

LIANG Y and ELTHON D, 1989: Geochemistry and petrology of spinel lherzolite xenoliths from Xalapasco de La Joya, San Luis Potosi, Mexico: partial melting and mantle metasomatism: J. Geophys. Res. 95, 15,859-15,877.

LYKINS R and JENKINS D, 1991: Experimental determination of pargasite stability relations in the presence of orthopyroxene: Contrib. Mineral. Petrol. 112, 405-413.

McCULLOCH MT and CHAPPELL BW, 1982: Nd isotopic characteristics of S- and I-type granites: Earth Planet. Sci. Lett. 58, 51-64.

McDONOUGH WF and FREY FA, 1990: Rare earth elements in upper mantle rocks, in LIPIN BR and McKAY GA, (eds): Geochemistry and mineralogy of rare earth elements: Reviews in Mineralogy 21, 99-145.

McDONOUGH WF, 1990: Constraints on the composition of the continental lithospheric mantle: Earth Planet. Sci. Lett. 101, 1-18.

McDONOUGH WF, and McCULLOCH MT, 1987: The southeast Australian lithospheric mantle: isotopic constraints on its growth and evolution: Earth Planet. Sci. Lett. 86, 327-340.

McDONOUGH WF, McCULLOCH MT, and SUN S-S, 1985: Isotopic and geochemical systematics in Tertiary-Recent basalts from southeastern Australia and implications for the evolution of the subcontinental lithosphere: Geochim. Cosmochim. Acta 49, 2051-2067.

MEEN JK, 1987: Mantle metasomatism and carbonatites: an experimental study of a complex relationship: Geol. Soc. Am. Spec. Paper 215, 91-100.

MEEN JK, EGGLER DH and AYERS JC, 1989: Experimental evidence for very low solubility of rare-earth elements in CO_2-rich fluids at mantle conditions: Nature 340, 301-303.

MELSON W and VAN ANDEL TH, 1966: Metamorphism in the Mid-Atlantic Ridge, 22°N latitude: Mar. Geol. 4, 165-186.

MENZIES M and WASS SY, 1983: CO_2- and LREE-rich mantle below eastern Australia: a REE and isotopic study of alkaline magmas and apatite-rich mantle xenoliths from the Southern Highlands Province, Australia: Earth Planet. Sci. Lett. 65, 287-302.

MENZIES M, ROGERS N, TINDLE A and HAWKESWORTH C, 1987: Metasomatic and enrichment processes in lithospheric peridotites, an effect of asthenosphere-lithosphere interaction, in MENZIES M (ed): Mantle metasomatism: Academic Press, London pp313-361.

MYSEN BO and GRIFFIN WL, 1973: Pyroxene stoichiometry and breakdown of omphacite: Am. Mineral. 58, 60-63.

MYSEN BO, 1983: Rare earth element partitioning between (H_2O+CO_2) vapor and upper mantle minerals: experimental data bearing on conditions of formation of alkali basalt and kimberlite: Neues Jahrb. Miner. Abh. 146, 41-65.

NAVON O and STOLPER E, 1987: Geochemical consequences of melt percolation: the upper mantle as a chromatographic column: J. Geol. 95, 285-307.

NELSON DR, CHIVAS AR, CHAPPELL BW and McCULLOCH MT, 1988: Geochemical and isotopic systematics in carbonatites and implications for the evolution of ocean-island sources: Geochim. Cosmochim. Acta 52, 1-17.

NEWTON RC and SHARP WE, 1975: Stability of forsterite+CO_2 and its bearing on the role of CO_2 in the mantle: Earth Planet. Sci. Lett. 26, 239-243.

NICKEL KG and GREEN DH, 1984: The nature of the uppermost mantle beneath Victoria, Australia as deduced from ultramafic xenoliths, in KORNPROBST J, (ed): Kimberlites II: The mantle-crust relationships: Amsterdam, Elsevier, pp161-178.

NICOLAS A and JACKSON MD, 1982: High temperature dykes in peridotite: Origin by hydraulic fracturing: J. Petrol. 23, 568-582.

NIELSON JE and NOLLER JS, 1987: Processes of mantle metasomatism: constraints from observations of composite peridotite xenoliths: Geol. Soc. Am. Spec. Paper 215, 61-76.

NIXON PH and BOYD FR, 1979: Garnet bearing lherzolites and discrete nodule suites from the Malaita alnoite, Solomon Islands, SW Pacific, and their bearing on oceanic composition and geotherm, in BOYD FR and MEYER HOA (eds): The mantle sample: inclusions in kimberlites and other volcanics: Proc. Int. Kimberlite Conf. 2, 400-423.

O'REILLY SY and GRIFFIN WL, 1985: A xenolith-derived geotherm for southeastern Australia and its geophysical implications: Tectonophysics 111,41-64.

O'REILLY SY and GRIFFIN WL, 1988: Mantle metasomatism beneath western Victoria, Australia: I. Metasomatic processes in Cr-diopside lherzolites: Geochim. Cosmochim. Acta 53, 433-447.

O'REILLY SY, GRIFFIN WL and RYAN CG, 1991: Residence of trace elements in metasomatised spinel lherzolite xenoliths: a proton microprobe study: Contrib. Mineral. Petrol. 109, 98-113.

OKAY AI, XU S and SENGOR AMC, 1989: Coesite from the Dabie Shan eclogites, central China: Eur. J. Mineral. 1, 595-598.

OTTONELLO G, 1980: Rare earth abundances in some spinel peridotite xenoliths from Assab (Ethiopia): Geochim. Cosmochim. Acta 44, 1855-1901.

OXBURGH ER and TURCOTTE DL, 1970: Thermal structure of island arcs: Geol. Soc. Am. Bull. 81, 1665-1688.

OXBURGH ER and TURCOTTE DL, 1976: The physico-chemical behaviour of the descending lithosphere: Tectonophys. 32, 107-128.

PEARCE JA, 1975: Basalt geochemistry used to investigate past tectonic environments on Cyprus: Tectonophys. 25, 41-67.

PREß S, WITT G, SECK HA, EONOV D, and KOVALENKO VI, 1986: Spinel peridotite xenoliths from the Tariat Depression, Mongolia: I. Major element chemistry and mineralogy of a primitive mantle xenolith suite: Geochim. Cosmochim. Acta 50, 2587-2600.

RANKIN AH and LEBAS MJ, 1974: Nahcolite ($NaHCO_3$) in inclusions in apatites from some E. African ijolites and carbonatites: Mineral. Mag. 41, 155-164.

RICHARDSON SH, HART SR and STAUDIGEL H, 1980: Vein mineral ages of old oceanic crust: J. Geophys. Res. 85, 7195-7200.

RINGWOOD AE, 1991: Phase transformations and their bearing on the constitution and dynamics of the mantle: Geochim. Cosmochim. Acta 55, 2083-2110.

RODEN MF, FREY FA and FRANCIS DM, 1984: An example of consequent mantle metasomatism in peridotite xenoliths from Nunivak Island, Alaska: J. Petrol. 25, 546-577.

RUDNICK RL, McDONOUGH WF and CHAPPELL BW, 1993: Carbonatite metasomatism in the northern Tanzanian mantle: petrographic and geochemical characteristics: Earth Planet. Sci. Lett. 114, 463-475.

RUDNICK RL, McDONOUGH WF and ORPIN A, 1992: Northern Tanzanian peridotite xenoliths: A comparison with Kaapvaal peridotites and inferences on metasomatic interactions: in press

RÅHEIM A, and GREEN DH, 1974: Experimental determination of the temperature and pressure dependence of the Fe-Mg partition coefficient for coexisting garnet and clinopyroxene: Contr. Mineral. Petrol. 48, 179-203.

SCHNEIDER ME, and EGGLER DH, 1986: Fluids in equilibrium with peridotite minerals: implications for mantle metasomatism: Geochim. Cosmochim. Acta 50, 711-724.

SHEPPARD SMF and DAWSON JB, 1975: Hydrogen, carbon and oxygen isotope studies of megacryst and matrix minerals from Lesothan, South African kimberlites: Phys. Chem. Earth 9, 747-763.

SILVA LC, LE BAS MJ, and ROBERTSON AHF, 1981: An oceanic carbonatite volcano on Santiago, Cape Verde Islands: Nature 294, 644-645.

SOBOLEV NV and SHATSKY VS, 1990: Diamond inclusions in garnets from metamorphic rocks: a new environment for diamond formation: Nature 343, 742-746.

SOBOLEV NV, GALIMOV EM, IVANOSKAYA NN and YEFIMOVA ES, 1979: Isotopic composition of the carbon from diamonds containing inclusions: Doklady Akademia Nauk USSR 249, 1217-1220.

SONG Y and FREY FA, 1989: Geochemistry of peridotite xenoliths in basalt from Hannuoba, Eastern China: implications for subcontinental mantle heterogeneity: Geochim. Cosmochim. Acta 53, 97-113.

STOLZ AJ and DAVIES GR, 1988: Chemical and isotopic evidence from spinel lherzolite xenoliths for episodic metasomatism of the upper mantle beneath Southeast Australia: J. Petrol. Spec. Issue, 303-330.

STOSCH H-G and LUGMAIR GW, 1986: Trace element and Sr and Nd isotope geochemistry of peridotite xenoliths from the Eifel (West Germany) and their bearing on the evolution of the subcontinental lithosphere: Earth Planet. Sci. Lett. 80, 281-298.

STOSCH H-G, and SECK HA, 1980: Geochemistry and mineralogy of two spinel peridotite suites from Dreiser Weiher, West Germany: Geochim. Cosmochim. Acta 44, 457-470.

SUN S-S and McDONOUGH WF, 1989: Chemical and isotopic systematics of oceanic basalts: implications for mantle composition and processes, in SAUNDERS, AD and NORRY, MJ (eds): Magmatism in the ocean basins: Geological Society Special Publication 42, 313-345.

SWEENEY RJ, GREEN DH and SIE SH, 1992: Trace and minor element partitioning between garnet and amphibole and carbonatitic melt: Earth Planet. Sci. Lett. 113, 1-14.

TAGIRI M and BAKIROV A, 1990: Quartz pseudomorph after coesite in garnet from a garnet-chloritoid-talc schist, Northern Tien-Shan, Kirghiz, USSR: Japan Academy of Science Proceedings 66, 135-139.

TAYLOR WR, 1985: The role of C-H-O fluids in upper mantle processes: a theoretical, experimental and spectroscopic study: Unpublished PhD thesis, University of Tasmania.

TAYLOR WR, 1986: A reappraisal of the nature of fluids included by diamond - a window to deep-seated mantle fluids and redox conditions, in HERBERT, HK (ed): Proceedings of the conference on stable isotopes and fluid processes in mineralization: Publ. Geol. Dept. and Extension Service, UWA 23.

THIBAULT Y and EDGAR AD, 1990: Patent mantle metasomatism: inferences based on experimental studies: Proc. Indian Acad. Sci. 99, 21-37.

THIBAULT Y, EDGAR AD and LLOYD FE, 1992: Experimental investigation of melts from a carbonated phlogopite lherzolite: implications for metasomatism in the continental lithospheric mantle: Am. Mineral. 77, 784-794.

TOKSÖZ MN, MINEAR JW and JULIAN BR, 1971: Temperature field and geophysical effects of a downgoing slab: J. Geophys. Res. 76, 1113-1138.

TOKSÖZ MN, SLEEP NH and SMITH AT, 1973: Evolution of the downgoing lithosphere and mechanisms of deep focus earthquakes: Geophys. J. R. Astro. Soc. 35, 285-310.

TORAMARU A and FUFII N, 1986: Connectivity of a melt phase in a partially molten peridotite: J. Geophys. Res. 91, 9239-9252.

TRULL T, NADEAU S, PINEAU F, POLVE M and JAVOY, M, 1993: C-He systematics in hotspot xenoliths: Implications for mantle carbon contents and carbon recycling: Earth Planet. Sci. Lett. 118, 43-64.

TWYMAN JD and GITTINS J, 1985: Alkalic carbonatite magmas: parental or derivative: J. Geol. 142, 706-707.

TWYMAN JD and GITTINS J, 1987: Alkalic carbonatite magmas: parental or derivative, in FITTON JG and UPTON BGJ, (eds): Alkaline Igneous Rocks, Oxford, Blackwell, pp 85-94.

VARNE R and GRAHAM AL, 1971: Rare earth abundances in hornblende and clinopyroxene of a hornblende lherzolite xenolith: implications for upper mantle fractionation processes: Earth Planet. Sci. Lett. 13, 11-18.

VARNE R, 1977: On the origin of spinel lherzolite inclusions in basaltic rocks from Tasmania and elsewhere: J. Petrol. 18, 1-23.

WALLACE ME and GREEN DH, 1988: An experimental determination of primary carbonatite composition: Nature 335, 343-346.

WALLACE ME, 1989: Stability of amphibole and carbonate in the upper mantle: Unpubl. PhD Thesis, University of Tasmania.

WANG X and LIOU JG, 1991: Regional ultrahigh-pressure coesite-bearing eclogitic terrane in central China: evidence from country rocks, gneiss, marble and metapelite: Geology 19. 1085-1088.

WANG X, JING Y, LIOU JG, PAN G, XIA M and MARUYAMA S, 1990: Field occurences and petrology of eclogites from the Dabie Mountains, Anhui, Central China: Lithos 25, 119-131.

WANG X, LIOU JG and MAO HK, 1989: Coesite-bearing eclogites from the Dabie Mountains in central China: Geology 17, 1085-1088.

WANG X, LIOU JG and MARUYAMA S, 1992: Coesite-bearing eclogites from the Dabie Mountains, Central China: petrogensis, P-T paths, and implications for regional tectonics: J. Geol. 100, 231-250.

WASS SY and ROGERS NW, 1980: Mantle metasomatism - precursor to continental alkaline volcanism: Geochim. Cosmochim. Acta 44, 1811-1823.

WASS SY, 1979: Fractional crystallization in the mantle of late-stage kimberlitic liquids - evidence in xenoliths from the Kiama area, NSW, Australia, in BOYD FR and MEYER HOA (eds): The mantle samples: inclusions in kimberlites and other volcanics: Washington p336.

WATSON EB and BRENAN JM, 1987: Fluids in the lithosphere: 1. Experimentally determined wetting characteristics of CO_2-H_2O fluids and their implications for fluid transport, host-rock physical properties, and fluid inclusion formation: Earth Planet. Sci. Lett. 85, 497-515.

WATSON EB, BRENAN JM and BAKER DR, 1990: Distribution of fluids in the continental mantle: Oxford Monographs on Geology and Geophysics 16, 111-125.

WELLS PRA, 1979: Chemical and thermal evolution of the Archean Sialic crust, south-west Greenland: J. Petrol. 20, 187-226.

WENDLANDT RF and HARRISON WJ, 1979: Rare earth partitioning between immiscible carbonate and silicate liquids and CO_2 vapor: results and implications for the formation if light rare earth enriched rocks: Contr. Mineral. Petrol. 69, 409-419.

WILSHIRE HG and PIKE JEN, 1975: Upper mantle diapirism: evidence from analogous features in alpine peridotites and ultramafic inclusions in basalt: Geology 3, 467-470.

WILSHIRE HG and SHERVAIS JW, 1975: Al-augite and Cr-diopside ultramafic xenoliths in basaltic rocks from Westen United States: structural and textural relationships: Phys. Chem. Earth 9, 257-272.

WILSHIRE HG, NIELSON JE, PIKE JE, MEYER CE and SCHWARZMAN EC, 1980: Amphibole-rich veins in lherzolite xenoliths, Dish Hill and Deadman Lake, California: Am. J. Sci. 280, 576-593.

WITT G and SECK HA, 1989: Origin of amphibole in recrystallized and porphyroclastic mantle xenoliths from Rhenish Massif: implications for the nature of mantle metasomatism: Earth Planet. Sci. Lett. 91, 327-340.

WYLLIE PJ and HUANG WL, 1976: Carbonation and melting reactions in the system CaO-MgO-SiO_2-CO_2 at mantle pressures with geophysical and petrological applications: Contrib. Mineral. Petrol. 54, 79-107.

WYLLIE PJ and HUANG WL, 1976: Petrogenetic grid for siliceous dolomites extended to mantle peridotite compositions and to conditions for magma generation: Am. Mineral. 61, 691-698.

WYLLIE PJ, 1987: Discussion of recent papers on carbonated peridotite, bearing on mantle metasomatism and magmatism: Earth Planet. Sci. Lett. 82, 391-397.

XUE X, BAARDSGAARD H, IRVING AJ and SCARFE CM, 1990: Geochemical and isotopic characteristics of lithospheric mantle beneath West Kettle River, British Columbia: Evidence from ultramafic xenoliths: J. Geophys. Res. 95, 15,879-15,891.

YAXLEY GM, CRAWFORD AJ and GREEN DH, 1991: Evidence for carbonatite metasomatism in spinel peridotite xenoliths from western Victoria, Australia: Earth Planet. Sci. Lett. 107, 305-317.

ZHANG Y and ZINDLER A, 1993: Distribution and evolution of carbon and nitrogen in Earth: Earth Planet. Sci. Lett. 117, 331-345.

ZINDLER A and JAGOUTZ E, 1975: Mantle cryptology: Geochim. Cosmochim. Acta 52, 319-333.

APPENDIX A

DETAILS OF ANALYTICAL METHODS USED IN THIS STUDY

A1: Electron probe microanalysis (EPMA)
A2: X-ray fluorescence spectroscopy (XRF)
A3: Instrumental neutron activation analysis (INAA)
A4: Isotope dilution (ID)
A5: Scanning electron micrscopy (SEM)

APPENDIX A: DETAILS OF ANALYTICAL METHODS USED IN THIS STUDY

A1. Electron probe microanalysis (EPMA)

Constituent mineral, glass and carbonate phases in the carbonatite metasomatised peridotite xenoliths (Chapters 2 and 3), the Czechoslovakian carbonated eclogites (Chapter 6), and all experimental runs (Chapters 4 and 5) were analysed using a Cameca SX50 electron probe microanalyser, at the Central Science Laboratory, University of Tasmania, which was calibrated using recognised international natural mineral standards (PAP data reduction). Below are listed the standards used in calibrating each element.

Na K_α (anorthoclase); Mg K_α (Mg-olivine); Al K_α (corundum); Si K_α (quartz); P K_α (apatite); Cl K_α (halite); K K_α (microcline); Ca K_α (apatite); Ti K_α (ilmenite); Cr K_α (chromite); Mn K_α (rhodonite); Ni K_α (nickel silicide).

Calibration was routinely checked before, during and after each EPMA session using appropriate secondary standards, the compositions of which are listed in table A1.

Table A1: Secondary standards used for routine checking of EPMA calibration. Column 1 is Durango apatite, 2 is Delegate clinopyroxene, and 3 is a chromite from New Caledonia.

	1	2	3
SiO_2	0.34	51.00	
Al_2O_3	0.07	5.50	9.92
Fe_2O_3	0.06		
FeO	0.00	4.01	13.04
MgO	0.01	16.08	15.20
CaO	54.02	21.06	
Na_2O	0.23	0.84	
K_2O	0.01	0.00	
TiO_2		0.52	
P_2O_5	40.78		
MnO	0.01	0.08	0.11
Cr_2O_3		0.68	60.50
H_2O	0.01		
F	3.23		
Cl	0.46		
Total	99.23	99.77	98.77

Analytical conditions varied depending on the phase being analysed. Carbonates and glasses were analysed using an accelerating voltage of 15kV and a beam current of 10nA. In order to minimize specimen damage, and volatile loss, the beam was usually defocussed, with the maximum diameter possible to prevent overlap with other adjacent phases. Other phases (silicate minerals, apatite, spinel) were analysed with an accelerating voltage of 15kV and 20nA beam current, generally with a focussed, 1μm beam.

Counting times varied between 10 and 30 seconds on peaks, and 5 and 15 seconds on background, depending on the elemental abundance. Below are listed the spectrometers used for counting each element;

For silicate, carbonate and glass analyses

Spectrometer	Elements
TAP	Na, Mg, Al, Si, P
PET	Cl, K, Ca, Ti
LiF	Cr, Mn, Fe, Ni

For apatite analyses

Spectrometer	Elements
TAP	F, Mg, Si, Sr, P
PET	Cl, Ca, Ba
LiF	Fe

For spinel analyses

Spectrometer	Elements
TAP	Mg, Al, Si
PET	Ti, Cr
LiF	Mn, Fe, Ni

A2. X-ray fluorescence analyses (XRF)

Major and minor elements, and some trace elements (Ba, Sc, Nb, Zr, Y, Sr, Rb, Cr, Ni, V) were determined using a Phillips PW 1410 X-ray Fluorescence spectrometer at the Geology Department, University of Tasmania.

Sample preparation was performed as follows. In order to avoid contamination of the analyses caused by possible minor infiltration of the peridotite xenolith by the host

magma, central portions of the nodules were cut out using a diamond saw, and then cleaned ultrasonically to remove fragments of the blade. The resultant blocks were coarse crushed between sheets of plastic, and then pulverized to powder in an agate ring mill.

Powders were prepared for major and minor element analysis by fusing 1.5g $LiBO_3$ flux, 0.02g $LiNO_3$ oxidiser and 0.28g of powdered sample in a Pt crucible, and quenching the melt into a glass disc. Further 5g splits of the xenolith powders were compressed into powder pills, which were used for XRF trace element analysis. Ignition loss (LOI) was determined on all samples by firing ≈1g of the pre-dried powder at 1000°C overnight.

The X-ray tube was operated at 60kV and 40mA for all elements, except Ba, Sc, La and Ce, for which 50kV and 50mA were used. Instrumental conditions and detection limits are listed in table A2. Three standards (TASUM-1, TASDOL and TASBAS) and a silica blank were utilized during analysis runs. Compositions of standards are listed in table A3.

A3. Intrumental neutron activation analysis (INAA)

INAA was performed on both wholerock material and clinopyroxene separates, at Becquerel Laboratories, Lucas Heights, New South Wales. Elements analysed were REE [La(0.1), Ce (1.0), Nd(2.0), Sm(0.05), Eu(0.2),Tb(0.5),Ho(0.5),Yb(0.1) and Lu(0.1)], and Sc(0.05), Hf(0.5), Ta(0.5) and Th(0.2). Numbers in paretheses are detection limits.

Wholerock samples were splits from pulverized material prepared for XRF (see section A2). Results are presented in table B1. INAA was also performed on clinopyroxene separates from samples 71000 and 71008. These were separated from the host rocks using the method described in section A4. Results are presented in table 3.1 (Chapter 3).

A4. Isotope Dilution (ID) analyses

Sm-Nd and Rb-Sr isotope analyses were performed at PRISE laboratories (ANU) on wholerock powders from samples 71001, 76993, 70965, 2631, 76989, 71008 and 71000. In addition, apatite and clinopyroxene separates from samples 71000 and 71008 were analysed. The results are presented in table 3.3 (Chapter 3).

Table A2: Instrumental conditions and detection limits for XRF analyses of peridotite xenoliths.

Major elements.

Oxide	Line	Tube	Crystal	Counter	Collimator	Vacuum	Time (sec)
SiO2	K alfa	Rh	PE	Flow	Coarse	YES	100
TiO2	K alfa	Rh	LiF200	Flow	Coarse	YES	20
Al2O3	K alfa	Rh	PE	Flow	Coarse	YES	100
Fe2O3	K alfa	Rh	LiF200	Flow	Fine	YES	20
MnO	K alfa	Rh	LiF200	Flow	Fine	YES	40
MgO	K alfa	Rh	TLAP	Flow	Coarse	YES	100
CaO	K alfa	Rh	LiF200	Flow	Fine	YES	20
Na2O	K alfa	Rh	TLAP	Flow	Coarse	YES	100
K2O	K alfa	Rh	PE	Flow	Coarse	YES	20
P2O5	K alfa	Rh	GE	Flow	Coarse	YES	40

Trace elements.

Element	Line	Tube	Crystal	Counter	Collimator	Vacuum	LLD (ppm)	Precision
Sc	K alfa	Cr	LiF200	Flow	Coarse	YES	1	10±1, 30±1
V	K alfa	Au	LiF220	Flow	Fine	YES	3	30±2, 100±1
Cr	K alfa	Au	LiF200	Flow	Fine	YES	2	10±2, 400±4
Ni	K alfa	Au	LiF200	Flow	Fine	YES	1	3±0.5, 20±0.5, 200±2
Rb	K alfa	Rh	LiF220	Scintillation	Fine	NO	2	10±1, 70±1, 170±2
Sr	K alfa	Rh	LiF220	Scintillation	Fine	NO	2	10±1, 200±2, 500±5
Y	K alfa	Rh	LiF220	Scintillation	Fine	NO	1.5	10±2, 20±1, 100±2
Zr	K alfa	Rh	LiF220	Scintillation	Fine	NO	1	100±2, 250±4, 500±10
Nb	K alfa	Rh	LiF220	Scintillation	Fine	NO	1	10±0.5, 20±1
Ba	L alfa	Cr	LiF200	Flow	Fine	YES	3	500±5, 1200±5

Table A3: Major, minor and trace element compositions of standards used during XRF analysis of peridotite xenoliths.

Sample	TASUM-1	TASBAS	TASDOL
SiO2	41.34	44.56	53.37
TiO2	0.01	2.31	2.47
Al2O3	0.77	14.14	13.20
Fe2O3	10.01	12.65	12.47
MnO	0.21	0.17	0.17
MgO	35.40	8.16	2.86
CaO	0.04	7.81	6.34
Na2O	0.00	5.43	3.19
K2O	0.00	1.86	1.73
P2O5	0.00	0.97	0.94
Others	0.40	0.40	0.31
LOI	11.92	1.56	2.96
TOTAL	100.10	100.02	100.01
Ba	5	204	395
Rb	0.7	16.5	70.7
Nb	0	61.4	11
La	0	43.4	33
Ce	0	89	69
Sr	6	1025	281
Nd	0	41.2	38
Zr	0	260	209
Y	0	23.1	52.8
Sc	13	13.1	27.5
V	32	163	255.4
Cr	5019	198	2.4
Ni	1595	154	4
Pb	2	5.9	11
Th	1	4.7	6.6
U	0.9	1.5	2.1

Wholerock material used were splits of material crushed in preparation for XRF analyses (see section A2 above).

Mineral separations were performed by first coarse crushing the sample between sheets of plastic with a hammer. The coarse crushed material was then subjected to magnetic separation, producing an olivine-rich fraction, and a fraction consisting dominantly of clinopyroxene and apatite. These phases were separated by hand picking under a binocular microscope. Only mineral grains which were free of visible inclusions and surface contaminants were selected for analyses.

The clinopyroxene separates were then cleaned ultrasonically in doubly distilled water for 10 minutes, followed by decanting, and rinsing in distilled water. This procedure was repeated 3 times. The clinopyroxene was then ultrasonically cleaned twice in 2 mol L^{-1} hydrochloric acid (AR-grade), rinsed four times in distilled water and dried at 120°C. Finally the material was crushed under AR acetone using an agate mortar and pestle, and redried. Apatite separates were prepared in the same manner, but without acid leaching.

The analyses were performed at The Australian National University on a Finnigan MAT 261 multicollector mass spectrometer, by Dr CM Fanning (71000, 71008, and mineral separates thereof), and by Dr S Eggins, using procedures which are described by McCulloch and Chappell (1982). Sr isotopic ratios were normalized to $^{86}Sr/^{88}Sr$ = 0.1194 and Nd to $^{146}Nd/^{144}Nd$ = 0.719. Precision for the Sr ratios is 0.003% or better at the 95% confidence limit, and 0.002% for Nd.

A5. Scanning electron microscopy (SEM)

SEM was used for examination of textures, and photography of back scattered electron images of experimental run products (Chapters 4 and 5). A Phillips 505 Scanning Electron Microscope, housed at the Central Science Laboratory, University of Tasmania was used. An accelerating voltage of 20 or 25 kV was used.

APPENDIX B

REPRESENTATIVE ELECTRON MICROPROBE ANALYSES OF MINERAL PHASES AND GLASSES IN WESTERN VICTORIAN, CARBONATITE METASOMATISED SPINEL PERIDOTITE XENOLITHS.

Table B1: Representative analyses of primary olivine grains. Fo is mol% forsterite.

Sample	76987	70965	70969	70972	71000	71001	71007	2631	2638	76988	76988	73797	76989	76990	76991	76992	70987	70997
Field No.	AN8									SH19	SH19		SH1	SH52	LE17	NO11		
											Poikilitic ol							
SiO2	40.06	41.12	41.00	40.85	40.67	40.40	41.10	40.43	40.11	40.47	40.92	40.92	41.04	41.06	40.89	40.06	40.25	40.88
TiO2	0.01	0.01	0.02	0.01	0.02	0.00	0.02	0.01	0.01	0.02	0.01	0.01	0.01	0.00	0.01	0.01		0.01
Al2O3	0.01	0.01	0.01	0.01	0.02	0.16	0.00	0.01	0.01	0.03	0.04	0.02	0.02	0.01	0.01	0.02		0.01
Cr2O3	0.01	0.01	0.02	0.02	0.02	0.02	0.03	0.01	0.02	0.01	0.04	0.01	0.01	0.02	0.02	0.03		0.01
MgO	47.68	49.09	49.49	49.76	48.72	47.88	49.21	49.03	46.67	48.80	50.03	48.90	49.49	49.02	48.48	48.43	46.17	48.93
CaO	0.03	0.05	0.03	0.04	0.05	0.03	0.02	0.03	0.04	0.03	0.21	0.01	0.03	0.05	0.03	0.04		0.04
MnO	0.21	0.10	0.14	0.20	0.11	0.24	0.11	0.19	0.32	0.14	0.08	0.13	0.11	0.15	0.20	0.19		0.14
FeO	10.84	9.69	8.92	8.69	9.97	10.82	9.66	9.03	12.50	10.08	8.17	9.15	8.84	9.82	10.48	9.89	13.40	10.36
NiO	0.34	0.35	0.35	0.36	0.27	0.35	0.39	0.36	0.35	0.34	0.30	0.34	0.36	0.37	0.34	0.32	0.37	0.35
Total	99.19	100.43	99.97	99.94	99.83	99.90	100.55	99.10	100.02	99.93	99.79	99.49	99.92	100.50	100.47	98.99	100.19	100.73
Fo	88.70	90.03	90.81	91.07	89.70	88.74	90.07	90.63	86.93	89.61	91.61	90.50	90.89	89.90	89.18	89.72	85.99	89.38
Si	0.9965	1.0029	1.0016	0.9981	0.9996	0.9972	1.0015	0.9981	0.9972	0.9952	0.9985	1.0050	1.0026	1.0018	1.0013	0.9945	1.0010	0.9980
Ti	0.0002	0.0001	0.0004	0.0001	0.0004	0.0000	0.0004	0.0002	0.0001	0.0003	0.0002	0.0002	0.0001	0.0001	0.0003	0.0002	0.0000	0.0001
Al	0.0003	0.0004	0.0002	0.0003	0.0005	0.0046	0.0001	0.0002	0.0002	0.0008	0.0012	0.0006	0.0005	0.0004	0.0002	0.0004	0.0000	0.0003
Cr	0.0002	0.0002	0.0003	0.0004	0.0003	0.0004	0.0006	0.0003	0.0003	0.0003	0.0008	0.0002	0.0002	0.0004	0.0004	0.0005	0.0000	0.0002
Mg	0.2255	1.7842	1.8013	1.8115	1.7844	1.7608	1.7866	1.8033	1.7289	1.7883	1.8191	1.7897	1.8014	1.7822	1.7686	1.7914	1.7109	1.7798
Ca	0.0008	0.0013	0.0009	0.0011	0.0013	0.0008	0.0005	0.0008	0.0010	0.0009	0.0055	0.0003	0.0008	0.0012	0.0009	0.0010	0.0000	0.0011
Mn	0.0044	0.0021	0.0028	0.0042	0.0022	0.0050	0.0023	0.0040	0.0067	0.0029	0.0017	0.0028	0.0024	0.0030	0.0042	0.0040	0.0000	0.0029
Fe	0.2255	0.1976	0.1823	0.1776	0.2048	0.2234	0.1969	0.1865	0.2599	0.2074	0.1667	0.1880	0.1806	0.2002	0.2146	0.2053	0.2787	0.2115
Ni	0.0079	0.0079	0.0078	0.0081	0.0061	0.0081	0.0088	0.0082	0.0081	0.0078	0.0068	0.0077	0.0083	0.0084	0.0078	0.0074	0.0085	0.0079
Total	3.0031	2.9967	2.9977	3.0014	2.9996	3.0002	2.9978	3.0015	3.0024	3.0039	3.0003	2.9944	2.9969	2.9977	2.9982	3.0048	2.9990	3.0017

Table B1: continued

Sample Field No.	71004	71008	70961	76993 SH34	76994 LE10	71003	71006	70982	76995 SH20	76996 SH8	71023	76997 SH40	76998 SH31
SiO2	40.28	40.49	40.19	40.58	40.07	40.75	40.08	41.11	40.96	41.22	40.64	40.95	41.20
TiO2	0.01	0.03	0.01	0.01	0.00	0.00	0.03	0.01	0.01	0.02	0.01	0.01	0.01
Al2O3	0.02	0.03	0.02	0.01	0.00	0.01	0.02	0.01	0.02	0.01	0.03	0.01	0.01
Cr2O3	0.01	0.01	0.03	0.02	0.00	0.01	0.02	0.02	0.04	0.03	0.01	0.00	0.01
MgO	48.85	47.63	46.97	49.15	47.21	49.45	46.95	50.09	50.01	48.88	49.34	49.74	49.49
CaO	0.04	0.03	0.05	0.03	0.03	0.03	0.04	0.04	0.06	0.02	0.02	0.05	0.03
MnO	0.18	0.23	0.20	0.13	0.18	0.16	0.12	0.17	0.10	0.17	0.17	0.15	0.10
FeO	9.36	11.53	12.64	9.14	11.13	8.46	11.94	8.91	8.32	10.22	8.67	8.82	8.79
NiO	0.35	0.32	0.34	0.38	0.35	0.41	0.34	0.37	0.40	0.35	0.43	0.43	0.38
Total	99.09	100.31	100.43	99.46	98.97	99.34	99.53	100.78	99.92	100.92	99.35	100.16	100.01
Fo	90.30	88.04	86.88	90.55	88.32	91.24	87.51	90.92	91.46	89.49	91.02	90.95	90.93
Si	0.9962	0.9982	0.9951	0.9982	0.9998	1.0010	0.9979	0.9973	0.9989	1.0029	0.9992	0.9987	1.0050
Ti	0.0001	0.0005	0.0001	0.0003	0.0000	0.0000	0.0005	0.0002	0.0001	0.0003	0.0001	0.0001	0.0001
Al	0.0005	0.0009	0.0004	0.0003	0.0000	0.0002	0.0006	0.0002	0.0007	0.0004	0.0010	0.0003	0.0003
Cr	0.0002	0.0003	0.0006	0.0004	0.0000	0.0003	0.0003	0.0004	0.0008	0.0005	0.0002	0.0001	0.0002
Mg	1.8001	1.7500	1.7330	1.8018	1.7555	1.8099	1.7419	1.8105	1.8174	1.7721	1.8076	1.8077	1.7985
Ca	0.0010	0.0009	0.0014	0.0007	0.0007	0.0008	0.0009	0.0011	0.0017	0.0006	0.0004	0.0013	0.0007
Mn	0.0037	0.0047	0.0041	0.0028	0.0039	0.0033	0.0025	0.0035	0.0020	0.0036	0.0035	0.0031	0.0020
Fe	0.1935	0.2378	0.2616	0.1880	0.2322	0.1738	0.2486	0.1807	0.1696	0.2080	0.1783	0.1799	0.1793
Ni	0.0081	0.0073	0.0078	0.0087	0.0081	0.0095	0.0078	0.0082	0.0091	0.0079	0.0098	0.0098	0.0085
Total	3.0033	3.0007	3.0042	3.0011	3.0002	2.9988	3.0012	3.0022	3.0003	2.9964	3.0001	3.0010	2.9947

Table B2: Representative analyses of primary and secondary orthopyroxene grains. Mg#= 100*Mg/(Mg+∑Fe).

Sample	71007	71004	71004	71008	71008	70961	76993	76994	71003	71006	70982	76995	76996	71023	76997	76998
Field No.							SH34	LE10				SH20	SH8		SH40	SH31
			Secondary opx		Secondary opx											
SiO2	57.71	56.20	57.81	56.23	56.87	57.12	57.47	56.76	55.92	56 25	57.48	57.00	59.04	57.57	56.99	57.28
TiO2	0.01	0.01	0.03	0.03	0.04	0.03	0.02	0.05	0.03	0 02	0.02	0.03	0.01	0.02	0.05	0.02
Al2O3	1.32	2.54	1.85	1.87	1.31	0.80	0.87	1.93	2.37	1.98	1.19	1.42	0.21	0.76	1.79	1.60
Cr2O3	0.29	0.04	0.35	0.54	0.37	0.30	0.30	0.49	0.54	0.39	0.35	0.36	0.15	0.26	0.42	0.33
MgO	34.73	34.04	34.75	33.13	33.55	34.81	34.65	33.50	33.84	32.90	34.92	34.81	34.85	34.69	34.70	34.63
CaO	0.40	0.44	0.47	0.86	0.66	0.60	0.43	0.51	0.37	0.53	0.48	0.49	0.34	0.35	0.35	0.42
MnO	0.19	0.21	0.12	0.18	0.17	0.13	0.14	0.16	0.15	0.21	0.17	0.13	0.16	0.17	0.17	0.13
FeO	6.20	5.97	5.53	7.27	7.19	5.99	5.71	6.55	5.61	7.40	5.54	5.63	6.48	5.48	5.52	5.52
NiO	0.11	0.09	0.26	0.08	0.09	0.10	0.07	0.11	0.08	0.07	0.09	0.11	0.07	0.10	0.07	0.09
Na2O	0.08	0.08	0.08	0.15	0.10	0.10	0.09	0.16	0.11	0.12	0.13	0.09	0.08	0.08	0.05	0.07
Total	101.05	99.62	101.25	100.34	100.35	99.97	99.75	100.23	99.03	99 88	100.40	100.07	101.40	99.48	100.12	100.09
Mg#	90.89	91.04	91.80	89.04	89.26	91.19	91.53	90.11	91.49	88.79	91.83	91.68	90.56	91.86	91.80	91.79
Si	1.9704	1.9447	1.9659	1.9487	1.9666	1.9720	1.9825	1.9591	1.9454	1.9555	1.9710	1.9625	2.0060	1.9889	1.9582	1.9677
Ti	0.0003	0.0002	0.0008	0.0007	0.0010	0.0008	0.0005	0.0014	0.0009	0.0006	0.0004	0.0007	0.0003	0.0004	0.0013	0.0004
Al	0.0531	0.1035	0.0741	0.0764	0.0534	0.0325	0.0353	0.0784	0.0972	0.0809	0.0481	0.0575	0.0086	0.0309	0.0724	0.0649
Cr	0.0078	0.0011	0.0094	0.0149	0.0101	0.0082	0.0082	0.0134	0.0148	0.0106	0.0095	0.0098	0.0042	0.0072	0.0115	0.0090
Mg	1.7672	1.7553	1.7609	1.7111	1.7288	1.7909	1.7809	1.7228	1.7542	1.7045	1.7844	1.7857	1.7643	1.7855	1.7767	1.7726
Ca	0.0147	0.0162	0.0171	0.0319	0.0245	0.0223	0.0160	0.0190	0.0140	0.0199	0.0176	0.0181	0.0124	0.0131	0.0130	0.0154
Mn	0.0056	0.0062	0.0035	0.0052	0.0050	0.0037	0.0040	0.0048	0.0044	0.0063	0.0049	0.0037	0.0047	0.0050	0.0050	0.0039
Fe	0.1771	0.1727	0.1572	0.2106	0.2079	0.1731	0.1648	0.1891	0.1632	0.2153	0.1588	0.1621	0.1840	0.1582	0.1587	0.1587
Na	0.0051	0.0056	0.0053	0.0100	0.0067	0.0065	0.0062	0.0107	0.0075	0.0078	0.0089	0.0058	0.0052	0.0051	0.0033	0.0045
Total	4.0013	4.0055	3.9942	4.0096	4.0040	4.0099	3.9983	3.9987	4.0015	4.0013	4.0037	4.0059	3.9897	3.9942	4.0002	3.9971
En	90.21	90.28	90.99	87.59	88.15	90.17	90.78	89.22	90.83	87.88	91.00	90.83	89.98	91.25	91.19	91.06
Fs	9.04	8.88	8.13	10.78	10.60	8.71	8.40	9.79	8.45	11.10	8.10	8.25	9.38	8.08	8.15	8.15
Wo	0.75	0.84	0.88	1.63	1.25	1.12	0.82	0.98	0.72	1.03	0.90	0.92	0.63	0.67	0.67	0.79

Table B3: Representative analyses of primary spinels. Mg*=100*Mg/(Mg+Fe^{2+}), Cr*= 100*Cr/(Cr+Al) and Fe^{3+}*=Fe^{3+}/∑Fe. Cations were calculated on the basis of perfect stoichiometry.

Sample	70965	70969	70972	71000	71001	71007	2631	2638	76988	73797	76989	76990	76991	76992	70987	70997	71004	71008	76993
Field No.									SH19		SH1	SH52	LE17	NO11					SH34
SiO2	0.05	0.03	0.03		0.01	0.06	0.02	0.01	0.01	0.01	0.05	0.19	0.00	0.10		0.04	0.07		0.02
TiO2	0.42	0.11	0.08	0.24	0.26	0.06	0.16	0.29	0.26	0.06	0.14	0.15	0.19	0.34	0.66	0.53	0.55	0.27	0.21
Fe2O3	2.45	1.73	1.86	2.07	3.64	1.99	2.52	6.94	3.00	5.59	2.28	2.64	4.43	3.25	2.49	3.26	2.17		2.01
Al2O3	10.51	13.03	12.34	23.44	6.01	24.87	12.47	13.28	15.36	12.68	11.66	11.26	14.01	12.67	32.36	20.26	23.73	21.60	15.30
Cr2O3	58.56	55.86	56.86	45.85	59.76	43.22	56.32	49.61	53.99	54.17	58.64	56.97	52.06	55.33	34.17	47.42	43.42	46.77	53.69
MgO	12.81	11.50	11.87	14.26	7.29	13.40	12.41	10.42	15.09	14.66	14.71	11.46	10.79	10.25	14.00	14.67	13.02	14.33	13.64
MnO	0.18	0.22	0.33		0.44	0.20	0.29	0.35	0.18	0.26	0.18	0.23	0.33	0.34		0.15	0.24		0.14
FeO	13.30	15.65	14.91	14.51	20.61	14.71	14.05	16.95	10.54	10.53	10.53	15.51	16.55	17.40	16.32	11.99	14.95	17.03	12.56
NiO	0.11	0.06	0.02		0.10	0.13	0.10	0.11	0.09	0.09	0.10	0.07	0.08	0.07		0.14	0.10		0.07
Total	98.39	98.19	98.30	100.37	98.12	98.64	98.34	98.05	98.52	98.05	98.29	98.49	98.44	99.75	100.00	98.45	98.25	100.00	97.64
Mg*	62.55	56.53	58.48	64.00	38.31	61.78	60.81	51.78	71.21	71.03	71.06	56.71	53.09	50.18	60.40	67.70	60.01	64.77	65.47
Cr*	78.85	74.15	75.51	56.69	86.93	53.76	75.14	71.42	70.16	74.08	77.09	77.19	71.32	74.50	41.40	61.03	55.04	59.16	70.13
Fe3+*	11.85	8.40	9.44	12.69	12.43	10.49	12.65	25.46	17.90	31.53	15.17	12.87	17.28	10.76	11.87	16.38	8.53	18.43	10.75
Ti	0.0104	0.0027	0.0020	0.0055	0.0068	0.0014	0.0040	0.0073	0.0062	0.0015	0.0034	0.0037	0.0047	0.0084	0.0146	0.0123	0.0128	0.0062	0.0051
Fe3+	0.0505	0.0397	0.0429	0.0526	0.0868	0.0445	0.0564	0.1638	0.0627	0.1323	0.0515	0.0636	0.0974	0.0599	0.0541	0.0636	0.0374	0.0801	0.0416
Al	0.4080	0.5054	0.4784	0.8388	0.2482	0.9029	0.4813	0.5205	0.5743	0.4833	0.4449	0.4400	0.5431	0.4904	1.1232	0.7449	0.8708	0.7790	0.5818
Cr	1.5208	1.4495	1.4748	1.0977	1.6513	1.0498	1.4543	1.3010	1.3506	1.3814	1.4968	1.4889	1.3502	1.4329	0.7935	1.1668	1.0661	1.1285	1.3663
Mg	0.6270	0.5625	0.5803	0.6435	0.3797	0.6135	0.6042	0.5150	0.7115	0.7046	0.7077	0.5645	0.5274	0.5003	0.6128	0.6803	0.6025	0.6517	0.6544
Mn	0.0050	0.0061	0.0092	0.0000	0.0130	0.0052	0.0080	0.0098	0.0048	0.0071	0.0049	0.0064	0.0092	0.0094	0.0000	0.0041	0.0063	0.0000	0.0039
Fe2+	0.3754	0.4326	0.4120	0.3620	0.6113	0.3795	0.3894	0.4796	0.2876	0.2874	0.2882	0.4309	0.4660	0.4968	0.4018	0.3246	0.4015	0.3545	0.3451
Ni	0.0029	0.0016	0.0005	0.0000	0.0028	0.0032	0.0025	0.0029	0.0023	0.0023	0.0026	0.0019	0.0021	0.0018	0.0000	0.0034	0.0025	0.0000	0.0018
Total	3.0000	3.0000	3.0000	3.0000	3.0000	3.0000	3.0000	3.0000	3.0000	3.0000	3.0000	3.0000	3.0000	3.0000	3.0000	3.0000	3.0000	3.0000	3.0000

Table B3: continued

Sample	76994	71006	76995	76996	71023	76998
Field No.	LE10		SH20	SH8		SH31
SiO2	0.03	0.01	0.01	0.03	0.01	0.02
TiO2	0.37	0.06	0.12	0.06	0.02	0.06
Fe2O3	5.38	1.87	2.31	2.86	1.47	1.33
Al2O3	24.70	43.75	24.09	6.64	19.74	29.83
Cr2O3	38.53	22.47	44.26	62.29	49.20	38.78
MgO	12.00	15.88	15.63	10.01	12.24	15.39
MnO	0.32	0.17	0.14	0.30	0.24	0.16
FeO	16.27	13.59	10.90	16.94	15.59	11.90
NiO	0.15	0.28	0.10	0.05	0.14	0.16
Total	97.87	98.08	97.56	99.18	98.71	97.63
Mg*	56.15	67.39	71.62	50.90	58.19	69.18
Cr*	51.07	25.57	55.14	86.26	62.51	46.52
Fe3+*	20.91	10.35	14.94	11.81	7.34	6.72
Ti	0.0088	0.0013	0.0028	0.0015	0.0006	0.0014
Fe3+	0.1156	0.0373	0.0497	0.0652	0.0328	0.0221
Al	0.9134	1.4589	0.8724	0.2655	0.7370	1.0564
Cr	0.9534	0.5013	1.0724	1.6663	1.2290	0.9188
Mg	0.5595	0.6678	0.7138	0.5047	0.5764	0.6873
Mn	0.0084	0.0041	0.0036	0.0086	0.0065	0.0041
Fe2+	0.4370	0.3231	0.2829	0.4869	0.4142	0.3061
Ni	0.0038	0.0064	0.0025	0.0014	0.0035	0.0039
Total	3.0000	3.0000	3.0000	3.0000	3.0000	3.0000

Table B4: Representative analyses of primary and annealed clinopyroxene grains.

Sample	76987	70965	70969	70972	71000	71001	71007	2631	2638	76988	76989	76990	76991	76992	70987	70997	71004	71008
Field No.	AN8									SH19	SH1	SH52	LE17	NO11				
SiO2	53.94	54.92	54.48	54.15	54.44	54.73	54.33	54.18	53.62	53.30	54.21	54.73	54.79	54.39	54.12	54.40	53.38	53.68
TiO2	0.02	0.09	0.04	0.03	0.10	0.34	0.11	0.03	0.08	0.14	0.04	0.03	0.06	0.19	0.38	0.23	0.56	0.03
Al2O3	1.87	2.51	2.69	2.25	4.09	1.65	3.16	1.90	1.96	2.48	2.81	2.25	2.64	2.56	3.77	2.79	4.07	3.54
Cr2O3	0.74	1.53	1.70	1.57	1.19	3.48	1.25	1.69	2.11	1.30	2.04	2.70	1.51	2.04	1.33	1.53	1.67	1.59
MgO	16.12	15.85	16.02	16.40	15.00	15.62	15.97	15.94	16 68	16.67	15.86	15.29	15.57	14.99	15.49	16.10	15.86	15.42
CaO	22.16	20.88	20.78	21.46	20.15	19.94	21.98	21.30	20.62	22.23	20.08	20.38	20.83	20.16	20.30	21.63	19.77	20.11
MnO	0.11	0.05	0.09	0.09	0.05		0.00	0.10	0.15	0.06	0.05	0.08	0.07	0.08		0.07	0.07	0.07
FeO	2.78	2.53	2.30	2.17	2.54	2.36	2.02	2.23	3.05	2.32	2.24	2.34	2.58	3.05	2.96	2.25	2.31	2.86
NiO	0.07	0.03	0.02	0.06	0.04		0.00	0.05	0.08	0.03	0.02	0.04	0.04	0.05		0.06	0.06	0.04
Na2O	1.37	1.80	1.77	1.51	2.06	2.05	1.50	1.74	1.35	1.09	2.02	2.24	2.03	2.38	1.66	1.56	1.93	2.17
Total	99.18	100.18	99.89	99.68	99.67	100.16	100.33	99.16	99.87	99.64	99.38	100.07	100.11	99.88	100.00	100.62	99.67	99.51
Mg#	91.16	91.77	92.55	93.08	91.33	92.20	93.37	92.72	90.69	92.75	92.65	92.10	91.51	89.74	90.33	92.73	92.44	90.58
Si	1.9782	1.9838	1.9736	1.9696	1.9700	1.9827	1.9592	1.9821	1.9586	1.9446	1.9726	1.9844	1.9823	1.9795	1.9566	1.9602	1.9352	1.9566
Ti	0.0006	0.0024	0.0010	0.0007	0.0027	0.0093	0.0031	0.0009	0.0022	0.0040	0.0012	0.0009	0.0016	0.0051	0.0103	0.0062	0.0152	0.0009
Al	0.0808	0.1068	0.1147	0.0962	0.1745	0.0706	0.1343	0.0820	0.0844	0.1068	0.1204	0.0959	0.1126	0.1096	0.1605	0.1186	0.1738	0.1519
Cr	0.0215	0.0435	0.0486	0.0450	0.0340	0.0997	0.0356	0.0490	0.0610	0.0375	0.0586	0.0774	0.0433	0.0586	0.0381	0.0436	0.0478	0.0457
Mg	0.8809	0.8529	0.8648	0.8888	0.8089	0.8434	0.8582	0.8692	0.9077	0.9062	0.8600	0.8258	0.8395	0.8128	0.8344	0.8645	0.8569	0.8371
Ca	0.8707	0.8080	0.8063	0.8362	0.7811	0.7738	0.8493	0.8347	0.8068	0.8688	0.7828	0.7915	0.8074	0.7858	0.7862	0.8349	0.7679	0.7852
Mn	0.0034	0.0014	0.0027	0.0029	0.0017	0.0000	0.0000	0.0031	0.0047	0.0019	0.0017	0.0025	0.0021	0.0026	0.0000	0.0021	0.0020	0.0022
Fe	0.0853	0.0765	0.0696	0.0661	0.0768	0.0713	0.0609	0.0682	0.0932	0.0708	0.0683	0.0708	0.0779	0.0929	0.0893	0.0678	0.0701	0.0870
Na	0.0974	0.1263	0.1246	0.1062	0.1445	0.1440	0.1047	0.1235	0.0956	0.0769	0.1422	0.1574	0.1426	0.1679	0.1165	0.1090	0.1357	0.1537
Total	4.0188	4.0016	4.0059	4.0117	3.9941	3.9948	4.0052	4.0128	4.0142	4.0176	4.0077	4.0066	4.0093	4.0149	3.9920	4.0068	4.0046	4.0204
En	47.96	49.09	49.68	49.62	48.53	49.95	48.53	49.05	50.21	49.10	50.26	48.92	48.67	48.05	48.80	48.92	50.56	48.97
Fs	4.64	4.40	4.00	3.69	4.61	4.23	3.44	3.85	5.15	3.84	3.99	4.19	4.52	5.49	5.22	3.84	4.13	5.09
Wo	47.40	46.51	46.32	46.69	46.86	45.83	48.03	47.10	44.63	47.07	45.75	46.89	46.81	46.46	45.98	47.25	45.31	45.94

Table B4: continued

Sample	70961	76993	71006	76998
Field No.		SH34		SH31
SiO2	54.18	53.97	53.77	54.01
TiO2	0.15	0.10	0.40	0.08
Al2O3	2.79	2.96	5.14	3.27
Cr2O3	1.79	1.70	1.27	1.43
MgO	15.81	15.74	15.21	16.01
CaO	20.73	20.06	20.57	21.31
MnO	0.07	0.07		0.04
FeO	2.47	2.29	2.42	2.09
NiO	0.04	0.04		0.02
Na2O	1.82	2.01	1.57	1.53
Total	99.86	98.92	100.34	99.79
Mg#	91.93	92.46	91.81	93.18
Si	1.9666	1.9721	1.9321	1.9572
Ti	0.0041	0.0026	0.0108	0.0021
Al	0.1192	0.1276	0.2177	0.1399
Cr	0.0515	0.0491	0.0362	0.0409
Mg	0.8548	0.8570	0.8145	0.8644
Ca	0.8061	0.7854	0.7917	0.8273
Mn	0.0023	0.0020	0.0000	0.0014
Fe	0.0751	0.0699	0.0726	0.0633
Na	0.1278	0.1421	0.1090	0.1077
Total	4.0075	4.0079	3.9846	4.0040
En	49.24	50.05	48.51	49.25
Fs	4.32	4.08	4.33	3.61
Wo	46.44	45.87	47.16	47.14

Table B5: Representative analyses of olivine grains in olivine+clinopyroxene replacement rims on primary orthopyroxene. "Patch" numbers in this and following tables refer to particular localities on the thin section used for EPMA .

Sample	71004	71004	71006	71006	71006	71007	71007	71007	71007	71008	71008	71023	71023	76998	76998	76998	76998	76998	76995
Field No.														SH31	SH31	SH31	SH31	SH31	SH20
Patch	C5	C13	C3	C5	C5	C6	C6	C6	C8	C14	C2	C6	C6	C1	C1	C3	C3	C10	C1
SiO2	42.05	39.91	40.81	40.73	40.95	40.25	40.54	40.99	40.15	41.08	41.38	41.12	41.09	40.45	40.92	41.65	41.63	43.14	40.98
MgO	45.12	48.99	48.91	49.47	48.95	49.75	49.14	50.70	48.37	49.42	50.09	50.16	51.10	48.05	46.99	50.56	47.85	45.77	49.88
CaO	0.53	0.24	0.20	0.21	0.19	0.14	0.38	0.19	0.02	0.27	0.40	0.15	0.20	0.30	0.94	0.28	0.39	0.24	0.16
MnO	0.24	0.24	0.12	0.18	0.21	0.15	0.22	0.20	0.21	0.12	0.07	0.22	0.07	0.07	0.14	0.10	0.12	0.14	0.13
FeO	10.98	7.87	9.51	9.17	9.23	7.44	7.91	7.32	9.79	8.70	7.94	6.87	5.70	9.16	9.11	7.60	8.99	8.45	8.21
NiO	0.25	0.30	0.20	0.10	0.12	0.14	0.17	0.19	0.41	0.12	0.32	0.11	0.35	0.32	0.37	0.25	0.26	0.24	0.25
Total	99.17	97.54	99.75	99.86	99.64	97.87	98.36	99.59	98.96	99.72	100.18	98.62	98.51	98.35	98.46	100.44	99.25	97.98	99.63
Fo	87.98	91.73	90.16	90.57	90.43	92.26	91.72	92.50	89.80	91.01	91.83	92.86	94.11	90.34	90.19	92.22	90.46	90.61	91.54
Si	1.0414	0.9970	1.0015	0.9971	1.0039	0.9979	1.0022	0.9976	0.9960	1.0042	1.0037	1.0079	1.0040	1.0055	1.0165	1.0055	1.0220	1.0636	1.0012
Mg	1.6648	1.8234	1.7883	1.8046	1.7882	1.8379	1.8106	1.8388	1.7880	1.8000	1.8105	1.8321	1.8603	1.7797	1.7394	1.8185	1.7503	1.6813	1.8159
Ca	0.0140	0.0063	0.0053	0.0054	0.0050	0.0038	0.0101	0.0049	0.0006	0.0071	0.0103	0.0038	0.0051	0.0081	0.0250	0.0073	0.0104	0.0062	0.0042
Mn	0.0051	0.0050	0.0026	0.0037	0.0043	0.0031	0.0045	0.0042	0.0044	0.0025	0.0014	0.0046	0.0015	0.0014	0.0029	0.0020	0.0026	0.0029	0.0028
Fe	0.2274	0.1644	0.1951	0.1878	0.1892	0.1542	0.1634	0.1490	0.2032	0.1778	0.1610	0.1408	0.1165	0.1904	0.1891	0.1534	0.1846	0.1742	0.1678
Ni	0.0057	0.0069	0.0047	0.0022	0.0027	0.0032	0.0039	0.0042	0.0095	0.0028	0.0071	0.0025	0.0080	0.0074	0.0085	0.0056	0.0059	0.0056	0.0057
Total	2.9583	3.0030	2.9974	3.0008	2.9932	3.0003	2.9948	2.9986	3.0016	2.9944	2.9940	2.9918	2.9954	2.9925	2.9814	2.9922	2.9757	2.9338	2.9976

Table B5: continued

Sample	76995	76995	76995	76995	76995	76995	76995	76997	76997	76997	76997	76996	76996	76996	76996	76996	76996
Field No.	SH20	SH20	SH20	SH20	SH20	SH20	SH20	SH40	SH40	SH40	SH40	SH8	SH8	SH8	SH8	SH8	SH8
Patch	C1	C5	C5	C5	C4	C1	C6	C1	C2	C2	C4	C2	C2	C2	C2	C10	C10
SiO2	40.97	41.03	41.09	40.72	40.38	41.04	40.35	41.24	40.92	40.70	40.92	42.61	42.48	42.63	41.90	41.67	41.70
MgO	50.13	49.92	49.57	50.05	49.83	49.29	49.38	47.80	47.77	47.37	48.09	51.16	52.19	51.41	50.91	50.22	51.71
CaO	0.23	0.26	0.28	0.25	0.17	0.51	0.18	0.23	0.29	0.47	0.34	0.12	0.17	0.11	0.12	1.04	0.15
MnO	0.20	0.14	0.12	0.02	0.14	0.12	0.06	0.17	0.22	0.18	0.15	0.11	0.08	0.13	0.20	0.12	0.08
FeO	8.42	8.18	8.60	7.46	7.97	8.25	7.46	11.11	10.93	11.22	10.32	7.03	6.51	6.99	7.67	6.55	6.44
NiO	0.29	0.35	0.36	0.37	0.21	0.34	0.28	0.36	0.19	0.23	0.27	0.29	0.26	0.18	0.20	0.24	0.19
Total	100.23	99.88	100.01	98.86	98.70	99.56	97.72	100.91	100.32	100.17	100.08	101.33	101.70	101.44	101.00	99.83	100.26
Fo	91.39	91.58	91.13	92.28	91.77	91.41	92.18	88.47	88.62	88.27	89.25	92.84	93.45	92.91	92.21	93.18	93.47
Si	0.9965	1.0002	1.0022	0.9996	0.9956	1.0039	1.0022	1.0075	1.0048	1.0024	1.0039	1.0143	1.0068	1.0138	1.0059	1.0094	1.0032
Mg	1.8170	1.8133	1.8015	1.8306	1.8305	1.7964	1.8272	1.7402	1.7481	1.7383	1.7580	1.8146	1.8434	1.8221	1.8213	1.8126	1.8535
Ca	0.0059	0.0067	0.0073	0.0066	0.0046	0.0134	0.0049	0.0061	0.0076	0.0125	0.0090	0.0032	0.0043	0.0027	0.0031	0.0271	0.0039
Mn	0.0041	0.0029	0.0024	0.0005	0.0030	0.0025	0.0012	0.0035	0.0046	0.0037	0.0030	0.0022	0.0017	0.0026	0.0040	0.0024	0.0016
Fe	0.1713	0.1668	0.1754	0.1531	0.1643	0.1688	0.1550	0.2269	0.2244	0.2309	0.2117	0.1400	0.1291	0.1390	0.1539	0.1326	0.1295
Ni	0.0065	0.0079	0.0081	0.0083	0.0047	0.0077	0.0065	0.0082	0.0044	0.0052	0.0062	0.0065	0.0058	0.0040	0.0043	0.0054	0.0043
Total	3.0012	2.9978	2.9969	2.9987	3.0026	2.9927	2.9969	2.9925	2.9938	2.9930	2.9918	2.9809	2.9910	2.9842	2.9926	2.9895	2.9960

Table B6: Representative analyses of clinopyroxene grains in olivine+clinopyroxene replacement rims on primary orthopyroxene.

Sample	71004	71004	71006	71006	71007	71008	71008	71008	71008	71008	71023	71023	76998	76995	76995	76995	76997	76997	76997	76996
Field No.													SH31	SH20	SH20	SH20	SH40	SH40	SH40	SH8
Patch	C5	C5	C3	C5	C6	C14	C2	C2	C1	C14	C6	C6	C1	C1	C1	C5	C1	C2	C2	C2
SiO2	47.70	49.61	51.01	50.73	52.37	51.25	53.22	52.37	53.06	54.10	53.75	51.62	54.52	53.67	54.32	54.14	51.54	54.23	51.05	55.27
TiO2	2.90	1.56	0.51	0.43	0.33	0.52	0.14	0.24	0.15	0.22	0.06	0.09	0.16	0.29	0.22	0.33	0.75	0.20	0.27	0.12
Al2O3	6.31	4.77	3.83	5.20	4.07	5.48	1.93	3.93	2.79	1.82	1.97	3.16	2.52	1.54	1.36	1.85	3.38	1.87	2.26	1.08
Cr2O3	0.45	1.47	2.16	3.13	3.29	2.65	2.04	2.80	1.84	1.75	2.18	3.39	1.02	1.17	0.68	1.23	1.16	0.73	0.90	4.29
MgO	15.29	15.96	16.31	15.89	16.62	16.20	16.73	17.26	16.35	17.61	17.25	15.80	18.55	18.56	19.18	18.42	16.64	19.10	20.10	16.88
CaO	23.61	22.36	22.33	21.00	19.42	22.28	22.08	19.48	22.25	21.98	21.75	22.08	20.42	20.93	21.07	21.02	21.44	20.94	19.19	18.07
MnO	0.02	0.01	0.00	0.00	0.14	0.00	0.06	0.03	0.07	0.06	0.11	0.14	0.07	0.08	0.05	0.09	0.10	0.03	0.19	0.16
FeO	1.97	1.62	2.36	2.34	2.21	1.91	2.45	2.77	2.41	2.66	1.94	1.55	2.44	2.58	2.80	2.53	3.67	2.99	3.44	2.51
NiO	0.04	0.01	0.05	0.00	0.00	0.04	0.09	0.04	0.00	0.01	0.05	0.03	0.03	0.03	0.10	0.00	0.08	0.09	0.02	0.03
Na2O	0.38	0.46	0.71	0.86	1.31	0.87	0.92	1.05	1.06	0.79	1.00	1.04	0.74	0.49	0.39	0.46	0.54	0.61	0.67	2.12
Total	98.66	97.84	99.28	99.58	99.74	101.18	99.66	99.95	99.97	101.01	100.07	98.90	100.49	99.35	100.18	100.08	99.30	100.80	98.09	100.52
Mg#	93.25	94.60	92.49	92.38	93.07	93.81	92.40	91.75	92.36	92.19	94.05	94.78	93.12	92.75	92.43	92.84	89.00	91.92	91.24	92.29
Si	1.7717	1.8455	1.8777	1.8562	1.9029	1.8464	1.9465	1.9008	1.9323	1.9477	1.9502	1.9049	1.9555	1.9555	1.9622	1.9556	1.8972	1.9490	1.8935	1.9918
Ti	0.0810	0.0437	0.0142	0.0118	0.0089	0.0141	0.0038	0.0066	0.0041	0.0060	0.0018	0.0026	0.0043	0.0080	0.0061	0.0091	0.0206	0.0055	0.0076	0.0032
Al	0.2761	0.2091	0.1659	0.2243	0.1743	0.2325	0.0830	0.1682	0.1197	0.0774	0.0844	0.1373	0.1065	0.0662	0.0577	0.0786	0.1467	0.0793	0.0986	0.0457
Cr	0.0131	0.0431	0.0629	0.0905	0.0945	0.0754	0.0590	0.0804	0.0531	0.0497	0.0624	0.0987	0.0290	0.0338	0.0194	0.0351	0.0337	0.0206	0.0263	0.1221
Mg	0.8461	0.8849	0.8946	0.8666	0.8998	0.8695	0.9120	0.9333	0.8871	0.9449	0.9325	0.8684	0.9913	1.0075	1.0325	0.9916	0.9127	1.0229	1.1110	0.9063
Ca	0.9393	0.8911	0.8806	0.8231	0.7559	0.8599	0.8652	0.7574	0.8680	0.8477	0.8455	0.8730	0.7846	0.8172	0.8153	0.8133	0.8457	0.8063	0.7627	0.6975
Mn	0.0007	0.0002	0.0000	0.0000	0.0042	0.0000	0.0018	0.0009	0.0023	0.0018	0.0035	0.0043	0.0022	0.0025	0.0017	0.0028	0.0031	0.0008	0.0060	0.0048
Fe	0.0613	0.0505	0.0726	0.0714	0.0670	0.0574	0.0750	0.0839	0.0734	0.0801	0.0590	0.0478	0.0732	0.0787	0.0846	0.0765	0.1128	0.0899	0.1066	0.0757
Na	0.0271	0.0335	0.0504	0.0613	0.0923	0.0608	0.0652	0.0736	0.0746	0.0553	0.0705	0.0746	0.0517	0.0343	0.0274	0.0320	0.0388	0.0425	0.0479	0.1482
Total	4.0163	4.0015	4.0189	4.0053	3.9999	4.0160	4.0114	4.0051	4.0145	4.0105	4.0099	4.0118	3.9983	4.0037	4.0069	3.9945	4.0113	4.0168	4.0603	3.9952
En	45.82	48.45	48.41	49.21	52.23	48.66	49.24	52.59	48.51	50.46	50.76	48.54	53.61	52.93	53.43	52.71	48.78	53.30	56.10	53.96
Fs	3.32	2.76	3.93	4.06	3.89	3.21	4.05	4.73	4.02	4.28	3.21	2.67	3.96	4.14	4.38	4.06	6.03	4.68	5.38	4.51
Wo	50.86	48.79	47.66	46.74	43.88	48.13	46.71	42.68	47.47	45.27	46.03	48.79	42.43	42.93	42.19	43.23	45.19	42.02	38.52	41.53

Table B6: continued

Sample	76996	76996	76996	76996	76996	76996
Field No.	SH8	SH8	SH8	SH8	SH8	SH8
Patch	C2	C2	C2	C10	C10	C10
SiO2	55.29	56.23	56.13	55.44	54.41	55.30
TiO2	0.02	0.03	0.06	0.13	0.09	0.07
Al2O3	1.21	0.52	0.73	1.44	1.38	0.93
Cr2O3	4.78	2.65	2.86	4.90	2.57	2.84
MgO	16.50	19.53	18.83	15.69	18.52	19.21
CaO	16.43	19.04	18.65	16.83	18.26	18.49
MnO	0.02	0.10	0.10	0.07	0.10	0.07
FeO	2.68	2.43	2.43	2.52	2.28	2.50
NiO	0.00	0.00	0.10	0.04	0.04	0.04
Na2O	2.68	1.17	1.46	2.88	1.38	1.34
Total	99.61	101.71	101.37	99.94	99.03	100.81
Mg#	91.66	93.47	93.24	91.74	93.54	93.18
Si	2.0051	1.9926	1.9973	2.0064	1.9794	1.9795
Ti	0.0006	0.0008	0.0015	0.0034	0.0026	0.0020
Al	0.0516	0.0218	0.0308	0.0613	0.0591	0.0392
Cr	0.1370	0.0741	0.0803	0.1402	0.0738	0.0804
Mg	0.8914	1.0312	0.9985	0.8461	1.0040	1.0248
Ca	0.6384	0.7229	0.7111	0.6524	0.7117	0.7090
Mn	0.0006	0.0030	0.0031	0.0023	0.0032	0.0022
Fe	0.0812	0.0720	0.0724	0.0762	0.0694	0.0750
Na	0.1885	0.0803	0.1010	0.2023	0.0972	0.0932
Total	3.9943	3.9988	3.9961	3.9906	4.0002	4.0053
En	55.33	56.47	56.03	53.73	56.24	56.66
Fs	5.04	3.94	4.07	4.84	3.89	4.14
Wo	39.63	39.58	39.90	41.43	39.87	39.20

Table B7 Representative analyses of apatite grains. F/Cl value calculated on an atomic basis.

Sample	76987	76987	76987	76987	76987	71000	71000	71007	71007	2631	2631	2631	2638	76988	76988	76988	73797	73797	73797
Field No.	AN8	AN8	AN8	AN8	AN8									SH19	SH19	SH19			
Grain	C1	C2	C2	C3	C3	C11	C17	C8	C7	C1	C3	C6	C8	C9a	C9b	C3	C7	C8	C6
			Clear rim	Core	Rim/OL														
P2O5	40.04	39.85	40.88	40.02	40.06	41.62	41.28	42.28	40.78	40.16	40.40	40.18	39.85	40.40	40.04	40.22	40.99	40.69	40.80
SiO2	0.15	0.13	0.32	0.16	0.31								0.11	0.30	0.33	0.31	0.34	0.23	0.57
MgO	0.60	0.59	0.55	0.69	0.62			0.52	0.36	0.08	0.11	0.09	1.09	0.55	0.53	0.37	0.58	0.70	0.58
CaO	51.87	52.05	54.39	51.56	51.56	53.16	52.76	53.23	54.84	53.16	53.30	52.77	49.59	52.86	53.04	53.23	53.31	52.82	52.47
FeO	0.16	0.15	0.17	0.13	0.23			0.21	0.16	0.15	0.10	0.05	0.41	0.14	0.18	0.23	0.29	0.20	0.22
SrO	1.22	1.24	0.36	1.37	1.21	1.42	1.43			1.25	1.17	1.72	2.32	0.47	0.47	0.49	0.53	0.84	0.67
F	1.78	1.57	2.68	1.75	2.31	1.47	1.41	1.58	2.05	4.83	4.29	4.47	1.66	2.12	2.12	2.77	2.64	1.82	2.10
Cl	1.10	1.23	0.27	1.23	0.82	1.98	2.09	1.35	1.52	0.53	0.69	0.85	0.66	0.99	0.98	0.80	0.26	0.63	0.47
	96.93	96.81	99.62	96.90	97.13	99.65	98.97	99.17	99.70	100.17	100.07	100.12	95.70	97.83	97.70	98.41	98.93	97.93	97.88
O=F,Cl	1.75	1.60	2.32	1.75	2.13	1.69	1.66	1.63	2.07	4.19	3.77	3.96	1.55	2.01	2.01	2.51	2.28	1.68	1.88
Total	95.18	95.21	97.31	95.15	95.00	97.97	97.30	97.54	97.63	95.98	96.30	96.17	94.15	95.82	95.70	95.90	96.65	96.25	96.01
P	5.8811	5.8809	5.7845	5.8800	5.8329	5.9541	5.9488	6.0144	5.7995	5.5560	5.6180	5.5854	5.9519	5.8378	5.8049	5.7523	5.8305	5.9044	5.8860
Si	0.0255	0.0230	0.0539	0.0283	0.0533	0.0000	0.0000	0.0000	0.0000	0.0000	0.0000	0.0000	0.0199	0.0510	0.0562	0.0516	0.0572	0.0402	0.0965
Mg	0.1563	0.1537	0.1371	0.1787	0.1597	0.0000	0.0000	0.1313	0.0889	0.0195	0.0281	0.0226	0.2859	0.1399	0.1360	0.0927	0.1444	0.1776	0.1469
Ca	9.6420	9.7209	9.7422	9.5877	9.5012	9.6234	9.6229	9.5836	9.8710	9.3079	9.3803	9.2843	9.3732	9.6663	9.7331	9.6358	9.5971	9.6990	9.5782
Fe	0.0233	0.0213	0.0237	0.0192	0.0331	0.0000	0.0000	0.0297	0.0223	0.0203	0.0141	0.0064	0.0602	0.0204	0.0263	0.0324	0.0401	0.0291	0.0315
Sr	0.1227	0.1258	0.0351	0.1374	0.1209	0.1388	0.1409	0.0000	0.0000	0.1180	0.1115	0.1636	0.2374	0.0467	0.0468	0.0480	0.0511	0.0831	0.0662
F	0.9778	0.8678	1.4160	0.9595	1.2570	0.7863	0.7610	0.8370	1.0870	2.4970	2.2304	2.3221	0.9254	1.1453	1.1485	1.4777	1.4026	0.9880	1.1329
Cl	0.3241	0.3624	0.0770	0.3611	0.2393	0.5664	0.6032	0.3825	0.4319	0.1472	0.1908	0.2375	0.1985	0.2850	0.2846	0.2294	0.0740	0.1817	0.1363
Total	17.1529	17.1557	17.2694	17.1518	17.1973	17.0689	17.0768	16.9785	17.3007	17.6659	17.5731	17.6219	17.0523	17.1923	17.2364	17.3200	17.1971	17.1032	17.0745
F/Cl	3.02	2.39	18.38	2.66	5.25	1.39	1.26	2.19	2.52	16.97	11.69	9.78	4.66	4.02	4.04	6.44	18.95	5.44	8.31

Table B7: continued

Sample	76989	76989	76990	76990	76990	76990	76990	76990	76991	76991	70997	71004	71008	71008	71008	70961	71023
Field No.	SH1	SH1	SH52	SH52	SH52	SH52	SH52	SH52	LE17	LE17							
Grain	C4	C3	C2	C2	C9	C9	C9	C9	C4	C3	C2	C15	C4	C14	C2	C11	C5
			Core	Rim/OL	Core	Rim/OL	Clear rim	Clear rim									
P2O5	40.03	39.89	40.27	39.87	40.74	39.34	41.04	39.98	40.55	38.92	39.53	37.81	40.32	40.29	41.74	40.07	38.94
SiO2	0.13	0.06	0.12	0.37	0.12	0.59	0.45	2.07	0.40	4.04	0.19	0.23				1.71	0.08
MgO	0.96	0.91	0.77	0.84	0.80	0.90	0.63	0.63	0.53	0.49	0.57	0.54				0.49	0.66
CaO	50.99	51.17	50.26	51.72	50.74	51.88	53.71	52.05	52.13	51.06	51.72	55.63	51.22	51.18	52.78	51.67	49.20
FeO	0.19	0.24	0.25	0.35	0.25	0.39	0.27	0.48	0.24	0.35	0.28	0.25				0.41	0.18
SrO	1.46	1.47	1.76	0.91	1.78	1.06	0.64	0.65	1.60	0.79	1.54	1.13	1.21	1.25	1.31	0.67	2.90
F	1.46	1.21	2.10	1.73	1.79	2.23	2.07	2.31	1.22	3.05	1.14	1.61	1.55	1.56	2.07	2.84	1.62
Cl	1.76	1.84	2.17	1.42	2.28	1.43	1.37	1.36	1.38	0.49	1.66	1.88	1.33	1.26	1.29	0.95	2.36
	96.97	96.80	97.69	97.21	98.49	97.82	100.18	99.53	98.05	99.19	96.63	99.09	95.63	95.54	99.19	98.82	95.95
O=F,Cl	1.62	1.44	2.25	1.77	2.02	2.20	2.05	2.25	1.33	2.68	1.33	1.78	1.60	1.60	2.03	2.61	1.89
Total	95.35	95.36	95.44	95.44	96.47	95.62	98.13	97.28	96.71	96.51	95.30	97.31	94.03	93.94	97.16	96.21	94.06
P	5.8887	5.9035	5.8319	5.8325	5.8693	5.7050	5.8011	5.6464	5.9270	5.4527	5.8855	5.5472	5.9938	5.9962	5.9512	5.6669	5.8221
Si	0.0227	0.0103	0.0206	0.0647	0.0211	0.1018	0.0749	0.3458	0.0699	0.6687	0.0331	0.0395	0.0000	0.0000	0.0000	0.2852	0.0143
Mg	0.2487	0.2375	0.1963	0.2154	0.2019	0.2309	0.1564	0.1570	0.1374	0.1206	0.1496	0.1402	0.0000	0.0000	0.0000	0.1227	0.1739
Ca	9.4926	9.5832	9.2107	9.5748	9.2514	9.5220	9.6092	9.3021	9.6440	9.0533	9.7459	10.3298	9.6364	9.6400	9.5239	9.2464	9.3086
Fe	0.0282	0.0352	0.0361	0.0503	0.0360	0.0554	0.0383	0.0665	0.0342	0.0481	0.0417	0.0361	0.0000	0.0000	0.0000	0.0578	0.0272
Sr	0.1467	0.1488	0.1742	0.0916	0.1753	0.1054	0.0624	0.0629	0.1599	0.0754	0.1569	0.1138	0.1232	0.1274	0.1279	0.0648	0.2972
F	0.7997	0.6709	1.1340	0.9431	0.9645	1.2069	1.0939	1.2196	0.6637	1.5956	0.6314	0.8832	0.8607	0.8673	1.1025	1.5024	0.9033
Cl	0.5168	0.5451	0.6276	0.4142	0.6553	0.4134	0.3873	0.3844	0.4036	0.1380	0.4944	0.5501	0.3953	0.3749	0.3677	0.2684	0.7061
Total	17.1442	17.1345	17.2315	17.1866	17.1749	17.3407	17.2235	17.1847	17.0396	17.1524	17.1386	17.6397	17.0094	17.0057	17.0732	17.2145	17.2526
F/Cl	1.55	1.23	1.81	2.28	1.47	2.92	2.82	3.17	1.64	11.56	1.28	1.61	2.18	2.31	3.00	5.60	1.28

Table B8: Representative analyses of amphibole and phlogopite.

Sample	71004	71006	71007	70987	71000	71004	71007
Mineral	Amph	Amph	Amph	Amph	Amph	Phlog	Phlog
P2O5	0.32	0.23	0.22	0.18			
SiO2	43.03	43.62	44.84	44.12	44.53	39.80	38.33
TiO2	3.30	0.72	0.73	3.24	0.98	1.36	1.32
Al2O3	12.36	13.86	12.33	12.69	13.06	16.91	15.78
Cr2O3	1.87	1.56	2.09	1.28	2.32	0.49	1.07
MgO	17.38	17.49	18.41	16.92	17.57	22.91	22.56
CaO	10.81	10.43	10.92	10.68	10.24	0.15	0.03
MnO	0.07	0.08	0.01			0.00	0.00
FeO	3.41	4.19	3.20	4.42	3.45	3.13	3.99
NiO	0.08	0.12	0.14			0.14	0.15
Na2O	3.25	3.63	3.65	3.21	3.41	0.96	1.55
K2O	1.25	0.91	0.92	1.11	1.03	7.91	8.20
Cl	0.04	0.07	0.13	0.08	0.10	0.21	0.18
Total	97.17	96.90	97.60	97.91	96.69	93.97	93.16
Mg#	90.10	88.15	91.12	87.23	90.09	92.87	90.97
Si	6.2042	6.2840	6.4027	6.2912	6.3830	5.6440	5.5600
Ti	0.3582	0.0782	0.0782	0.3469	0.1060	0.1460	0.1440
Al	2.1064	2.3590	2.0803	2.1386	2.2128	2.8280	2.6980
Cr	0.2137	0.1773	0.2365	0.1438	0.2626	0.0540	0.1220
Fe	0.4107	0.5051	0.3818	0.5265	0.4132	0.3720	0.4840
Mn	0.0083	0.0097	0.0013	0.0000	0.0000	0.0000	0.0000
Mg	3.7375	3.7564	3.9192	3.5979	3.7550	4.8420	4.8780
Ca	1.6703	1.6096	1.6708	1.6311	1.5731	0.0220	0.0040
Na	0.9075	1.0129	1.0116	0.8885	0.9469	0.2640	0.4360
K	0.2292	0.1678	0.1679	0.2010	0.1883	1.4320	1.5180
Total	15.8459	15.9600	15.9504	15.7655	15.8409	15.6040	15.8440

Table B9: Representative analyses of amphibole±phlogopite decompression fusion glasses.

Sample	76987	70956	70956	70969	70969	70969	70969	70972	70972	71000	71000	71000	71000	71000	71000	71001	71001	71001	71001	71001	71001	71007	76988	76988
Field No.	AN8																						SH19	SH19
Glass patch	C2	C1	C2	C8	C4	C3	C2	C6	C5	C10	C2	C11	C12	C7	C6	C2	C4	C3	C1	C8	C11	C7	C1	C2
P2O5	1.02	0.18	0.15	0.81	0.78	1.05	0.95	0.67	0.46	0.16	0.75	1.55	0.87	1.43	1.57	1.32	1.85	1.82	1.54	1.56	1.61	0.52	1.06	1.40
SiO2	53.11	56.61	56.52	52.81	53.59	52.21	52.91	53.49	53.46	49.76	51.20	49.50	49.86	49.39	47.64	54.54	53.11	53.13	49.67	49.11	49.01	56.47	52.71	52.14
TiO2	0.44	1.83	1.73	1.51	0.87	1.86	1.58	1.30	0.46	1.14	0.89	0.91	0.95	0.79	0.77	1.93	2.13	1.73	2.72	2.59	2.74	1.06	2.00	2.09
Al2O3	20.34	22.35	21.86	20.95	20.45	19.80	19.71	20.75	21.35	21.32	22.57	20.50	21.67	21.19	21.18	17.83	16.82	16.51	17.10	17.34	16.46	24.44	19.97	19.82
Cr2O3	0.02	0.06	0.12	0.00	0.04	0.02	0.01	0.03	0.08		0.35	0.71		0.27								0.03	0.01	0.01
MgO	3.04	3.05	3.04	2.11	1.90	2.32	2.21	2.21	1.78	3.15	3.23	3.57	3.24	3.41	3.63	3.21	3.56	3.54	2.65	2.96	3.09	1.52	2.40	2.59
CaO	7.26	5.29	5.78	4.22	3.68	4.63	4.64	4.28	3.47	7.75	6.14	7.56	8.19	7.35	8.06	3.85	4.37	3.93	5.62	6.16	6.86	4.48	5.30	5.68
MnO	0.08	0.02	0.10	0.01	0.01	0.07	0.04	0.06	0.00													0.05	0.07	0.05
FeO	4.28	2.61	2.44	2.83	2.65	4.13	4.11	3.56	2.05	2.86	3.19	2.85	3.53	3.12	3.31	4.38	5.69	5.27	8.10	7.59	8.23	1.82	5.61	5.87
NiO	0.03	0.01	0.04	0.00	0.00	0.02	0.05	0.02	0.02													0.00	0.02	0.02
Na2O	7.95	6.09	6.56	6.34	6.21	6.34	5.99	6.61	6.32	7.55	8.23	6.82	7.79	7.82	7.06	7.00	9.75	6.98	6.13	6.72	5.56	1.27	6.67	5.79
K2O	2.51	1.74	1.91	6.03	7.05	5.52	5.83	5.68	7.93	2.13	2.16	4.50	2.46	2.06	2.19	1.97	1.88	2.38	3.22	3.17	3.25	1.48	4.01	3.41
Cl	0.22	0.21	0.16	0.18	0.18	0.20	0.19	0.12	0.18	0.13	0.24	0.26	0.17	0.21	0.24	0.34	0.38	0.35	0.18	0.20	0.15	0.23	0.19	0.18
TOTAL	100.31	99.86	100.25	97.00	96.62	97.12	97.27	98.10	97.09	95.79	98.20	97.16	97.83	95.61	94.08	95.04	97.68	93.82	95.39	95.84	95.35	92.84	98.97	97.65
																						near apatite		
Mg#	55.87	67.60	68.97	57.00	56.11	50.00	48.90	52.51	60.80	66.25	64.34	69.03	62.05	66.07	66.15	56.61	52.72	54.46	36.83	41.00	40.09	59.73	43.26	44.04
Σalkalies	10.46	7.83	8.47	12.37	13.26	11.85	11.82	12.29	14.25	9.68	10.39	11.32	10.25	9.88	9.25	8.98	11.63	9.37	9.35	9.89	8.81	2.74	10.68	9.20
K2O/Na2O	0.32	0.29	0.29	0.95	1.13	0.87	0.97	0.86	1.25	0.28	0.26	0.66	0.32	0.26	0.31	0.28	0.19	0.34	0.53	0.47	0.58	1.17	0.60	0.59

Table B9: continued

Sample	76988	76988	76988	76989	76989	76989	76989	76990	76990	76991	76991	76991	76991	70987	70987	70987	70997	71004	71004	71004	71004	71008	71008	70961
Field No.	SH19	SH19	SH19	SH1	SH1	SH1	SH1	SH52	SH52	LE17	LE17	LE17	LE17											
Glass patch	C3	C4	C8	C9	C3	C4	C8	C3	C7	C1	C3	C5	C7	C1	C2	C5	C6	C5	C3	C2	C10	C2	C1	C10
P2O5	0.99	0.85	0.63	1.17	1.10	0.79		1.19	0.46	0.25	1.27	0.28	0.18	1.28	1.48	1.23	1.16	0.83	0.88	0.84	0.87	1.60	1.37	0.73
SiO2	54.05	52.63	52.91	54.75	54.29	49.59	55.00	57.96	56.13	57.76	56.58	57.51	56.80	48.39	48.19	49.20	52.25	52.05	52.49	52.60	53.16	51.82	52.00	64.54
TiO2	0.69	0.85	0.84	1.26	0.65	0.53	0.96	0.80	0.74	0.98	0.97	1.09	1.12	3.25	3.17	4.15	2.30	2.71	2.63	2.92	2.58	0.80	0.79	1.58
Al2O3	22.34	22.95	23.03	20.44	18.02	15.78	20.94	18.53	20.95	23.38	19.88	23.73	23.68	19.19	17.43	18.49	21.05	20.40	21.37	21.22	20.71	21.85	21.51	16.94
Cr2O3	0.05	0.11	0.06	0.15	0.00	0.00	0.00	0.00	0.20	0.04	0.04	0.03	0.07				0.02					0.07	0.05	0.03
MgO	2.69	2.73	2.75	2.79	7.67	11.09	2.81	3.17	2.69	2.19	2.29	1.78	2.20	3.10	4.53	2.43	2.86	2.22	2.26	2.08	2.16	3.30	3.20	2.45
CaO	5.87	6.37	5.78	5.13	5.76	4.14	5.05	5.44	6.05	3.56	7.28	3.26	4.21	7.37	7.21	6.44	5.96	4.55	4.03	4.12	4.54	7.66	7.44	2.18
MnO	0.08	0.08	0.00	0.07	0.03	0.10	0.05	0.07	0.00	0.01	0.03	0.01	0.05				0.10					0.05	0.09	0.02
FeO	4.46	4.07	4.28	4.46	4.05	4.95	3.81	4.65	3.64	3.05	3.88	3.29	2.85	6.37	8.93	4.67	5.16	3.72	1.97	2.40	2.99	3.82	4.59	2.10
NiO	0.03	0.00	0.00	0.01	0.07	0.14		0.05	0.00	0.00	0.00	0.00	0.02				0.06					0.03	0.06	0.02
Na2O	7.40	7.10	7.18	7.00	4.10	5.77	4.70	5.35	5.81	6.86	6.79	8.37	9.02	6.46	5.93	6.39	5.77	6.52	6.95	6.71	6.53	5.50	5.40	4.58
K2O	2.11	2.17	2.25	2.82	2.27	2.35	3.31	3.21	3.69	1.78	1.73	2.19	2.16	3.22	3.14	2.87	3.61	6.16	5.75	5.94	5.69	3.28	2.60	3.93
Cl	0.24	0.17	0.20	0.36	0.28	0.24	0.28	0.33	0.24	0.13	0.25	0.13	0.11	0.14	0.17	0.16	0.20	0.19	0.15	0.17	0.16	0.18	0.18	0.10
TOTAL	99.99	99.23	99.27	99.24	97.19	94.69	96.91	99.56	100.15	99.75	99.71	101.37	102.31	97.49	98.70	94.80	99.34	98.51	97.60	98.16	98.52	98.36	97.90	98.47
Mg#	51.83	54.42	53.40	52.77	77.13	79.96	56.82	54.91	56.85	56.10	51.23	49.16	57.97	46.44	47.48	48.11	49.69	51.54	67.15	60.70	56.28	60.65	55.39	67.56
Σalkalies	9.50	9.27	9.43	9.82	6.37	8.12	8.01	8.56	9.50	8.64	8.52	10.55	11.18	9.68	9.07	9.26	9.38	12.68	12.70	12.65	12.22	8.77	8.00	8.51
K2O/Na2O	0.28	0.31	0.31	0.40	0.55	0.41	0.70	0.60	0.64	0.26	0.26	0.26	0.24	0.50	0.53	0.45	0.63	0.95	0.83	0.89	0.87	0.60	0.48	0.86

Table B9: continued

Sample	70961	70961	70961	70961	70961	70961	70961	71006	71006	71006	71006	70982	76995	76995	76995	76995	76995	76995	76996	76996	76996	76996	76996	71023
Field No.													SH20	SH20	SH20	SH20	SH20	SH20	SH8	SH8	SH8	SH8	SH8	
Glass patch	C12	C2	C4	C5	C6	C7	C8	C2	C3	C4	C1	C3	C1	C10	C6	C5	C4	C3	C2	C6	C9	C11	C12	C6
P2O5	1.13	0.74	0.72	0.65	0.92	0.96	0.34	0.33	0.40	0.29	0.52	0.95	0.16	0.09	0.04	0.31	0.12	0.09	0.20	1.05	0.72	1.10	0.24	0.44
SiO2	52.77	62.28	59.93	61.49	61.77	59.00	66.42	48.97	52.29	50.30	51.06	59.49	62.58	64.00	64.40	59.14	63.54	60.38	73.63	65.96	66.08	67.88	63.48	57.68
TiO2	2.16	1.71	1.62	1.44	1.49	1.79	1.20	0.78	0.83	1.01	0.96	0.91	0.86	0.77	0.93	1.70	0.92	0.55	0.25	0.25	0.32	0.24	0.35	0.18
Al2O3	19.76	17.55	20.36	20.04	18.59	17.90	17.27	22.53	23.53	22.59	22.11	20.66	19.98	19.46	19.11	18.62	19.67	24.14	13.39	15.82	17.09	12.71	18.45	24.65
Cr2O3	0.19	0.03	0.10	0.04	0.06	0.01	0.02	0.31			0.06	0.07	0.02	0.05	0.04	0.27	0.00	0.09	0.08	0.09	0.07	0.00	0.17	0.07
MgO	2.04	1.35	1.88	1.82	1.77	2.14	1.23	4.07	3.18	3.03	3.43	2.70	2.20	2.15	1.22	1.95	2.14	0.76	3.26	3.98	3.49	4.14	2.97	2.48
CaO	5.01	2.56	3.91	3.43	2.87	5.08	1.38	7.58	7.78	7.23	7.04	5.44	4.55	4.61	4.65	6.03	4.26	6.39	1.18	3.00	2.46	3.56	1.91	4.01
MnO	0.09	0.02	0.03	0.03	0.02	0.05	0.02	0.05			0.09	0.04	0.00	0.00	0.00	0.03	0.00	0.00	0.03	0.03	0.04	0.09	0.02	0.04
FeO	6.01	3.77	2.71	2.27	2.25	3.18	1.51	3.47	3.18	3.83	4.22	2.22	1.94	1.86	1.22	1.61	1.66	0.57	3.10	3.08	3.36	4.01	2.91	1.74
NiO	0.00	0.01	0.01	0.02	0.00	0.02	0.03	0.02			0.02	0.01	0.02	0.04	0.00	0.01	0.00	0.02	0.03	0.01	0.01	0.03	0.00	0.01
Na2O	6.30	4.97	6.04	6.15	5.03	5.16	4.75	6.83	7.20	7.29	7.43	6.22	5.95	5.78	5.68	6.04	5.74	6.69	6.76	6.17	6.72	6.68	6.41	9.48
K2O	4.28	4.48	3.68	3.69	3.83	3.60	4.04	2.46	3.05	2.97	2.49	2.65	1.89	1.41	1.24	1.15	1.79	0.43	1.70	2.97	1.65	1.60	1.59	1.04
Cl	0.18	0.09	0.09	0.13	0.11	0.12	0.09	0.15	0.15	0.16	0.13	0.16	0.15	0.14	0.10	0.39	0.18	0.04	0.10	0.14	0.15	0.15	0.14	
TOTAL	98.79	98.83	100.37	100.56	97.78	98.04	97.99	97.22	101.16	98.39	99.03	100.57	100.13	100.27	98.58	96.93	99.88	100.07	103.50	101.50	101.44	101.11	98.40	101.38
Mg#	37.72	39.01	55.27	58.85	58.24	54.55	59.25	67.64	64.04	58.53	59.13	68.45	66.90	67.35	64.15	68.38	69.70	70.30	65.18	69.73	64.92	64.76	64.49	71.82
Σalkalies	10.58	9.45	9.72	9.84	8.85	8.77	8.80	9.29	10.24	10.26	9.92	8.87	7.83	7.19	6.92	7.19	7.52	7.11	8.46	9.14	8.36	8.29	8.00	10.52
K2O/Na2O	0.68	0.90	0.61	0.60	0.76	0.70	0.85	0.36	0.42	0.41	0.34	0.43	0.32	0.24	0.22	0.19	0.31	0.06	0.25	0.48	0.25	0.24	0.25	0.11

Table B9: continued

Sample	76998	76998	76998	76998	76998	76998
Field No.	SH31	SH31	SH31	SH31	SH31	SH31
Glass patch	C1	C2	C6	C3	C5	C9
P2O5	0.09	0.10	0.07	0.11	0.11	0.07
SiO2	56.06	58.29	62.68	56.50	60.00	57.76
TiO2	0.09	0.42	0.53	0.37	0.52	0.14
Al2O3	27.53	24.78	19.07	26.21	22.16	25.93
Cr2O3	0.04	0.10	0.02	0.02	0.00	0.04
MgO	0.11	0.39	3.99	0.43	0.50	0.08
CaO	10.01	6.99	3.60	8.93	5.86	8.57
MnO	0.00	0.03	0.00	0.03	0.00	0.01
FeO	0.31	0.53	1.41	0.65	0.82	0.21
NiO	0.08	0.01	0.01	0.04	0.04	0.04
Na2O	5.57	6.77	5.33	5.50	6.33	6.43
K2O	0.32	0.96	1.71	0.68	0.91	0.31
Cl	0.01	0.05	0.08	0.09	0.05	0.01
TOTAL	100.14	99.33	98.43	99.47	97.18	99.51
Mg#	38.24	56.65	83.40	54.06	52.06	40.19
Σalkalies	5.89	7.73	7.04	6.18	7.24	6.73
K2O/Na2O	0.06	0.14	0.32	0.12	0.14	0.05

Table B10: Representative analyses of olivine microphenocrysts included in amphibole±phlogopite glass patches.

Sample	70965	70965	70969	70969	76989	76989	76990	76990	76991	76991	76991	70997	70961	70961	70961	70961	70961	70961	71006	71006
Field No.					SH1	SH1	SH52	SH52	LE17	LE17	LE17									
Glass patch	C1	C2	C3	C2	C9	C8	C3	C7	C1	C5	C7	C6	C10	C12	C2	C4	C5	C6	C2	C3
SiO2	41.91	41.65	41.74	41.51	42.05	41.36	40.72	41.47	41.78	41.76	41.92	41.62	41.28	39.31	39.57	39.46	40.55	42.01	40.84	40.94
MgO	52.64	52.55	48.38	50.89	51.90	51.51	49.21	49.14	52.00	51.16	52.00	52.20	50.63	44.93	45.09	47.59	48.21	49.95	50.83	50.53
CaO	0.30	0.31	0.45	0.27	0.17	0.16	0.17	0.21	0.25	0.30	0.29	0.21	0.13	0.27	0.19	0.21	0.22	0.22	0.26	0.27
MnO	0.06	0.09	0.16	0.09	0.05	0.10	0.15	0.10	0.12	0.17	0.08	0.03	0.07	0.18	0.28	0.18	0.19	0.21	0.11	0.17
FeO	5.06	5.01	7.84	6.99	6.08	6.20	8.78	9.19	5.62	6.21	5.73	5.97	8.28	14.34	14.85	11.20	10.63	10.82	6.95	7.32
NiO	0.30	0.36	0.31	0.39	0.32	0.38	0.33	0.34	0.33	0.38	0.33	0.33	0.32	0.29	0.31	0.31	0.31	0.34	0.32	0.28
Total	100.27	99.96	98.89	100.14	100.56	99.71	99.36	100.44	100.10	99.98	100.35	100.36	100.72	99.32	100.27	98.95	100.11	103.54	99.32	99.50
Fo	94.88	94.92	91.66	92.84	93.83	93.68	90.90	90.51	94.28	93.63	94.18	93.97	91.59	84.81	84.40	88.33	88.99	89.17	92.87	92.48
Si	1.0031	1.0004	1.0241	1.0037	1.0070	1.0011	1.0009	1.0085	1.0043	1.0078	1.0053	0.9994	0.9982	0.9936	0.9926	0.9873	0.9981	0.9989	0.9967	0.9986
Mg	1.8771	1.8808	1.7687	1.8337	1.8520	1.8577	1.8027	1.7810	1.8623	1.8396	1.8582	1.8677	1.8241	1.6920	1.6853	1.7744	1.7683	1.7698	1.8484	1.8366
Ca	0.0076	0.0080	0.0119	0.0070	0.0044	0.0043	0.0045	0.0054	0.0065	0.0079	0.0074	0.0055	0.0034	0.0073	0.0050	0.0057	0.0057	0.0057	0.0068	0.0070
Mn	0.0011	0.0019	0.0033	0.0019	0.0010	0.0020	0.0030	0.0020	0.0024	0.0034	0.0016	0.0007	0.0015	0.0039	0.0059	0.0039	0.0039	0.0042	0.0022	0.0034
Fe	0.1013	0.1006	0.1608	0.1414	0.1217	0.1254	0.1805	0.1868	0.1130	0.1252	0.1149	0.1199	0.1675	0.3030	0.3116	0.2344	0.2188	0.2150	0.1419	0.1493
Ni	0.0067	0.0081	0.0071	0.0087	0.0070	0.0085	0.0074	0.0077	0.0073	0.0084	0.0072	0.0074	0.0072	0.0068	0.0071	0.0071	0.0070	0.0076	0.0073	0.0064
Total	2.9969	2.9996	2.9759	2.9963	2.9930	2.9989	2.9991	2.9915	2.9957	2.9922	2.9947	3.0006	3.0018	3.0064	3.0074	3.0127	3.0019	3.0011	3.0033	3.0014

Table B10: continued

Sample	71006	71006	76995	76995	76995	76995	76998	76998	76998	76998
Field No.			SH20	SH20	SH20	SH20	SH31	SH31	SH31	SH31
Glass patch	C4	C1	C1	C10	C5	C3	C1	C2	C3	C9
SiO2	40.91	41.03	41.04	41.00	41.01	40.85	41.44	41.07	41.69	41.60
MgO	50.31	50.82	50.41	49.57	50.34	49.87	50.10	50.26	50.71	50.72
CaO	0.27	0.24	0.20	0.21	0.14	0.14	0.21	0.18	0.19	0.16
MnO	0.10	0.13	0.07	0.06	0.11	0.07	0.13	0.12	0.12	0.14
FeO	6.92	7.19	8.43	8.79	8.00	7.97	7.59	7.13	7.42	7.25
NiO	0.39	0.43	0.39	0.37	0.32	0.39	0.18	0.38	0.36	0.32
Total	98.89	99.84	100.54	100.01	99.92	99.30	99.65	99.14	100.49	100.20
Fo	92.84	92.65	91.42	90.95	91.82	91.77	92.16	92.62	92.41	92.57
Si	1.0022	0.9973	0.9955	1.0010	0.9986	1.0009	1.0084	1.0038	1.0059	1.0059
Mg	1.8361	1.8408	1.8224	1.8032	1.8267	1.8208	1.8165	1.8307	1.8230	1.8273
Ca	0.0071	0.0062	0.0052	0.0054	0.0038	0.0037	0.0055	0.0047	0.0050	0.0042
Mn	0.0020	0.0028	0.0015	0.0013	0.0022	0.0015	0.0026	0.0024	0.0025	0.0029
Fe	0.1417	0.1461	0.1710	0.1795	0.1628	0.1633	0.1545	0.1458	0.1497	0.1466
Ni	0.0088	0.0097	0.0088	0.0085	0.0073	0.0089	0.0040	0.0087	0.0080	0.0072
Total	2.9978	3.0027	3.0045	2.9990	3.0014	2.9991	2.9916	2.9962	2.9941	2.9941

Table B11: Representative analyses of clinopyroxene microphenocrysts included in amphibole±phlogopite glass patches.

Sample	70965	70965	71000	71007	76988	76988	76988	76988	76988	76989	76989	76990	76990	76990	76991	76991	76991	70987	70997	70997
Field No.					SH19	SH19	SH19	SH19	SH19	SH1	SH1	SH52	SH52	SH52	LE17	LE17	LE17			
Glass patch	C1	C2	C2	C6	C1	C2	C3	C4	C8	C9	C8	C3	C4	C7	C1	C5	C7	C3	C6	C7
SiO2	52.79	51.44	50.50	51.60	51.37	51.12	52.24	51.61	51.49	53.52	50.83	53.44	52.40	53.19	52.78	52.51	52.74	51.74	51.84	51.82
TiO2	0.59	0.63	0.87	0.33	0.34	0.34	0.29	0.49	0.65	0.25	0.36	0.25	0.38	0.26	0.45	0.42	0.41	1.11	0.73	0.60
Al2O3	2.62	3.52	6.12	5.31	3.87	3.39	2.44	4.59	7.03	2.83	4.87	2.53	3.53	2.98	2.73	3.10	2.91	6.48	4.29	4.11
Cr2O3	1.30	3.11	2.58	3.04	2.04	1.36	1.28	1.65	1.33	2.00	2.65	1.72	3.20	1.83	2.15	2.71	2.45	1.35	2.31	2.65
MgO	17.07	16.19	14.85	15.47	16.26	18.07	16.71	15.82	14.00	16.78	17.45	17.07	16.01	16.71	16.32	16.31	16.85	14.21	16.33	16.57
CaO	22.73	22.40	22.53	22.07	22.53	21.00	23.71	22.18	20.58	21.83	18.12	21.52	21.21	22.46	22.75	22.05	21.83	20.36	22.51	21.41
MnO	0.00	0.01		0.00	0.03	0.05	0.03	0.01	0.02	0.05	0.05	0.12	0.04	0.05	0.05	0.00	0.00		0.00	0.00
FeO	1.57	1.70	1.92	1.62	2.01	2.80	2.02	1.87	2.58	1.96	2.04	2.43	1.84	2.03	1.96	1.93	1.95	3.23	1.78	1.75
NiO	0.16	0.10		0.00	0.05	0.08	0.05	0.07	0.02	0.03	0.04	0.00	0.07	0.15	0.04	0.07	0.01		0.12	0.08
Na2O	1.40	0.99	0.63	0.94	0.79	0.89	0.54	1.09	1.60	1.13	1.83	0.90	1.20	0.86	0.87	1.15	0.90	1.38	0.80	1.05
Total	100.22	100.11	100.00	100.38	99.30	99.09	99.32	99.38	99.30	100.36	98.24	99.98	99.88	100.53	100.09	100.25	100.04	99.85	100.71	100.03
Mg#	95.09	94.42	93.23	94.44	93.51	92.00	93.65	93.79	90.63	93.86	93.86	92.60	93.93	93.61	93.70	93.76	93.90	88.70	94.25	94.41
Si	1.9186	1.8788	1.8403	1.8690	1.8865	1.8813	1.9195	1.8877	1.8748	1.9347	1.8708	1.9401	1.9086	1.9254	1.9213	1.9094	1.9161	1.8759	1.8759	1.8837
Ti	0.0162	0.0174	0.0238	0.0090	0.0095	0.0094	0.0081	0.0136	0.0179	0.0068	0.0100	0.0067	0.0105	0.0072	0.0124	0.0115	0.0111	0.0302	0.0199	0.0163
Al	0.1121	0.1516	0.2626	0.2268	0.1677	0.1470	0.1055	0.1979	0.3017	0.1205	0.2112	0.1082	0.1516	0.1271	0.1171	0.1327	0.1248	0.2769	0.1829	0.1763
Cr	0.0372	0.0898	0.0742	0.0870	0.0593	0.0395	0.0372	0.0477	0.0382	0.0573	0.0772	0.0494	0.0921	0.0523	0.0619	0.0779	0.0703	0.0387	0.0659	0.0763
Mg	0.9244	0.8810	0.8061	0.8348	0.8898	0.9907	0.9150	0.8621	0.7593	0.9040	0.9571	0.9237	0.8687	0.9012	0.8855	0.8840	0.9120	0.7675	0.8805	0.8974
Ca	0.8849	0.8766	0.8797	0.8563	0.8866	0.8279	0.9334	0.8691	0.8026	0.8454	0.7143	0.8372	0.8278	0.8709	0.8871	0.8590	0.8497	0.7908	0.8727	0.8338
Mn	0.0000	0.0003	0.0000	0.0000	0.0009	0.0015	0.0008	0.0004	0.0005	0.0015	0.0016	0.0035	0.0012	0.0016	0.0015	0.0000	0.0000	0.0000	0.0000	0.0000
Fe	0.0477	0.0521	0.0585	0.0491	0.0617	0.0862	0.0620	0.0571	0.0785	0.0591	0.0627	0.0738	0.0561	0.0615	0.0595	0.0588	0.0592	0.0978	0.0537	0.0531
Na	0.0986	0.0704	0.0447	0.0662	0.0565	0.0638	0.0387	0.0770	0.1131	0.0790	0.1307	0.0637	0.0847	0.0603	0.0611	0.0810	0.0634	0.0970	0.0561	0.0738
Total	4.0398	4.0187	3.9899	3.9982	4.0190	4.0487	4.0206	4.0163	4.0013	4.0098	4.0450	4.0062	4.0014	4.0081	4.0076	4.0143	4.0073	3.9946	4.0080	4.0106
En	49.78	48.68	46.22	47.97	48.41	52.01	47.89	48.21	46.29	49.98	55.19	50.35	49.56	49.15	48.33	49.06	50.08	46.34	48.73	50.29
Fs	2.57	2.88	3.35	2.82	3.36	4.52	3.25	3.19	4.78	3.27	3.61	4.02	3.20	3.35	3.25	3.26	3.25	5.91	2.97	2.98
Wo	47.65	48.44	50.43	49.21	48.23	43.47	48.86	48.60	48.93	46.75	41.19	45.63	47.23	47.50	48.42	47.67	46.66	47.75	48.30	46.73

Table B11: continued

Sample	71004	71008	71008	71008	71008	70961	70961	70961	70961	70961	71006	71006	76995	76995	76995	76998	76998	76998	76998
Field No.													SH20	SH20	SH20	SH31	SH31	SH31	SH31
Glass patch	C2	C1	C2	C2	C6	C4	C5	C6	C8	C10	C2	C1	C5	C3	C1	C1	C2	C3	C9
SiO2	51.54	51.87	51.82	51.68	47.37	51.58	52.61	51.80	52.54	53.02	47.97	51.11	50.62	51.89	51.23	50.73	50.50	52.45	52.18
TiO2	1.30	0.38	0.23	0.28	0.40	0.77	0.74	0.72	0.59	0.65	1.02	0.43	0.73	0.58	0.53	0.33	0.39	0.41	0.25
Al2O3	4.99	4.03	3.73	3.71	8.62	3.58	3.32	2.81	2.22	1.90	8.40	4.90	4.62	3.94	5.22	6.16	5.80	3.98	4.39
Cr2O3	1.45	2.36	2.54	2.20	3.94	2.03	1.60	1.95	1.84	1.84	2.21	1.57	1.33	0.86	3.48	1.76	2.41	1.48	2.72
MgO	16.56	16.58	17.10	17.31	13.99	16.24	16.53	16.61	17.58	17.90	13.98	16.42	16.33	16.86	16.09	15.68	15.79	16.38	16.36
CaO	21.91	21.39	21.65	21.72	21.37	22.41	21.91	22.48	21.57	20.93	22.42	22.03	22.21	21.58	19.39	22.42	21.59	23.10	21.32
MnO		0.00	0.00	0.00	0.00	0.08	0.06	0.10	0.07	0.08	0.00	0.05	0.13	0.05	0.00	0.05	0.05	0.02	0.01
FeO	1.68	2.13	2.00	1.96	2.05	2.88	2.77	3.00	2.46	2.57	1.16	1.98	2.83	2.56	2.01	1.66	1.87	2.13	1.62
NiO		0.04	0.18	0.14	0.03	0.04	0.05	0.09	0.05	0.06	0.11	0.15	0.09	0.08	0.03	0.05	0.09	0.01	0.04
Na2O	0.57	0.83	0.77	0.71	1.14	0.78	0.81	0.76	0.79	0.84	0.75	0.64	0.58	0.51	1.44	0.86	0.87	0.55	0.92
Total	100.00	99.60	100.00	99.69	98.92	100.39	100.40	100.31	99.71	99.79	98.01	99.29	99.46	98.92	99.41	99.70	99.35	100.51	99.81
			core	rim															
Mg#	94.61	93.28	93.84	94.03	92.40	90.94	91.40	90.80	92.72	92.53	95.54	93.67	91.15	92.15	93.46	94.38	93.78	93.19	94.75
Si	1.8665	1.8927	1.8881	1.8870	1.7562	1.8812	1.9082	1.8936	1.9189	1.9315	1.7822	1.8724	1.8606	1.9028	1.8691	1.8494	1.8499	1.8978	1.8953
Ti	0.0354	0.0105	0.0062	0.0077	0.0111	0.0212	0.0202	0.0197	0.0163	0.0179	0.0285	0.0117	0.0202	0.0161	0.0144	0.0089	0.0107	0.0111	0.0069
Al	0.2130	0.1731	0.1600	0.1594	0.3766	0.1537	0.1420	0.1211	0.0955	0.0814	0.3677	0.2117	0.2002	0.1703	0.2246	0.2647	0.2504	0.1698	0.1877
Cr	0.0415	0.0680	0.0730	0.0635	0.1154	0.0585	0.0458	0.0563	0.0532	0.0529	0.0649	0.0455	0.0386	0.0248	0.1005	0.0506	0.0698	0.0425	0.0781
Mg	0.8936	0.9014	0.9284	0.9416	0.7731	0.8826	0.8932	0.9047	0.9568	0.9718	0.7739	0.8962	0.8943	0.9212	0.8748	0.8518	0.8616	0.8834	0.8854
Ca	0.8500	0.8360	0.8454	0.8494	0.8490	0.8757	0.8513	0.8804	0.8442	0.8167	0.8923	0.8647	0.8744	0.8478	0.7579	0.8756	0.8471	0.8957	0.8298
Mn	0.0000	0.0000	0.0000	0.0000	0.0000	0.0024	0.0019	0.0031	0.0021	0.0023	0.0000	0.0016	0.0041	0.0017	0.0000	0.0014	0.0015	0.0006	0.0002
Fe	0.0509	0.0649	0.0609	0.0598	0.0636	0.0879	0.0840	0.0916	0.0752	0.0784	0.0361	0.0606	0.0868	0.0785	0.0613	0.0507	0.0572	0.0645	0.0491
Na	0.0400	0.0585	0.0541	0.0499	0.0820	0.0549	0.0568	0.0539	0.0561	0.0595	0.0541	0.0458	0.0413	0.0362	0.1018	0.0611	0.0619	0.0382	0.0648
Total	3.9909	4.0059	4.0162	4.0192	4.0282	4.0195	4.0086	4.0252	4.0188	4.0139	4.0004	4.0102	4.0205	4.0038	4.0051	4.0146	4.0104	4.0046	3.9973
En	49.80	50.01	50.60	50.88	45.86	47.81	48.85	48.21	51.00	52.05	45.46	49.20	48.19	49.86	51.64	47.91	48.79	47.92	50.18
Fs	2.83	3.60	3.32	3.23	3.77	4.76	4.60	4.88	4.01	4.20	2.12	3.32	4.68	4.25	3.62	2.85	3.24	3.50	2.78
Wo	47.37	46.38	46.08	45.89	50.36	47.43	46.56	46.91	45.00	43.75	52.41	47.47	47.13	45.89	44.74	49.24	47.97	48.58	47.03

Table B12: Representative analyses of spinel microphenocrysts included in amphibole±phlogopite glass patches. Mg*, Cr* and Fe^{3+*} are defined in caption for table B3. Cation calculations assumed perfect stoichiometry.

Sample	70965	70969	70972	70972	71000	71001	71007	76989	76989	76990	76990	76990	76991	76991	76991	76992	76992	70987	70997
Field No.								SH1	SH1	SH52	SH52	SH52	LE17	LE17	LE17	NO11	NO11		
Glass Patch	C1	C10	C1	C6	C2	C1	C9	C9	C8	C8	C7	C3	C1	C7	C5	C6	C11	C3	C6
SiO2	0.53	0.08	0.35	0.15	0.24		0.07	0.08	0.09	0.06	0.27	0.11	0.10	0.14	0.27	0.10	0.07	0.00	0.05
TiO2	1.68	0.39	0.44	0.28	0.40	0.31	0.46	0.39	0.55	0.57	0.50	0.63	0.75	0.85	0.77	1.72	1.56	0.52	1.15
Fe2O3	5.38		4.08	4.66	2.12	3.25	4.76	3.72	3.80	6.86	5.51	5.74	7.39	6.67	7.28	6.57	4.73	3.57	3.27
Al2O3	19.75	24.73	21.10	17.40	43.18	5.40	26.04	19.85	21.75	19.92	20.02	20.37	16.83	21.29	18.00	13.90	10.66	31.31	30.04
Cr2O3	44.02	38.32	46.83	45.03	25.84	65.66	38.38	48.08	45.91	43.01	44.82	44.80	45.41	43.25	45.19	49.37	54.52	33.96	37.54
MgO	16.35	11.10	16.90	9.64	21.32	14.70	14.54	16.37	16.84	12.92	13.65	14.20	15.15	16.56	15.21	13.78	12.01	12.84	18.48
MnO		0.17					0.18	0.14	0.11	0.20	0.14	0.24	0.14	0.17	0.24	0.25	0.29		0.17
FeO	12.10	21.35	10.09	18.22	6.89	10.69	12.61	9.12	8.75	14.33	13.51	12.73	9.57	8.73	9.95	11.87	14.34	17.80	7.46
NiO		0.25		0.13			0.19	0.15	0.17	0.20	0.19	0.21	0.18	0.20	0.21	0.19	0.11	0.00	0.37
Total	99.81	96.39	99.79	95.51	99.99	100.01	97.23	97.90	97.98	98.07	98.61	99.03	95.50	97.86	97.12	97.76	98.29	100.00	98.53
Mg*	71.85	52.57	75.57	47.92	85.26	71.03	66.54	75.46	76.45	60.79	63.67	65.58	72.31	75.31	71.55	64.65	57.63	56.21	79.45
Cr*	59.86	50.90	59.76	63.39	28.59	89.05	49.65	61.84	58.54	59.10	59.96	59.53	64.35	57.61	62.68	70.39	77.38	42.05	45.54
Fe3+*	32.63	16.39	29.26	16.71	25.35	21.53	22.86	23.90	24.09	27.58	24.81	25.79	36.28	34.34	34.68	24.47	15.35	15.17	18.12
Ti	0.0387	0.0093	0.0100	0.0071	0.0081	0.0076	0.0107	0.0091	0.0127	0.0136	0.0119	0.0148	0.0181	0.0197	0.0184	0.0420	0.0387	0.0116	0.0252
Fe3+	0.1416	0.0928	0.1020	0.1049	0.0505	0.0801	0.0993	0.0772	0.0751	0.1498	0.1203	0.1200	0.1592	0.1305	0.1521	0.1180	0.0790	0.0792	0.0460
Al	0.7149	0.9273	0.7557	0.6887	1.3805	0.2085	0.9463	0.7268	0.7874	0.7456	0.7430	0.7488	0.6433	0.7757	0.6759	0.5324	0.4170	1.0996	1.0368
Cr	1.0661	0.9612	1.1222	1.1922	0.5527	1.6962	0.9331	1.1778	1.1121	1.0773	1.1129	1.1016	1.1613	1.0544	1.1353	1.2656	1.4265	0.7980	0.8668
Mg	0.7463	0.5249	0.7633	0.4810	0.8596	0.7157	0.6662	0.7558	0.7688	0.6098	0.6389	0.6579	0.7301	0.7609	0.7202	0.6659	0.5923	0.5686	0.8043
Mn	0.0000	0.0046	0.0000	0.0000	0.0000	0.0000	0.0048	0.0037	0.0028	0.0053	0.0037	0.0062	0.0039	0.0044	0.0065	0.0070	0.0080	0.0000	0.0042
Fe2+	0.2924	0.4735	0.2467	0.5227	0.1486	0.2919	0.3350	0.2458	0.2368	0.3934	0.3646	0.3454	0.2796	0.2494	0.2864	0.3641	0.4355	0.4430	0.2080
Ni	0.0000	0.0063	0.0000	0.0034	0.0000	0.0000	0.0047	0.0037	0.0043	0.0052	0.0047	0.0053	0.0046	0.0050	0.0054	0.0050	0.0030	0.0000	0.0087
Total	3.0000	3.0000	3.0000	3.0000	3.0000	3.0000	3.0000	3.0000	3.0000	3.0000	3.0000	3.0000	3.0000	3.0000	3.0000	3.0000	3.0000	3.0000	3.0000

Table B12: continued

Sample	71008	71006	71006	71006	71006	76995	76995	76995	76995	76998	76998
Field No.						SH20	SH20	SH20	SH20	SH31	SH31
Glass Patch	C2	C1	C2	C3	C4	C3	C5	C9	C10	C3	C2
SiO2	0.53	0.08	0.09	0.12	0.50	0.13	0.17	0.06	0.18	0.91	0.13
TiO2	0.44	0.24	0.27	0.45	0.64	0.59	0.87	0.45	0.78	0.70	0.27
Fe2O3	3.60	2.77	2.49	2.57	3.97	4.04	5.30	3.65	3.07	6.02	2.00
Al2O3	32.14	46.86	43.68	38.72	33.01	25.55	22.67	27.71	22.53	25.70	35.62
Cr2O3	34.65	20.90	23.36	26.86	32.51	41.61	42.93	40.49	45.53	39.32	31.10
MgO	18.34	20.70	20.18	17.77	18.56	15.00	14.18	16.50	14.49	15.72	17.59
MnO		0.16	0.05	0.07	0.13	0.18	0.13	0.13	0.10	0.16	0.08
FeO	9.65	6.88	6.86	9.46	7.57	12.80	13.62	10.88	13.21	11.29	9.29
NiO		0.37	0.26	0.20	0.22	0.11	0.12	0.13	0.11	0.31	0.18
Total	99.35	98.96	97.24	96.21	97.11	100.01	99.99	100.00	100.00	100.12	96.26
Mg*	78.23	83.79	83.48	76.23	80.53	66.74	63.75	72.24	65.06	70.13	76.68
Cr*	41.90	22.98	26.35	31.70	39.72	52.14	55.89	49.43	57.48	50.59	36.87
Fe3+*	29.43	23.84	21.77	16.14	28.28	18.94	21.85	20.22	13.17	28.60	14.06
Ti	0.0096	0.0049	0.0055	0.0097	0.0140	0.0133	0.0200	0.0100	0.0179	0.0159	0.0059
Fe3+	0.0917	0.0504	0.0459	0.0459	0.0772	0.0782	0.1028	0.0706	0.0537	0.1202	0.0382
Al	1.0975	1.4940	1.4310	1.3214	1.1422	0.9069	0.8192	0.9655	0.8123	0.9131	1.2310
Cr	0.7917	0.4458	0.5120	0.6133	0.7525	0.9882	1.0380	0.9439	1.0983	0.9350	0.7190
Mg	0.7898	0.8322	0.8336	0.7649	0.8098	0.6714	0.6462	0.7250	0.6588	0.7044	0.7665
Mn	0.0000	0.0036	0.0011	0.0018	0.0032	0.0046	0.0034	0.0032	0.0026	0.0040	0.0021
Fe2+	0.2198	0.1610	0.1650	0.2385	0.1957	0.3347	0.3675	0.2787	0.3538	0.3000	0.2332
Ni	0.0000	0.0081	0.0058	0.0046	0.0053	0.0027	0.0030	0.0031	0.0027	0.0074	0.0041
Total	3.0000	3.0000	3.0000	3.0000	3.0000	3.0000	3.0000	3.0000	3.0000	3.0000	3.0000

Table B13: Representative analyses of carbonate, with textural setting indicated. Ca/Mg+Fe calculated on an atomic basis.

Sample	76995	73797	73797	76993
Field No.	SH20			SH34
	Inclusion in glass	Inclusion in OL	Vein	Inclusion in glass
P2O5	1.01	1.01	2.49	0.93
SiO2	0.02	1.33	0.36	0.00
MgO	3.25	4.76	2.18	4.27
CaO	52.25	57.14	53.75	55.69
MnO	0.01	0.00	0.00	0.00
FeO	0.14	0.39	0.46	0.08
NiO	0.01	0.05	0.02	0.06
Na2O	0.03	0.04	0.07	0.03
K2O	0.01	0.01	0.00	0.00
TOTAL	56.73	64.74	59.34	61.06
Mg#	97.60	95.56	88.32	98.96
Ca/Mg+Fe	11.28	8.24	15.87	9.28

APPENDIX C

GEOCHEMISTRY OF WESTERN VICTORIAN SPINEL PERIDOTITE XENOLITHS

Table C1: Major, minor and trace element data for carbonatized spinel peridotite suite

Table C1: Major, minor and trace element whole-rock analyses of western Victorian spinel peridotite xenoliths. Analytical details are given in Appendix A. Mg# = 100*mol Mg/(mol Mg+mol Fe^{2+}). Quoted errors are range of duplicate analyses.

Sample	70965	70969	70972	71000	71001	71007	2631	76988
Field No.								SH19
SiO2	43.87	42.00	42.68	42.56	41.18	43.53	42.82	42.85
TiO2	0.08	0.04	0.02	0.06	0.10	0.06	0.07	0.06
Al2O3	0.98	0.49	0.68	1.21	0.92	1.11	0.93	1.19
Fe2O3	9.12	10.56	8.19	9.56	11.08	9.82	9.17	10.22
Cr2O3	0.51	0.27	0.73	0.41	0.45	0.40	0.44	
MnO	0.15	0.16	0.13	0.15	0.18	0.14	0.15	0.15
MgO	40.91	44.75	43.70	41.88	42.53	42.84	43.17	42.37
CaO	4.29	2.26	3.55	3.76	2.72	2.38	2.72	3.31
Na2O	0.54	0.21	0.30	0.37	0.65	0.33	0.50	0.50
K2O	0.03	0.07	0.05	0.06	0.07	0.07	0.09	0.13
P2O5	0.02	0.25	0.14	0.47	0.77	0.09	0.21	0.30
LOI	-0.60	-0.65	-0.31	-0.61	-0.61	-0.28	-0.50	-0.55
TOTAL	99.90	100.41	99.86	99.88	100.04	100.49	99.77	100.53
Mg#	89.89	89.36	91.36	89.67	88.38	89.63	90.32	89.15
La	2.30	14.20	7.76	18.50	45.50		24.80	
Ce	6.94	29.30	18.20	37.00	90.10		44.40	
Nd	5.60	14.20	12.00	18.40	38.40		21.30	
Sm	1.71	2.80	2.47	2.91	6.54		3.44	
Eu	0.63	0.74	0.77	0.80	1.90		0.83	
Tb	0.40	0.36	0.30	<0.28	0.64		0.29	
Ho	0.40	0.38	<0.23	<0.23	0.53		0.21	
Yb	0.50	0.43	0.36	0.40	0.50		0.45	
Lu	0.08	0.06	<0.05	0.06	<0.07		0.05	
Rb	2	2	2	<2	<2	2	3	<2
Ba	25.5±3.5	37	59	18	22	94±2	40	30
Th	<0.40	1.24	0.85	1.95	5.53		2.77	
Nb	18	6	7	10	17	4	11	23.4
Ta	0.92	0.65	<0.30	0.34	<0.30		<0.33	
Sr	90	116	124	189	471	144	184	99.7
Zr	59	10	14	37.3	46.1	31.2	17	28.2
Hf	0.58	<0.28	0.27	0.88	1.00		0.24	
Y	5	6	6	7	12	5	5	3.9
Sc	11.8±0.1	5.1	9	8.7	6.6	8.75±0.05	7.9	8.6
Ni	2135	2599	2324	2144	2411	2453	2256	2233
Cr	3021	1760	4555	2611	2789	2474	2586	2442
V	43.6	17.2	30.3	37.7	25.3	33.8	35.1	37.5

Table C1: continued

Sample	73797	76989	76990	76991	73770	70987	70997	71004
Field No.		SH1	SH52	LE17				
SiO2	42.15	41.20	41.75	42.55	40.85	43.16	42.03	41.92
TiO2	0.03	0.00	0.00	0.01	0.09	0.15	0.10	0.20
Al2O3	1.17	0.72	0.77	0.63	0.59	1.01	0.91	1.44
Fe2O3	8.86	9.37	10.71	10.34	12.93	10.11	10.82	9.58
Cr2O3						0.31	0.35	0.43
MnO	0.16	0.14	0.16	0.15	0.20	0.15	0.16	0.14
MgO	43.69	43.97	43.08	44.95	42.92	42.98	41.42	42.71
CaO	2.45	3.27	2.51	2.12	2.15	2.01	3.76	3.36
Na2O	0.79	0.51	0.44	0.32	0.35	0.29	0.29	0.32
K2O	0.21	0.04	0.06	0.03	0.06	0.06	0.02	0.04
P2O5	0.25	0.64	0.38	0.00	0.14	0.06	0.04	0.12
LOI	-0.38	-0.55	-0.60	-0.73	-0.97	-0.69	-0.46	-0.21
TOTAL	99.38	99.31	99.26	100.37	99.31	99.60	99.44	100.05
Mg#	90.71	90.29	88.85	89.60	86.80	89.39	88.35	89.83
La	8.16	26.80	19.30	2.43		2.66		7.06
Ce	20.10	52.70	34.80	6.50		5.46		16.20
Nd	11.70	20.80	14.50	4.50		4.01		9.70
Sm	2.51	3.45	2.80	1.23		0.94		1.96
Eu	0.74	0.94	0.77	0.42		0.30		0.46
Tb	0.29	0.32	0.28	0.19		<0.10		0.28
Ho	0.26	0.22	0.27	0.22		<0.10		0.29
Yb	0.34	0.30	0.30	0.32		0.14		0.39
Lu	0.04	0.04	0.04	0.04		0.02		0.06
Rb	5	<2	<2	<2	<2	3	<2	2
Ba	48	46	18	12	7	22	40	86
Th	0.71	2.51	2.65	<0.10		0.60		0.83
Nb	12	12.5	12	11.6	2.8	2	3	7
Ta	<0.20	0.51	0.60	0.38		<0.30		1.14
Sr	121.4	266.1	192.4	69.8	70.5	47	97	107
Zr	26.1	12.4	37.5	24.3	19.4	16.7	29.2	29
Hf	0.28	0.19	0.54	0.30		0.49		0.57
Y	7.5	6.4	5.4	3.2	4.3	5	5	5
Sc	8.5	7	7.8	5	4.9	8.1	10.8	8.1
Ni	2272	2361	2339	2363	2423	2251	2206	2204
Cr	2959	2615	3097	1996	1605	1853	2406	2416
V	39.5	28.8	32.7	26.8	24.6	34.4	40.6	38.4

Table C1: continued

Sample	71008	70961	76993	76994	71003	71006	70982	77000
Field No.			SH34	LE10				NO7
SiO2	41.94	43.58	42.15	42.59	43.52	44.36	44.16	43.75
TiO2	0.05	0.10	0.05	0.11	0.04	0.12	0.01	0.01
Al2O3	1.09	1.05	0.59	1.01	1.00	2.59	0.60	0.65
Fe2O3	11.93	10.31	9.09	10.41	10.25	11.19	8.93	9.08
Cr2O3	0.40				0.58	0.47		
MnO	0.16	0.17	0.14	0.17	0.14	0.17	0.14	0.14
MgO	41.54	42.20	44.86	42.53	44.20	38.42	45.63	45.55
CaO	3.16	1.87	2.22	2.53	0.82	2.55	0.63	0.79
Na2O	0.32	0.68	0.33	0.38	0.11	0.55	<0.20	<0.20
K2O	0.05	0.17	0.05	0.13	0.04	0.14	0.04	0.04
P2O5	0.55	0.11	0.15	0.13	0.05	0.05	0.06	0.06
LOI	-0.68	-0.71	-0.47	-0.58	-0.43	-0.56	-0.60	-0.11
TOTAL	100.51	99.53	99.16	99.41	100.32	100.05	99.60	99.96
Mg#	87.34	89.02	90.72	89.00	89.52	87.18	91.01	90.86
La	28.70							
Ce	55.50							
Nd	22.10							
Sm	3.54							
Eu	1.00							
Tb	<0.30							
Ho	<0.24							
Yb	0.38							
Lu	0.05							
Rb	<2	4	<2	5	<2	4	2	3
Ba	26±1	28	26	36	25	47	9	20
Th	3.04	-						
Nb	7	8.6	4.8	1.9	<1	5	2.3	4.1
Ta	0.76							
Sr	187	69.1	86.1	184.7	20	101	36.2	62.7
Zr	23	31.9	30.2	4.2	1.1	20	4.5	2.2
Hf	0.44							
Y	8	4.2	4.4	8.9	<2	6	<2	1.9
Sc	8.3±0.4	7.3	7.4	8.8	9.1	13.2	6.1	6.8
Ni	2275	2287	2671	2375	2516	2010	2454	2431
Cr	2549	3122	3183	2973	3351	2794	2182	3205
V	34.5	31.7	28.6	41.3	36.1	68.3	19.5	27.9

Table C1: continued

Sample	76999	76995	76996	71023	76997
Field No.	SH11	SH20	SH8		SH40
SiO2	43.65	47.02	42.19	43.73	42.66
TiO2	0.01	0.03	0.00	0.00	0.04
Al2O3	0.62	1.40	0.46	0.79	0.77
Fe2O3	8.82	8.34	11.68	8.65	8.56
Cr2O3					
MnO	0.14	0.12	0.19	0.11	0.12
MgO	45.08	41.62	44.34	45.62	45.52
CaO	1.09	0.95	0.98	0.81	1.55
Na2O	<0.20	<0.20	0.32	0.00	0.25
K2O	0.04	0.07	0.06	0.00	0.04
P2O5	0.12	0.02	0.24	0.04	0.14
LOI	-0.57	-0.43	-0.73	-0.46	-0.47
TOTAL	99.00	99.14	99.73	99.29	99.18
Mg#	91.01	90.81	88.26	91.27	91.33
La		2.28		9.20	
Ce		5.00		15.40	
Nd		2.61		6.72	
Sm		0.51		0.90	
Eu		0.15		0.26	
Tb		0.07		0.12	
Ho		0.07		0.11	
Yb		0.13		0.08	
Lu		0.02		0.01	
Rb	<2	<2	<2	<2	<2
Ba	22	25	5	33	19
Th		0.31		2.32	
Nb	7.8	5	7.3	1.8	5.5
Ta		0.32		<0.20	
Sr	73.9	32.7	116	75.4	47.6
Zr	19.4	8.8	6.6	<2	15.8
Hf		0.19		<0.10	
Y	2.5	<2	4.3	<2	2.2
Sc	6.1	8.5	4.7	6.2	7.3
Ni	2432	2108	2442	2447	2700
Cr	2725	3845	2848	2466	2042
V	26.7	47.1	21.9	32.3	29.9

APPENDIX D

REPRESENTATIVE ELECTRON MICROPROBE ANALYSES OF MINERAL PHASES FROM MAGNESIAN WEHRLITE+CO_2 EXPERIMENTAL RUNS

Table D1: Representative olivine compositions. Fo is mol% forsterite.

Composition	71001					70965						
Run No	T-3301	T-3172	T-3197	T-3491	T-3188	T-3482	T-3315	T-3586	T-3447	T-3327	T-3469	T-3336
T (°C)	900	900	1050	1070	1100	900	900	1050	1000	1050	1070	1150
$\%CO_2$	1	5	5	5	5	1	5	10	5	5	5	5
SiO_2	39.49	40.76	39.42	41.07	40.27	40.74	41.71	40.95	40.94	40.91	41.27	41.07
MgO	47.52	47.19	47.77	48.48	47.70	47.95	47.19	49.33	48.24	48.45	48.82	48.56
CaO	0.18	0.09	0.13	0.20	0.09	0.16	0.17	0.20	0.41	0.19	0.26	0.20
MnO	0.30	0.29	0.33	0.28	0.25	0.26	0.26	0.20	0.24	0.25	0.16	0.26
FeO	11.59	11.51	11.45	11.32	11.66	10.60	10.12	9.44	9.64	10.31	9.72	9.72
NiO	-	-	-	-	-	0.28	0.25	0.35	0.23	0.26	0.33	0.28
Total	99.08	99.85	99.10	101.35	99.97	100.00	99.70	100.47	99.70	100.38	100.56	100.08
Fo	87.96	87.96	88.15	88.42	87.94	88.97	89.26	90.30	89.93	89.33	89.95	89.91
Si	0.9877	1.0077	0.9854	0.9999	0.9963	1.0032	1.0246	0.9988	1.0067	1.0021	1.0058	1.0060
Mg	1.7711	1.7381	1.7794	1.7588	1.7585	1.7593	1.7274	1.7927	1.7674	1.7684	1.7727	1.7722
Ca	0.0048	0.0024	0.0035	0.0052	0.0025	0.0043	0.0044	0.0053	0.0108	0.0050	0.0069	0.0052
Mn	0.0063	0.0061	0.0070	0.0058	0.0052	0.0055	0.0054	0.0041	0.0051	0.0052	0.0034	0.0053
Fe	0.2424	0.2380	0.2393	0.2305	0.2411	0.2182	0.2080	0.1925	0.1980	0.2112	0.1980	0.1990
Ni	-	-	-	-	-	0.0064	0.0057	0.0079	0.0054	0.0060	0.0074	0.0063
Total	3.0123	2.9923	3.0146	3.0001	3.0037	2.9968	2.9754	3.0012	2.9933	2.9979	2.9942	2.9940

Table D2: Representative orthopyroxene compositions. Mg#=100*Mg/(Mg+ΣFe).

Composition	71001				70965				
Run No	T-3301	T-3197	T-3491	T-3188	T-3315	T-3586	T-3447	T-3327	T-3469
T (°C)	900	1050	1070	1100	900	1050	1000	1050	1070
$\%CO_2$	1	5	5	5	5	10	5	5	5
SiO_2	55.10	54.53	55.28	54.90	56.72	56.47	54.96	55.23	56.19
TiO_2	0.13	0.23	0.27	0.23	0.05	0.05	0.28	0.15	0.11
Al_2O_3	1.86	2.92	3.74	3.06	0.98	1.62	2.80	2.90	2.21
Cr_2O_3	1.25	0.75	1.20	0.98	0.68	0.68	0.92	0.97	0.89
MgO	30.83	31.92	31.48	30.97	33.49	33.83	32.10	32.38	33.09
CaO	1.05	2.14	1.71	1.89	0.72	1.11	1.38	1.49	1.34
MnO	0.28	0.28	0.24	0.25	0.20	0.18	0.15	0.31	0.20
FeO	9.57	7.59	7.46	7.31	6.86	5.98	6.46	6.86	6.24
NiO	-	-	-	-	0.18	0.11	0.08	0.12	0.13
Na_2O	0.28	0.32	0.31	0.31	0.11	0.10	0.42	0.31	0.17
K_2O	0.02	0.02	0.00	0.05	0.01	0.00	0.05	0.02	0.01
Total	100.38	100.71	101.70	99.95	100.06	100.14	99.60	101.06	100.62
Mg#	85.16	88.23	88.26	88.30	89.70	90.98	89.76	89.30	90.43
Si	1.9361	1.8998	1.9008	1.9202	1.9700	1.9526	1.9194	1.9142	1.9400
Ti	0.0035	0.0059	0.0070	0.0061	0.0014	0.0013	0.0075	0.0039	0.0027
Al	0.0770	0.1199	0.1517	0.1260	0.0403	0.0661	0.1162	0.1183	0.0898
Cr	0.0347	0.0206	0.0326	0.0270	0.0186	0.0185	0.0255	0.0267	0.0242
Fe	0.2811	0.2212	0.2145	0.2139	0.1991	0.1728	0.1906	0.1988	0.1801
Mn	0.0084	0.0084	0.0070	0.0075	0.0059	0.0053	0.0046	0.0091	0.0058
Mg	1.6139	1.6571	1.6129	1.6139	1.7332	1.7427	1.6707	1.6722	1.7025
Ca	0.0396	0.0801	0.0630	0.0710	0.0268	0.0413	0.0523	0.0554	0.0495
Na	0.0194	0.0217	0.0210	0.0209	0.0074	0.0067	0.0285	0.0210	0.0111
K	0.0009	0.0007	0.0002	0.0023	0.0002	0.0001	0.0022	0.0010	0.0005
Total	4.0147	4.0352	4.0107	4.0088	4.0029	4.0072	4.0175	4.0204	4.0061
En	83.42	84.62	85.32	85.00	88.47	88.47	89.06	87.31	86.81
Fs	14.53	11.30	11.35	11.26	10.17	10.16	8.83	9.96	10.32
Wo	2.05	4.09	3.33	3.74	1.37	1.37	2.11	2.73	2.87

Table D3: Representative clinopyroxene compositions. Mg# as in table D2. En=enstatite, Fs=ferrosilite, Wo=wollastonite.

Composition	70965						
Run No	T-3482	T-3315	T-3586	T-3447	T-3327	T-3469	T-3336
T (°C)	900	900	1050	1000	1050	1070	1150
$\%CO_2$	1	5	10	5	5	5	5
P_2O_5	0.17	0.19	0.16	0.11	0.14	0.14	0.15
SiO_2	54.17	53.76	53.68	52.46	53.14	53.78	53.49
TiO_2	0.15	0.19	0.15	0.21	0.25	0.26	0.27
Al_2O_3	1.79	1.28	1.62	1.74	2.28	2.33	3.63
Cr_2O_3	1.31	1.34	0.87	1.11	1.25	1.24	1.91
MgO	17.01	17.20	17.45	19.03	17.67	17.40	18.69
CaO	21.10	20.88	21.31	20.16	19.85	20.46	15.96
MnO	0.16	0.20	0.15	0.18	0.20	0.11	0.21
FeO	3.15	3.68	3.31	3.87	3.66	3.24	3.99
NiO	0.07	0.09	0.04	0.00	0.06	0.08	0.03
Na_2O	1.19	1.07	0.82	0.98	1.18	1.04	1.62
K_2O	0.00	0.00	0.01	0.04	0.03	0.01	0.03
Total	100.27	99.88	99.58	99.90	99.72	100.09	99.96
Mg#	90.59	89.29	90.37	89.75	89.59	90.53	89.31
Si	1.9680	1.9938	1.9638	1.9452	1.9421	1.9532	1.9321
Ti	0.0042	0.0052	0.0041	0.0060	0.0070	0.0071	0.0073
Al	0.0766	0.0558	0.0697	0.0762	0.0982	0.0997	0.1544
Cr	0.0377	0.0394	0.0253	0.0325	0.0361	0.0356	0.0545
Fe	0.0957	0.1140	0.1014	0.1201	0.1119	0.0984	0.1205
Mn	0.0050	0.0062	0.0046	0.0056	0.0062	0.0034	0.0064
Mg	0.9206	0.9503	0.9513	1.0512	0.9625	0.9417	1.0061
Ca	0.8211	0.7501	0.8351	0.7213	0.7773	0.7961	0.6176
Na	0.0835	0.0773	0.0585	0.0708	0.0837	0.0732	0.1132
K	0.0002	0.0000	0.0003	0.0020	0.0012	0.0005	0.0012
Total	4.0125	3.9921	4.0140	4.0309	4.0262	4.0089	4.0133
En	50.10	52.38	50.39	55.54	51.98	51.28	57.68
Fs	5.21	6.28	5.37	6.35	6.04	5.36	6.91
Wo	44.69	41.34	44.24	38.11	41.97	43.36	35.41

Table D4: Representative amphibole analyses. Mg# as in table D2. Cation calculations assume perfect stoichiometry.

Composition	71001		70965	
Run No	T-3301	T-3172	T-3482	T-3315
T (°C)	900	900	900	900
$\%CO_2$	1	5	1	5
P_2O_5	0.24	0.18	0.26	0.20
SiO_2	48.33	48.58	49.73	47.91
TiO_2	0.93	0.74	0.62	0.45
Al_2O_3	7.31	6.50	7.21	7.41
Cr_2O_3	1.39	1.35	1.70	1.29
MgO	21.86	22.72	20.16	21.89
CaO	7.91	9.25	11.80	8.35
MnO	0.11	0.12	0.14	0.12
FeO	5.70	5.38	4.05	4.75
NiO	-	-	0.06	0.12
Na_2O	4.00	3.49	3.11	3.42
K_2O	0.60	0.44	0.30	0.32
Total	98.38	98.76	99.14	96.22
Mg#	87.24	88.28	89.87	89.15
Si	6.758	6.773	6.908	6.811
Al	1.205	1.068	1.181	1.242
Fe^{2+}	0.200	0.188	0.186	0.169
Fe^{3+}	0.467	0.439	0.285	0.395
Mg	4.556	4.721	4.173	4.638
Mn	0.013	0.014	0.016	0.014
Ti	0.098	0.078	0.065	0.048
Cr	0.154	0.149	0.187	0.145
Na	1.085	0.943	0.838	0.943
Ca	1.185	1.382	1.756	1.272
K	0.107	0.078	0.053	0.058
Ni	-	-	0.000	0.014
Total	15.828	15.833	15.648	15.749

Table D5: Representative carbonate compositions. Mg# as in table D2. CM1 is primary carbonatite melt composition of Wallace and Green (1988), CM2 is estimate of carbonatite melt composition from this study, made on basis of normative calculation, and CM3 is carbonatite melt estimate based on cpx/melt partitioning and quench phase compositions. See Chapter 4 for explanation.

Composition	71001				70965					QUENCH PHASES		CBTE ESTIMATES		
Run No	T-3172	T-3301	T-3197	T-3491	T-3315	T-3447	T-3560	T-3586	T-3469	T-3690	T-3690	CM1	CM2	CM3
T (°C)	900	900	1050	1070	900	1000	1050	1050	1070	(Na,Mg)-	Dolomite			
%CO_2	5	1	5	5	5	5	5	10	5	carbonate				
P_2O_5	0.00	0.00	0.43	1.64	0.00	0.42	0.35	0.32	0.57	1.96	1.22	0.48	0.18	1.55
SiO_2	0.78	1.77	2.08	5.26	3.82	5.46	20.18	8.54	18.16	9.10	0.12	2.94	3.00	4.13
TiO_2	0.00	0.00	0.12	0.02	0.00	0.02	0.54	0.21	0.14	0.28	0.05	0.45	-	0.16
Al_2O_3	0.00	0.00	0.31	0.41	0.00	0.09	5.55	1.92	1.12	0.32	0.04	1.95	-	0.16
Cr_2O_3	0.00	0.00	0.75	0.09	0.00	0.02	0.08	0.22	0.27	0.09	0.03	0.22	-	0.05
MgO	41.29	41.48	22.04	11.35	23.47	17.29	6.94	14.38	18.73	17.60	11.49	14.19	13.94	14.22
CaO	2.92	2.68	29.11	34.33	28.01	29.80	16.87	28.11	21.04	9.53	33.03	21.29	24.02	22.53
MnO	0.29	0.49	0.34	0.18	0.25	0.26	0.28	0.31	0.26	0.60	0.74	-		0.68
FeO	6.65	6.27	4.48	2.92	4.13	4.50	5.17	4.46	4.67	9.41	5.51	4.61	3.16	7.26
NiO	-	-	-	-	0.00	0.09	0.02	0.04	0.12	-	0.00	-	-	0.04
Na2O	0.00	0.00	0.05	0.31	0.04	0.82	3.41	0.73	0.63	21.92	0.00	4.99	5.41	9.79
K2O	0.00	0.00	0.05	0.10		0.15	0.17	0.16	0.10	0.17	0.00	0.35	0.30	0.08
Total	51.93	52.69	59.76	56.61	59.72	58.92	59.56	59.40	65.80	70.98	52.43	51.49	50.00	60.64
Mg#	91.71	92.18	89.76	87.38	91.01	87.26	70.52	85.18	87.72	76.92	78.79	84.58	88.71	77.75

APPENDIX E

REPRESENTATIVE ELECTRON MICROPROBE ANALYSES OF MINERAL PHASES FROM GARNET AMPHIBOLITE + CARBONATE EXPERIMENTAL RUNS

Table E1: Representative clinopyroxene compositions. Mg#=100*Mg/(Mg+ΣFe).

Run No	T-3821	T-3812	T-3605	T-3230	T-3734	T-3736	T-3212	T-3221	T-3237	T-3210	T-3228	T-3551	T-3805	T-3811	T-3818	T-3782	T-3780	T-3794	T-3817	T-3819
P(kbar)	15	15	15	20	20	20	20	20	25	25	25	27	30	30	30	30	30	30	30	35
T(°C)	750	850	1000	700	850	850	850	950	750	850	950	1000	700	850	850	900	900	900	900	750
Carbonate	10% CC	10% CC	10% CC	10% CC	0% CC	3% CC	10% CC	10% CC	10% CC	10% CC	10% CC	10% CC	10% CC	10% CC	10% MAG	0% CC	10% CC	10% MAG	10% CC+ 10% MAG	10% CC
P2O5	0.12	0.14	0.12	0.17	0.10	0.17	0.19	0.14	0.14	0.15	0.19	0.15	0.15	0.13	0.13	0.06	0.10	0.18	0.10	0.09
SiO2	47.89	48.45	46.11	52.68	51.28	51.00	50.74	46.62	52.39	51.50	50.60	49.64	52.80	53.21	53.58	53.43	52.61	51.71	53.34	52.91
TiO2	2.11	1.08	1.36	0.40	0.64	0.85	0.72	1.28	0.43	0.65	0.91	0.87	0.53	0.50	0.61	0.47	0.50	0.33	0.50	0.38
Al2O3	8.11	11.32	11.96	12.09	10.72	9.94	11.51	12.77	12.39	12.39	11.67	12.69	7.98	11.34	12.14	9.93	10.42	13.31	10.55	10.48
Cr2O3	0.01	0.02	0.05	0.04	0.06	0.01	0.04	0.05	0.05	0.02	0.03	0.04	0.00	0.10	0.05	0.06	0.04	0.03	0.08	0.08
MgO	8.42	8.18	9.17	7.23	9.47	8.79	7.96	7.87	6.88	7.93	8.36	8.11	8.64	8.46	9.20	9.70	9.08	13.03	10.08	7.55
CaO	20.58	19.17	20.43	14.30	16.48	18.08	16.74	19.71	14.58	15.12	16.47	16.87	15.52	15.95	13.31	15.30	16.68	11.51	15.66	14.31
MnO	0.19	0.15	0.16	0.12	0.22	0.08	0.13	0.15	0.06	0.15	0.09	0.07	0.09	0.26	0.17	0.10	0.02	0.19	0.08	0.22
FeO	8.95	8.59	8.45	7.17	7.73	8.08	8.38	8.20	7.74	8.10	7.30	7.42	9.29	5.52	5.13	4.90	5.00	7.47	4.25	8.13
NiO	0.03	0.01	0.03	0.02	0.09	0.03	0.01	0.03	0.00	0.04	0.03	0.02	0.05	0.03	0.00	0.09	0.07	0.05	0.02	0.00
Na2O	1.80	2.34	1.44	4.93	2.88	2.90	3.60	2.33	5.00	4.22	3.50	3.49	4.37	4.51	4.86	4.70	4.33	3.05	4.40	5.26
K2O	0.06	0.04	0.02	0.03	0.02	0.04	0.04	0.05	0.01	0.03	0.10	0.05	0.00	0.02	0.07	0.04	0.02	0.03	0.06	0.00
Total	98.29	99.50	99.30	99.18	99.68	99.96	100.06	99.20	99.68	100.60	99.25	99.42	99.44	100.01	99.25	98.78	98.87	100.89	99.12	99.41
Mg#	62.64	62.92	69.49	64.25	68.59	65.96	62.86	67.27	61.31	63.56	67.11	66.08	65.66	73.21	76.17	77.90	76.39	75.66	80.87	64.43
Si	1.8282	1.8079	1.7284	1.9237	1.8806	1.8780	1.8643	1.7440	1.9094	1.8685	1.8639	1.8287	1.9487	1.9226	1.9295	1.9459	1.9216	1.8412	1.9297	1.9378
Ti	0.0604	0.0304	0.0383	0.0110	0.0177	0.0236	0.0199	0.0360	0.0119	0.0177	0.0252	0.0241	0.0146	0.0135	0.0166	0.0129	0.0137	0.0089	0.0136	0.0104
Al	0.3659	0.4989	0.5297	0.5217	0.4644	0.4325	0.4997	0.5645	0.5336	0.5440	0.5079	0.5524	0.3480	0.4841	0.5164	0.4275	0.4497	0.5602	0.4511	0.4534
Cr	0.0004	0.0006	0.0015	0.0012	0.0017	0.0004	0.0012	0.0015	0.0014	0.0006	0.0009	0.0012	0.0001	0.0028	0.0014	0.0018	0.0012	0.0008	0.0022	0.0024
Fe2+	0.2857	0.2682	0.2248	0.2189	0.2370	0.2488	0.2575	0.2134	0.2358	0.2457	0.2248	0.2286	0.2485	0.1667	0.1544	0.1493	0.1527	0.2225	0.1286	0.2274
Mg	0.4791	0.4550	0.5122	0.3934	0.5175	0.4821	0.4358	0.4387	0.3737	0.4287	0.4589	0.4452	0.4753	0.4555	0.4935	0.5263	0.4942	0.6915	0.5436	0.4119
Ca	0.8418	0.7663	0.8204	0.5594	0.6475	0.7132	0.6589	0.7899	0.5691	0.5877	0.6499	0.6658	0.6137	0.6174	0.5135	0.5968	0.6527	0.4389	0.6069	0.5613
Na	0.1334	0.1691	0.1046	0.3490	0.2046	0.2068	0.2564	0.1690	0.3531	0.2968	0.2499	0.2492	0.3129	0.3156	0.3391	0.3320	0.3066	0.2107	0.3086	0.3738
Total	3.9949	3.9964	4.0000	3.9784	3.9710	3.9854	3.9936	4.0000	3.9878	3.9899	3.9815	3.9951	4.0000	3.9783	3.9645	3.9925	3.9925	3.9747	3.9843	4.0000

Table E2: Representative garnet compositions. Cations calculated assuming perfect stoichiometry. Mg# as in table E1. Mg*=100*Mg/(Mg+Fe^{2+}). Almandine does not include any ferric iron component.

Run No	T-3230	T-3734	T-3736	T-3212	T-3221	T-3237	T-3210	T-3228	T-3551	T-3805	T-3811	T-3818	T-3782	T-3780	T-3794	T-3817	T-3819
P(kbar)	20	20	20	20	20	25	25	25	27	30	30	30	30	30	30	30	35
T(°C)	700	850	850	850	950	750	850	950	1000	700	850	850	900	900	900	900	750
Carbonate	10% CC	0% CC	3% CC	10% CC	10% CC	10% CC	10% CC	10% CC	10% CC	10% CC	10% CC	10% MAG	0% CC	10% CC	10% MAG	10%CC+ 10% MAG	10%CC
P2O5	0.40	0.33	0.21	0.26	0.12	0.21	0.33	0.24	0.19	0.22	0.34	0.56	0.31	0.20	0.11	0.29	0.21
SiO2	39.62	38.17	37.80	38.51	38.24	37.35	38.28	38.16	38.69	37.75	37.95	38.33	38.43	38.08	40.14	37.82	37.83
TiO2	1.11	1.06	1.35	1.27	1.16	0.76	1.41	2.24	1.77	0.64	1.36	0.99	1.31	1.31	0.47	1.80	0.64
Al2O3	21.28	20.59	20.30	21.12	20.28	21.12	21.11	20.31	20.88	20.58	20.73	21.30	21.15	20.86	22.42	20.57	21.11
Cr2O3	0.04	0.00	0.05	0.04	0.04	0.02	0.08	0.08	0.03	0.02	0.03	0.01	0.05	0.03	0.06	0.05	0.07
MgO	12.56	6.45	5.82	4.96	5.44	4.78	6.73	7.85	9.53	4.52	6.78	10.80	9.47	7.36	14.50	8.09	5.58
CaO	7.75	8.88	12.11	12.90	15.38	10.21	11.79	11.54	11.29	12.03	10.58	7.62	9.39	11.82	5.74	10.71	11.68
MnO	0.35	0.80	0.68	0.66	0.75	0.65	0.33	0.40	0.26	0.54	0.43	0.36	0.32	0.35	0.31	0.41	0.52
FeO	15.90	21.70	19.86	20.52	17.38	24.07	19.98	18.18	17.00	22.56	21.24	18.72	18.45	18.45	15.51	19.19	21.49
NiO	0.02	0.01	0.00	0.00	0.01	0.00	0.04	0.00	0.02	0.02	0.01	0.02	0.03	0.03	0.03	0.04	0.02
Na2O	0.60	0.17	0.18	0.12	0.26	0.11	0.16	0.19	0.19	0.14	0.19	0.21	0.19	0.22	0.13	0.13	0.11
K2O	0.02	0.02	0.02	0.01	0.01	0.01	0.02	0.03	0.01	0.00	0.01	0.01	0.01	0.01	0.00	0.00	0.01
Total	99.65	98.18	98.38	100.37	99.07	99.30	100.26	99.22	99.86	99.01	99.67	98.93	99.11	98.72	99.42	99.09	99.26
Mg#	58.47	34.62	34.31	30.12	35.80	26.14	37.49	43.48	49.98	26.32	36.28	50.68	46.51	41.55	62.48	49.87	31.66
Mg*	63.54	34.62	35.38	30.12	38.69	27.42	38.98	44.43	52.75	27.71	38.67	54.10	47.40	43.49	64.40	59.53	33.44
Si	2.951	3.004	2.965	2.974	2.960	2.935	2.936	2.939	2.926	2.968	2.919	2.925	2.957	2.944	2.967	2.812	2.946
Al	1.869	1.910	1.877	1.923	1.851	1.957	1.909	1.844	1.861	1.908	1.898	1.916	1.919	1.901	1.954	1.803	1.938
Fe2+	0.800	1.428	1.242	1.325	0.995	1.482	1.204	1.127	0.962	1.383	1.245	1.042	1.145	1.102	0.883	0.807	1.290
Fe3+	0.190	0.000	0.060	0.000	0.131	0.100	0.078	0.044	0.113	0.101	0.134	0.153	0.042	0.091	0.076	0.386	0.109
Mg	1.394	0.756	0.680	0.571	0.628	0.560	0.769	0.901	1.074	0.530	0.785	1.228	1.032	0.848	1.597	1.187	0.648
Mn	0.022	0.053	0.045	0.043	0.049	0.043	0.021	0.026	0.017	0.036	0.028	0.023	0.021	0.023	0.019	0.026	0.034
Ti	0.062	0.063	0.080	0.074	0.068	0.045	0.081	0.130	0.101	0.038	0.079	0.057	0.076	0.076	0.026	0.101	0.037
Cr	0.002	0.000	0.003	0.002	0.002	0.001	0.005	0.005	0.002	0.001	0.001	0.001	0.003	0.002	0.004	0.003	0.004
Na	0.087	0.026	0.027	0.018	0.039	0.017	0.024	0.028	0.028	0.021	0.029	0.031	0.028	0.033	0.019	0.019	0.017
Ca	0.619	0.749	1.018	1.067	1.276	0.860	0.969	0.952	0.915	1.013	0.880	0.623	0.774	0.979	0.455	0.853	0.975
K	0.002	0.002	0.002	0.001	0.001	0.001	0.002	0.003	0.001	0.000	0.001	0.001	0.001	0.001	0.000	0.000	0.001
Ni	0.001	0.001	0.000	0.000	0.001	0.000	0.002	0.000	0.001	0.001	0.001	0.001	0.002	0.000	0.002	0.002	0.001
Total	7.999	7.992	7.999	7.998	8.001	8.001	8.000	7.999	8.001	8.000	8.000	8.000	8.000	8.000	8.002	8.000	8.000
Gr	22.00	25.54	34.63	36.01	44.02	29.63	32.94	31.95	31.01	34.62	30.24	21.53	26.23	33.42	15.50	29.96	33.47
Py	49.56	25.78	23.13	19.27	21.66	19.30	26.14	30.23	36.39	18.11	26.98	42.45	34.97	28.95	54.41	41.69	22.25
Alm	28.44	48.69	42.24	44.72	34.32	51.07	40.92	37.82	32.60	47.27	42.78	36.02	38.80	37.62	30.09	28.35	44.28

Table E3: Representative amphibole compositions. Cations calculated assuming perfect stoichiometry. Mg# and Mg* as in table E2.

Run No	T-3821	T-3812	T-3605	T-3230	T-3734	T-3736	T-3212
P(kbar)	15	15	15	20	20	20	20
T(°C)	750	850	1000	700	850	850	850
Carbonate	10% CC	10% CC	10% CC	10% CC	0% CC	3% CC	10% CC
P2O5	0.08	0.08	0.09	0.11	0.10	0.15	0.11
SiO2	44.54	42.92	41.77	47.14	46.43	48.14	47.14
TiO2	0.82	1.37	2.01	0.77	0.93	0.95	1.20
Al2O3	13.91	15.63	15.63	13.64	14.58	15.00	14.21
Cr2O3	0.03	0.01	0.05	0.01	0.02	0.03	0.03
MgO	10.96	9.83	10.92	10.08	10.51	9.33	9.66
CaO	8.66	9.91	10.98	9.60	8.49	9.15	11.10
MnO	0.20	0.20	0.13	0.16	0.15	0.09	0.11
FeO	13.19	13.62	12.03	11.39	11.87	9.53	10.41
NiO	0.02	0.02	0.05	0.02	0.04	0.07	0.07
Na2O	3.41	3.33	2.92	3.75	2.86	3.39	3.28
K2O	0.35	0.51	0.42	0.23	0.28	0.41	0.35
Total	96.16	97.42	97.01	96.92	96.25	96.24	97.67
Mg#	59.68	56.26	61.80	61.19	61.21	63.57	62.32
Mg*	72.29	60.04	64.20	61.19	69.43	63.57	62.32
Si	6.496	6.297	6.154	6.847	6.700	6.936	6.785
Al	2.392	2.703	2.715	2.336	2.481	2.548	2.411
Fe2+	0.913	1.430	1.337	1.384	0.995	1.148	1.253
Fe3+	0.696	0.241	0.145	0.000	0.437	0.000	0.000
Mg	2.382	2.149	2.398	2.182	2.260	2.003	2.072
Mn	0.025	0.025	0.016	0.020	0.018	0.011	0.013
Ti	0.090	0.151	0.223	0.084	0.101	0.103	0.130
Cr	0.003	0.001	0.006	0.001	0.002	0.003	0.003
Na	0.964	0.947	0.834	1.056	0.800	0.947	0.915
Ca	1.353	1.558	1.733	1.494	1.313	1.413	1.712
K	0.065	0.095	0.079	0.043	0.052	0.075	0.064
Ni	0.002	0.002	0.006	0.002	0.005	0.008	0.008
Total	15.381	15.599	15.646	15.449	15.164	15.195	15.366

Table E4: Representative carbonate compositions. Mg# as in table E1.

Run No	T-3821	T-3230	T-3212	T-3237	T-3210	T-3228	T-3551	T-3805	T-3811	T-3818	T-3780	T-3794	T-3819
P(kbar)	15	20	20	25	25	25	27	30	30	30	30	30	35
T(°C)	750	700	850	750	850	950	1000	700	850	850	900	900	750
Carbonate	10% CC	10% CC	10% CC	10% CC	10% CC	10% CC	10% CC	10% CC	10% CC	10% MAG	10% CC	10% MAG	10% CC
MgO	0.39	10.9	1.92	14.06	10.99	3.11	4.78	13.03	7.49	40.82	3.33	40.15	15.22
CaO	60.05	39.68	59.08	31.86	44.42	56.37	58.4	39.03	48.67	1.99	56.56	2.49	29.72
MnO	0.15	0.38	0.17	0.18	0.12	0.12	0.07	0.28	0.14	0.00	0.12	0.13	0.17
FeO	0.98	10.07	3.32	11.19	6.04	2.64	3.15	11.78	5.30	2.80	2.79	9.01	8.27
Total	61.57	61.03	64.49	57.29	61.57	62.24	66.40	64.11	61.60	45.61	62.80	51.78	53.38
Mg#	41.49	65.86	50.75	69.13	76.43	67.73	73.00	66.35	71.59	96.29	68.02	88.82	76.63
Calcite	97.87	63.29	91.82	52.97	68.95	89.82	86.51	58.83	76.98	3.26	89.25	3.81	51.83
Magnesite	0.88	24.18	4.15	32.51	23.73	6.89	9.85	27.32	16.48	93.15	7.31	85.43	36.92
Siderite	1.25	12.54	4.03	14.52	7.32	3.28	3.64	13.86	6.54	3.59	3.44	10.76	11.26

Table E5: Glass analyses from some of the runs. These represent averages of several broad-beam analyses of glass+quench pools, and should be considered estimates only, because of quench modification of the melt. Mg# as in table E1.

Run No	T-3605	T-3237	T-3210	T-3228	T-3551	T-3794	T-3780
P(kbar)	15	25	25	25	27	30	30
T(°C)	1000	750	850	950	1000	900	900
Carbonate	10% CC	10% CC	10% CC	10% CC	10% CC	10% MAG	10% CC
P2O5	0.58	0.24	0.14	0.23	0.32	0.14	0.24
SiO2	51.89	57.11	55.06	44.39	52.38	53.35	43.40
TiO2	0.58	0.60	0.33	1.13	0.94	0.47	0.65
Al2O3	19.22	14.88	14.70	12.55	14.14	9.95	10.81
Cr2O3	0.05	0.06	0.07	0.03	0.02	0.06	0.00
MgO	0.67	2.28	5.68	6.57	4.71	8.27	4.70
CaO	6.01	5.52	12.90	12.87	11.64	11.18	10.44
MnO	0.12	0.00	0.02	0.11	0.09	0.03	0.06
FeO	3.75	1.53	5.60	6.73	4.69	3.47	4.97
NiO	0.00	0.00	0.00	0.03	0.00	0.06	0.04
Na2O	1.36	0.86	3.51	2.60	2.29	4.11	2.72
K2O	0.77	0.29	0.13	0.59	0.52	0.32	0.75
Total	85.01	83.38	98.12	87.84	91.75	91.40	78.79
Mg#	24.27	72.69	64.39	63.50	64.15	80.94	62.72
Normalized							
P2O5	0.68	0.29	0.14	0.26	0.35	0.15	0.30
SiO2	61.04	68.50	56.11	50.53	57.09	58.36	55.08
TiO2	0.68	0.72	0.34	1.29	1.02	0.51	0.83
Al2O3	22.61	17.85	14.98	14.29	15.41	10.88	13.72
Cr2O3	0.06	0.08	0.07	0.03	0.03	0.06	0.00
MgO	0.79	2.73	5.79	7.47	5.13	9.04	5.97
CaO	7.07	6.63	13.15	14.66	12.69	12.24	13.25
MnO	0.14	0.00	0.02	0.13	0.10	0.03	0.08
FeO	4.41	1.83	5.70	7.66	5.11	3.80	6.31
NiO	0.00	0.00	0.00	0.04	0.00	0.06	0.05
Na2O	1.60	1.03	3.57	2.96	2.50	4.50	3.46
K2O	0.91	0.35	0.14	0.67	0.56	0.35	0.95
Total	100.00	100.00	100.00	100.00	100.00	100.00	100.00

APPENDIX F

REPRESENTATIVE ELECTRON MICROPROBE ANALYSES OF CARBONATE PHASES AND GARNET IN CZECH ECLOGITES

Table F1; Carbonate phases
Table F2; Garnet

Table F1: Representative carbonate analyses from Czech eclogites. Mg# = 100*Mg/(Mg+ΣFe). Abbreviations; CC=calcite, DOL=dolomite, MAG=magnesite, GA=garnet, QZ=quartz. R/DOL etc means, for example, the analysed point was close to the rim of the phase in contact with dolomite. Also, "incGA" refers to a carbonate inclusion in garnet etc.

Sample	H323	H323	H323	H323	H323	H323	H323	H323	H323
Patch	C3	C3	C3	C4	C4	C1	C1	C1	C5
Phase	Mag	Mag	Dol	CC	Dol	CC	CC	Mag	Mag
Number	16	18	MEAN	MEAN	29	13	14	1	MEAN
MgO	39.00	39.42	20.71	1.02	18.07	0.39	2.60	39.91	37.25
CaO	0.37	0.29	32.42	62.31	29.45	56 02	56.17	0.27	0.45
MnO	0.03	0.12	0.09	0.47	0.06	1.32	0.88	0.12	0 13
FeO	13.12	12.38	7.14	1.35	4.99	1.91	1.26	12.40	15.07
Total	52.52	52.21	60.36	65.15	52.56	59.64	60.91	52.70	52.90
Mg#	84.12	85 02	83.80	57.48	86.59	26.60	78.65	85.16	81.50
Location	R/DOL	CORE				CORE	R/MAG	CORE	
Ca	0.57	0.45	48.53	96.19	50.37	96.51	92.43	0.42	0.71
Mg	83 64	84.63	43.13	2.19	42.98	0.93	5.95	84.80	80.92
Fe	15.79	14.92	8.34	1.62	6.66	2.57	1.62	14.78	18.37

Sample	K670	K670	K670	K670	K670	K670	C960	C960	C960	C960	C960
Patch	C1	C1	C2	C2	C3	C3	C2	C4	C4	C5	C6
Phase	Mag	Dol	Mag	Dol	Mag	Dol	CC	Mg-CC	Mg-CC	CC	CC
Number	3	2	7	6	9	8	MEAN	6	7	13	14
MgO	39.00	18.12	36.95	18.35	38.45	18.37	0.81	2.49	9.62	0.31	0.20
CaO	0 41	28 87	0.51	29.00	0.48	28.74	53.96	51.15	36.40	57.41	55.08
MnO	0 18	0 13	0.18	0.20	0.18	0.06	0.59	0.09	0.09	0.31	0.08
FeO	13.91	5.82	15.96	5.12	14.34	5.07	1.67	1.13	3.51	0.95	0.40
Total	53.49	52.94	53.60	52.67	53.45	52.24	57.04	54.86	49.61	58.99	55.77
Mg#	83.32	84.73	80.49	86.46	82.69	86.59	46.34	79.73	83.00	36.39	47.13
Location	CORE		CORE		CORE		incGA	incGA	incR/GA	PATCH	VEIN
Ca	0.62	49.25	0.79	49.56	0 74	49.34	95.68	92.16	69.32	98.00	98.93
Mg	82.80	43.00	79.85	43.61	82.08	43.87	2.00	6 25	25 47	0.73	0.51
Fe	16.57	7.75	19.36	6.83	17.18	6.79	2.32	1.59	5.22	1.27	0.57

Sample	H321	H321	H321	H321	H321	H321	H321	H321	H321	H321	H321	H321
Patch	C2a	C2a	C2a	C2a	C2a	C2a	C2a	C2a	C2a	C3	C2	C2
Phase	Mag	Dol	CC	CC	CC	Mag	Mag	Mag	Dol	Mag	Mag	Dol
Number	38	39	40	41	44	35	30	27	MEAN	80	2	1
MgO	35.68	18.49	6.49	1.66	1.70	38.54	38.19	37.88	20.42	37.85	37.11	20.42
CaO	3.28	34.42	52.73	62.40	63.49	0.39	0.56	0.47	30.64	0.46	0.39	32 84
MnO	0.09	0.24	0.37	0.37	0.41	0.07	0.17	0.09	0.25	0.15	0.17	0.16
FeO	12.69	7.39	3.59	1.43	1.45	13.49	13.79	13.98	7.87	14.12	14.88	6.45
Total	51.73	60.54	63.18	65.86	67.04	52.50	52.71	52.42	59.18	52.57	52.54	59.87
Mg#	83.36	81.69	76.30	67.48	67.69	83.58	83.15	82.84	82.21	82.69	81.64	84.94
Location	CORE	R/MAG	R/DOL	CORE	R/DOL	R/CC	CORE	R/DOL		CORE	CORE	RIM
Ca	5.21	52 22	81.68	94.79	94.79	0.60	0.86	0.74	47.00	0.72	0.61	49.54
Mg	79 02	39.03	13 98	3 51	3.53	83.07	82.43	82.23	43.57	82.09	81.14	42.86
Fe	15.77	8.75	4.34	1.69	1.68	16.32	16.71	17.03	9.43	17.18	18.25	7.60

Sample	H324	H324	H324	H324	H324	H324	H324	H324	H324	H324	D521	D521	D521
Patch	C3	C4	C4	C5.1	C5.1	C5.1	C5.2	C5.2	C5.2	C5.3	C6	C6	C6
Phase	CC	Dol	CC	CC	Dol	Dol	CC	Dol	Dol	CC	Dol	Dol	CC
Number	Mean	7	8	14	15	29	30	34	43	50	20	22	18
MgO	0.00	18.43	0.51	0.29	18.52	18.72	1.30	18.22	18.09	0.85	16.81	17.70	1.99
CaO	56.50	29.17	56.00	55.06	29.17	29.88	53.94	29.39	28.59	54.46	31.64	29.90	51.99
MnO	0.00	0.00	0.07	0.15	0.04	0.08	0.15	0.10	0.00	0.16	0.06	0.02	0.08
FeO	0.03	4.71	0.33	0.16	4.24	4.65	1.02	4.52	5.03	0.54	5.42	5.93	0.76
Total	56.53	52.30	56.92	55.65	51.97	53.32	56.41	52.22	51.71	56.00	53.93	53.55	54.82
Mg#	0.00	87.46	73.32	76.61	88.62	87.76	69.45	87.78	86.50	73.83	84.68	84.18	82.45
Location	inc QZ	inc QZ	inc QZ	R/DOL	R/CC	CORE	R/DOL	R/CC	CORE	CORE	R/CC	CORE	
Ca	99.95	49.88	98.30	99.06	50.09	50.18	95.38	50.45	49.57	97.15	53.40	50.55	93.93
Mg	0.00	43.83	1.25	0.72	44.23	43.72	3.21	43.50	43.62	2.10	39.46	41.62	5.01
Fe	0.05	6.28	0.45	0.22	5.68	6.10	1.41	6.05	6.81	0.75	7.14	7.82	1.07

Table F2: Representative garnet analyses from Czech eclogites. Symbols as in table F1, with the addition of CPX (clinopyroxene), AM (amphibole), BD (kelyphite on garnet). Table is arranged as a series of traverse across garnet grains. Analyses from, and including the first analysis denoted by a rim symbol (eg; R/CC) to the next (eg; R/QZ) represents a sequence of evenly space analyses across an individual garnet grain from a rim in contact with calcite, to the opposite rim in contact with quartz, and so on.

Sample	C960	C960	C960	C960	C960	C960	C960	C960	C960	C960	C960	C960	C960	C960	C960	C960	C960	C960	C960	C960	C960
Patch	C4	C4	C4	C4	C4	C4	C4	C4	C4	C4	C4	C4	C4	C4	C4	C5	C5	C5	C5	C5	C5
Number	17	18	19	20	21	22	23	24	25	26	27	28	29	30	31	47	48	49	50	51	52
P2O5	0.02	0.05	0.02	0.00	0.02	0.04	0.04	0.03	0.01	0.00	0.03	0.07	0.05	0.05	0.02	0.03	0.05	0.04	0.03	0.04	0.05
SiO2	35.57	39.11	37.69	37.72	38.15	37.70	36.61	33.85	38.05	38.10	38.53	38.44	38.41	38.30	38.68	39.51	39.49	39.87	39.47	39.76	39.60
TiO2	0.04	0.05	0.03	0.16	0.02	0.01	0.00	0.11	0.14	0.14	0.05	0.07	0.06	0.14	0.08	0.02	0.01	0.03	0.01	0.07	0.01
Al2O3	26.99	22.04	23.76	21.64	21.77	23.76	26.59	31.33	21.35	21.32	21.60	21.50	21.55	21.56	21.63	22.16	22.36	21.77	22.34	22.31	22.17
Cr2O3	0.03	0.01	0.01	0.01	0.01	0.07	0.05	0.00	0.07	0.02	0.07	0.04	0.07	0.08	0.09	0.01	0.05	0.00	0.00	0.01	0.01
MgO	4.46	6.95	6.18	4.71	5.21	4.73	4.99	4.62	4.36	4.54	5.04	5.29	5.49	5.83	5.86	8.51	9.07	9.79	9.63	9.54	9.56
CaO	9.83	10.60	10.28	11.54	10.19	10.34	9.31	9.73	11.11	10.77	10.06	9.46	9.64	9.59	10.05	9.14	9.27	8.82	8.90	8.96	9.10
MnO	0.99	0.48	0.58	0.86	1.11	0.89	0.79	0.69	0.81	0.79	0.66	0.64	0.68	0.52	0.34	0.51	0.41	0.36	0.35	0.38	0.21
FeO	22.51	21.25	21.75	22.83	24.18	22.70	22.47	19.10	24.19	24.04	24.43	24.90	24.39	23.83	23.31	20.37	19.70	19.27	19.75	19.84	19.64
NiO	0.00	0.00	0.00	0.00	0.00	0.00	0.07	0.01	0.02	0.00	0.00	0.00	0.06	0.00	0.00	0.01	0.02	0.00	0.00	0.00	0.04
Na2O	0.06	0.02	0.03	0.02	0.01	0.02	0.11	0.09	0.02	0.02	0.02	0.02	0.04	0.03	0.02	0.01	0.01	0.01	0.00	0.02	0.04
K2O	0.00	0.00	0.02	0.01	0.00	0.00	0.04	0.02	0.01	0.00	0.01	0.00	0.00	0.00	0.00	0.01	0.02	0.01	0.00	0.00	0.00
Total	100.49	100.55	100.35	99.49	100.66	100.25	101.08	99.57	100.13	99.72	100.49	100.44	100.43	99.92	100.06	100.29	100.47	99.99	100.50	100.92	100.42
	R/CCinc														R/QZ	R/CC					
Mg#	26.08	36.83	33.63	26.87	27.74	27.07	28.35	30.14	24.32	25.18	26.88	27.46	28.61	30.38	30.94	42.68	45.07	47.53	46.49	46.15	46.45
Si	2.7402	2.9864	2.8931	2.9555	2.9599	2.9118	2.7952	2.5854	2.9755	2.9843	2.9888	2.9869	2.9822	2.9774	2.9929	2.9974	2.9830	3.0138	2.9757	2.9856	2.9883
Ti	0.0022	0.0028	0.0016	0.0094	0.0012	0.0006	0.0000	0.0060	0.0082	0.0081	0.0030	0.0041	0.0037	0.0080	0.0046	0.0011	0.0008	0.0018	0.0007	0.0037	0.0004
Al	2.4499	1.9831	2.1490	1.9980	1.9905	2.1630	2.3931	2.8199	1.9681	1.9681	1.9753	1.9691	1.9714	1.9755	1.9720	1.9813	1.9907	1.9397	1.9853	1.9747	1.9716
Cr	0.0016	0.0007	0.0007	0.0006	0.0007	0.0043	0.0030	0.0000	0.0041	0.0014	0.0045	0.0025	0.0044	0.0049	0.0054	0.0006	0.0027	0.0000	0.0000	0.0005	0.0004
Fe2+	1.4503	1.3568	1.3958	1.4962	1.5688	1.4661	1.4346	1.2200	1.5817	1.5747	1.5850	1.6182	1.5837	1.5495	1.5081	1.2922	1.2445	1.2184	1.2455	1.2458	1.2398
Mn	0.0645	0.0313	0.0374	0.0572	0.0730	0.0580	0.0513	0.0444	0.0537	0.0526	0.0432	0.0418	0.0444	0.0345	0.0222	0.0326	0.0260	0.0229	0.0225	0.0244	0.0134
Mg	0.5117	0.7910	0.7074	0.5498	0.6022	0.5443	0.5676	0.5263	0.5084	0.5301	0.5825	0.6126	0.6348	0.6761	0.6756	0.9621	1.0212	1.1035	1.0820	1.0678	1.0754
Ca	0.8114	0.8669	0.8454	0.9690	0.8469	0.8558	0.7619	0.7966	0.9306	0.9036	0.8358	0.7879	0.8017	0.7985	0.8330	0.7432	0.7504	0.7146	0.7192	0.7206	0.7360
Total	8.0319	8.0189	8.0304	8.0358	8.0433	8.0039	8.0068	7.9986	8.0302	8.0229	8.0183	8.0232	8.0262	8.0244	8.0138	8.0105	8.0194	8.0146	8.0309	8.0231	8.0253
Gr	29.26	28.76	28.67	32.14	28.06	29.86	27.56	31.33	30.81	30.04	27.83	26.10	26.54	26.40	27.61	24.80	24.88	23.53	23.61	23.75	24.12
Py	18.45	26.24	23.99	18.24	19.95	18.99	20.54	20.70	16.83	17.62	19.40	20.29	21.02	22.36	22.39	32.10	33.86	36.34	35.51	35.19	35.24
Alm	52.29	45.01	47.34	49.63	51.98	51.15	51.90	47.98	52.36	52.34	52.77	53.61	52.44	51.24	49.99	43.11	41.26	40.13	40.88	41.06	40.63

Table F2: continued

Sample	C960	C960	C960	C960	H321	H321	H321	H321	H321	H321	H321	H321	H321	H321	H321	H321	H321	H321	H321	H321	H321
Patch	C5	C5	C5	C5	4	5	6	9	10	14	16	17	18	19	20	21	22	23	24	1	2
Number	53	54	55	56	C2	C2	C2	C2	C2	C2	C2	C2	C2	C2	C2	C2	C2	C2	C2	C2a	C2a
P2O5	0.04	0.03	0.06	0.02	0.10	0.07	0.09	0.11	0.09	0.09	0.12	0.07	0.13	0.13	0.10	0.18	0.13	0.11	0.13	0.16	0.14
SiO2	39.29	39.70	39.68	39.48	37.84	37.80	37.60	37.50	37.03	37.17	37.21	36.86	37.29	36.93	36.89	37.06	37.19	37.24	37.32	38.45	38.87
TiO2	0.02	0.00	0.01	0.00	0.07	0.28	0.21	0.57	0.98	0.73	0.36	0.33	0.24	0.25	0.17	0.18	0.19	0.17	0.15	0.06	0.09
Al2O3	21.95	22.35	22.18	22.40	21.48	21.47	21.35	21.14	20.63	20.82	20.84	20.64	20.50	20.42	20.62	20.46	20.66	20.33	21.16	21.85	21.82
Cr2O3	0.03	0.00	0.01	0.02	0.00	0.03	0.03	0.09	0.13	0.06	0.06	0.04	0.07	0.01	0.00	0.04	0.00	0.00	0.05	0.02	0.02
MgO	8.99	9.49	9.79	9.61	7.03	6.86	6.95	5.81	6.31	6.56	6.86	6.76	6.12	5.70	5.84	5.40	5.45	5.56	6.37	5.94	6.46
CaO	8.91	8.97	8.57	8.47	7.38	7.53	7.77	10.70	8.98	8.15	7.07	7.61	8.80	9.44	8.67	9.79	9.58	10.98	8.40	10.01	8.64
MnO	0.48	0.24	0.30	0.31	0.48	0.55	0.67	0.59	0.54	0.71	0.70	0.68	0.70	0.83	0.71	0.75	0.85	0.78	0.60	0.54	0.51
FeO	20.32	19.77	19.93	19.97	24.68	24.54	24.39	22.95	23.96	24.28	25.05	24.71	24.80	24.21	25.24	25.06	24.92	23.90	24.50	22.88	23.77
NiO	0.00	0.01	0.00	0.04	0.00	0.00	0.09	0.01	0.04	0.00	0.00	0.00	0.00	0.02	0.03	0.01	0.00	0.00	0.00	0.04	0.00
Na2O	0.03	0.03	0.03	0.01	0.02	0.00	0.04	0.03	0.03	0.05	0.04	0.05	0.02	0.04	0.02	0.03	0.04	0.05	0.04	0.01	0.03
K2O	0.00	0.00	0.00	0.00	0.00	0.01	0.00	0.00	0.00	0.00	0.00	0.02	0.00	0.02	0.00	0.00	0.01	0.00	0.00	0.00	0.01
Total	100.05	100.58	100.56	100.34	99.08	99.14	99.18	99.49	98.72	98.62	98.30	97.77	98.66	98.00	98.29	98.96	99.01	99.13	98.69	99.94	100.36
				R/QZ	R/DOL														R/CPX	R/DOL	
Mg#	44.11	46.12	46.69	46.19	33.68	33.26	33.67	31.11	31.94	32.51	32.79	32.79	30.54	29.57	29.21	27.75	28.05	29.32	31.66	31.63	32.65
Si	2.9881	2.9885	2.9890	2.9803	2.9644	2.9592	2.9502	2.9382	2.9295	2.9395	2.9531	2.9442	2.9605	2.9557	2.9476	2.9503	2.9529	2.9520	2.9499	2.9808	2.9963
Ti	0.0012	0.0000	0.0007	0.0002	0.0041	0.0165	0.0126	0.0333	0.0585	0.0434	0.0215	0.0196	0.0141	0.0153	0.0101	0.0108	0.0110	0.0103	0.0086	0.0032	0.0050
Al	1.9669	1.9827	1.9689	1.9927	1.9828	1.9808	1.9743	1.9525	1.9239	1.9405	1.9492	1.9435	1.9186	1.9263	1.9412	1.9196	1.9338	1.8993	1.9718	1.9962	1.9821
Cr	0.0019	0.0000	0.0005	0.0014	0.0000	0.0017	0.0020	0.0054	0.0080	0.0039	0.0038	0.0024	0.0041	0.0007	0.0000	0.0023	0.0000	0.0000	0.0034	0.0012	0.0013
Fe2+	1.2920	1.2446	1.2559	1.2606	1.6166	1.6063	1.6004	1.5036	1.5852	1.6060	1.6626	1.6510	1.6468	1.6209	1.6865	1.6685	1.6545	1.5846	1.6193	1.4833	1.5325
Mn	0.0308	0.0153	0.0193	0.0201	0.0315	0.0363	0.0442	0.0391	0.0363	0.0474	0.0471	0.0457	0.0471	0.0563	0.0480	0.0508	0.0571	0.0520	0.0398	0.0352	0.0336
Mg	1.0196	1.0652	1.0999	1.0819	0.8211	0.8004	0.8125	0.6790	0.7438	0.7737	0.8110	0.8054	0.7240	0.6806	0.6959	0.6408	0.6450	0.6572	0.7501	0.6863	0.7428
Ca	0.7259	0.7238	0.6913	0.6854	0.6197	0.6316	0.6527	0.8984	0.7608	0.6906	0.6007	0.6516	0.7488	0.8097	0.7424	0.8348	0.8149	0.9325	0.7110	0.8311	0.7135
Total	8.0263	8.0202	8.0255	8.0225	8.0401	8.0330	8.0490	8.0495	8.0460	8.0449	8.0489	8.0633	8.0640	8.0655	8.0717	8.0779	8.0692	8.0880	8.0539	8.0173	8.0071
Gr	23.90	23.86	22.69	22.64	20.27	20.79	21.29	29.16	24.62	22.49	19.54	20.96	24.00	26.03	23.76	26.55	26.16	29.38	23.08	27.70	23.87
Py	33.57	35.11	36.10	35.73	26.86	26.34	26.50	22.04	24.07	25.20	26.38	25.91	23.21	21.88	22.27	20.38	20.71	20.71	24.35	22.87	24.85
Alm	42.54	41.03	41.22	41.63	52.87	52.87	52.20	48.80	51.30	52.31	54.08	53.12	52.79	52.10	53.97	53.07	53.12	49.92	52.57	49.43	51.27

Table F2: continued

Sample	H321	H321	H321	H321	H321	H321	H321	H321	H321	H321	H321	H321	H321	H321	H321	H321	H321	H321	H321	H321	H321
Patch	3	4	5	6	7	8	9	10	11	12	13	14	15	16	17	19	20	54	55	56	57
Number	C2a	C2a	C2a	C2a	C2a	C2a	C2a	C2a	C2a	C2a	C2a	C2a	C2a	C2a	C2a	C2a	C2a	C2a	C2a	C2a	C2a
P2O5	0.15	0.11	0.13	0.11	0.14	0.09	0.10	0.13	0.12	0.10	0.11	0.05	0.10	0.09	0.08	0.16	0.12	0.09	0.15	0.15	0.16
SiO2	38.35	38.31	38.31	38.45	38.30	38.33	38.01	38.37	38.47	38.30	38.40	38.36	38.49	38.51	37.39	38.44	38.28	40.94	38.41	38.21	38.29
TiO2	0.18	0.12	0.14	0.06	0.13	0.10	0.12	0.10	0.16	0.07	0.15	0.04	0.02	0.01	0.04	0.05	0.07	0.01	0.06	0.17	0.29
Al2O3	21.47	21.60	21.56	21.69	21.40	21.60	21.45	21.35	21.38	21.78	21.38	21.67	21.73	21.63	24.14	21.72	21.58	21.55	21.72	21.52	21.28
Cr2O3	0.00	0.06	0.00	0.03	0.00	0.00	0.01	0.00	0.00	0.02	0.02	0.02	0.04	0.00	0.03	0.07	0.05	0.02	0.05	0.12	0.15
MgO	6.63	7.33	6.70	7.19	6.90	6.72	6.74	6.79	6.86	6.50	6.68	7.70	7.21	7.16	7.48	6.98	6.64	10.68	5.64	5.60	5.59
CaO	8.32	7.00	7.94	6.33	7.29	7.19	7.13	7.26	7.39	8.37	7.89	6.26	6.94	7.06	5.74	7.61	8.57	7.44	9.80	9.71	9.37
MnO	0.62	0.55	0.64	0.64	0.56	0.63	0.63	0.62	0.60	0.56	0.57	0.50	0.48	0.63	0.70	0.55	0.56	0.49	0.50	0.50	0.49
FeO	24.10	24.48	24.48	25.32	25.27	24.92	25.23	24.76	24.63	24.11	24.22	24.54	24.70	24.63	24.31	24.43	23.61	21.84	23.56	23.65	24.01
NiO	0.06	0.00	0.00	0.01	0.02	0.06	0.00	0.01	0.01	0.00	0.03	0.03	0.00	0.01	0.00	0.00	0.01	0.00	0.00	0.00	0.01
Na2O	0.04	0.04	0.04	0.03	0.03	0.03	0.02	0.03	0.03	0.02	0.06	0.00	0.03	0.01	0.02	0.00	0.03	0.04	0.01	0.05	0.06
K2O	0.00	0.00	0.01	0.01	0.01	0.02	0.00	0.00	0.02	0.00	0.01	0.13	0.01	0.01	0.00	0.00	0.00	0.10	0.00	0.01	0.00
Total	99.92	99.61	99.95	99.86	100.06	99.68	99.43	99.41	99.65	99.83	99.51	99.31	99.72	99.76	99.93	100.01	99.52	103.19	99.89	99.67	99.68
																	R/GA	R/DOL			
Mg#	32.89	34.80	32.77	33.62	32.74	32.48	32.24	32.84	33.19	32.44	32.97	35.87	34.21	34.14	35.41	33.75	33.37	46.58	29.90	29.67	29.34
Si	2.9804	2.9770	2.9764	2.9847	2.9776	2.9851	2.9723	2.9943	2.9936	2.9744	2.9921	2.9840	2.9857	2.9879	2.8804	2.9779	2.9795	3.0218	2.9855	2.9814	2.9900
Ti	0.0104	0.0067	0.0081	0.0033	0.0078	0.0056	0.0069	0.0057	0.0092	0.0043	0.0088	0.0025	0.0011	0.0004	0.0024	0.0027	0.0039	0.0006	0.0032	0.0099	0.0168
Al	1.9669	1.9785	1.9741	1.9844	1.9613	1.9823	1.9774	1.9641	1.9603	1.9935	1.9635	1.9870	1.9863	1.9783	2.1916	1.9834	1.9800	1.8745	1.9899	1.9788	1.9583
Cr	0.0000	0.0039	0.0000	0.0019	0.0000	0.0000	0.0006	0.0000	0.0000	0.0009	0.0010	0.0012	0.0022	0.0000	0.0016	0.0040	0.0030	0.0009	0.0028	0.0072	0.0091
Fe2+	1.5665	1.5911	1.5907	1.6436	1.6431	1.6231	1.6503	1.6160	1.6025	1.5659	1.5783	1.5967	1.6023	1.5986	1.5664	1.5831	1.5370	1.3477	1.5310	1.5430	1.5681
Mn	0.0409	0.0361	0.0422	0.0423	0.0369	0.0416	0.0415	0.0408	0.0395	0.0370	0.0376	0.0332	0.0315	0.0417	0.0453	0.0363	0.0371	0.0308	0.0330	0.0330	0.0323
Mg	0.7678	0.8492	0.7755	0.8323	0.7999	0.7807	0.7853	0.7901	0.7961	0.7521	0.7764	0.8930	0.8334	0.8285	0.8588	0.8064	0.7699	1.1753	0.6531	0.6509	0.6512
Ca	0.6927	0.5826	0.6613	0.5264	0.6074	0.5999	0.5976	0.6069	0.6157	0.6960	0.6591	0.5218	0.5764	0.5872	0.4739	0.6319	0.7148	0.5881	0.8164	0.8114	0.7836
Total	8.0257	8.0251	8.0284	8.0189	8.0339	8.0182	8.0319	8.0179	8.0170	8.0241	8.0168	8.0194	8.0189	8.0226	8.0205	8.0257	8.0252	8.0398	8.0149	8.0156	8.0094
Gr	22.88	19.27	21.84	17.53	19.91	19.97	19.70	20.14	20.43	23.09	21.87	17.33	19.14	19.48	16.35	20.91	23.66	18.90	27.21	27.00	26.09
Py	25.36	28.09	25.62	27.72	26.22	25.99	25.89	26.22	26.41	24.95	25.76	29.65	27.67	27.49	29.62	26.69	25.48	37.78	21.77	21.66	21.69
Alm	51.75	52.63	52.54	54.74	53.87	54.04	54.41	53.63	53.16	51.95	52.37	53.02	53.20	53.03	54.03	52.40	50.87	43.32	51.02	51.34	52.22

Table F2: continued

Sample	H321	H321	H321	H321	H321	H321	H321	H321	H321	H321	H321	H321	H321	H321	H321	H321	H323	H323	H323	H323	H323
Patch	58	59	60	61	62	63	64	65	66	67	68	69	70	71	72	73	1	2	3	4	6
Number	C2a	C2a	C2a	C2a	C2a	C2a	C2a	C2a	C2a	C2a	C2a	C2a	C2a	C2a	C2a	C2a	C6	C6	C6	C6	C6
P2O5	0.13	0.13	0.11	0.13	0.17	0.14	0.17	0.15	0.13	0.14	0.14	0.13	0.13	0.14	0.13	0.15	0.02	0.04	0.02	0.05	0.03
SiO2	38.36	38.09	38.35	38.19	38.13	38.32	38.28	38.26	38.22	38.27	38.21	38.47	38.36	38.31	38.08	38.33	37.99	38.20	37.81	38.03	38.21
TiO2	0.09	0.14	0.12	0.17	0.14	0.24	0.21	0.20	0.24	0.27	0.27	0.11	0.16	0.11	0.12	0.11	0.05	0.02	0.07	0.11	0.13
Al2O3	21.63	21.62	21.42	21.29	21.38	21.37	21.35	21.53	21.45	21.57	21.29	21.63	21.50	21.48	21.58	21.59	21.24	21.15	21.00	20.95	20.83
Cr2O3	0.00	0.00	0.00	0.00	0.05	0.02	0.00	0.00	0.00	0.00	0.04	0.00	0.04	0.11	0.04	0.04	0.06	0.00	0.08	0.03	0.04
MgO	5.75	5.97	5.99	5.88	5.87	5.80	5.81	5.85	5.99	5.98	5.89	6.00	5.83	5.61	5.61	5.67	6.66	5.96	5.62	5.80	6.24
CaO	8.67	7.59	7.39	7.75	8.09	8.28	8.33	8.42	8.44	8.55	8.82	8.47	8.90	9.17	9.26	9.98	8.16	9.17	9.94	9.02	8.50
MnO	0.54	0.52	0.54	0.47	0.51	0.50	0.46	0.53	0.45	0.52	0.52	0.47	0.45	0.45	0.52	0.42	0.43	0.33	0.44	0.49	0.53
FeO	24.59	25.48	25.67	25.57	25.34	24.87	24.93	24.96	24.55	24.23	24.07	24.81	24.27	24.01	24.26	23.46	24.36	24.15	23.46	24.31	24.55
NiO	0.00	0.00	0.05	0.00	0.00	0.03	0.02	0.00	0.01	0.00	0.04	0.07	0.00	0.01	0.03	0.02	0.00	0.00	0.00	0.00	0.01
Na2O	0.04	0.06	0.04	0.03	0.07	0.05	0.07	0.05	0.09	0.08	0.09	0.06	0.05	0.04	0.02	0.03	0.02	0.00	0.01	0.04	0.04
K2O	0.00	0.00	0.00	0.00	0.00	0.01	0.02	0.02	0.01	0.00	0.01	0.00	0.02	0.00	0.00	0.01	0.00	0.00	0.01	0.00	0.00
Total	99.67	99.60	99.67	99.48	99.74	99.61	99.65	99.98	99.57	99.60	99.38	100.20	99.71	99.43	99.64	99.80	98.98	99.02	98.46	98.82	99.11
																R/QZ	R/AM				
Mg#	29.41	29.47	29.37	29.07	29.23	29.35	29.34	29.48	30.32	30.55	30.38	30.11	29.98	29.40	29.17	30.10	32.76	30.56	29.92	29.84	31.19
Si	2.9898	2.9799	2.9978	2.9930	2.9834	2.9953	2.9937	2.9821	2.9856	2.9848	2.9911	2.9880	2.9905	2.9943	2.9759	2.9837	2.9784	2.9959	2.9858	2.9954	2.9994
Ti	0.0050	0.0085	0.0071	0.0100	0.0081	0.0143	0.0121	0.0115	0.0142	0.0158	0.0156	0.0062	0.0095	0.0064	0.0068	0.0063	0.0027	0.0010	0.0042	0.0063	0.0079
Al	1.9866	1.9932	1.9737	1.9661	1.9715	1.9683	1.9683	1.9777	1.9749	1.9830	1.9639	1.9798	1.9758	1.9787	1.9881	1.9810	1.9623	1.9551	1.9543	1.9451	1.9268
Cr	0.0000	0.0000	0.0001	0.0000	0.0028	0.0009	0.0000	0.0001	0.0001	0.0000	0.0024	0.0000	0.0025	0.0070	0.0023	0.0022	0.0034	0.0000	0.0050	0.0017	0.0027
Fe2+	1.6029	1.6668	1.6780	1.6760	1.6585	1.6256	1.6305	1.6272	1.6036	1.5802	1.5756	1.6119	1.5820	1.5692	1.5859	1.5274	1.5969	1.5841	1.5493	1.6013	1.6113
Mn	0.0354	0.0344	0.0354	0.0311	0.0338	0.0328	0.0304	0.0353	0.0298	0.0344	0.0343	0.0312	0.0297	0.0295	0.0346	0.0275	0.0285	0.0221	0.0297	0.0329	0.0351
Mg	0.6677	0.6965	0.6976	0.6868	0.6849	0.6753	0.6772	0.6803	0.6978	0.6950	0.6874	0.6944	0.6773	0.6534	0.6533	0.6576	0.7781	0.6972	0.6614	0.6811	0.7303
Ca	0.7241	0.6357	0.6187	0.6509	0.6784	0.6933	0.6978	0.7034	0.7066	0.7147	0.7397	0.7045	0.7436	0.7678	0.7753	0.8327	0.6856	0.7701	0.8405	0.7610	0.7145
Total	8.0118	8.0150	8.0083	8.0139	8.0213	8.0058	8.0100	8.0175	8.0127	8.0079	8.0101	8.0159	8.0109	8.0064	8.0221	8.0184	8.0360	8.0255	8.0303	8.0249	8.0280
Gr	24.18	21.20	20.66	21.60	22.45	23.16	23.22	23.36	23.49	23.91	24.63	23.40	24.76	25.68	25.72	27.59	22.40	25.24	27.55	25.01	23.38
Py	22.30	23.23	23.30	22.79	22.67	22.55	22.53	22.59	23.20	23.24	22.89	23.06	22.56	21.85	21.67	21.79	25.42	22.85	21.68	22.38	23.90
Alm	53.52	55.58	56.04	55.61	54.89	54.29	54.25	54.04	53.31	52.85	52.47	53.54	52.68	52.47	52.61	50.62	52.18	51.91	50.78	52.62	52.72

Table F2: continued

Sample	H323	H323	H323	H323	H323	H323	H323	H323	H323	H323	H323	H323	K670	K670	K670	K670	K670	K670	K670	K670	K670
Patch	7	8	10	11	12	14	15	16	17	18	19	20	1	2	5	6	8	9	11	12	14
Number	C6	C6	C6	C6	C6	C6	C6	C6	C6	C6	C6	C6	C3	C3	C3	C3	C3	C3	C3	C3	C3
P2O5	0.04	0.02	0.05	0.04	0.02	0.05	0.04	0.00	0.02	0.02	0.02	0.00	0.07	0.07	0.09	0.08	0.12	0.11	0.12	0.09	0.10
SiO2	38.03	37.89	37.55	39.20	37.73	37.83	37.76	37.89	37.45	37.45	37.60	37.65	37.76	37.83	37.32	37.33	36.86	37.24	36.88	38.37	36.93
TiO2	0.08	0.14	0.10	0.14	0.09	0.07	0.09	0.06	0.15	0.15	0.12	0.06	0.00	0.03	0.10	0.11	0.10	0.12	0.16	0.10	0.14
Al2O3	20.76	20.75	20.67	19.62	20.87	21.09	20.97	20.97	20.63	20.63	20.67	20.95	21.52	21.66	21.45	20.78	20.96	20.88	20.82	20.78	20.67
Cr2O3	0.00	0.00	0.00	0.03	0.00	0.00	0.01	0.03	0.05	0.05	0.04	0.05	0.03	0.00	0.00	0.00	0.04	0.05	0.00	0.02	0.06
MgO	6.17	6.13	6.11	6.52	6.59	6.43	6.35	6.31	5.20	5.20	4.96	5.80	6.21	5.92	4.82	4.39	3.63	3.50	3.54	3.20	3.57
CaO	8.07	8.15	8.52	7.81	6.95	7.84	7.74	7.74	9.97	9.97	10.17	9.36	6.44	7.03	8.46	8.24	9.12	9.00	8.81	8.22	8.76
MnO	0.52	0.45	0.54	0.42	0.49	0.51	0.52	0.50	0.48	0.48	0.56	0.35	0.32	0.44	0.75	0.83	0.81	0.94	0.98	1.18	1.03
FeO	25.06	25.71	24.56	23.50	25.62	24.91	24.89	25.33	24.39	24.39	24.31	24.08	27.06	27.31	26.77	27.05	27.49	27.59	27.54	26.68	27.66
NiO	0.00	0.03	0.00	0.04	0.00	0.04	0.04	0.01	0.04	0.04	0.01	0.00	0.06	0.03	0.00	0.00	0.00	0.00	0.00	0.02	0.02
Na2O	0.01	0.05	0.05	0.58	0.04	0.06	0.01	0.05	0.04	0.04	0.02	0.01	0.01	0.03	0.04	0.14	0.05	0.07	0.05	0.49	0.07
K2O	0.00	0.00	0.00	0.01	0.00	0.00	0.01	0.01	0.01	0.01	0.00	0.01	0.00	0.00	0.01	0.01	0.00	0.01	0.00	0.00	0.00
Total	98.73	99.31	98.16	97.92	98.40	98.84	98.43	98.91	98.42	98.42	98.48	98.32	99.48	100.34	99.81	98.95	99.18	99.51	98.90	99.15	98.99
												R/AM(DOL)	R/DOL								
Mg#	30.51	29.84	30.72	33.09	31.42	31.52	31.25	30.76	27.54	27.54	26.66	30.04	29.03	27.86	24.30	22.45	19.06	18.46	18.65	17.63	18.70
Si	3.0002	2.9827	2.9835	3.1064	2.9867	2.9806	2.9858	2.9854	2.9782	2.9782	2.9869	2.9801	2.9683	2.9565	2.9466	2.9811	2.9524	2.9716	2.9625	3.0585	2.9669
Ti	0.0047	0.0080	0.0061	0.0083	0.0055	0.0043	0.0056	0.0033	0.0089	0.0089	0.0073	0.0038	0.0000	0.0016	0.0062	0.0068	0.0062	0.0073	0.0097	0.0062	0.0086
Al	1.9298	1.9256	1.9357	1.8323	1.9468	1.9582	1.9546	1.9478	1.9334	1.9334	1.9354	1.9548	1.9939	1.9950	1.9959	1.9558	1.9781	1.9640	1.9710	1.9521	1.9566
Cr	0.0000	0.0000	0.0000	0.0020	0.0000	0.0000	0.0005	0.0021	0.0034	0.0034	0.0023	0.0029	0.0019	0.0000	0.0000	0.0000	0.0025	0.0033	0.0000	0.0010	0.0036
Fe2+	1.6532	1.6924	1.6320	1.5577	1.6961	1.6413	1.6462	1.6692	1.6222	1.6222	1.6151	1.5941	1.7789	1.7846	1.7675	1.8067	1.8412	1.8413	1.8501	1.7786	1.8580
Mn	0.0346	0.0301	0.0361	0.0282	0.0329	0.0343	0.0345	0.0333	0.0322	0.0322	0.0375	0.0236	0.0213	0.0293	0.0504	0.0559	0.0547	0.0633	0.0668	0.0797	0.0697
Mg	0.7258	0.7199	0.7235	0.7704	0.7771	0.7556	0.7482	0.7417	0.6164	0.6164	0.5871	0.6845	0.7276	0.6892	0.5673	0.5230	0.4335	0.4169	0.4241	0.3806	0.4274
Ca	0.6819	0.6876	0.7256	0.6629	0.5894	0.6617	0.6557	0.6536	0.8498	0.8498	0.8653	0.7935	0.5420	0.5882	0.7154	0.7048	0.7824	0.7697	0.7579	0.7020	0.7538
Total	8.0302	8.0465	8.0425	7.9681	8.0344	8.0360	8.0310	8.0364	8.0445	8.0445	8.0369	8.0372	8.0338	8.0444	8.0492	8.0342	8.0511	8.0374	8.0422	7.9587	8.0445
Gr	22.28	22.18	23.55	22.16	19.24	21.63	21.50	21.33	27.52	27.52	28.21	25.83	17.78	19.21	23.45	23.22	25.59	25.42	25.00	24.54	24.80
Py	23.71	23.22	23.48	25.76	25.37	24.70	24.53	24.20	19.96	19.96	19.14	22.28	23.87	22.51	18.60	17.24	14.18	13.77	13.99	13.30	14.06
Alm	54.01	54.59	52.97	52.08	55.38	53.66	53.97	54.47	52.52	52.52	52.65	51.89	58.35	58.28	57.95	59.54	60.23	60.81	61.02	62.16	61.13

Table F2: continued

Sample	K670	K670	K670	K670	K670	K670	K670	K670	K670	K670	K670	K670	K670	K670	K670	K670	K670	K670	K670	K670
Patch	15	16	17	18	20	21	22	23	24	25	115	116	117	118	119	120	121	123	125	126	127
Number	C3	C3	C3	C3	C3	C3	C3	C3	C3	C3	C6	C6	C6	C6	C6	C6	C6	C6	C6	C6	C6
P2O5	0.09	0.10	0.10	0.10	0.09	0.07	0.10	0.10	0.09	0.09	0.06	0.07	0.10	0.08	0.10	0.09	0.08	0.08	0.13	0.10	0.13
SiO2	36.97	36.62	36.53	36.64	36.54	36.65	36.63	36.37	36.79	37.16	37.86	37.65	37.75	37.26	37.29	37.19	37.08	37.15	37.03	36.98	37.89
TiO2	0.16	0.15	0.13	0.16	0.14	0.32	0.12	0.10	0.13	0.13	0.01	0.04	0.05	0.05	0.10	0.13	0.10	0.13	0.14	0.12	0.11
Al2O3	20.91	20.75	20.70	20.79	20.70	20.51	20.74	20.55	20.76	21.07	21.55	21.50	21.45	21.22	21.06	21.04	20.99	20.94	21.04	20.79	20.53
Cr2O3	0.00	0.01	0.02	0.02	0.00	0.04	0.04	0.00	0.00	0.07	0.03	0.00	0.00	0.05	0.00	0.00	0.00	0.00	0.00	0.00	0.00
MgO	3.57	3.36	2.90	2.79	3.01	2.96	3.12	3.29	3.87	4.24	6.18	5.42	5.20	4.54	3.97	3.77	3.77	3.61	3.76	3.81	3.76
CaO	8.58	8.58	8.75	8.88	8.38	8.44	8.57	8.48	7.91	7.97	6.72	7.07	7.57	8.14	8.20	8.60	8.29	8.65	8.84	8.61	8.45
MnO	1.08	0.92	0.95	0.88	0.86	0.76	0.72	0.72	0.71	0.55	0.41	0.32	0.39	0.53	0.77	0.95	0.95	1.45	1.49	1.45	1.62
FeO	27.94	28.29	29.06	28.92	29.03	28.78	29.13	29.30	28.41	27.98	27.15	27.43	27.49	27.51	28.25	27.71	27.81	27.54	27.11	26.78	26.90
NiO	0.00	0.00	0.00	0.00	0.00	0.00	0.00	0.00	0.00	0.00	0.01	0.00	0.03	0.03	0.00	0.01	0.03	0.00	0.02	0.01	0.01
Na2O	0.06	0.04	0.04	0.05	0.06	0.03	0.06	0.04	0.02	0.00	0.03	0.03	0.03	0.02	0.01	0.04	0.03	0.02	0.05	0.03	0.04
K2O	0.00	0.02	0.01	0.02	0.00	0.00	0.00	0.00	0.00	0.01	0.01	0.00	0.00	0.01	0.00	0.01	0.01	0.00	0.00	0.00	0.01
Total	99.37	98.83	99.18	99.24	98.80	98.56	99.22	98.93	98.69	99.28 R/QZ	100.02 R/QZ	99.52	100.06	99.43	99.75	99.52	99.12	99.56	99.62	98.67	99.44
Mg#	18.57	17.48	15.08	14.68	15.59	15.51	16.04	16.68	19.54	21.25	28.85	26.06	25.20	22.73	20.04	19.50	19.46	18.94	19.83	20.21	19.94
Si	2.9586	2.9534	2.9482	2.9528	2.9556	2.9664	2.9510	2.9428	2.9611	2.9617	2.9627	2.9679	2.9670	2.9593	2.9647	2.9639	2.9668	2.9640	2.9529	2.9700	3.0161
Ti	0.0095	0.0090	0.0080	0.0097	0.0088	0.0195	0.0070	0.0058	0.0081	0.0077	0.0008	0.0021	0.0028	0.0027	0.0060	0.0076	0.0059	0.0080	0.0083	0.0074	0.0063
Al	1.9725	1.9722	1.9694	1.9748	1.9731	1.9563	1.9694	1.9595	1.9694	1.9786	1.9877	1.9971	1.9875	1.9866	1.9733	1.9760	1.9794	1.9685	1.9776	1.9680	1.9261
Cr	0.0002	0.0006	0.0011	0.0010	0.0000	0.0026	0.0027	0.0000	0.0000	0.0047	0.0021	0.0000	0.0000	0.0028	0.0003	0.0000	0.0000	0.0000	0.0000	0.0000	0.0000
Fe2+	1.8702	1.9079	1.9614	1.9489	1.9640	1.9484	1.9627	1.9828	1.9126	1.8651	1.7771	1.8084	1.8071	1.8268	1.8778	1.8470	1.8610	1.8371	1.8079	1.7987	1.7908
Mn	0.0729	0.0628	0.0652	0.0602	0.0589	0.0520	0.0488	0.0490	0.0485	0.0374	0.0272	0.0216	0.0260	0.0354	0.0519	0.0640	0.0643	0.0977	0.1008	0.0984	0.1091
Mg	0.4264	0.4041	0.3483	0.3353	0.3626	0.3576	0.3749	0.3969	0.4646	0.5032	0.7206	0.6374	0.6089	0.5374	0.4706	0.4474	0.4496	0.4291	0.4471	0.4556	0.4461
Ca	0.7353	0.7411	0.7570	0.7669	0.7260	0.7319	0.7395	0.7349	0.6820	0.6806	0.5635	0.5967	0.6371	0.6922	0.6980	0.7347	0.7107	0.7391	0.7553	0.7405	0.7202
Total	8.0455	8.0512	8.0585	8.0496	8.0490	8.0347	8.0560	8.0716	8.0462	8.0390	8.0416	8.0314	8.0364	8.0432	8.0425	8.0405	8.0377	8.0437	8.0500	8.0386	8.0146
Gr	24.25	24.27	24.68	25.13	23.78	24.09	24.03	23.60	22.29	22.32	18.41	19.61	20.87	22.65	22.91	24.25	23.52	24.59	25.09	24.73	24.36
Py	14.06	13.24	11.36	10.99	11.88	11.77	12.18	12.74	15.19	16.50	23.54	20.95	19.94	17.58	15.45	14.77	14.88	14.28	14.85	15.21	15.08
Alm	61.68	62.49	63.96	63.87	64.34	64.14	63.78	63.66	62.52	61.17	58.05	59.44	59.19	59.77	61.64	60.98	61.60	61.13	60.06	60.06	60.56

Table F2: continued

Sample	K670	K670	K670	K670	K670	K670	K670	K670	K670	K670	D521	D521	D521	D521	D521	D521	D521	D521	D521	D521	D521
Patch	128	130	131	132	133	135	136	137	138	139	43	44	45	46	47	48	49	50	51	52	53
Number	C6	C6	C6	C6	C6	C6	C6	C6	C6	C6	C1	C1	C1	C1	C1	C1	C1	C1	C1	C1	C1
P2O5	0.10	0.15	0.09	0.12	0.12	0.11	0.11	0.04	0.09	0.08	0.06	0.07	0.06	0.09	0.08	0.05	0.08	0.06	0.05	0.08	0.08
SiO2	37.36	37.25	36.69	37.24	37.24	36.73	37.51	37.38	37.38	37.60	38.53	38.75	38.81	38.09	38.36	38.17	38.31	38.35	38.29	38.37	38.24
TiO2	0.20	0.22	0.02	0.13	0.09	0.04	0.12	0.02	0.01	0.01	0.01	0.02	0.00	0.02	0.01	0.03	0.01	0.01	0.00	0.01	0.00
Al2O3	20.42	20.75	20.95	20.96	21.21	20.92	21.01	21.21	21.38	21.64	21.74	21.72	21.79	21.65	21.68	21.58	21.60	21.64	21.51	21.68	21.50
Cr2O3	0.00	0.00	0.02	0.02	0.00	0.07	0.12	0.20	0.05	0.06	0.00	0.03	0.03	0.02	0.02	0.04	0.00	0.01	0.00	0.04	0.02
MgO	3.52	3.69	3.77	4.07	4.40	4.17	4.54	5.56	6.03	7.22	8.70	7.91	7.97	6.89	6.69	6.38	6.74	6.89	6.54	6.43	6.49
CaO	9.28	9.59	7.72	9.22	8.24	8.10	8.39	6.11	6.04	5.70	4.74	4.92	4.82	5.00	5.04	5.05	5.24	4.58	4.89	4.83	4.68
MnO	1.87	1.50	1.69	1.26	1.21	0.97	0.66	0.71	0.69	0.39	0.12	0.13	0.20	0.25	0.29	0.24	0.19	0.30	0.18	0.22	0.30
FeO	26.33	26.31	27.83	26.33	26.98	27.51	26.73	27.90	27.74	25.81	24.84	26.03	26.30	27.45	27.82	28.53	27.78	28.29	28.49	28.84	28.61
NiO	0.00	0.00	0.05	0.06	0.00	0.00	0.00	0.04	0.00	0.02	0.00	0.00	0.00	0.00	0.06	0.07	0.00	0.00	0.00	0.00	0.00
Na2O	0.23	0.06	0.04	0.04	0.04	0.03	0.03	0.01	0.03	0.02	0.02	0.03	0.02	0.03	0.01	0.01	0.02	0.02	0.01	0.01	0.02
K2O	0.00	0.00	0.00	0.01	0.00	0.00	0.00	0.02	0.01	0.00	0.02	0.01	0.02	0.00	0.00	0.01	0.00	0.00	0.00	0.01	0.00
Total	99.31	99.53	98.87	99.43	99.52	98.64	99.21	99.18	99.43	98.54	98.78	99.61	100.03	99.50	100.06	100.16	99.96	100.15	99.96	100.53	99.94
										R/QZ	R/BD(CC)										
Mg#	19.23	19.98	19.45	21.60	22.52	21.28	23.23	26.21	27.92	33.26	38.44	35.13	35.08	30.92	29.99	28.49	30.20	30.28	29.04	28.45	28.80
Si	2.9908	2.9688	2.9534	2.9641	2.9579	2.9523	2.9775	2.9652	2.9537	2.9621	2.9943	3.0021	2.9970	2.9816	2.9895	2.9827	2.9876	2.9869	2.9921	2.9859	2.9917
Ti	0.0119	0.0134	0.0010	0.0077	0.0053	0.0024	0.0074	0.0013	0.0005	0.0006	0.0005	0.0009	0.0001	0.0012	0.0008	0.0015	0.0004	0.0008	0.0002	0.0004	0.0000
Al	1.9263	1.9489	1.9875	1.9664	1.9855	1.9816	1.9662	1.9824	1.9910	2.0092	1.9908	1.9831	1.9831	1.9970	1.9913	1.9875	1.9855	1.9863	1.9807	1.9885	1.9826
Cr	0.0000	0.0000	0.0015	0.0011	0.0001	0.0043	0.0077	0.0128	0.0030	0.0038	0.0001	0.0017	0.0019	0.0015	0.0013	0.0027	0.0000	0.0006	0.0000	0.0025	0.0014
Fe2+	1.7630	1.7538	1.8737	1.7522	1.7920	1.8489	1.7744	1.8504	1.8332	1.7007	1.6140	1.6864	1.6984	1.7967	1.8134	1.8647	1.8117	1.8424	1.8617	1.8769	1.8718
Mn	0.1268	0.1013	0.1153	0.0846	0.0815	0.0658	0.0442	0.0475	0.0463	0.0262	0.0076	0.0086	0.0132	0.0164	0.0191	0.0157	0.0125	0.0197	0.0116	0.0148	0.0196
Mg	0.4197	0.4379	0.4525	0.4828	0.5210	0.4999	0.5371	0.6571	0.7100	0.8474	1.0079	0.9134	0.9179	0.8042	0.7769	0.7429	0.7838	0.8003	0.7619	0.7463	0.7572
Ca	0.7958	0.8192	0.6662	0.7859	0.7009	0.6971	0.7135	0.5190	0.5110	0.4810	0.3944	0.4084	0.3989	0.4194	0.4210	0.4230	0.4377	0.3818	0.4091	0.4030	0.3920
Total	8.0342	8.0433	8.0511	8.0446	8.0441	8.0524	8.0281	8.0358	8.0488	8.0308	8.0097	8.0046	8.0105	8.0180	8.0133	8.0207	8.0192	8.0188	8.0174	8.0182	8.0163
Gr	26.72	27.21	22.26	26.02	23.25	22.89	23.59	17.15	16.73	15.88	13.08	13.58	13.23	13.89	13.98	13.96	14.43	12.62	13.49	13.32	12.98
Py	14.09	14.54	15.12	15.98	17.29	16.41	17.75	21.71	23.25	27.98	33.41	30.36	30.44	26.63	25.80	24.51	25.84	26.46	25.12	24.66	25.07
Alm	59.19	58.25	62.62	58.00	59.46	60.70	58.66	61.14	60.02	56.15	53.51	56.06	56.33	59.49	60.22	61.53	59.73	60.92	61.39	62.02	61.96

Table F2: continued

Sample	D521	D521	D521	D521	H324	H324	H324	H324	H324	H324	H324	H324	H324	H324	H324	H324	H324	H324	H324
Patch	54	55	56	57	1	2	3	4	5	6	7	8	9	10	11	12	13	14	15
Number	C1	C1	C1	C1	C1	C1	C1	C1	C1	C1	C1	C1	C1	C1	C1	C1	C1	C1	C1
P2O5	0.05	0.10	0.07	0.10	0.10	0.15	0.12	0.16	0.15	0.15	0.16	0.23	0.15	0.14	0.12	0.16	0.14	0.11	0.11
SiO2	38.39	38.21	38.42	38.63	38.36	38.32	38.29	38.50	38.20	38.41	38.27	38.16	38.11	38.11	38.31	38.24	38.47	38.43	38.43
TiO2	0.02	0.00	0.01	0.03	0.04	0.03	0.01	0.17	0.04	0.07	0.07	0.11	0.07	0.07	0.20	0.09	0.12	0.02	0.00
Al2O3	21.60	21.76	21.63	21.61	21.64	21.67	21.64	21.50	21.58	21.60	21.65	21.44	21.55	21.39	21.37	21.56	21.52	21.48	21.57
Cr2O3	0.00	0.01	0.02	0.02	0.02	0.00	0.03	0.03	0.01	0.00	0.00	0.02	0.00	0.02	0.00	0.00	0.03	0.01	0.02
MgO	6.77	7.30	6.65	6.15	5.55	5.25	4.80	4.99	5.28	5.14	5.31	4.99	5.08	5.03	4.97	5.39	5.34	5.73	5.61
CaO	4.77	4.92	4.70	4.55	8.23	8.64	9.79	9.04	7.92	8.31	7.65	8.67	7.96	8.57	8.87	8.21	8.55	7.67	8.52
MnO	0.20	0.20	0.17	0.13	0.54	0.54	0.47	0.49	0.40	0.58	0.58	0.56	0.52	0.46	0.53	0.44	0.49	0.51	0.60
FeO	28.07	27.97	28.66	29.85	25.37	25.66	24.82	25.22	26.18	25.91	26.09	25.92	26.27	25.70	25.50	26.21	25.81	25.71	25.05
NiO	0.02	0.01	0.00	0.00	0.01	0.00	0.09	0.03	0.00	0.04	0.01	0.00	0.03	0.00	0.09	0.05	0.00	0.00	0.00
Na2O	0.01	0.01	0.00	0.05	0.01	0.01	0.01	0.04	0.02	0.03	0.02	0.05	0.03	0.04	0.06	0.03	0.04	0.03	0.02
K2O	0.01	0.00	0.01	0.02	0.01	0.00	0.00	0.00	0.00	0.01	0.01	0.01	0.00	0.00	0.01	0.00	0.00	0.02	0.01
Total	99.91	100.50	100.35	101.15	99.88	100.26	100.08	100.18	99.79	100.26	99.81	100.15	99.77	99.53	100.03	100.40	100.52	99.73	99.93
			R/BD(CORE)		R/BD														R/BD
Mg#	30.05	31.76	29.27	26.86	28.06	26.73	25.64	26.05	26.43	26.14	26.60	25.56	25.65	25.86	25.80	26.82	26.95	28.44	28.53
Si	2.9947	2.9656	2.9900	2.9973	2.9924	2.9863	2.9895	3.0014	2.9917	2.9962	2.9950	2.9876	2.9899	2.9941	2.9969	2.9822	2.9910	3.0027	2.9952
Ti	0.0009	0.0000	0.0007	0.0019	0.0024	0.0015	0.0008	0.0099	0.0026	0.0044	0.0040	0.0067	0.0040	0.0042	0.0115	0.0054	0.0071	0.0013	0.0001
Al	1.9860	1.9902	1.9843	1.9763	1.9894	1.9902	1.9910	1.9756	1.9920	1.9855	1.9967	1.9778	1.9932	1.9812	1.9705	1.9821	1.9724	1.9781	1.9814
Cr	0.0000	0.0007	0.0010	0.0015	0.0014	0.0000	0.0018	0.0015	0.0009	0.0000	0.0000	0.0012	0.0000	0.0010	0.0000	0.0003	0.0019	0.0006	0.0012
Fe2+	1.8313	1.8155	1.8655	1.9368	1.6550	1.6720	1.6207	1.6444	1.7147	1.6898	1.7079	1.6968	1.7237	1.6887	1.6683	1.7096	1.6785	1.6800	1.6327
Mn	0.0129	0.0131	0.0113	0.0084	0.0360	0.0358	0.0314	0.0325	0.0268	0.0384	0.0381	0.0368	0.0347	0.0307	0.0354	0.0288	0.0324	0.0337	0.0399
Mg	0.7867	0.8451	0.7720	0.7113	0.6456	0.6098	0.5590	0.5794	0.6160	0.5980	0.6191	0.5826	0.5948	0.5890	0.5799	0.6267	0.6191	0.6678	0.6518
Ca	0.3990	0.4087	0.3917	0.3785	0.6875	0.7215	0.8190	0.7554	0.6646	0.6945	0.6417	0.7269	0.6692	0.7216	0.7437	0.6861	0.7123	0.6424	0.7114
Total	8.0115	8.0389	8.0166	8.0120	8.0098	8.0171	8.0132	8.0002	8.0093	8.0067	8.0026	8.0163	8.0095	8.0105	8.0063	8.0212	8.0147	8.0067	8.0135
Gr	13.22	13.32	12.93	12.51	23.01	24.02	27.31	25.36	22.19	23.29	21.62	24.18	22.40	24.06	24.86	22.70	23.67	21.48	23.75
Py	26.07	27.53	25.48	23.50	21.61	20.31	18.64	19.45	20.57	20.05	20.85	19.38	19.91	19.64	19.38	20.73	20.57	22.33	21.76
Alm	60.70	59.15	61.58	63.99	55.39	55.67	54.05	55.20	57.24	56.66	57.53	56.44	57.69	56.30	55.76	56.56	55.77	56.18	54.50